Growth and anisotropic transport properties of self-assembled InAs nanostructures in InP

DISSERTATION

zur Erlangung des akademischen Grades
doctor rerum naturalium
(Dr. rer. nat.)
im Fach Physik

eingereicht an der
Mathematisch-Naturwissenschaftlichen Fakultät I
der Humboldt-Universität zu Berlin

von
Dipl.-Phys. Oliver Bierwagen
geboren am 30.12.1975 in Berlin

Präsident der Humboldt-Universität zu Berlin:
Prof. Dr. Christoph Markschies

Dekan der Mathematisch-Naturwissenschaftlichen Fakultät I:
Prof. Dr. Christian Limberg

Gutachter:

1. Prof. W. T. Masselink
2. Prof. R. Fornari
3. Prof. G. J. Salamo

eingereicht am:	13.02.2007
Tag der mündlichen Prüfung:	14.05.2007

Abbreviations/Symbols

0D, 1D, 2D, 3D	zero-, one-, two-, three-dimensional
N	in sample names : grown on nominally oriented (N) substrate
O	in sample names : grown on vicinal (A) substrate, 2° off toward [110]
P	in sample names : grown on vicinal (B) substrate, 2° off toward [$\bar{1}$10]
Q	in sample names : grown on vicinal (C) substrate, 2° off toward [100]
B	magnetic field
e	electron charge
E	energy
E_C, E_V, E_F	conduction (sub)band edge, valence (sub)band edge
E_F	Fermi energy
F	electric field
h, $\hbar$	Planck constant, $h/2\pi$, reduced Planck constant
j	current density
k	Boltzmann constant
k_F	Fermi wavevector
l_e, l_Φ	mean free path, dephasing length
λ_F	Fermi wavelength
m^*, m_e	effective mass, mass of the free electron
ML	monolayer, equals half the lattice constant
μ	carrier mobility
n	carrier density (positive for electrons)
ω_c	cyclotron frequency
QD	quantum dot
QDash	quantum dash - short quantum wire, elongated quantum dot
QW	quantum well
QWr	quantum wire
R_H, r_H	Hall coefficient, Hall scattering factor
σ, ρ, $R_\square$	conductivity, resistivity, sheet resistance
ρ^{2D}	2D density of states
t	time
T	absolute temperature
τ, τ_Φ	momentum relaxation time, dephasing time
v_F	Fermi velocity

Abstract

Self-assembled InAs nanostructures in InP, comprising quantum wells, quantum wires, and quantum dots, are studied in terms of their formation and properties. In particular, the structural, optical, and anisotropic transport properties of the nanostructures are investigated. The focus is a comprehending exploration of the anisotropic in-plane transport in large ensembles of laterally coupled InAs nanostructures.

The self-assembled Stranski-Krastanov growth of InAs nanostructures is studied by gas-source molecular beam epitaxy on both nominally oriented and vicinal InP(001). I demonstrate that the off-cut direction of vicinal substrates — largely independent of growth conditions — determines the morphology of nanostructures, i.e. quantum dot, quantum wire, or two-dimensional growth; whereas, on nominally oriented substrates, the morphology is very strongly dependent on the growth conditions.

The optical properties of InAs nanostructures embedded in InP are investigated, and their principal applicability for optical devices, particularly operating in the technologically important 1.55 μm wavelength range, is shown. Optical polarization of the interband transitions arising from the nanostructure type is demonstrated by photoluminescence and transmission spectroscopy.

The experimentally convenient four-contact van der Pauw Hall measurement of rectangularly shaped semiconductors, usually applied to isotropic systems, is extended to yield the anisotropic transport properties. This extended van der Pauw method is greatly used for the transport measurements.

Temperature dependent transport measurements are performed in large ensembles of laterally closely spaced nanostructures. The transport of quantum wire-, quantum dash- and quantum dot containing samples is highly anisotropic with the principal axes of conductivity aligned to the <110> directions. The direction of higher mobility is [$\bar{1}$10], which is parallel to the direction of the quantum wires. In extreme cases, the anisotropies exceed 30 for electrons, and 100 for holes. The extreme anisotropy for holes is due to diffusive transport through extended states in the [$\bar{1}$10] , and hopping transport through laterally localized states in the [110] direction, within the same sample. The data is discussed in terms of two-dimensional carrier systems with anisotropic scattering, and in terms of coupled 1D or 0D structures:
In the anisotropic-2D context, the principal mobilities at low temperature are dominated by interface roughness scattering in the [110] direction, and by remote impurity scattering in the [$\bar{1}$10] direction.

In the coupled nanostructure context, I demonstrate that the transport anisotropy results from *directionally anisotropic tunnel coupling* between adjacent nanostructures rather than from the nanostructure shape anisotropy.

The contribution to conductivity resulting from weak localization — a quantum mechanical effect based on electron self-interference — is studied in InAs quantum wells, coupled quantum wires, and coupled quantum dots. It is demonstrated that the weak-localization correction shows a directional anisotropy equal to the anisotropy of the total conductivity, which is typical for anisotropic 2-dimensional systems. This result suggests that even for a conductivity anisotropy ratio as high as 38, the coupling between the quantum wires plays a more important role than the quasi-one-dimensional nature of the electron transport in describing the quantum mechanical contributions due to weak localization.

A novel 5-terminal electronic switching device based on gate-controlled transport anisotropy is proposed. The gate-control of the transport anisotropy in modulation-doped, self-organized InAs quantum wires embedded in InP is demonstrated. These quantum wires are shown to be a candidate for implementation of the device.

Keywords:
InAs on InP, MBE, self-assembled growth, nanostructure, quantum well, quantum wire, quantum dot, transport anisotropy, coupling, scattering, tunneling, hopping, van der Pauw, photoluminescence, transmission, absorption, polarization

Zusammenfassung

Diese Arbeit untersucht das Wachstum und die Eigenschaften von selbstorganisierten InAs Nanostrukturen in InP. Die Nanostrukturen - Quantengräben, Quantendrähte, und Quantenpunkte - werden bezüglich ihrer Struktur, ihrer optischen Eigenschaften und ihrer anisotropen Transporteigenschaften untersucht. Der Schwerpunkt ist dabei eine umfassende Untersuchung des lateralen Ladungsträgertransports in grossen Ensembles lateral gekoppelter Nanostrukturen.

Das selbstorganisierte Stranski-Krastanov Wachstum von InAs auf exakt orientiertem und vizinalem InP(001) wird mittels Gasquellen-Molekularstrahlepitaxie untersucht. Es wird gezeigt, dass die Misorientierung des vizinalen InP, weitestgehend unabhängig von den Wachstumsbedingungen, die Morphologie (Quantendraht oder Quantenpunkt) der Nanostrukturen bestimmt. Auf exakt orientiertem Substrat, hingegen, hängt die Morphologie stark von den Wachstumsbedingungen ab.

Die Untersuchung der optischen Eigenschaften von InAs Nanostrukturen in InP zeigen die prinzipielle Anwendbarkeit dieser Strukturen für Optische Bauelemente, insbesondere im technologisch interessanten Bereich von 1.55 μm. Die optische Polarisation der Interbandübergänge aufgrund des Nanostrukturtyps wird mittels Photoluminszenz- und Transmissionsspektroskopie demonstriert.

Die experimentell unaufwändige Vierkontakt van der Pauw Hall Messung rechteckiger Halbleiter wird normalerweise zur Ermittlung isotroper Transporteigeschaften eingesetzt. Eine Erweiterung dieser Methode zur Ermittlung der anisotropen Transporteigenschaften wird entwickelt und experimentell verifiziert. Die erweiterte van der Pauw Methode wird im Rahmen dieser Arbeit routinemäßig eingesetzt.

Temperaturabhängige Transportmessungen werden an grossen Ensembles von dicht gepackten Quantendrähten, und Quantenpunkten durchgeführt. Es zeigt sich, dass die Transporteigenschaften anisotrop sind. Die Hauptachsen der Leitfähigkeit sind entlang der <110> Richtungen. Die [$\bar{1}$10] Richtung, parallel zu den Quantendrähten, ist dabei die Richtung der höheren Leitfähigkeit. In Extremfällen übersteigt die Transportanisotropie Werte von 30 für Elektronen und 100 für Löcher. Die hohe Anistropie für Löcher basiert auf diffusiven Transport in der [$\bar{1}$10] Richtung und Hopping Transport in der [110] Richtung, innerhalb der selben Probe. Die Transportdaten werden im

Kontext eines 2-dimensionalen Ladungsträgersystems mit anisotropen Beweglichkeiten, und im Kontext gekoppelter 1- oder 0-dimensionaler Nanostrukturen diskutiert:
Im Kontext eines anisotropen 2-dimensionalen Systems, sind die Beweglichkeiten bei kryogenischen Temperaturen dominiert von Grenzflächenrauhigkeitsstreuung (interface roughness scattering) entlang der [110] Richtung und durch Streuung an entfernten Störstellen (remote impurity scattering) entlang der [$\bar{1}$10] Richtung.
Im Kontext gekoppelter Nanostrukturen, wird gezeigt, dass die Transportanisotropie auf *anisotroper Tunnelkopplung* zwischen benachbarten Nanostrukturen beruht, und weniger durch die Form der Nanostruktur bestimmt wird.

Der Beitrag zur Leitfähigkeit durch die Schwache Lokalisierung — einem quantenmechanischen Effekt der Selbstinterferenz des Elektrons — wird untersucht in Quantengräben, gekoppelten Quantedrähten, und gekoppelten Quantenpunkten. Es wird gezeigt, dass der Beitrag durch die Schwache Lokalisierung die gleiche Anisotropie aufweist wie die Leitfähigkeit selbst, was typisch für anisotrope 2-dimensionale Ladungsträgersysteme ist. Dieses Resultat legt nahe, dass, selbst für eine Anisotropie von 38, die Kopplung zwischen den Quantendrähten eine wichtigere Rolle in der Beschreibung der Schwachen Lokalisierung in diesen Proben spielt als der quasi 1-dimensionale Charakter des Elektronenstransports.

Ein neuartiges elektronisches Bauelement basierend auf Gate-kontrollierter Transportanisotropie wird vorgeschlagen. Die Kontrolle der Transportanisotropie von InAs Quantendrähten in InP mittels einer Gatelektrode wird demonstriert. Es wird gezeigt, dass dies Quantendrähte für eine Implementierung des Bauelements geeignet sind.

Schlagwörter:
InAs auf InP, MBE, Selbstorganisation, Nanostruktur, Quantengraben, Quantendraht, Quantenpunkt, Transport, Anisotropie, Kopplung, Streuung, Tunneln, Hopping Transport, van der Pauw, Photolumineszenz, Transmission, Absorption, Polarisation

Parts of this work have been published as

- O. Bierwagen, C. Walther, W. T. Masselink, and K.-J. Friedland, *Weak localization in laterally coupled quantum wires*, Phys. Rev. B **67**, 195331–195335 (2003).
- O. Bierwagen, C. Walther, W. T. Masselink, and K.-J. Friedland, *Weak localization in laterally-coupled quantum wires*, DPG Frühjahrstagung, Dresden (2003).
- O. Bierwagen, R. Pomraenke, S. Eilers and W. T. Masselink, *Mobility and carrier density in materials with anisotropic conductivity revealed by van der Pauw measurements*, Phys. Rev. B. **70**, 165307(1–6) (2004).
- H. Kirmse, W. Neumann, O. Bierwagen, R. Pomraenke, and W. T. Masselink, *Structural and chemical characterization of multi-stacked InAs nanowires on vicinal InP by TEM*, The 13th European Microscopy Congress, University of Antwerp, Belgium (2004).
- O. Bierwagen and W. T. Masselink, *Self-organized growth of InAs quantum wires and dots on InP(001): The role of vicinal substrates*, Appl. Phys. Lett. **86**, 113110(1–3) (2005).
- Vas. P. Kunets, Yu. I. Mazur, G. J. Salamo, O. Bierwagen, and W. T. Masselink, *Doped-channel micro-Hall devices: Size and geometry effects*, J. Appl. Phys. **98**, 094503(1–5) (2005).
- O. Bierwagen and W. T. Masselink, *The effect of substrate off-cut on the morphology of self- organized InAs nanostructures on InP(001)*, The 17th Indium Phosphide and Related Materials Conference, Glasgow, Scotland, UK (2005).
- O. Bierwagen and W. T. Masselink, *Electronic switching device based on gate-controlled conductivity anisotropy*, Appl. Phys. Lett. **90**, 133507(1–3) (2007).
- O. Bierwagen, R. Pomraenke, S. Dreßler, and W. T. Masselink, *Anisotropic tunneling and transport in planar arrays of coupled nanostructures*, submitted to Phys. Rev. Lett. (2007).

Contents

List of Figures

List of Tables

Chapter 1

Introduction

Semiconductor nanostructures constitute an active area of research due to their unique physical properties, mostly based on their characteristic density of states. Fig. 1.1 shows different types of nanostructures. The most widely applied and investigated nanostructure is the quantum well (QW) in which carriers can move freely in two directions but are quantized in the other direction. Today's high electron mobility transistors (HEMTS) and semiconductor lasers, used for information and communication technology, are based on semiconductor QWs. The preparation of semiconductor QWs has been enabled by epitaxial growth techniques that allow the growth of high quality crystal layers with precision down to monoatomic layers. Further

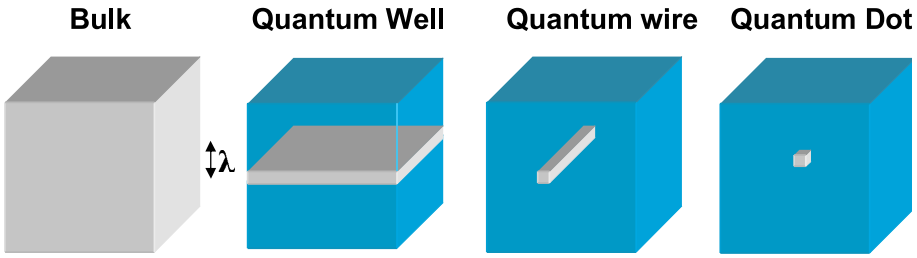

Figure 1.1: Schematic of different types of confinement for charge carriers. Carriers with de Broglie wavelength λ are confined to the light grey volume. Confinement of the carriers in one direction on length scales smaller or of the order of λ leads to effective quantization effects in this direction. Since λ is typically on the order of 10 nm, nanometer size structures "nanostructures" result in these quantization effects. Carriers can move freely in a "bulk" material, whereas they are confined in one, two, or all three directions in a "quantum well", "quantum wire", or "quantum dot", respectively.

confinement so that carriers can move freely only in one direction results in a

quantum wire (QWr) and the complete confinement in all three dimensions results in a quantum dot (QD). The intermediate case between QWr and QD is a significantly elongated QDs, which is called quantum dash (QDash) or quantum stick. *Specifically, the confinement will effectively reduce the dimensionality, if the energy level spacing of the present carriers due to the confinement is greater than the level broadening (e.g. thermal broadening k_BT).*

The quasi-1-dimensional and quasi-0-dimensional nanostructures (QWr and QD) are not only interesting for the understanding of their physics but offer improvements of electronic devices such as lasers [10] and transistors [146, 147], and the realization of novel devices such as single photon sources [111], all of them based on the peaked density of electronic states in 1D and 0D systems.

A quantum well is created, as schematically shown in Fig. 1.1, in a semiconductor heterostructure consisting of the well material (light grey) embedded in the surrounding barrier material. In this work InAs is used as the well material and InP forms the barrier. These semiconductors show a type-I band alignment, i.e. conduction and valence band form a potential well in the InAs (see Fig. 1.2, left) for electrons and holes, respectively. The resulting localization of electrons and holes to the InAs allows for transport investigations of the InAs nanostructures using electrons *and* holes as probes, which is done in this work. In addition, the spatial overlap of electrons and holes localized to the InAs is a prerequisite for efficient interband transitions in optical applications. Due to the confinement, the ground state energies of electrons and holes (denoted as E_{C0} and E_{V0}) is shifted away from the band edges. The increasing shift with decreasing well width allows to adjust the interband transition energy ($E_{C0} - E_{V0}$), and thus the corresponding wavelength for optical applications, to values between the bandgaps of InAs and InP. Fig. 1.2, right, shows the bandgap of most of the III-V semiconductors (excluding the nitrides) over their lattice constant. The room temperature bandgap of InAs (0.35 eV) and that of InP (1.34 eV) delimit the wavelength range for optical devices based on interband transitions of InAs nanostructures embedded in InP to the interval from 3.5 μm to 0.926 μm. This interval includes the 1.55 μm that is technologically important for fiber communication, suggesting the application potential of InAs/InP nanostructures for this purpose.

The difference in lattice constant (lattice mismatch) of 3.2% between InAs and InP leads to a compressive strain in InAs layers grown on InP substrates. This strain is utilized in the self-organized (also called self-assembled) formation of InAs quantum wires and quantum dots. Arrays of closely spaced, defect free QWrs or QDs (depending on growth conditions)

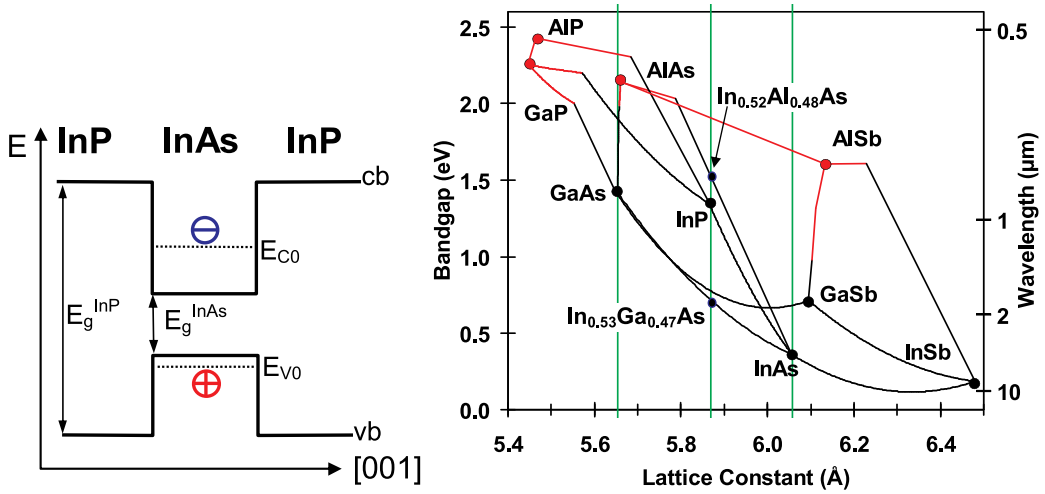

Figure 1.2: **left:** Type I heterostructure confining both electrons (blue open disk with inserted minus symbol) and holes (red open disc with inserted plus symbol) into the well material (InAs) surrounded by the barrier material (InP). Conduction band (cb) and valence band (vb), and the quantized electron and hole ground states (E_{C0}, E_{V0}) for the [001] direction are shown. **right:** Bandgap and corresponding optical wavelength versus lattice constant for III-V semiconductors and their alloys (excluding the nitrides). Labeled dots denote the binaries, wheras the connecting lines mark the alloys formed by the connected binaries. The ternaries $In_{0.52}Al_{0.48}As$ and $In_{0.53}Ga_{0.47}As$ with the same lattice constant as InP are explicitely shown.

covering the entire substrate surface form during the self-organized growth in the Stranski-Krastanov growth mode of InAs on InP substrates. Overgrowth with InP leads to InAs nanostructures embedded in InP schematically shown in Fig. 1.1. The InP barrier results in a confinement of the carriers not only in the vertical direction but also in one or both lateral directions for QWrs or QDs. The close spacing of the nanostructures (QWrs and QDs) facilitates the carrier transport in large ensembles of the nanostructures due lateral coupling between adjacent nanostructures. In addition, the associated high areal density of nanostructures is advantageous for optical applications.

To date, the transport due to lateral coupling between self-assembled nanostructures is not well investigated in general, and in particular no such data exists for InAs nanostructures in InP. The main focus of this thesis is the detailed investigation of carrier transport, which turns out to be anisotropic, in laterally-coupled, self-assembled InAs nanostructures in an InP matrix.

This work is organized as follows:

- The preparation of InAs nanostructures embedded in an InP matrix and their structural properties are discussed in chapter 2, in particular with respect to the effect of substrate misorientation on the nanostructure shape.

- The optical properties, particularly the polarization of interband emission and absorption, of the nanostructures are briefly shown in chapter 3.

- In chapter 4, the methodology for the investigation of the anisotropic carrier transport in large ensembled of nanostructures is prepared. The main focus of this chapter is the extension of the experimentally convenient Van der Pauw technique for the measurement of anisotropic transport in my samples.

- The processing of samples for transport measurements is briefly described in chapter 5, whereas detailed processing protocols are given in appendix B.

- Chapter 6 gives a detailed account of the transport investigations of my InAs nanostructures. It will elucidate the transport of electrons and holes from the point of view of a 2-dimensional anisotropic carrier system, and from the point of view of coupled 1-dimensional or 0-dimensional nanostructures. Thus relevant scattering mechanisms, and coupling mechanisms are identified.

- A novel electronic switching, that can be based on the transport properties of coupled InAs quantum wires, is proposed in chapter 7.

- Finally, the results of this thesis are summarized in chapter 8.

The foci of this work are on chapters 2, 4, and 6.

Chapter 2

Preparation of InAs/InP nanostructures

The present chapter describes the preparation and structural properties of the InAs nanostructures investigated in this work. After a brief introduction into the growth methods and the structural characterization methods, the growth is described and the relevant processes are discussed in detail.

The self-organized formation of semiconductor nanostructures is a subtle issue as it depends stronger on detailed growth parameters than the growth of flat semiconductor layers. It will be shown that the substrate misorientation, growth temperature, nominal thickness, growth rate, group V flux, details of growth interruptions (time, temperature, group V flux) strongly influence the final nanostructure shape. In contrast to the widely investigated self-organized InAs/GaAs nanostructures, the InAs/InP material system provides not only self-organized quantum dots but also self-organized quantum wires. An additional peculiarity is the change of the group V element between InAs and InP which involves As-P exchange processes during the growth of the interfaces, that in-turn affect the nanostructure size and shape.

My investigations focus on a systematic study of growth on substrates with different misorientation (off-cut). It will be shown that the off-cut direction of vicinal substrates — largely independent of growth conditions — determines the morphology of nanostructures, i.e. quantum dot, quantum wire, or two-dimensional growth; whereas, on nominally oriented substrates, the morphology is very strongly dependent on the growth conditions. Examples of the growth on the ternaries $In_{0.53}Ga_{0.47}As$ and $In_{0.52}Al_{0.48}As$ will demonstrate that the nanostructure shape not only depends on off-cut and growth conditions but also on the matrix material.

The results discussed in all succeeding chapters are based on the nanos-

tructures described here.

2.1 Growth by gas-source molecular beam epitaxy

The samples investigated in this work were grown with gas-source molecular beam epitaxy (GSMBE) which is a variety of molecular beam epitaxy (MBE). Other epitaxial techniques used to grow InAs/InP nanostructures are chemical beam epitaxy (CBE), and metalorganic chemical vapor deposition (MOCVD) which is synonymous to metalorganic vapor phase epitaxy (MOVPE). Molecular beam epitaxy (MBE) is an epitaxial growth technique that allows to grow layers with monolayer (ML, 1 ML = 1/2 lattice constant) precision, which makes it a versatile research tool. A schematic MBE growth chamber is shown in Fig. 2.1.

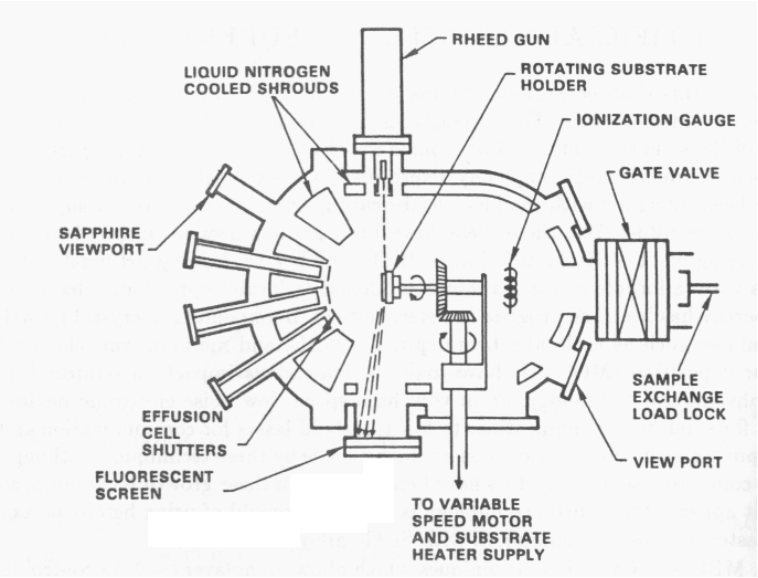

Figure 2.1: Schematic of an MBE growth chamber.[162]

The III-V semiconductor layers are grown in an ultra high vacuum (UHV) environment by depositing the atoms or molecules of the constituent group III and group V elements on the heated substrate where they form the III-V semiconductor layer. In our GSMBE system, the group III elements In, Ga, Al, and the n- and p-dopants Si and Be are stored in effusion cells shown on the left side of the schematic. By heating these cells, the elements are thermally evaporated. Due to the cell geometry the evaporating atoms form a

beam with thermal velocity that impinges on the heated substrate (substrate holder in the center of the schematic). The vacuum ensures a high purity of the grown layers, and that the mean free path of the evaporated elements is large enough to allow the formation of a directed beam. The cell temperature is an important parameter that determines the beam flux of the elements, which is proportional to the vapor pressure, and depends exponentially on the cell temperature. Shutters are placed in front of the cell openings in order to turn the flux on (shutter open) or off (shutter closed). In our GSMBE the group V elements P and As are supplied as hydrides PH_3 and AsH_3 . The use of gaseous group-V precursors contrasts our GSMBE to conventional MBE systems that use thermally evaporated solid P and As. The hydrides are injected into the system through a high temperature cracking cell operated at 850°C. The cracking products at this temperature are mainly the dimers P_2/As_2, and atomic and molecular hydrogen H and H_2 [130] mainly resulting from the reaction

$$2MH_3 \quad \rightarrow \quad M_2 + 3H_2 \ , \tag{2.1}$$

with M symbolizing either As or P. A high-capacity turbo pump (>1500 l/s) extracts the hydrogen from the growth chamber which results in a typical chamber pressure of $1{\cdot}10^{-5}$ torr, that is still sufficient to have molecular beams. The group V flux is controlled by mass flow controller for the hydrides. Typical mass flows are around 1 sccm, i.e. a mass flow equivalent to 1 cm^3/s at atmospheric pressure. Valves are used to abruptly turn on and off the hydride mass flow. In addition, a shutter is placed in front of the cracking cell to abruptly turn on and off the group V beam. *The group V flux given in this work as AsH_3 or PH_3 flux in sccm is the equivalent to the beam-equivalent pressure in solid-source MBE given in torr.*

The growth rate is controlled by the group III flux as these elements once deposited on the substrate cannot evaporate from it at the growth temperatures used in this work (400 to 500°C). The group V flux, in contrast, has to be larger than the group III flux in order to ensure that all group III atoms are used to form the III-V compound. An insufficient group V flux leads to the formation of group III metal droplets which degrades the sample surface. Any excess group V elements evaporate from the substrate, which makes the group V flux a less crucial parameter. Typical growth rates are 0.1 to 1 ML/s (corresponds to approximately 0.1 to 1 μm/h at a monolayer thickness of $\simeq$ 3 Å for InAs and InP). These growth rates on the one hand allow for layer thicknesses with ML precision but on the other hand involve long growth times for μm-thick layers.

2.1.1 Vicinal substrates

All III-V semiconductors used in this work have a cubic lattice with a zincblende crystal structure. The samples are grown on monocrystalline InP substrates prepared to have an exactly oriented (nominal) (001) surface, and substrate surfaces that are misoriented by an angle of 2° into different directions (vicinal substrates). As a result of this misorientation, the surface of vicinal substrates consist of steps with height of 1 ML and an average step width of 8.4 nm which is schematically shown in Fig. 2.2. The following terminology is

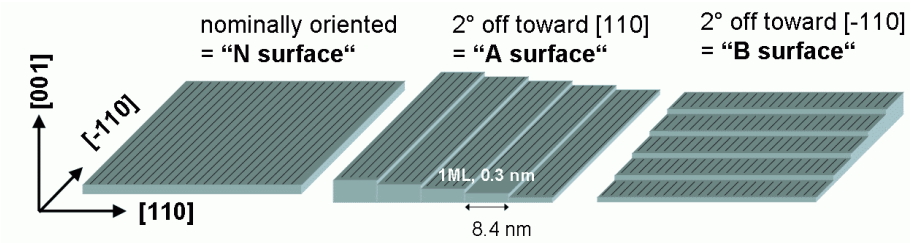

Figure 2.2: Surfaces of InP(001) substrates with different off-cut. Black lines along [-110] symbolize the dimer rows of the 2x4 reconstruction.

used within this thesis. Nominally oriented substrates are called "N surface", misoriented substrates 2° off toward [110] are called "A surface", substrates 2° off toward [$\bar{1}$10] are called "B surface". In addition, substrates 2° off toward [100], which is inbetween the A- and B-surface, are called "C surface". In sample names, the appendix N, O, P, and Q are used for samples grown on N, A, B, and C surfaces, respectively.

2.1.2 Processes during MBE growth

The following list summarizes the most relevant processes in MBE growth.

1. Impinging atoms/molecules are adsorbed at the substrate surface. These adsorbed atoms are called ad-atoms.

2. The substrate temperature allows these ad-atoms to diffuse on the surface, which is a necessary condition to form smooth layers.

3. The diffusing ad-atoms are incorporated into the crystal (nucleation), which is energetically favorable at surface steps. They can further diffuse along the step to find a kink that is a more favorable nucleation site. If the ad-atoms do not hit a step, they can also nucleate to form a new island that is bounded by steps. Vicinal substrates contain a

much higher density of steps in comparison to nominal substrates which makes the nucleation at these steps very likely.

4. Ad-atoms, mainly group V, that are not incorporated into the crystal desorb from the surface. At the growth temperatures used in this work, group III atoms cannot desorb from the surface.

As the adsorption rate for group III elements is higher than the desorption rate, MBE is a growth technique that does not operate in a thermodynamical equilibrium.

2.1.3 Surface reconstruction

In order to saturate dangling bonds, the "reconstructed" crystal surface has a different lattice than the bulk. The resulting periodicity differs from that of the underlying bulk. The size of the surface unit cell in the mutually perpendicular surface directions is an integer multiple a, b of the underlying bulk lattice constant. Thus, the surface reconstructions are termed $(a \times b)$ reconstructions. The symmetry of the surface lattice can be observed by reflection high-energy electron diffraction (see section 2.3) that shows additional diffraction streaks between the bulk-streaks, and optical methods (ellipsometry, reflection anisotropy spectroscopy). For a fixed surface symmetry, however, there usually exist different reconstructions (microscopic arrangements of the surface atoms). A symmetry with $a \neq b$ represents an anisotropic surface. For example, the (2×4) reconstruction observed in the InAs growth in this work, consists of As dimer rows in the $[\bar{1}10]$ direction that are separated by trenches.

2.2 Strained layer epitaxy and self-assembly

Epitaxy is a growth type in which the layer (grown film) adopts the crystal structure of the substrate. As all III-V semiconductors used in this work form a zinc-blende structure the adoption is done by simply assuming the lateral (in-plane) lattice constant $a^{\parallel}$ of substrate. The relaxed lattice constants a of the materials grown in this work are $a_{InP} = 5.86875$ Å for InP, and the ternaries $In_{0.53}Ga_{0.47}As$ and $In_{0.52}Al_{0.48}As$, and $a_{InAs} = 6.05838$ Å for InAs. This corresponds to a lattice mismatch

$$\epsilon = \frac{a_{layer} - a_{substrate}}{a_{substrate}} \tag{2.2}$$

of 3.2% for an InAs layer with respect to an InP substrate. In what ways the lattice mismatch can be accommodated is schematically illustrated in Fig 2.3.

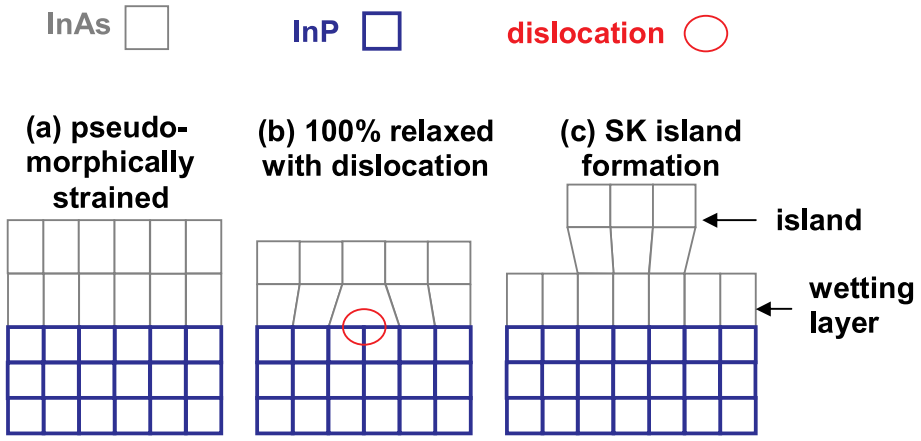

Figure 2.3: Schematic of biaxially strained layers. (a) Pseudomorphically strained, (b) relaxed by dislocation, and (c) relaxed by island formation via Stranski-Krastanov growth mode.

If the substrate (InP layer) is much thicker than the layer (InAs) on top of it, the substrate will maintain its relaxed lateral lattice constant, and the mismatch is accommodated in the layer. The thin InAs layer grows pseudomorphically by assuming the (smaller) lateral lattice constant of the InP substrate ($a^{\parallel}_{layer} = a^{\parallel}_{substrate}$) as shown in Fig. 2.3a. The InAs is biaxially, compressively strained with the in-plane strain component $\epsilon_{\parallel}$ and the resulting out of plane strain component $\epsilon_{\perp}$:

$$\epsilon_{\parallel} = \frac{a^{\parallel}_{layer} - a_{layer}}{a_{layer}} \tag{2.3}$$

$$\epsilon_{\perp} = -\frac{\epsilon_{\parallel}}{\nu} \, . \tag{2.4}$$

With the Poisson ratio ν of the layer ($\nu = 0.9201$ for InAs) the vertical lattice constant of the strained layer is

$$a^{\perp}_{layer} = a_{layer}(1 + \epsilon_{\perp}) \tag{2.5}$$

$a^{\perp}_{InAs} = 6.2645$ Å for an InAs layer on InP. With increasing InAs thickness h, the total strain energy in the InAs layer also increases. If h exceeds a critical thickness h_{crit}, the strain can be relaxed by the formation of dislocations (Fig. 2.3b). Different models, such as [113, 132], show a decrease of critical

thickness h_{crit} with increasing lattice mismatch. The layer assumes its relaxed lattice constant laterally and vertically if the strain is completely relaxed by dislocations. An alternative mechanism to relax the strain is the formation of islands by the Stranski-Krastanov (SK) growth mode [168] as shown in Fig. 2.3c. If a certain critical thickness h_{3D} of the pseudomorphic layer is exceeded, the layer material self-organizes into dislocation-free, coherent islands with a thin, pseudomorphically strained wetting layer underneath. This transition from a (2D) layer-by-layer growth into the growth of (3D) island is called 2D-3D transition. The SK-growth mode is widely used to form self-assembled nanostructures in the InAs/GaAs, InGaAs/GaAs, Ge/Si, InAs/InP [19], InP/GaP [73], and other material systems. As schematically shown in Fig. 2.3c, the total strain relaxation is accomplished by a decreasing local strain with increasing height inside the island.

This strain relaxation of InAs/InP nanostructures has been investigated by several groups: X-ray diffraction measurements of uncapped, self-assembled InAs QWrs have been used to show the reduction of average strain with increasing height within the QWr [70, 114]. Owing to the nanostructure's elongated shape, however, the strain relaxes only in the [110] direction (direction of the width) whereas no strain relaxation occurs in the $[\bar{1}10]$ direction (along the wires) as measured in Refs. [57, 70, 114], i.e. the in-plane strain is anisotropic. The application of InAs nanostructures requires them to be capped leading to a different strain distribution than in uncapped nanostructures. Based on grazing incidence anomalous X-ray diffraction in combination with finite difference calculation and the input from TEM images on the nanostructure cross-sectional shape, the local strain within InAs QDashes *embedded in InP* has been obtained [99].

The presence of a wetting layer underneath InAs nanostructures in InP is directly visible in cross-sectional transmission electron images shown in Refs. [116, 54, 55]. The existence of a WL has been proven by indirect methods: capacitance spectroscopy [133], photoconductivity [97], and its thickness has been quantified to ≤ 1 ML by X-ray diffraction [99], 2 ML by photoluminescence [28].

The general advantages of self-assembled nanostructures over processed ones is that their formation requires no processing steps, and that they are intrinsically free from defects and dislocations. The random component to the self-assembly, though, poses a challenge to the control of their size uniformity and arrangement. This challenge is approached in different ways. Strategies for the homogenization of the size distribution involve sophisticated overgrowth procedures that truncate oversized InAs quantum dots on InP [131, 149], and homogenization by "strain filtering" due to vertical stacking of InAs quantum wire layers on InP [3]. Additionally, the vertical stacking

allows to obtain vertically ordered nanostructures as theoretically described in Ref. [157]. Vertical ordering has been experimentally demonstrated as correlation of InAs QWrs in InP [54], QDs in $In_{0.53}Ga_{0.47}As$ [104], and anti-correlation of InAs QWrs in an $In_{0.52}Al_{0.48}As$ matrix [171, 104]. Horizontal linear ordering of self-assembled QDs has been demonstrated with InGaAs QD chains on GaAs substrates [193]. A recent development is the ultimate control of the horizontal arrangement of self-assembled InAs nanostructures on InP by a combination of substrate pre-structuring to define the areal density and horizontal locations of quantum dots, and subsequent growth on these templates. The experimental realization of this concept has been shown for InAs QDs on InP [13, 33].

2.2.1 Kinetic and thermodynamical aspects

The formation of 3D islands in the SK growth mode is governed by thermodynamics determining the energetically favored morphology of the grown layer, and by the growth kinetics determining to what extent the layer may attain the energetically favored morphology.

Thermodynamics

As an example for thermodynamical considerations Ref. [176] shows theoretically in a model that 3D islands with an initially symmetric shape (QDs) that grow in size transform into elongated islands (QWrs) which becomes energetically favorable. In the InAs/InP system, this mechanism, however, has been observed neither in my work nor in published work of other groups. One reason may be that the model assumes only a lateral growth of the QDs, whereas InAs nanostructures clearly also grow in height.

A general approach to the total energy of InAs nanostructures taken in Ref. [198] considers the change of energy ΔE of a pseudomorphically strained layer that forms 3D nanostructures on a wetting layer:

$$\begin{aligned} \Delta E &= \Delta E_{surface(-110)} + \Delta E_{surface(110)} \\ &\quad + \Delta E_{edge(-110)} + \Delta E_{edge(110)} - \Delta E_{strain} \end{aligned} \tag{2.6}$$

with $\Delta E_{surface(-110)}$ the energy cost to form the nanostructure sidewalls along the $[\bar{1}10]$ direction, $\Delta E_{surface(110)}$ the energy cost to form the nanostructure sidewalls along the [110] direction, $\Delta E_{edge(-110)}$ the energy cost to form edges along the $[\bar{1}10]$ direction, $\Delta E_{edge(110)}$ the energy cost to form edges along the [110] direction, and ΔE_{strain} the energy gain due to the elastic strain relaxation. The elongation of the QWrs into the $[\bar{1}10]$ direction may be

explained in this picture by $\Delta E_{surface(110)} + \Delta E_{edge(110)} > \Delta E_{surface(-110)} + \Delta E_{edge(-110)}$.

In terms of strain relaxation ΔE_{strain}, symmetrical QDs are favorable as the strain can relax in both lateral directions, which is in contrast to QWrs that can relax only in the direction of their width. Moreover, the greater height of the InAs QDs in comparison to the InAs QWrs (observed from structural investigations) also supports a higher degree of strain relaxation in the QDs.

Furthermore, Eq. 2.6 suggests that a lower areal density of higher and larger nanostructures is energetically favorable as increased height allows a higher degree of strain relaxation (higher ΔE_{strain}), and the distribution of a fixed amount of InAs among less and larger islands decreases the total sidewall area and edge length (lower $\Delta E_{surface(-110)} + \Delta E_{surface(110)} + \Delta E_{edge(-110)} + \Delta E_{edge(110)}$). A manifestation of this consideration is the Ostwald ripening [124, 208] which is the conglomeration of smaller dots to form larger dots.

Kinetics

Growth kinetics govern the re-organization of the 2D layer into 3D islands by surface transport of the InAs. The usually group-V rich growth conditions and the fact that In atoms are much more mobile than the As [65] result in a re-organization through the surface transport of the In atoms. The average surface diffusion length l_s of the atoms depends on diffusivity D_s, and the diffusion time τ_s that equals either the inverse growth rate $1/R$ (R in ML/s) during In deposition (In can diffuse only until it gets overgrown by the next ML), or by annealing time (no In deposition) [76]:

$$l_s = \sqrt{2 D_s \tau_S} \tag{2.7}$$

$$D_s = D_0 \ \exp(-E_h/kT) \ . \tag{2.8}$$

The diffusivity D_s given in Eq. 2.8 depends on the growth temperature T and the hopping barrier E_h. Thus, the surface re-organization can be reduced by kinetical limitations such as

1. an increase in growth rate R to decrease $\tau_s = 1/R$,
2. a reduction of growth temperature to decrease D_s,
3. an increase of the hopping barrier E_h to decrease D_s.

The hopping barrier can be effectively changed by altering the surface stoichiometry, e.g. the As fraction. Decreasing the As flux has been found to

form smaller islands of higher areal density in growth experiments of both GaAs on 2×4 reconstructed GaAs(001) [197] and InAs on 2×4 reconstructed InAs(001) [125]. These results have been interpreted in terms of a reduced diffusion length at lower As flux, which is somewhat counterintuitive. Ref. [144] corroborates this interpretation by demonstrating that the 2D-3D transition of a 2D InAs film grown on InP is inhibited under low AsH_3 flux, and activated with increasing substrate temperature. As an extreme case of a low As flux, Ref. [179] demonstrates the suppression of the 2D-3D transition of a 12 ML-thick InAs layer on $In_{0.52}Al_{0.48}As$ (on InP(001) substrate) on an In-rich 4×2 reconstructed surface at a low growth temperature of 380°C.

2.2.2 Current understanding of QWr formation

Different explanations for the formation of InAs QWrs into the $[\bar{1}10]$ direction are given in the literature. A common basis of all these explanations is the (2×4) reconstruction consisting of dimer rows into the $[\bar{1}10]$ direction during the growth of the QWrs. Further it has been demonstrated that a reconstruction with lower As coverage (4×2) leads to the growth of QDs [25]. The transformation of elongated InAs nanostructures (QWrs, QDashes) into QDs has been triggered by a change of the (2×4) reconstruction into both, an As deficient (4×2) reconstruction [198], and into an As rich reconstruction [45].

The detailed mechanisms proposed to form the QWrs, though are varying. As kinetic argument, the anisotropic ad-atom diffusion on the surface is suggested to nucleate elongated island during the growth of the first ML of InAs [67]. Indeed, the (2×4) reconstruction gives rise to anisotropic surface roughness even in non-strained III-V surfaces [25]. Thermodynamically, this anisotropy is interpreted in terms of different energies for the formation of steps into the $[\bar{1}10]$ direction (A steps) and the [110] direction (B steps) [204]. Kinetic Monte Carlo simulations of the growth of unstrained InAs on (2×4) reconstructed InAs [64] show that grown 2D InAs islands are elongated into the $[\bar{1}10]$ direction because InAs A steps are energetically more favorable than B steps. This energetic difference results in straight A steps and rough B steps in agreement with the experimental observation of Ref. [198]. Refs. [25, 67] argue that the anisotropic 2D InAs islands undergo a 2D-3D transition preserving their anisotropy which agrees with the theory of Ref. [32] that SK growth takes place via the 2D-3D transition of 2D islands. Ref. [198] on the other hand just uses the thermodynamic argument of the lower A step energy for the total energy of the 3D nanostructure in Eq. 2.6. A different approach is taken in Refs. [57, 63] basing their explanation on the measured anisotropic surface stress during growth of InAs on

InP under (2 × 4) reconstruction. These measurements show that the stress building up in the [110] direction is higher than that in the [$\bar{1}$10] direction, and conclude that the critical stress that triggers the 2D-3D transition is reached in the [110] direction at first. Consequently, only the stress in the [110] direction is relaxed by the 2D-3D transition as directly observed in their measurements.

My own investigations (Ref. [16], section 2.5.2) show that surface steps on vicinal surfaces can either enhance the formation of QWrs or trigger the formation of QDs instead of QWrs counteracting the effect of the (2 × 4) reconstruction. Furthermore, my AFM images (Figs. 2.14a in section 2.5.1, and 2.15a in section 2.5.2) of InAs layers below the critical thickness for the 2D-3D transition do not show anisotropic 2D islands on nominal substrates as assumed by Refs. [25, 67]. The suppression of QWrs by a deviation from the (2 × 4) reconstruction (through As deficient or As rich surfaces) agrees with my observations using higher substrate temperature (section 2.5.3) or cooling under As flux (section 2.5.4).

2.3 Reflection high-energy electron diffraction

Reflection high-energy electron diffraction (RHEED) is an important technique to in-situ monitor the growth process. The RHEED setup containing the RHEED gun and the fluorescent screen is included in Fig. 2.1. RHEED employs an electron beam with typical energy of 10 to 20 keV impinging on the growth surface at glancing incidence. Due to the glancing incidence the electrons penetrate only very few (about two) atomic layers into the surface making this technique highly surface sensitive. Indeed, the sampled volume corresponds to the two-dimensional reconstructed surface lattice. As a consequence the reciprocal lattice degenerates into a set of lattice rods. The reflected and diffracted beam hits a phosphor screen. The projection of the reciprocal lattice rods on the screen results in a characteristic pattern. Analyzing these patterns along different crystallographic directions - for (001) surfaces typically [110] and [$\bar{1}$10] - allows to find the symmetry of the surface reconstruction. Apart from the surface reconstruction the diffraction pattern gives information about the surface morphology - a streaky pattern usually corresponding to a flat surface. In the case of a surface with 3-dimensional nanostructures the streaks transform into wedges due to the reflection of the electron beam at the side facets of the nanostructures. Thus island formation in the SK growth mode can be observed "live" with RHEED as demonstrated by Fig. 2.4 showing the RHEED pattern of InAs before and after the 2D-3D transition. Before the transition a streaky 2×4 RHEED is visible (a,b). In

the [110] azimuth (2×) the streaks (a) decompose into elongated dots (b), whereas in the [$\bar{1}$10] azimuth the streaks (b) transform into wedges (d).

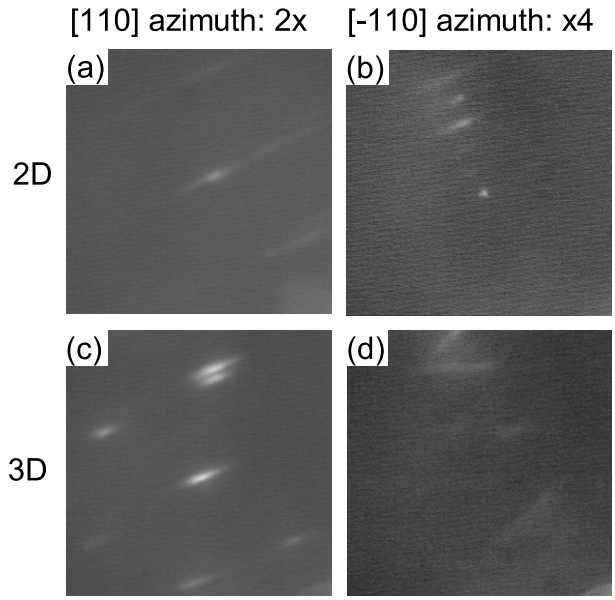

Figure 2.4: RHEED pattern of InAs along the [$\bar{1}$10] (b,d) and [110] (a,c) azimuth before (a,b) and after (c,d) the 2D-3D transition in the Stranski-Krastanov growth mode.

2.3.1 Surface reconstructions and temperature calibration

The surface reconstructions depend mainly on the III/V-ratio respectively group V flux if no growth takes place, and on the substrate temperature. Going from low to high temperatures the following surface reconstruction of CBE grown InAs(001) have been reported [83]: (1×2), (2×3), (2×4), and (4×2). In contrast for solid-source MBE grown InAs(001) only (2×4), and (4×2) reconstructions have been observed for the same temperature range [126].

With increasing temperature for CBE grown InP(001) [83], and GS-MBE grown InP(001) [190] the (2×2), (2×1), and (2×4) reconstructions have been identified. On InP(001) prepared using solid source MBE, additionally a c(4×4) (for lowest temperatures), and a c(2×8) (highest temperatures) [95] have been reported. Unlike InAs or GaAs for InP no (4×2) reconstruction was found at higher temperatures. With increasing temperature the (2×4)

reconstruction persists until the surface degrades due to metal droplet formation.

For the formation of self-assembled nanostructures the growth temperature is a crucial parameter as it influences the surface reconstruction, and the surface mobility of the ad-atoms, which have great impact on the resulting morphology. This makes the control of the growth temperature a fundamental issue. In the growth chamber used for the present work the substrate is radiatively heated. The temperature is measured not directly at the sample but at the heater. Therefore, the controlled temperature is the heater temperature. As a consequence the actual sample temperature differs from the measured temperature. It additionally depends on the sample holder, and material and surface dependent absorption properties of the substrate (plus the layers grown on top of it). To ensure a reproducibility of growth temperature a temperature calibration was done during growth by virtue of the temperature dependence of the InP surface reconstruction. For particular fixed PH_3 fluxes the temperature was slowly ramped down during a growth interruption on the InP buffer layer starting with a (2×4) reconstruction. The temperature (measured at the heater) at which the reconstruction changed into (2×1) was then taken as the reference temperature. A particular growth temperature was then given by its difference to this reference temperature. The accuracy of this method is estimated to be better than 10 K. Thus, the heater temperature difference between different holders to obtain the same substrate temperature (reconstruction) has been measured. The quoted temperatures are the equivalent heater temperatures by using a fixed particular holder.

2.3.2 RHEED oscillations for growth rate calibration

The intensity of the reflected electron beam depends on the atomic surface roughness with high intensity for atomically flat surfaces and low intensity for a rough surface. An impressive manifestation of this behavior are RHEED intensity oscillation that can be observed if the growth takes place in a layer-by-layer mode (Frank-van der Merwe mode [76]). In this mode, starting on a completed monolayer being atomically smooth (with high reflectivity) deposition of a fractional monolayer leads to an atomically rough surface (with low reflectivity) consisting of many, laterally small, monolayer high islands. As more material is deposited, these islands grow in size, and finally merge into another complete monolayer. Apparently, this monolayer by monolayer cycle results in an oscillation of the RHEED intensity which can, thus, be used to in-situ measure the growth rate. A non-vicinal surface (low density of surface steps), and a low enough surface mobility (low growth temperature,

high group V flux) are prerequisites for the layer-by-layer growth.

Usually the growth rate of the group III elements is measured with the RHEED-oscillation method. In principle, also the group V rate can be determined in the same way. Growing InP by GS-MBE in a group-V limited mode, i.e. with excess group-III flux, the RHEED oscillation frequency was shown to depend on the group-V flux [127]. Alternatively, the As-incorporation rate on a metal rich surface in presence of only a group-V flux was determined using RHEED oscillations with CBE grown GaAs [34].

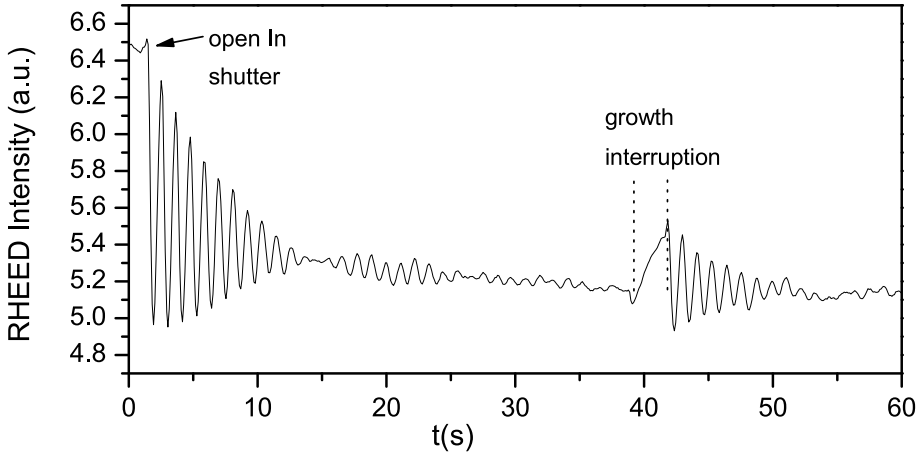

Figure 2.5: RHEED oscillations of InP(001).

In the present work, RHEED oscillations were employed to measure the growth rates of InP, GaAs, and AlAs for different In, Ga, and Al cell temperatures, thus yielding a calibration of growth-rate over cell temperature. In detail, the specular RHEED reflection was projected by a lens on a photo diode with the photo current over time being captured on a computer. Figure 2.5 shows an example of RHEED oscillations captured during InP growth. A damping of the oscillation amplitude, its recovery after a growth interruption, and a beating can be observed. The damping of the oscillations is caused by a long-range roughening of the surface during growth. A growth interruption, however, smoothes the surface to recover the oscillation amplitude. The beating, not always observed, is caused by a flux inhomogeneity of the growth rate across the area sampled by the electron beam (typically 1 cm long) [26]. The data presented here shows a flux variation of approximately 9 %. Taking the inverse of the time between two adjacent oscillation maxima (or minima) one obtains the instantaneous growth rate yielding information about *the evolution* of growth rate. An example for the time evolution of the InP growth rate is given in figure 2.6. After a long (>10 min) growth interruption to prepare a smooth starting surface, RHEED oscillations were

recorded with short (<5 s) growth interruptions to recover the damped out oscillations. The initial growth rate of 0.93 ML/s decays within approximately 2 minutes towards its equilibrium value of 0.83 ML/s. This transient can be explained by a cooling of the In from the front side of the cell with open shutter. Longer growth interruptions (minutes) result again in an increased initial growth rate. Shown in the graph is the effect of a 30 s growth interruption. The respective measured transients after a long growth interruption for the Ga (Al) cell were a rate reduction of 10 % (12) % within 2 minutes (20 s) toward the steady state value. These transients should be taken into account if high precision for layer thicknesses or ternary compositions is required.

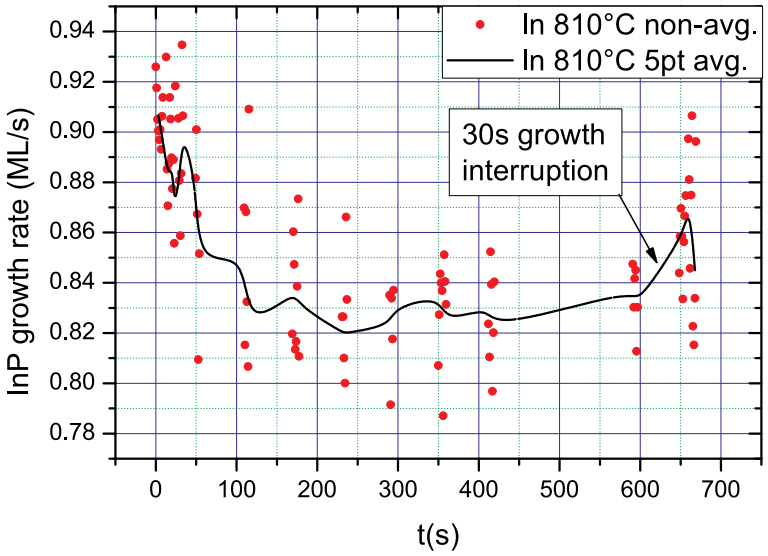

Figure 2.6: Growth rate as function of open shutter time. Shutter was opened at t=0. Circles: instantaneous growth rate, Line: growth rate averaged over 5 monolayers. Rate transient reflects the cell cooling after opening the shutter.

2.4 Post growth structural characterization

In this work, atomic force microscopy (AFM) is extensively employed to determine the shape of the InAs nanostructures grown on the sample surface. The functional principle of an AFM is illustrated and explained in Fig. 2.7. The resulting images show the scanned surface area with the height at each point represented by a color (from dark color=low to bright color=high). AFM images always represent the convolution of the tip shape with the sample surface morphology which necessitates a critical evaluation of the

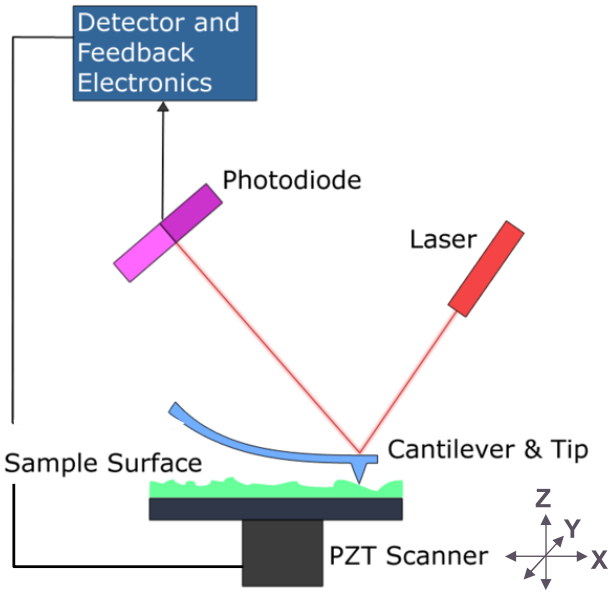

Figure 2.7: (Reproduced from www.wikipedia.org) Schematic of an atomic force microscope. The sample is mounted on a piezo tube scanner that can move in the x,y, and z direction. A fine tip (typical tip radius 10 nm) at the end of the elastic cantilever (force constant in the range of 1 N/m) is in contact with the sample surface. The cantilever deflection is measured with a laser beam reflected at the cantilever backside. The sample surface morphology is measured by scanning the sample in X direction under the cantilever. The feedback electronics keeps the cantilever deflection constant by accordingly extending or retracting the scanner in the Z direction. Thus, the Z extension of the piezo tube scanner for each X position represents the height of the sample surface at this position. After scanning a line in X direction, the scanner moves a small step into the Y direction to the next scan line.

images. This convolution effect is relevant if the morphological features on the sample are on a smaller or comparable lateral size scale as the AFM tip. An anisotropically shaped tip, for example, will result in anisotropic features of the image even if the surface morphology of the sample consists of isotropic features. A simple method to distinguish anisotropic tip from really anisotropic sample features is to repeat the measurement after rotating the sample by 90°. If the anisotropic features are not due to the tip shape, this rotation will lead to a rotation of the features in the AFM image by the same angle. This method was used in the present work. Another critical point is the apparent height of the nanostructures which is prone to

be underestimated by AFM if the tip is too large to fit between adjacent structures.

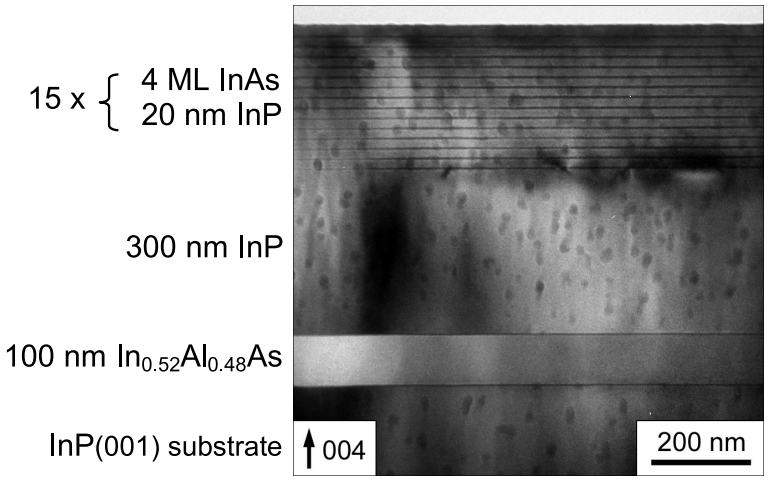

Figure 2.8: Bright-field cross sectional transmission electron micrograph of a sample with a 15 period InAs/InP superlattice. The layer description is given at the left side. Dark horizontal lines in the top part represent the thin InAs layer.

An alternative method that does not suffer from tip-sample convolution is transmission electron microscopy (TEM) as the probing electron beam is much smaller than the AFM tip. TEM, however, requires an elaborate sample preparation, and gives results that are integrated over the transmitted thickness. Information on the morphology of overgrown InAs nanostructures that cannot be obtained with AFM is obtained by cross-sectional TEM (XTEM). A XTEM image of a typical sample containing an InAs/InP superlattice is shown in Fig. 2.8. The absence of dislocations in this image demonstrate the coherent growth of the InAs nanostructures. A superlattice is a multiply repeated layer sequence (4 ML InAs/20 nm InP in the given example) which creates an artificial lattice in the growth direction with lattice constant (usually) much larger than the crystal lattice constant.

A complementary method to TEM is X-ray diffraction (XRD). The X-ray beam has a diameter in the range of 1 mm which is the lateral extension of the sampled area. In contrast to the structural information of individual nanostructures, this method precisely determines chemical compositions and thickness of grown layers laterally averages over the beam diameter. Figure 2.9, left, shows the schematic X-ray setup. Rocking curves in the vicinity of the substrate's (004) symmetric reflex are taken by measuring the intensity of the Bragg reflected X-rays as function of the incidence angle θ. The

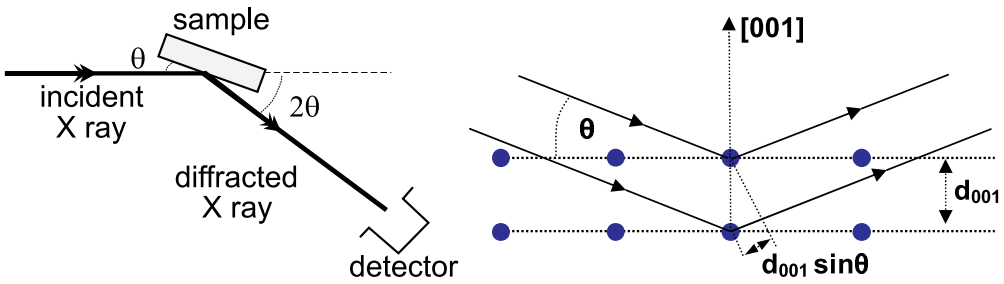

Figure 2.9: Method of X-ray diffraction. **left:** [74] Schematic setup. The angle between incident monochromatic X-ray and sample surface parallel is Θ. The angle between incident and diffracted beam is 2θ. **right:** Schematic of Bragg reflection of X-ray at the atomic planes of the crystal lattice. Solid lines with arrows denote the incident and diffracted X-ray radiation. The horizontal lines denote the crystal lattice planes with atoms represented by blue solid circles. The plane-plane distance is d_{001}. The diffracted radiation from the top and bottom planes interfere constructively if their path difference $2d_{001}sin\theta$ equals a multiple n of the wavelength λ.

position of the detector is locked at 2θ with respect to the incident beam. Peaks in the rocking curve appear at angles θ that fulfill the Bragg condition (see Fig. 2.9, right)

$$n\lambda \quad = \quad 2d_{001}sin\theta \tag{2.9}$$

with X-ray wavelength λ(=1.5405 Å in our instrument), diffraction order n (=4 in our case), and d_{001} the vertical lattice constant of the diffracting layer.

Figure 2.10 shows the rocking curve of a 30 period superlattice sample with a lattice-mismatched InAlAs buffer layer as an example for the application of XRD in this work. The composition of ternary layers, e.g. the $In_{0.52}Al_{0.48}As$ layer, is obtained through the measurement of their vertical lattice constant d_{001} using Eq. 2.9. A prerequisite for the correct calculation of the composition, though, is the pseudomorphic growth of layer. This ensures that the lateral lattice constant $a^{\parallel}$ is known. Using the measured $a^{\perp} = d_{001}$ and the known $a^{\parallel} = a_{substrate}$ the relaxed lattice constant a can be calculated based on Eqs. 2.3, 2.4, and 2.5

$$a \quad = \quad \frac{\nu a^{\perp} + a^{\parallel}}{\nu + 1} \tag{2.10}$$

for known poisson ratio ν. Using Vegard's law

$$a_{A(x)B(1-x)} \quad = \quad xa_A + (1-x)a_B \tag{2.11}$$

the composition x of the ternary A_xB_{1-x} can be obtained from the $a_{A(x)B(1-x)}$ determined by XRD, and the known a_A, a_B. Furthermore, the rocking curves

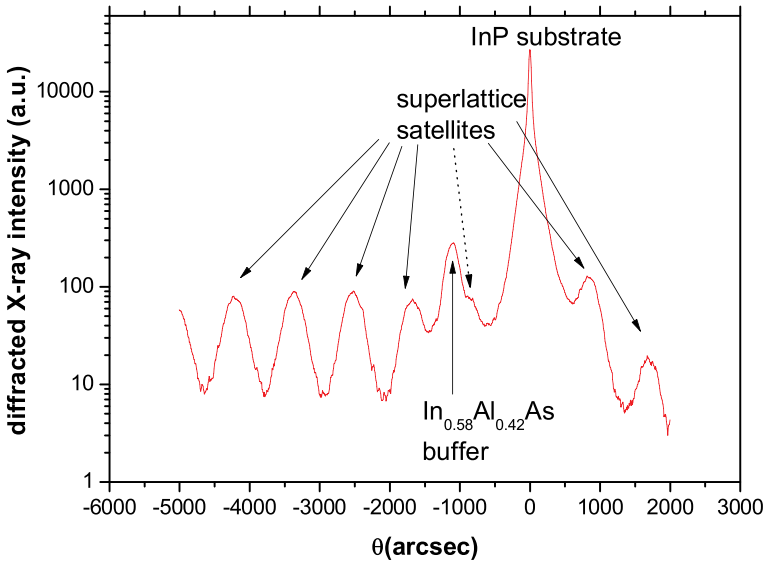

Figure 2.10: Rocking curve of a 30 period InAs/InP superlattice. For simplicity, the angle θ given in the graph is the difference of the actual angle to the Bragg angle of the InP substrate. All peaks are labeled according to their origin. The zeroth order satellite is denoted by a dotted line. The satellite peaks are broadened due to the extremely rough InAs/InP interface formed between the InAs QWrs within the InP matrix. The InAlAs layer peak is visible due to the lattice mismatch to InP.

of superlattices are evaluated with respect to the thickness and average composition of a superlattice period. Analogous to the diffraction of light at a grating, the diffraction of X-rays at the superlattice produces satellite peaks in the rocking curve (shown in Fig. 2.10). According to the Bragg condition (Eq. 2.9) the superlattice period D is calculated from two adjacent satellite peaks n, and $n+1$, with respective Bragg angles θ_n and $\theta_{n+1} = \theta_n + \Delta\theta$ as

$$D = \frac{\lambda}{2sin\theta_{n+1} - 2sin\theta_n} \simeq \frac{\lambda}{2\Delta\theta cos\theta_B} \tag{2.12}$$

with Bragg angle of the zeroth order satellite θ_B. The Bragg angle of the zeroth order satellite reflects the vertical lattice constant d_{001}^{SL} of an alloy with the average composition of one superlattice period. For the investigated InAs/InP samples, one period is considered a ternary $InAs_xP_{1-x}$. Multiplying x with the superlattice period D one obtains the thickness of the InAs layer (under the assumption that the InP contains no residual As).

In addition to the structural investigations, photoluminescence (PL) is used to estimate the thickness of grown InAs layers. The energy of the PL peak decreases with increasing InAs QW thickness. Calculation of the peak energy as function of InAs thickness are used to give quantitative results on the InAs thickness based on the PL peak energy. A detailed discussion of this method is given in chapter 3.

2.5 Growth of InAs/InP heterostructures

The samples used in this work were grown in a Riber 32P GSMBE system on semi-insulating InP(001) substrates, including nominally oriented (N) and misoriented (A, B, and C) surfaces. Most growth runs included N, A, and B substrates mounted next to each other on one holder. The grown structures (schematically shown in Fig. 2.11, left) each consist of an InAs layer capped with 43 nm thick InP (for PL measurements) and another InAs layer (for AFM measurements) on top, deposited under the same growth conditions as the capped one. In detail, 100 nm $In_{0.52}Al_{0.48}As$, lattice matched to InP, followed by a several 100-600 nm-thick InP buffer were grown at 450°C heater temperature (measured with a thermocouple) at growth rates of 0.8 and 0.4 monolayers (MLs) per second. With the $In_{0.52}Al_{0.48}As$ layer I suppress any unintentional formation of an electron gas at the interface of InP-substrate to InP-buffer interface that would lead to a parallel conductivity in modulation doped samples (see section 6.5.2 for details). The growing InP surface had a 2×4 reconstruction as observed by reflection high energy electron diffraction (RHEED). Our configuration allows the RHEED to be observed on all substrate pieces; the reconstruction symmetry was the same on all investigated substrate orientations for all my RHEED observations mentioned.

The key growth sequence that determines the structural properties of the InAs layer is schematically illustrated in Figure 2.11, right, and described as follows. The InP buffer was annealed under a cracked PH_3 flux of 1.5 sccm for $t_1 = 60$ s to smoothen the surface. For samples with the InAs layers grown at a different temperature, the annealing continued during the temperature change. For each InAs layer, the growth chamber was pumped for $t_2 = 3$ s without flux to pump residual P out of the chamber. Then the InP surface was exposed to a cracked AsH_3 flux for $t_3 = 15$ s which prepares an As containing surface to avoid P carry-over into the subsequent InAs layer. This process already forms a thin InAs due to the P-As-exchange (PAsX, discussed in section 2.5.1). Additional InAs was deposited during t_{InAs} and annealed for $t_4 = 10$ s at the same temperature. The 2D-3D transition that

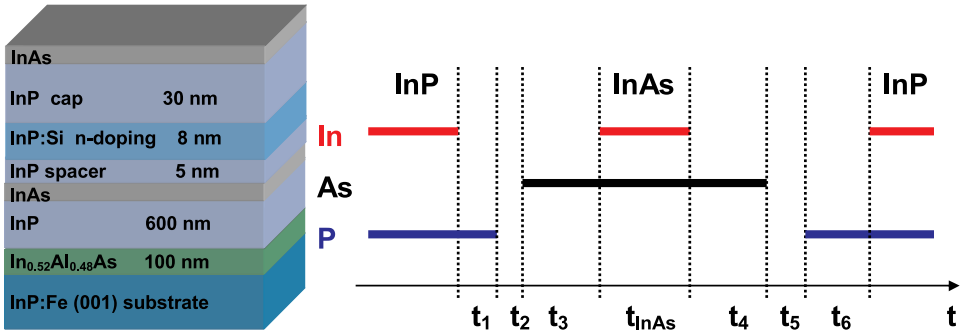

Figure 2.11: **left:** Principle layer structure of modulation-doped InAs/InP samples. **right:** Control sequence of the In, As, and P molecular beam for the growth of InAs nanostructures embedded in an InP matrix. The molecular beams impinging on the substrate are represented by colored bold line. Red top line - In, black central line - As_2, and blue bottom line - P_2. Times of the different phases are denoted at the time-axis in the bottom.

forms the self-assembled nanostructures was observed by RHEED during this anneal. The AsH_3 flux was kept constant throughout this procedure. If the growth temperature was lowered for the following InP cap layer, the annealing continued during the change. The cap layer was grown by pumping the growth chamber for $t_5 = 3$ s, to pump residual As out of the chamber. In preparation of the InP growth, the sample was subsequently exposed to a cracked PH_3 flux for $t_6 = 5$ s forming a P containing surface. This process also transforms parts of the InAs into InP due to As-P exchange (AsPX, discussed in section 2.5.6). The InP cap layer is deposited subsequently. For the InAs top layer, the same sequence as described for the capped InAs was used, beginning with the annealing of the InP. After the InAs annealing, the samples were cooled down under a cracked AsH_3 flux and taken out of the growth chamber for AFM and PL measurements. Several structures were grown with varying InAs deposition thickness, growth rate, and substrate temperature. For QWr formation, the optimal InAs deposition conditions are: a substrate temperature of 450°C, a deposition rate of 0.4 ML/s, and an AsH_3 flux of 0.6 sccm; under these conditions the InAs grows with a 2×4 reconstruction as observed by RHEED.

The following sections will elucidate in a temporal order the relevant phases of the growth with their dependencies on growth parameters.

Summary

The "default" growth sequence and parameters optimized to obtain the InAs nanostructures investigated in this work are: substrate heater temperature (growth temperature) of 450°C, AsH_3 flux of 0.6 sccm, 15 s annealing of the InP buffer in AsH_3 flux, InAs deposition of 4 ML at a growth rate of 0.4 ML/s, 10 s annealing of the InAs to allow for 2D-3D transition (deposition and annealing of InAs with a (2×4) surface reconstruction), 5 s annealing with PH_3 flux of 1.5 sccm, deposition of the InP cap layer at 0.4 ML/s with a (2×4) surface reconstruction.

2.5.1 P-As exchange process

In contrast to most of the other III-V heterointerfaces, a unique feature of the InAs/InP heterointerface is the change of the group V sublattice giving rise to P-As exchange and As-P exchange processes during the growth.

Current understanding of P-As exchange

The annealing of InP surfaces under an As flux in a solid-source MBE system has been shown to produce a thin pseudomorphic InAs layer of maximum 2 ML thickness through the replacement of desorbing P by impinging As [117]. By the surface photo-absorption method, P-As exchange has been shown at substrate temperatures above 360°C, at which P desorption starts, for an AsH_3 flux on the InP(001) surface [87] in a MOVPE reactor. In a solid-source MBE system at an As flux of $1.5 \cdot 10^{-5}$ torr the thickness of the InAs layer formed by PAsX has been determined by XPS to increase with increasing substrate temperature from 1.25 ML at 450°C to 2.6 ML at 575°C [172]. A STM study of the InAs layer formed by an AsH_3 flux on the InP surface focuses on the surface reconstructions involved in this process [102]. It also shows that the exchange starts at 350°C, and that an InAs film of 7.3Å thickness forms. A cross-sectional STM study of InAs QDs grown on InP(311)B determines 2 ML of additional InAs due to PAsX [30]. In Ref. [24] the amount of excess InAs formed by PAsX is determined to be 4-5 ML through the calculation of the volume of grown InAs nanostructures from AFM images. The same study shows that significantly less excess InAs forms on $In_{0.53}Ga_{0.47}As$ and $In_{0.52}Al_{0.48}As$ buffers as these contain no P to be replaced by As. Even though this kind of calculation has a high uncertainty due to the AFM-inherent tip-surface convolution resulting in an increased apparent lateral size of the nanostructures, it clearly shows the qualitative trend. The formation of InAs QWr exclusively by PAsX has been demon-

strated with solid-source MBE in Ref. [198]. A subsequent reduction of the As flux resulted in the decomposition of the QWrs into QDs. The amount of excess InAs due to PAsX was determined to be 2.1 ML based on the volume of QWrs measured with STM [199].

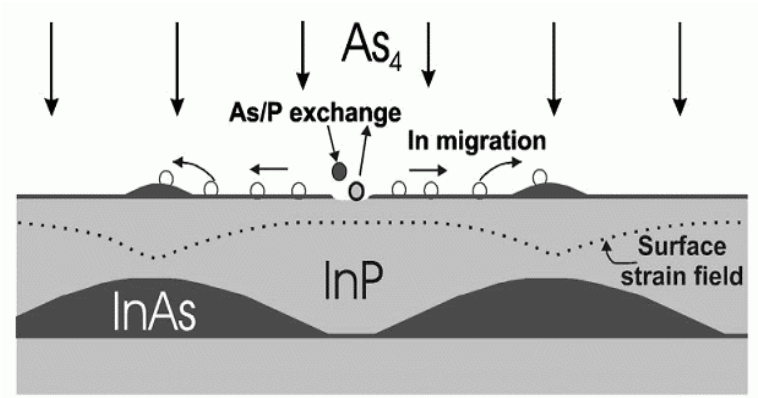

Figure 2.12: InAs growth by P-As exchange and strain-driven surface migration.[54] See text for explanation.

The limitation to the thickness of the InAs formed by PAsX is understood in terms of protecting the InP from further P desorption by the formed InAs layer. If strain-driven transport of In ad-atoms on the surface plays a role, however, the amount of excess InAs due to PAsX is *not* limited. Figure 2.12 illustrates this mechanism that has been used by the authors of Refs [201, 68, 23, 54] to explain their experimental results. Desorbing P atoms are replaced by the impinging As. The InAs formed in this way is laterally strained to match the underlying InP layer. If the strain in the surface is non-homogeneous it is energetically favorable for the InAs to form in regions with a lateral lattice constant close to that of relaxed InAs. Such a strain inhomogeneity may arise from existing InAs nanostructures whose apex is more relaxed than the InAs wetting layer [201], or from the strain field inside the InP from to buried InAs nanostructures [54]. Since In atoms from the surface are mobile, they can migrate to the energetically favorable regions and form InAs with the impinging As. These regions can be the more relaxed apex of existing InAs nanostructures on the InP, or InP regions with higher lateral lattice constant due to the strain field from buried InAs nanostructures. The energetically unfavorable regions continue supplying In from the InP layer because no protective InAs layer forms there to limit the PAsX. As result of this described mechanism, the excess InAs due to PAsX during the growth of InAs QDs by MOCVD at high growth temperatures and AsH_3 flux has been shown to be 17 ML [201]. The formation of QDs

with heights in the range of 100 nm, in this case, has been explained by the migration of In ad-atoms to the dot apex. Lower growth temperatures and AsH_3 flux have been shown to result in less excess InAs. The insertion of an $In_{0.53}Ga_{0.47}As$ layer underneath the InAs effectively suppressed the formation of excess InAs. Similarly, the insertion of a 1 ML-thick GaAs layer prior to InAs deposition has been used to suppress PAsX, and optimize the PL properties of InAs QDs [6]. On the other hand, the formation of QDs and QWrs only by PAsX on InP buffers with a built in strain field induced by buried InAs nanostructures has been observed and explained by strain-driven In migration in MOVPE [23] and MBE growth [54], respectively.

The determination of the abruptness of the InAs/InP interface seems a very difficult issue. Based on the data from grazing-incidence X-ray anomalous diffraction measurements are best fit to the model of QWr shape if a transition layer with thickness below 1 ML is considered [99], whereas XRD measurements in Ref. [114] are best fit to the model by tentatively assuming 2-3 ML. A value of 2 ML is given in Ref. [63]. The effect of a possible transition layer is not considered within this thesis. The thorough analysis of XRD data on smooth InAs QWs may yield additional insight.

Own investigations on P-As exchange in GSMBE

The amount of InAs formed by PAsX reduced by the amount transformed into InP by AsPX during capping is determined in two quantum well samples. A 15 period superlattice with InAs layers that were formed only by PAsX (sample HU932), and an InAs single QW grown by the deposition of 2 ML InAs (sample HU1463N) have been analyzed with low temperature PL. Additionally, the superlattice sample was analyzed with XRD. One period of HU932 consists of the InAs layer formed during a 120 s growth interruption with As flux, followed by a $t_6 = 10$ s P flux before capping with 25 nm InP. The single QW sample HU1463N has been grown with a PAsX time of $t_3 = 15$ s, and AsPX time $t_6 = 10$ s. Figure 2.13 shows the PL spectra taken at T=6 K, and the XRD spectrum. The PL peak positions at T=6 K indicate an InAs thicknesses of 4 ML in HU1463N, and 3 ML in HU932. In contrast, the analysis of satellites in the XRD data of HU932 (based on Eqs. 2.12, 2.10, 2.11) yields a total InAs contents of 4.5 ML per period with a total period thickness of $D = 257.5$ Å. The resulting discrepancy of 1.5 ML InAs is attributed to the incorporation of residual As from the growth chamber into the InP spacer layers. The higher incorporation rate of As compared to P [49, 79] leads to a disproportionally high As content even at a low background As pressure. The corresponding average spacer composition is $InP_{0.983}As_{0.017}$. The simulated rocking curve based on this spacer compositon

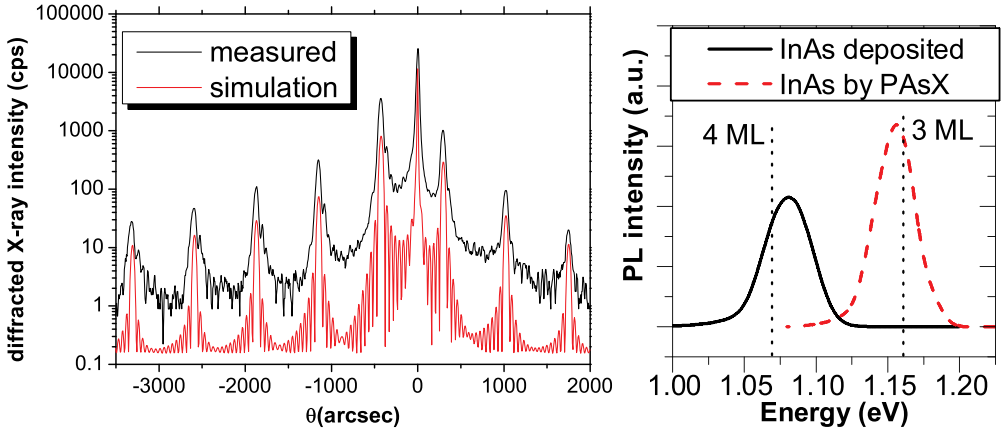

Figure 2.13: **left:** XRD rocking curve of a 15 period InAs/InP superlattice (HU932), InAs formed only by PAsX. The simulated curve is shown below the measured one. **right:** PL spectra taken at 6 K. Superlattice sample (HU932) with InAs formed only by PAsX, and a single InAs QW sample (HU1463N) grown by 2 ML InAs deposition. The calculated PL energies for 3 ML and 4 ML thick InAs QWs at T=0 K are given as reference.

and a 3 ML thick InAs layer shown in Fig. 2.13 agrees with the experimental data.

Based on these results, the amount of excess InAs is determined to 2 ML for the 15 s PAsX (HU1463N), and 3 ML for 120 s PAsX (HU932), both at an AsPX time of 10 s. The results for the comparably long time of 120 s suggest a saturation of the PAsX at 3 ML due to the protective effect of the InAs layer, whereas the results from the sample with thickness of 2 ML at relatively short 15 s suggest a quick PAsX of the first 2 ML. This value is in agreement with most of the aforementioned results from other groups. I used PAsX times (t_3 in Fig. 2.11right) of 15 s and AsPX times (t_6 in Fig. 2.11right)of 10 s as standard parameters for the growth of my samples. Therefore, an excess of 2 ML InAs is assumed for all InAs/InP samples.

The morphology of InP surfaces with different orientation (N, A, B) after a long anneal in As has been measured with AFM. During the annealing RHEED observations show a 2D-3D transformation only on the B-type substrate after 7 minutes, whereas the RHEED pattern on the other substrates indicates planar layers. The morphologies shown in Fig. 2.14 show markedly different results for the different misorientations. The layer formed on nominally oriented substrate (Fig. 2.14a) shows a smooth surface with large monolayer terraces. The fact that no nanostructures have formed shows that the thickness of the InAs is below the critical thickness for SK growth suggest-

ing a limited PAsX. On the A-type substrate, a surface modulation with a wire-like morphology (along the direction of the surface steps) is visible. In comparison to InAs nanostructures grown by InAs deposition on this type of substrate, the surface modulation formed by PAsX is low, suggesting a limited PAsX. In marked contrast, the InAs on the B-type substrate forms giant InAs dots of typically 100 nm base length and 50 nm height. These dots look similar to those of Ref. [201] that formed at the highest temperature and AsH_3 flux used in that study. The volume of my dots clearly demonstrates unlimited PAsX due to surface diffusion as illustrated in Fig. 2.12.

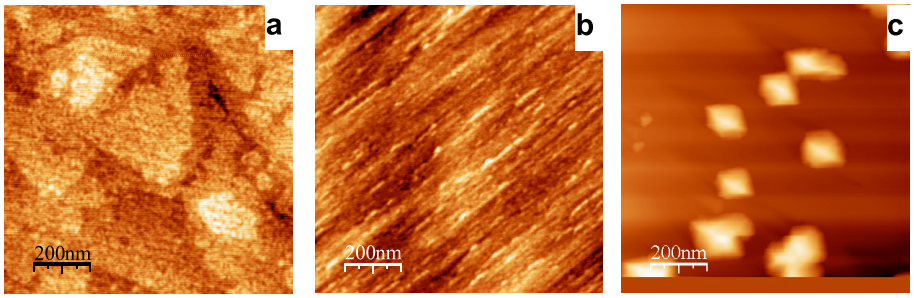

Figure 2.14: AFM images of nominal InP (a), A-type vicinal InP (b), and B-type vicinal InP (c) after an anneal under As flux for 15 minutes. The lateral size is 1 μm $\times$ 1 μm for all images. The height scales are 1.2 nm (a,b), and 80 nm (c).

Summary

The P-As exchange process typically forms a 2 ML-thick InAs layer on the expense of the underlying InP through the replacement of desorbing P by impinging As. This process can be suppressed by growth temperatures below the P desorption temperature (360°C). Non-homogeneous strain distribution can drive a lateral material transport resulting in unlimited P-As exchange in regions with unfavorable strain for InAs and accumulation of this formed InAs in regions with favorable strain. On B surfaces the P-As exchange is unlimited due to spontaneous formation of 3D islands.

2.5.2 The role of vicinal substrates

Practical technological applications of self-organized InAs nanostructures require a high level of understanding and control of the nanostructure formation and morphology. One most basic issue is the control of the nanostructure type — quantum dot or quantum wire.

Self-organized growth of InAs on the InP(001) surface has been demonstrated to lead to the formation of quantum dots *or* quantum wires parallel to the [$\bar{1}$10] direction using four different epitaxial growth techniques. For growth on nominally oriented (N surface) InP(001), the results under a variety of conditions may be summarized as follows: Metalorganic vapor phase epitaxy (MOVPE, MOCVD) [109] appears to result exclusively in the formation of QDs. Chemical-beam epitaxy (CBE) [137] generally results QDs but a mix of QWrs and QDs is also apparently possible [69]. Using gas-source molecular beam epitaxy (GSMBE), the growth of QDs [1] as well as of QWrs [191] has been reported. The most commonly used growth technique for InAs/InP nanostructures is solid-source molecular-beam epitaxy (MBE), for which the shape of self-organized nanostructures can depend on details such as buffer [62] or even surface reconstruction [198].

The miscut of vicinal substrates has also been shown to play an important role in influencing the type and arrangement of self-organized InAs nanostructures on InP. Off-cuts from InP (001) have been reported toward [110] (A surface), toward [$\bar{1}$10] (B surface), and toward [100] (C surface), usually with a magnitude of 2°. This off-cut angle results in monolayer steps every 8.4 nm. On A surfaces, these steps (A steps) run parallel to the direction of InAs quantum wires. Self-organized QDs appear to form more readily on a C surface than on an N surface using MOCVD [128]. Using CBE, it was demonstrated that off-cut substrates lead to an earlier formation of QDs than do nominally oriented substrates [38] and that QWrs form more easily and more uniformly on A surfaces than on N surfaces [68, 69]. QWr formation was also reported on A surfaces grown using GSMBE [191]. Using MBE, QWrs were found on N surfaces and on A surfaces, while QDs were observed on C surfaces [150].

This section demonstrates that self-organized nanostructures grown by GSMBE on vicinal InP (001) substrates occur as either quantum wires or as quantum dots depending on the off-cut direction and generally independently of other growth conditions. This result is in marked contrast to the growth of nanostructures on nominally oriented substrates for which the details of the growth conditions play a determining role on the resulting morphology. The growth of self-organized quantum dots and quantum wires on nominally oriented and vicinal substrates is investigated for varying InAs depositions, deposition rates, and deposition temperatures; whereas for the nominally oriented substrates, the growth conditions determine the type of nanostructure, on vicinal substrates, it is only the off-cut which is important. Thus, the use of vicinal substrates represents a robust way to determine the nanostructure type in the InAs/InP system.

The effect of the surface misorientations (N, A, B surfaces) for different

InAs layer thickness is discussed first. Figure 2.15 shows AFM images of a sample with 2 ML, 4 ML, and 6 ML of deposited InAs, all using a substrate temperature of T=450°C. All AFM images were taken in-air with a Park Scientific Instruments model CP operating in contact mode. The deposition of 2 ML InAs onto the N surface results in a 2-dimensional (2D) layer with large monolayer terraces; on the A surface short, flat, closely packed quantum wires parallel to the surface steps formed; the 2 ML onto the B surface results in quantum dots with low areal density, roughly aligned parallel to the surface steps. The height of the QWrs is about 0.6 to 1.2 nm (measured at the edge between QWrs and flat areas between the QWrs) and the QDs are 3 to 7 nm high. These results demonstrate that misoriented substrates lead to an earlier onset of islanding (three dimensional growth, 3D growth) than nominal surfaces, consistent with the same effect reported for CBE grown samples [38].

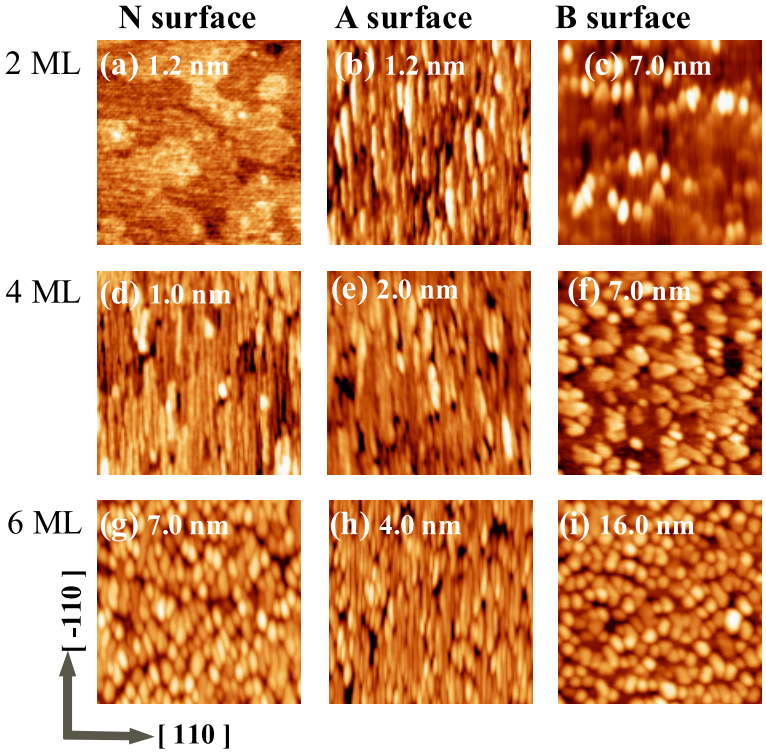

Figure 2.15: AFM 0.5μm × 0.5μm, InAs/InP different InAs thickness. The height scales are given in parentheses and inside the images.
2 ML deposited: (a) "N" (12 Å), (b) "A" (12 Å), (c) "B" (70 Å).
4 ML deposited: (d) "N" (10 Å), (e) "A" (20 Å), (f) "B" (70 Å).
6 ML deposited: (g) "N" (70 Å), (h) "A" (40 Å), (i) "B" (160 Å).

When the deposited InAs is increased to 4 ML, 3D growth also begins on N surfaces. The onset of 3D growth with a critical thickness (between 2 and 4 ML of deposited InAs in my case) indicates a nanostructure formation in the Stranski-Krastanov growth mode. The AFM images show long, flat, and closely packed quantum wires on both the N surface (0.6 to 0.9 nm high) and A surface (0.9 to 1.5 nm high), but dots (typically 3 to 5 nm high) of higher areal density and with random alignment on the B surface. The QD's areal density of $5{\cdot}10^{10}$ cm^{-2} on the B surface is as high as that obtained in Ref. [50] on (311)B InP substrates which have been intentionally used to obtain a high density of QDs. Similar morphologies for the N and A surfaces were obtained using solid-source MBE [150]. The PL spectra of the 4-ML samples (Fig. 2.16) also show the similarity of the structures on N and A surfaces. The lower PL energy on the B surface also substantiates the AFM results showing that the dots are higher than the wires. The room temperature PL of the N surface sample (not shown here) peaks at 0.808 eV (1.54 μm) with a linewidth of 60 meV, demonstrating the application potential of the QWrs for lasers operating at 1.55 μm. Cross-sectional transmission electron microscopy (TEM) images (see Fig. 2.17) of a stack of 15 InAs(4 ML)/InP(20 nm) layers grown under the same growth conditions confirm that also the capped InAs nanostructures are wire-like on A surfaces and dot-like on B surfaces. (The InP spacer between the InAs layers is thick enough to suppress any influence due to the strain fields of the previous InAs layer.) The height of the wires (2.4 nm) is bigger than the height determined with AFM, due to tip-sample convolution. The precise cross-sectional shape of the QWrs cannot be resolved with these images. Published results from other groups on similar structures show a trapezoid cross-section with (114) facets and flat top [67, 116]. The height of the dots (3 nm), on the other hand, is smaller than that determined by AFM (4 nm), suggesting a shrinking of the InAs nanostructures due to the replacement As atoms by P atoms (As-P exchange) when exposed to the a P flux before capping. Owing to As-P exchange and/or tip-sample convolution of AFM, the width of the capped QDs at their base is approximately 15 nm (see TEM image Fig. 2.17c) as opposed to the apparent width of uncapped QDs of 50 nm (see AFM image Fig. 2.15f).

When the InAs deposition is further increased to 6 ML, I find quantum dots on the N surfaces elongated in the [$\bar{1}$10] direction (quantum sticks, quantum dashes), typically 3 to 5 nm high; the A surface results in longer quantum sticks and quantum wires (typically 2.5 nm high); the B surface results in the growth of dots (typically 5 to 10 nm high). The RHEED of the annealed InAs surface shows clear wedges in the [$\bar{1}$10] azimuth indicating the presence of 3D structures.

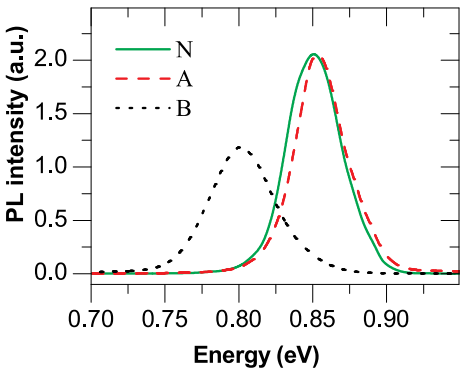

Figure 2.16: Photoluminescence at 5 K of 4 ML InAs deposited on different InP(001) surfaces. Nominal surface (N), misoriented toward [110] (A), and misoriented toward [$\bar{1}$10] (B).

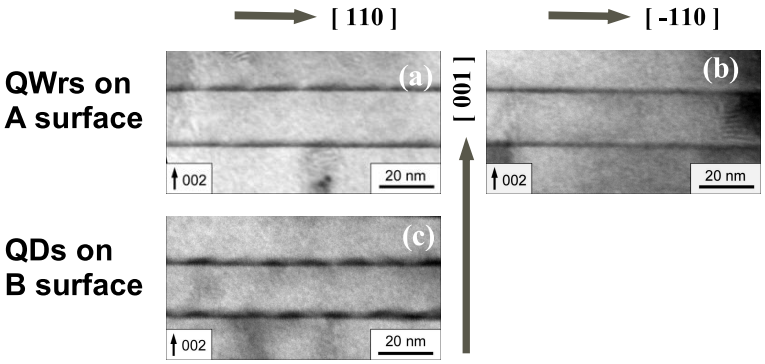

Figure 2.17: Cross sectional TEM, 002 dark-field images of (a,b) quantum wires on "A" surface and (c) quantum dots on "B" surface. The black areas indicate InAs, grey areas indicate InP.

The pitch period of the quantum wires formed by 2 ML InAs on the A surface, by 4 ML InAs on the N and A surfaces, and by 6 ML InAs on the A surface is about 20 nm in every case. I infer from this result that the presence of the steps on the A surface (spacing 8.4 nm) supports the wire formation, but does not determine the pitch period. Thus, the growth of these self-organized QWrs may be contrasted to that of tilted superlattices [56]. A similar pitch period is also reported in wires on N surfaces in [198] and in [62]; I conclude that the pitch period is explained by the mismatch [62] rather than the step period.

That the presence and direction of surface steps due to misorientation plays such a dominant role in determining the shape of the nanostructures is an interesting phenomenon whose microscopic background cannot be fully

explained. One important component to an explanation is the fact that InAs A steps (forming the long edge of these islands) are energetically more favorable than steps along [110] (B steps), resulting in straight A steps and rough B steps [64, 198]. The energetically favorable A steps determine the direction of the QWrs. Furthermore, it is known that ad-atoms tend to attach themselves to existing steps during growth. The formation of QWrs along the $[\bar{1}10]$ direction on N and A surfaces can then be understood based on these points: On A surfaces InAs preferably nucleates at the A steps resulting in a higher local InAs coverage along the steps than on the terraces between steps. This higher local coverage leads to an earlier 2D-3D transition in comparison to N surfaces with a uniform nucleation of InAs. The same argument holds for steps on B and C surface. The steps on B (and C) surfaces, on the other hand, impede the formation of wires in the $[\bar{1}10]$ direction. Experimentally I see that instead of forming QWrs into the [110] direction, the InAs forms high QDs, even for low InAs deposition. Kinetically, the roughness (kinks) along the B steps provide preferred nucleation sites for the ad-atoms leading to a non-uniform nucleation along the B steps. This non-uniformity results in the formation of local InAs clusters that later undergo a 2D-3D transition. Thermodynamically, dots incorporate lower strain energy than do wires, i.e. ΔE_{strain} (in Eq. 2.6) is higher for dots. This argument may explain that it is now energetically favorable for InAs to nucleate on top of existing InAs islands forming dots (less strain) than to form uniformly along B steps. In addition, the more dot-like shape on N surface at a deposition of 6 ML compared to 4 ML suggests an energetic trade-off by lowering the strain energy (dot shape) and increasing the surface and step energy (incorporating more B steps). To theoretically confirm this explanation, more sophisticated kinetic Monte Carlo simulations that include the local strain distribution would be necessary.

InAs deposition onto the C surface results in similar nanostructure characteristics as on the B surface, both in terms of morphology as well of PL (not shown here). AFM images (Fig. 2.18) show that the quantum dots tend to align along the steps ([010] direction) and even quantum sticks form in this direction. This trend of QD alignment on C surfaces can also be seen in samples grown on GaInAsP with CBE [61], and with MBE grown samples on InP [150].

Summary

Vicinal substrates result in an onset of 3D growth at lower deposited InAs thickness than nominally oriented (001) substrates. Vicinal surface misoriented by 2° toward [110] (A surfaces) support the formation of the type of

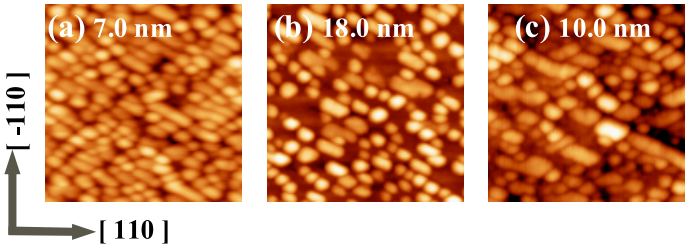

Figure 2.18: AFM 0.5μm × 0.5μm, InAs/InP on "C" surface. The height scales are given in parentheses and inside the images.
(a) 4 ML, lower growth rate, (70 Å)
(b) 6 ML, default growth conditions, (180 Å)
(c) 6 ML on $In_{0.52}Al_{0.48}As$, (100 Å).

QWrs that also grow on exactly oriented (001) surfaces (N surfaces). Vicinal (001) surface misoriented by 2° toward [$\bar{1}$10] (B surfaces) lead to the formation QDs. Similar QDs form on C surfaces (misoriented by 2° toward [100]). In addition, these QDs are roughly aligned along the surface steps ([010] direction) demonstrating the potential of in-plane alignment of QDs through vicinal substrates.

2.5.3 Influence of growth parameters on InAs nanostructures

To gain more insight into the growth kinetics and dynamics, parameters that influence the ad-atom surface diffusion, such as growth temperature, growth rate, and As flux were varied, and the resulting InAs morphologies were measured with AFM. These investigations include nominal (N) and vicinal (A, B) substrates.

Influence of growth temperature

The effect of growth temperature on the morphology of self-organized nanostructures was investigated by depositing 4 ML of InAs at different temperatures (including 450°C discussed already). Unless explicitely noted, all other growth conditions were maintained (PAsX for 15 s, InAs growth rate 0.4 ML/s, AsH_3 flux 0.6 sccm, post deposition anneal for 10 s). Figure 2.19 shows the resulting morphologies with images f-h representing the already discussed sample grown at 450°C as reference.

To suppress 2D-3D growth transition, samples were grown at a low substrate temperature of 380°C (to reduce ad-atom diffusivity D_s), high growth

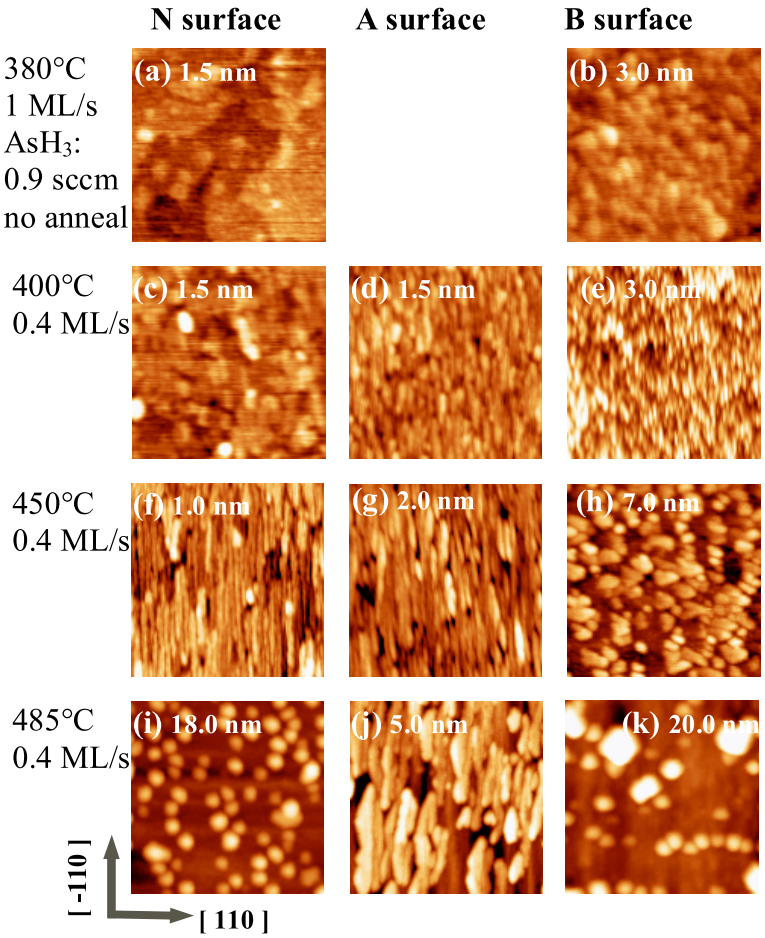

Figure 2.19: AFM 0.5μm $\times$ 0.5μm, InAs/InP different growth temperature. The height scales are given in parentheses and inside the images.
380°C, higher growthrate: (a) "N" (15 Å), (b) "B" (30 Å).
400°C: (c) "N" (15 Å), (d) "A" (15 Å), (e) "B" (30 Å).
450°C: (f) "N" (10 Å), (g) "A" (20 Å), (h) "B" (70 Å).
485°C: (i) "N" (180 Å), (j) "A" (50 Å), (k) "B" (200 Å).

rate and without annealing (reduce ad-atom diffusion time τ_s). The AsH_3 flux was chosen as low as possible to still have an As-rich (2 $\times$ 4) reconstructed surface, as in all other samples. On the nominally oriented substrate (Fig. 2.19a), the InAs surface is quite smooth without InAs nanostructures. Monolayer terraces similar to those on the 2 ML-sample can be seen. This sample serves as reference QW sample with the same nominal InAs coverage (4 ML) as the nanostructure-containing samples compared to it. On the B surface (Fig. 2.19b), a rougher layer formed without discernable nanostruc-

tures indicating preferred nucleation at B step kinks but insufficient surface transport for a 2D-3D transition.

A relaxation of the kinetic restrictions by increasing the substrate temperature to 400°C, and applying the standard growth rate and annealing, results in overall rougher surfaces (Fig. 2.19c-e). On the A surface shallow wires are discernable, whereas the nominal surface contains no wires. The B surface shows QDashes oriented along $[\bar{1}10]$. These morphologies suggest a surface diffusion sufficient to reach the steps of the vicinal substrate.

At 450°C, QWrs form on N, and A surfaces, and QDs with average height of 4.5 nm on the B surface as discussed in the previous section.

The effect of the higher temperature of 485°C on the N surface is that low areal density quantum dots form instead of the wires seen at T=450°C; these QDs are roughly 10 nm in height. When the group V flux is changed from PH_3 to AsH_3 on the InP buffer, the RHEED pattern changes from $\times 4$ to $\times 1$ in the $[\bar{1}10]$ azimuth indicating a change in surface reconstruction – probably into the In-rich (4×2) reconstruction of the InAs that formed by PAsX. This reconstruction remains until wedges form due to the 2D to 3D transition during the AsH_3 annealing of the deposited InAs. It is tentatively concludes that the formation of QDs instead of QWrs is thermodynamically favorable due to the reduced strain energy of QDs compared to QWrs, and possible A steps being no more energetically favorable on the (4×2) reconstructed InAs surface. This explanation is consistent with the observation in Ref. [198] that QDs appear on the (4×2) reconstructed InAs that are elongated into the [110] direction - the direction of the dimer rows of this reconstruction.

On the A surface, elongated nanostructures appear that are higher (about 3.5 nm), wider, less ordered than the quantum wires, and are no more closely packed. On the B surface two classes of QDs are formed: A class of smaller dots with an average height of 11 nm that show alignment along the B steps, and a class of large dots with heights in excess of 30 nm and a lower areal density. The lower areal density of nanostructures on the A, and B surface is kinetically favored due to higher ad-atom surface diffusivity D_s, and thermodynamically due to the larger size (same arguments as for Ostwald ripening).

Influence of As flux

In these experiments, the As flux was varied for fixed growth conditions (PAsX for 15 s, 4 ML of InAs deposited, growth temperature 450°C, InAs growth rate 0.4 ML/s, post deposition anneal for 10 s). The actual As content of the surface, that determines the kinetics, is a function of the As flux/In flux ratio during the InAs deposition. Please note, that in our GSMBE the As

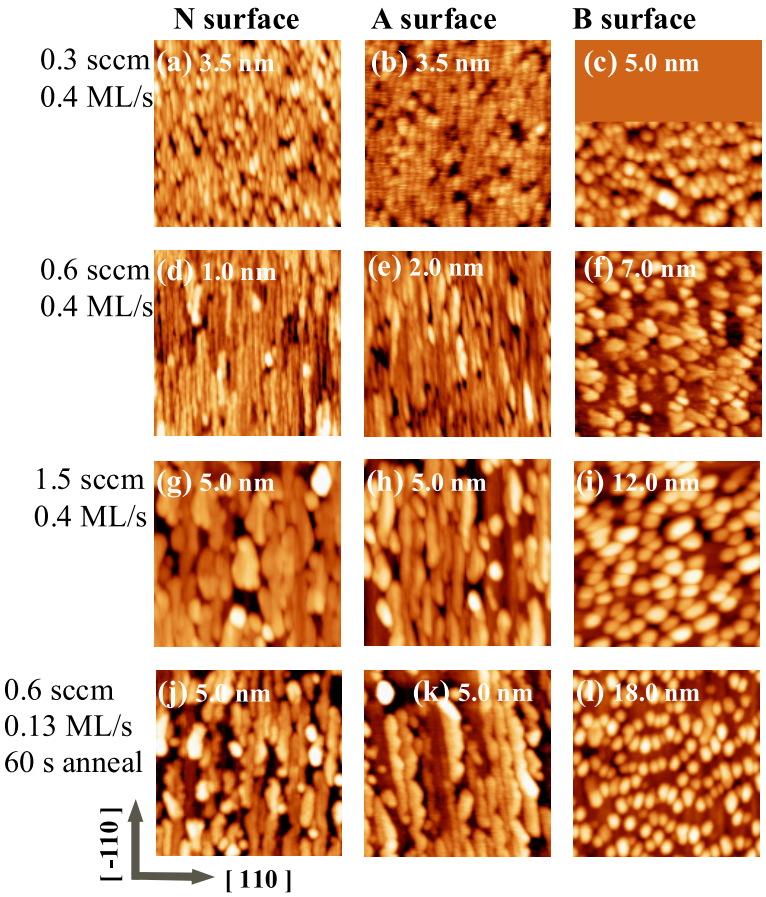

Figure 2.20: AFM 0.5μm × 0.5μm, InAs/InP different AsH_3 flux and growthrate. The height scales are given in parentheses and inside the images.
0.3 sccm, 0.4 ML/s: (a) "N" (35 Å), (b) "A" (35 Å), (c) "B" (50 Å).
0.6 sccm, 0.4 ML/s: (d) "N" (10 Å), (e) "A" (20 Å), (f) "B" (70 Å).
1.5 sccm, 0.4 ML/s: (g) "N" (50 Å), (h) "A" (50 Å), (i) "B" (120 Å).
0.6 sccm, 0.13 ML/s, 60 s anneal: (j) "N" (50 Å), (k) "A" (50 Å), (l) "B" (180 Å).

flux is controlled by the AsH_3 flux, which is given as the parameter in sccm. Figure 2.20 shows the resulting morphologies with images d-f representing the already discussed reference sample grown at 0.6 sccm. The samples shown in sub-figures j-l were grown at the standard As flux but at lower growth rate (lower In flux) corresponding to a higher surface-As content than the reference sample. For each AsH_3 flux, the morphologies on N and A surfaces are very similar (Fig. 2.20a,b; d,e; g,h; j,k), but differ markedly from the

morphology on B surfaces (QDs at all AsH_3 fluxes, Fig. 2.20c; f; i; l).

At AsH_3 fluxes of 0.3 sccm and 0.6 sccm (reference sample) the morphologies are very similar. Narrow, closely spaced QWrs form on N, and A surfaces. These QWrs are shorter at the lower AsH_3 flux.

Similarly, at a higher surface As content (AsH_3 flux of 1.5 sccm or growth rate 0.13 ML/s at 0.6 sccm) thicker, higher, less ordered QWrs form similar to those formed at higher substrate temperature on the A surface (Fig. 2.19j).

Hence, with increasing diffusivity due to increasing surface As content, the morphology on N and A surfaces develops from short narrow wires, over long narrow wires, to thick, high, and less ordered wires. This development suggests thick QWr to be energetically preferred to thin QWrs on N and A surfaces.

An alternative explanation is based on the shape of 2D InAs islands nucleating at different As fluxes and their subsequent 2D-3D transition. Ref. [66] shows with a combination of kinetic Monte Carlo simulations and scanning tunneling microscopy that the nucleation of InAs on InAs(001) results in a decreased number of 2D islands at higher As flux. The theory of Ref. [32] that suggests the SK growth to function via 2D islands that undergo a 2D-3D transition if they exceed a critical size. Thus, the narrow or thick QWrs may be seen as large or small 2D islands (depending on As flux) that underwent the 2D-3D transition.

On the B surface, QD height drasticly increases with increasing AsH_3 flux, whereas the areal density of QDs decreases only slightly. Possible underlying mechanisms for this dependency will be discussed in Sec. 2.5.5

Summary

Growth temperature and AsH_3 flux influence the nanostructure shape through their impact on growth kinetics. Low growth temperatures can be used to suppress the 2D-3D growth transition, and were used to grow a QW reference sample with the same nominal InAs thickness as the QWr and QD samples. At high growth temperatures, QDs form also on N surfaces, and the height of QDs on B surfaces is increased. A high AsH_3 flux creates thicker, less ordered QWrs on N and A surfaces, and higher QDs on B surfaces.

2.5.4 Post deposition modifications of InAs nanostructures

The final shape of InAs nanostructures on InP can be strongly modified by surface transport of In after the deposition of the InAs layer: The QWrs discussed in Ref. [2] have been formed during the 2D-3D transition by in-situ

annealing an MBE-deposited 2D InAs layer at elevated temperature. The influence of group V overpressure on the final shape of CBE-grown InAs nanostructures has been investigated in Ref. [68]. The authors point out that a cooldown of samples under either As or P overpressure modifies the nanostructure shape due to the combination of P-As exchange or As-P exchange and strain induced surface transport (as described in section 2.5.1). A cooldown in vacuum resulting in an In-rich surface is shown to preserve the nanostructure shape. Optimized sample cooling under As overpressure has been shown to trigger the ripening of MBE-grown QDashes into QDs of low areal density [45].

Own investigations of post-deposition modifications

Figure 2.21 shows AFM images of InAs surfaces grown by depositing 4 ML InAs under the default conditions described in section 2.5 but cooled down in vacuum (unless otherwise noted).

A comparison of the morphologies on N surfaces with (Fig. 2.21b) and without (Fig. 2.21a) 10 s annealing at growth temperature after the InAs deposition corroborates the in-situ RHEED observation that the 2D-3D transition happens during the annealing. On the un-annealed surface shallow islands with the shape and arrangement of the QWrs are visible.

The capping of InAs nanostructures by InP at lower temperatures may be necessary to reduce their decomposition by As-P-exchange (see section 2.5.6). The influence of the cooling process required to reach the lower temperature on the nanostructure morphology was investigated. The (fast) cooldown in vacuum (see Fig. 2.21b-d) instead of As overpressure (see Fig. 2.20d-f) results in better defined nanostructures. The shape, areal density, and arrangement, however, does not change significantly.

A slow cooldown under As overpressure (temperature drop of 30 K during 260 s, see Fig. 2.21e-g) transforms the small nanostructures (Fig. 2.21b-d) into larger, higher ones of smaller areal density and regular shape. This process can be seen as a step of the ripening described in Ref. [45]. Somewhat counterintuitively, though, an annealing at growth temperature for 100 s causes no significant morphological changes as shown in Fig. 2.22a,b for N surfaces. Also the QD morphology on B surfaces shows no significant changes in terms of height or areal density (compare Fig. 2.21d to Fig. 2.22c). The shape of the dots, however, is clearly anisotropic with a length in the $[\bar{1}10]$ direction approximately twice the length in the [110] direction on the 100 s-annealed sample. Such anisotropy of InAs QDs on InP has been also observed by other groups [28, 140]. The dots on the sample annealed for 10 s, in contrast, seem less anisotropic. The occurrence of the described ripening

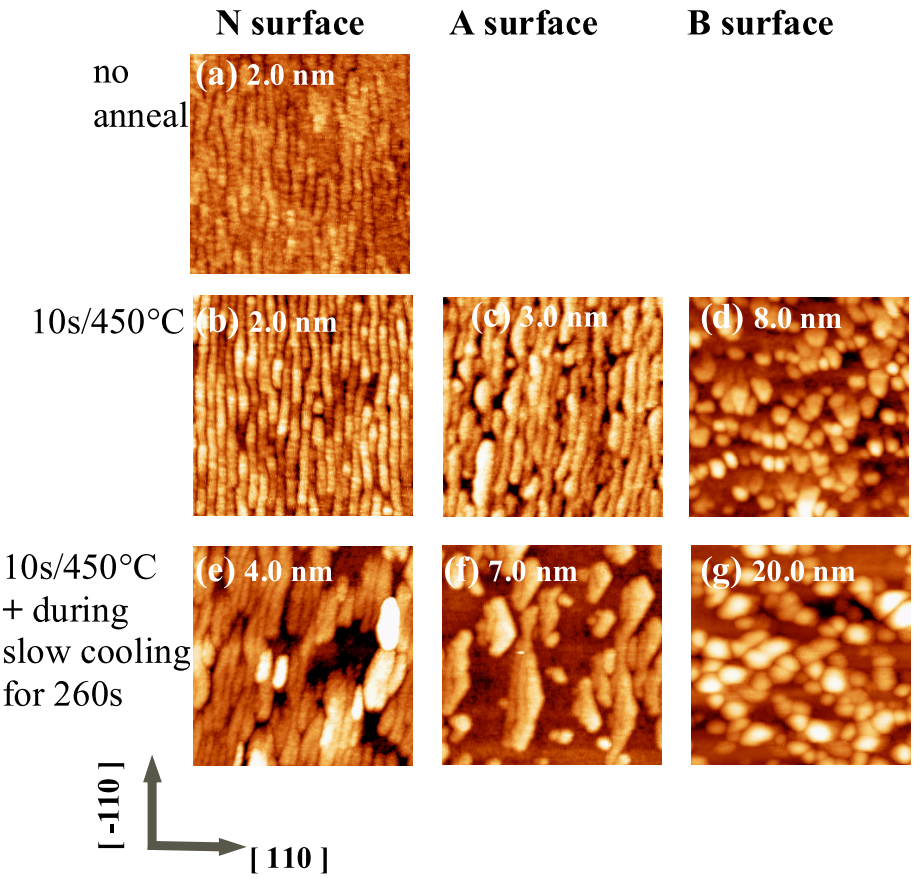

Figure 2.21: AFM $0.5\mu\text{m} \times 0.5\mu\text{m}$, InAs/InP different post-deposition treatment. The height scales are given in parentheses and inside the images. Immediate cooldown in vacuum after InAs deposition:
(a) "N" (20 Å).
10 s annealing with As flux at 450°C, rapid cooldown in vacuum:
(b) "N" (20 Å), (c) "A" (30 Å), (d) "B" (80 Å).
10 s annealing with As flux at 450°C, slow cooldown with As flux:
(e) "N" (40 Å), (f) "A" (70 Å), (g) "B" (200 Å).

only at lower temperatures suggests the As content of the surface and/or the reconstruction to be the decisive factor, and not the temperature. Indeed, Ref. [45] describes the disappearance of the (2×4) reconstruction during the cooling. This reconstruction has been suggested to favor more anisotropic nanostructures [59], which is in agreement with the argument of a lower energy for A steps (steps along the $[\bar{1}10]$ direction) of Ref. [64]. It thus follows, that the ripening is not simple kinetically enhanced by high temperature and consequently surface diffusivity but rather due to the thermodynamics

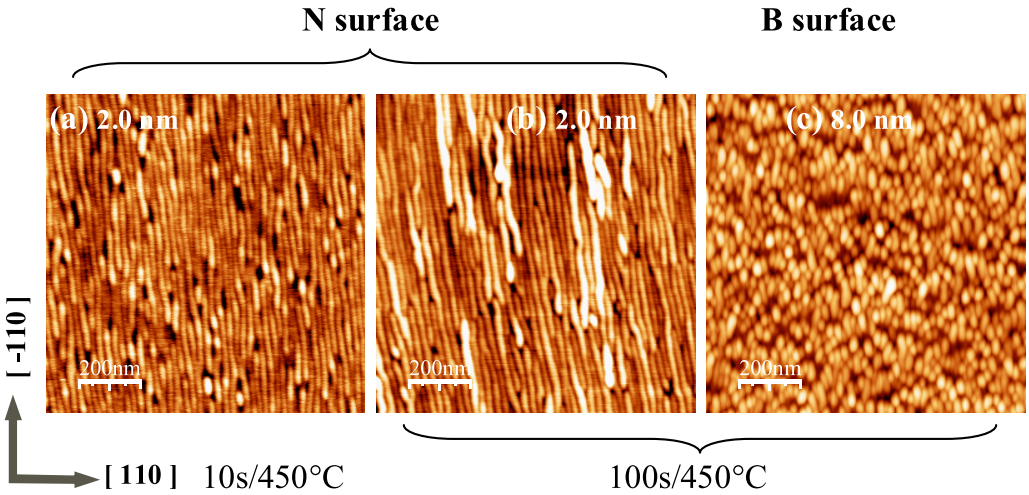

Figure 2.22: AFM $1.0\mu\text{m} \times 1.0\mu\text{m}$, InAs/InP different in-situ post-deposition annealing times. The height scales are given in parentheses and inside the images. Rapid cooldown in vacuum.
10s/450°C with As flux: (a) "N" (20 Å).
100 s annealing at 450°C with As flux: (b) "N" (20 Å), (c) "B" (80 Å).
The QWrs have an average length of 600 nm, some exceeding 1 μm. The QDs are elongate into the $[\bar{1}10]$ direction with typical length to width ratio of 2.

of what nanostructure shape is energetically favorable at different surface reconstructions. Finally, this argument would also explain the elongated dots on the B surface after a longer anneal at growth temperature with a (2×4) reconstruction (Fig. 2.22c).

Summary

The group V flux and substrate temperature after the InAs deposition influence the final InAs morphology significantly. The annealing at growth temperature (450°C) for 10 s is necessary for the 2D-3D transition that forms the InAs nanostructures through surface In diffusion. A slow cooling under As overpressure leads to a coalescence of the nanostructures (ripening) whereas a longer annealing at growth temperature under As overpressure does not change the nanostructures significantly. The ripening is tentatively attributed to a changed surface reconstruction at lower temperatures under As overpressure which makes the narrow long wires energetically less favorable. Rapid cooling in vacuum preserves the shape of surface InAs nanostructures.

2.5.5 QD size and density on B surface - P-As exchange

The height and areal density of QDs grown on B surfaces for a fixed amount of 4 ML deposited InAs under different growth conditions is analyzed. Based on the estimated total InAs volume of all QDs conclusions will be drawn on whether ripening (no change in overall QDs volume) or P-As exchange (increase of overall QDs volume) determine the final QD areal density and height. The data is summarized in Tab. 2.1 and discussed as follows.

A low AsH_3 flux results in a higher areal density of lower QDs in comparison to those grown at "default" conditions. The total InAs volume in the QDs is the similar for both samples. Higher AsH_3 flux ("more AsH_3 ") or growth temperature ("higher T_{growth}") or a slow cooling with AsH_3 flux ("slow cool in As"), on the other hand, leads to the formation of higher QDs with a lower areal density. The increased height, though, is not compensated by a lower areal density which results in a larger total InAs volume in the QDs. Assuming the same wetting layer thickness for all samples, this larger volume strongly suggests the incorporation of excess InAs formed by P-As exchange. Also excess InAs is incorporated into the tall QDs with a high areal density formed at a lower growth rate and a longer annealing time.

Thus, the increased dot height observed at modified growth conditions is primarily an effect of excess InAs formed by P-As exchange in conjunction with strain driven surface transport of In to the QDs. This effect was already described without deposited InAs on B surfaces in Sec. 2.5.1. The method of estimating the QD volume based on AFM images is prone to high uncertainties due to tip-sample convolution that does not allow a precise determination of the lateral QD size. The measured QD height, though, is not affected by this phenomenon if the tip fits between the QDs. It seems reasonable to assume that the lateral size of the QDs does not decrease with increasing height, which is sufficient to support the qualitative results of this conclusion. Deeper AFM investigations with reproducibly sharp AFM tips would allow a more precise calculation of the InAs volume in the QDs based on measured lateral size, height and shape of the QDs.

Summary

On B surfaces, a deviation from the default growth conditions to higher growth temperature, higher AsH_3 flux, a slow cooling under As overpressure, or low growth rate increases the QD height. Excess InAs formed due to P-As exchange supplies the material for the height increase of the QDs.

Table 2.1: Average height h_{avg} and areal density taken from AFM images of QDs grown on B surface at different conditions. To compare the InAs volume per area in the QDs, the product of height and areal density product is calculated. Under the assumption of the same shape and lateral size of all QDs this product is a measure of the InAs volume per area in the QDs. The * denotes the drasticly increased lateral QD size that has been taken into account: The QDs of the sample grown with "more AsH_3 " have longer baselengths, the >30 nm-high QDs of the sample "higher T_{growth}" are at least twice as long and wide as the QDs grown under the "default" conditions.

growth parameters	AFM image Figure	h_{avg} nm	QD density 10^{10}cm^{-2}	h_{avg} × density nm ×10^{10}cm^{-2}
default	2.20 f	4.5	5.0	23
cool in vacuum	2.21 d	5.0	5.2	26
longer InAs anneal	2.22 c	5.0	6.0	30
slow cool in As	2.21 g	10	3.5	35
less AsH_3	2.20 c	3.0	7.8	23
more AsH_3	2.20 i	8.0	4.4	>35*
lower growth rate + longer InAs anneal	2.20 l	11	6.3	69
higher T_{growth}	2.19 k	11/>30	1.1/0.3	>48*

2.5.6 As-P exchange process during capping

Capping of the grown InAs nanostructures is a necessary step for most of the applications that involve their optical properties and their transport properties. During the capping of InAs nanostructures with InP, though, the exchange of As by impinging P (AsPX) transforms parts of the InAs into InP. A net surface In transport opposite to that shown in Fig. 2.12 actively disassembles the nanostructures and forms InP between the nanostructures at areas with a lattice constant close to that of relaxed InP as described in Ref. [68]. This strain driven net In transport makes the AsPX faster on nanostructures than on smooth InAs QWs. The utilization of the AsPX to modify the size of InAs QDs in a controlled manner by a double cap procedure has been demonstrated in Refs. [138, 149]. This procedure involves the growth of a thin cap with the tops of tall dots sticking out. These tops are truncated by AsPX prior to the growth of the remaining cap. Ref. [55] demonstrates the tailoring of the size on InAs QWrs by AsPX, and shows that the AsPX is virtually suppressed at substrate temperatures below 380°C. A cross-sectional STM study of identically grown InAs QDs on InP(311)B with

different cap layers measured an average QD height of 2.9 nm for an InP cap, and 3.5 nm for an $In_{0.53}Ga_{0.47}As$ cap. The difference is attributed to the height reduction of 0.6 nm due to AsPX during the capping with InP.

Own investigations of As-P exchange

As-P exchange was observed in-situ with RHEED by the disapperance of wedges in the RHEED image upon annealing of 3D InAs nanostructures under a P flux at growth temperature.

Furthermore, InAs nanostructures were capped with InP at different growth temperatures in order to control of the AsPX. In the reference sample (HU1591) the growth temperature was not changed for the capping. The temperature reduction, performed in the other samples, by approximately 60°C after the formation of the nanostructures (at typically 450°C) is, however, prone to change the nanostructure morphology due to the In surface migration as discussed in section 2.5.4. In order to suppress this re-organization of the surface, a rapid temperature reduction (substrate heater off for 40 s) was performed in sample HU1603 before capping. (The actual substrate temperature was deduced from the RHEED pattern.) A 5 nm InP cap was grown immediately after the temperature reduction at 390°C to protect the InAs nanostructures, followed by a substrate heating to the original growth temperature and growth of the remaining cap at 450°C. The room temperature PL of the reference sample HU1591 and low-temperature-capped sample HU1603 are given in Fig. 3.3, right (in chapter 3). The QWr containing samples (on N, and A surfaces) show no significant red-shift. The large red-shift of the QD containing sample (grown on B surface) due to the low-temperature-capping suggests a significant AsPX at 450°C as compared to 390°C. The thicknesses deduced from the PL peak position are 48 Å and 30 Å for low-temperature-capped and default capped sample, respectively. A comparison of the QD height of capped QDs (TEM image, Fig. 2.17c) with the height of QDs grown at the same conditions on the sample surface (measured with AFM, see Tab. 2.1, "default" growth conditions) comes to similar results. The comparison indicates a height reduction from 5 nm (AFM dot height + assumed wetting layer thickness) to 3 nm (capped dot height). Thus, the much faster AsPX process with QDs on B surfaces than with QWrs on N or A surfaces leads to a height of QDs capped at the InAs growth temperature close to the height of the QWrs. The faster As-P exchange on B surfaces coincides with the faster P-As exchange.

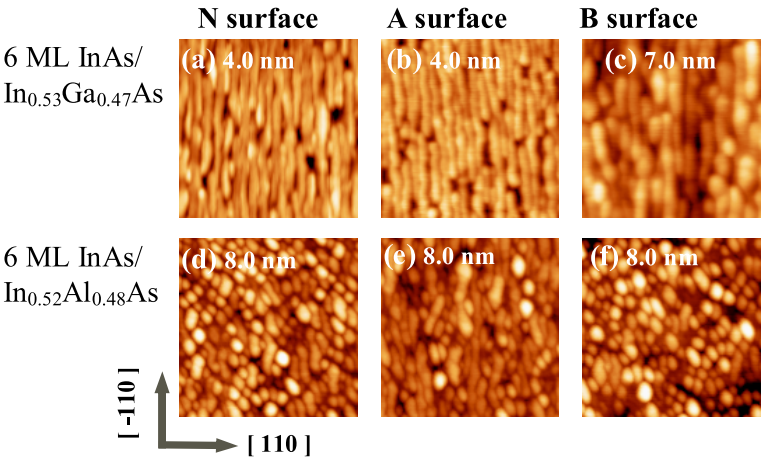

Figure 2.23: AFM 0.5μm $\times$ 0.5μm, , 6 ML InAs on lattice matched ternaries. The height scales are given in parentheses and inside the images. $In_{0.53}Ga_{0.47}As$: (a) "N" (40 Å), (b) "A" (40 Å), (c) "B" (70 Å) $In_{0.52}Al_{0.48}As$: (d) "N" (80 Å), (e) "A" (80 Å), (f) "B" (80 Å).

Summary

As-P exchange reduces the size of InAs nanostructures upon capping with InP by transforming InAs into InP. The As-P exchange is stronger on the QDs on B surfaces than on the QWrs on N or A surfaces, and can be reduced by choosing lower growth temperatures during capping. Overgrown QWrs and QDs at default growth conditions are 2.4 nm and 3.0 nm high.

2.5.7 InAs on $In_{0.53}Ga_{0.47}As$ and $In_{0.52}Al_{0.48}As$

To what extent the substrate off-cut influences InAs nanostructures grown on the lattice matched ternaries was tested for $In_{0.52}Al_{0.48}As$ and $In_{0.53}Ga_{0.47}As$ buffers. AFM images of 6 ML deposited on InGaAs and InAlAs (InAs grown under same default growth conditions as in the 4 ML InAs/InP sample) are shown in Fig. 2.23. A deposition thickness of 6 ML InAs was chosen to have the same total InAs thickness as the 4 ML deposited InAs on InP due to the additional 2 ML InAs formed on InP by P-As exchange.

On $In_{0.53}Ga_{0.47}As$ quantum wires formed on N, and A surfaces. They even form (though less pronounced) on B surfaces. On $In_{0.52}Al_{0.48}As$ quantum dots formed irrespective of the substrate misorientation. Only on A surfaces also short quantum wires are present. On N surfaces, this tendency of dots to form on $In_{0.52}Al_{0.48}As$, and wires to form on $In_{0.53}Ga_{0.47}As$ was also observed with MBE for a deposition of 3 ML [24]. (Opposite results were demonstrated

in [103], where the MBE growth of 6 ML of InAs on $In_{0.52}Al_{0.48}As$ forms quantum wires, and in Ref. [207] where MBE growth of 6 ML of InAs on $In_{0.53}Ga_{0.47}As$ formed quantum dots.) On these ternaries the influence of the steps seems, however, to be much less significant than on InP. Instead, the morphology of the ternary buffer as well as alloying effects with the InAs layer, as suggested in [24], influence the InAs morphology for my growth conditions.

2.6 Conclusion

In conclusion, InAs nanostructures on InP grow in the Stranski-Krastanov growth mode on a 1-2 ML-thick wetting layer. Surface steps on vicinal InP(001) surfaces play a decisive role in the self-organized formation, shape, and alignment of InAs nanostructures during gas-source MBE growth. The data show that the misorientation facilitates the nucleation of nanostructures, but that the quantum wires do not simply occur one per step. As a consequence, the growth of InAs quantum wells is best accomplished on nominally oriented substrates but also quantum wires parallel to $[\bar{1}10]$, and quantum dots can be grown on this orientation by varying the growth conditions. On substrates off-cut toward [110], nanostructures elongated into $[\bar{1}10]$ form for all growth conditions investigated, and quantum dots could not be grown on these substrates. (Among these elongated nanostructures is the type of QWr described for nominally oriented substrates.) Conversely, an off-cut toward $[\bar{1}10]$ always leads to the formation of quantum dots but never to quantum wires. An off-cut toward [100] leads to similar results as the previous orientation with a discernable alignment of the QDs along the step direction. This tendency of the quantum dots to align along the steps might be exploited for the realization of quantum-dot chains by optimizing the growth conditions and varying the off-cut angle.

Thus, in contrast to the nominally oriented substrates, vicinal substrates provide a rather growth-condition-independent template for the robust realization of defined quantum dots or quantum wires. In order to obtain quantum wires also with MOVPE I suggest growth experiments on surfaces off-cut toward [110]. On other matrix materials with the same lattice mismatch, namely $In_{0.53}Ga_{0.47}As$ and $In_{0.52}Al_{0.48}As$, the influence of the off-cut seems to be less significant.

In addition to the deposited InAs, a 2 ML thick InAs layer forms due to the P-As exchange process. On substrates off-cut to $[\bar{1}10]$ this process seems not to be limited to 2 ML due to strain induced surface transport of In. As a result, the volume and height of QDs grown with the same amount

of deposited InAs depends strongly on the impact of growth conditions on the P-As exchange. Thus, areal densities between $1 \cdot 10^{10}$ and $8 \cdot 10^{10}$ cm^{-2} and average QD heights from 3 nm to 11 nm are found.

The quantum wires that are investigated in the following chapters are closely spaced with a lateral period of 20 nm, and a height after overgrowth of typically 2.4 nm. Their length is varying with typical lengths of 200 nm to 600 nm. (Some quantum wires are longer than 1 μm.) These QWrs are grown on nominally oriented substrates and on substrates off-cut toward [110]. The formation is related to the (2×4) surface reconstruction.

The quantum dots investigated in the following chapters are generally higher than QWrs that are grown on a different substrate orientation under the same growth conditions. Typically the quantum dots have an areal density of $5 \cdot 10^{10}$ cm^{-2} and a height of 5 nm. After capping, their height is reduced to 3 nm, and their baselength is approximately 15 nm. The QDs are likely to have an anisotropic base with the longer axis into the $[\bar{1}10]$ direction. This height reduction is a result of the As-P exchange process during capping of the InAs with InP.

Reference samples containing InAs quantum wells instead of QWrs or QDs have been grown using the same nominal InAs thickness. In these samples the formation of nanostructures by 2D-3D growth transition has been inhibited by kinetic limitations such as low growth temperature, high growth rate, and low As flux.

Chapter 3

Optical properties

This chapter gives a brief overview of the grown nanostructures' optical properties and will demonstrate their principal applicability for optical devices (that are summarized in section 3.1). A band diagram involving heavy hole, light hole, and electron states is employed to calculate the interband transition energies in section 3.2. The polarization dependence of the nanostructures' interband transitions is investigated in terms of emission in section 3.3 and absorption in section 3.4. Whereas literature data exists on polarized emission properties on InAs nanostructures, no detailed data exists on their *polarized* interband absorption. In section 3.4, polarization dependent absorption spectra of a quantum dot sample, a quantum wire sample, and a reference quantum well sample in combination with the calculated transition energies allow to identify the interband transitions involved in the absorption. The oppositely polarized absorption peaks in both QWr and QD samples are shown to originate from the transitions of heavy-hole like and light-hole like valence band states to the conduction band states. A description of the discussed structures is given in terms of their growth (deposited InAs thickness, superlattice, substrate misorientation and respective nanostructure type) and AFM images showing the corresponding uncapped nanostructures.

3.1 Optical applications of InAs/InP nanostructures

InAs has a direct band gap (see Fig. 3.1), i.e. the electrons in the conduction band minimum (Γ-valley), and the heavy holes and light holes in the valence band maximum have the same momentum (wave vector). As a consequence, transitions between the valence band maxima and conduction band minima can be mediated by photons without requiring additional phonons to com-

pensate for a momentum difference between electron and hole. In addition, the InAs/InP interface is a type-I interface that results in a confinement of electrons and holes in the InAs. Both these properties support an efficient radiative recombination of electrons and holes in the InAs. In addition, the reduced dimensionality of quantum wires, and quantum dots is proposed to increase the temperature stability of semiconductor lasers [10], and to reduce their threshold currents. Thus, currently the largest application potential of InAs nanostructures grown on InP substrates is considered to be optical devices - mainly for the telecommunication wavelength of 1.55 μm which can easily be reached in this material system. Lasers for 1.55 μm have been demonstrated based on InAs QDs [145, 4, 7], InAs QDashes [181, 155], and QWrs [169]. In addition, lasers with longer wavelength up to 1.9 μm, for gas sensing applications, and lasers with a broad (250 nm) gain profile have been demonstrated based on quantum dashes [164]. The usage of InAs quantum dots in infrared photodetectors (QDIPS) has been demonstrated [107, 205]. Furthermore, the application of InAs QDs for mode lockers (as saturable absorber) [81], for optical charge storage [134], and recently as single photon source within photonic crystals [39] has been proposed.

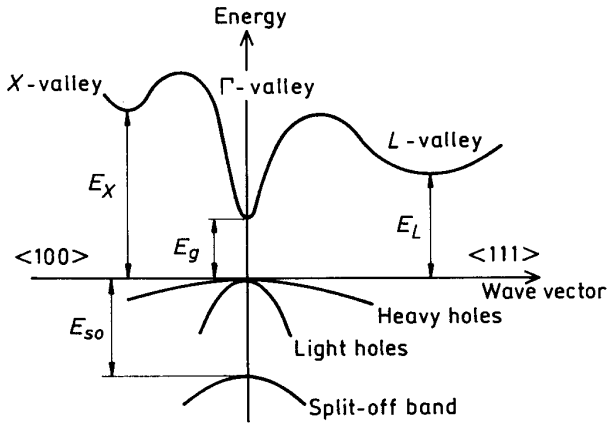

Figure 3.1: Schematic band structure of InAs. [100]

3.2 Interband transitions

My optical investigations probe the nanostructure's interband transitions, i.e. transitions between electrons (e) in the conduction band (cb), and heavy holes (hh) or light holes (lh) of the valence band. Both transitions, emission and absorption, are measured by photoluminescence (PL) and transmission measurements.

Owing to their flat character (height much smaller than width, length, see chapter 2), the capped nanostructures can be treated in a simplified way as a biaxially strained InAs quantum well. This approximation is justified because the smallest dimension (height) leads to the largest confinement energy, while the lateral confinement results in a much smaller contribution (see following calculation). The biaxial strain of the InAs grown pseudomorphically on the InP results in a lifting of the valence band degeneracy at the gamma point into a lh and a hh band, as well as in anisotropic effective masses ($m^{[001]} \neq m^{<110>}$). Table 3.1 summarizes the theoretically calculated data taken from different references. Despite the variation of the values for

Table 3.1: Band gaps E_g^{hh} and E_g^{lh} between cb/hh and cb/lh, and effective masses (in units of the free electron mass m_e) of e, lh and hh for InAs biaxially strained to InP at T=0 K from different references.

Ref.	E_g^{hh} (meV)	E_g^{lh} (meV)	$m_e^{[001]}$ (m_e)	$m_e^{<110>}$ (m_e)	$m_{hh}^{[001]}$ (m_e)	$m_{hh}^{<110>}$ (m_e)	$m_{lh}^{[001]}$ (m_e)	$m_{lh}^{<110>}$ (m_e)
InP [188]	1424	1424	**0.08**	0.08	**0.53**	0.88	**0.12**	0.11
InAs [188]	417	417	0.026	0.026	0.33	0.51	0.027	0.013
InAs on InP								
[84]	368	529	-	-	-	-	-	-
[160] sp^3s*	511	670	0.063	0.049	0.041	0.071	0.120	0.109
[160] sp^3d^5s*	443	600	0.039	0.025	0.030	0.041	0.099	0.062
[116]	495	650	0.044	0.025	0.034	0.025	-	-
[141]	471	-	0.029	0.029	0.137	0.137	-	-
used here	**471**	**629**	**0.045**	-	**0.035**	-	**0.11**	-

band gap and effective masses, the strain-induced hh-lh separation varies only between 155 and 161 meV. Additionally, the strain results in higher effective masses for light holes than for heavy holes. A band diagram of an InAs QW that includes heavy holes and light holes, and the calculated transition energies for different well widths w are shown in Fig. 3.2 and Tab. 3.2. The subband edges are calculated based on the states in a finite quantum well (envelope function and effective mass approximation) using the program *efsqw* of Ref. [72] and the bold values of the table. The band offsets are taken from Ref. [141] as 439/281 meV for heavy/light holes, and 514 meV for electrons. Based on TEM images (Fig. 2.17), the height of the overgrown nanostructures (equals the well width) is determined to be in the range of 20 to 30 Å. The calculations yield that well widths up to 40 Å provide only one confined state for electrons and heavy holes. Hence, only e1-hh1 and e1-lh1 transitions are expected since there are no excited states. In the thickness

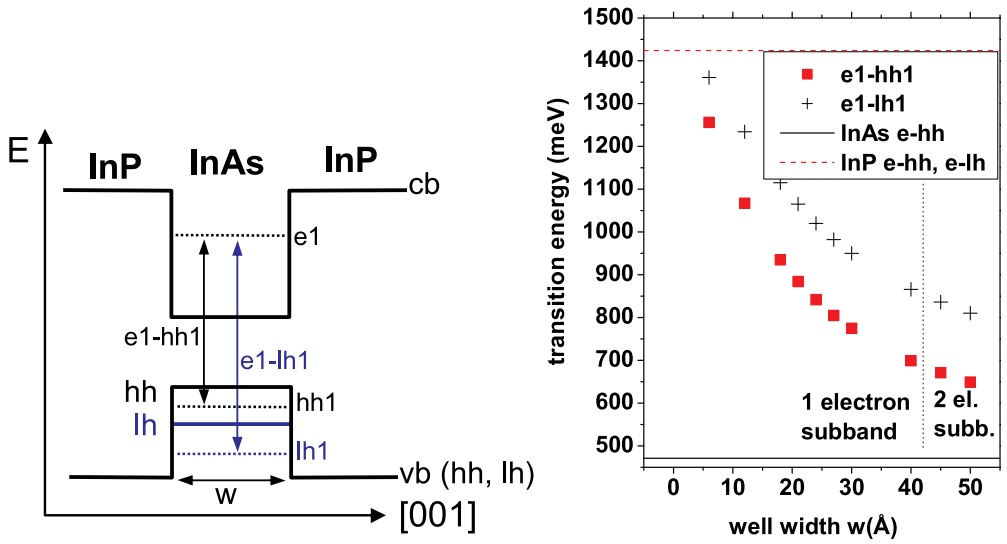

Figure 3.2: **left:** Band diagram of a strained InAs QW of width w on InP including the hh-lh splitting. The ground subbands of e, hh, and lh are marked. The interband transitions are marked with arrows and labeled accordingly. **right:** Calculated transition energies at T=0 K. In the range of 18 to 30 Å the spacing is 3 Å corresponding to approximately 1 ML on InAs.

range of 20 to 30 Å, a thickness change by 1 ML results in transition energy shift of approximately 40 meV. The splitting between e1-hh1 and e1-lh1 in this thickness range is calculated to approximately 180 meV. The energy contributions due to vertical confinement for electron (holes) range from 200 meV to 300 meV (100 meV to 180 meV) in the thickness range of 30 Å to 18 Å. In contrast, the energy contribution due to lateral confinement (with a well width >15(20) nm) is <31(20) meV and <16(10) meV for electrons and holes, respectively. In a rough approximation of separated lateral and vertical confinement, this energy contribution increases the transition energy of a QWr in comparison to a QW by less than 47 meV. The transition due to the first excited states of the lateral confinement is 50 to 150 meV higher in energy (for lateral size of 30 to 15 nm) than the ground state transition.

More sophisticated calculations of the interband transitions in QDs and QDashes are used in Refs. [116] and [78], respectively. These calculations completely include the lateral confinement. The calculations for the 2.4 nm-high QDashes of Ref. [116], that have a cross-section similar to my QWRs, result in a ground state transition at 848 meV, and a transition energy difference between ground state and first excited state of the lateral confinement of 152 meV. This difference corresponds to an average width of 15 nm according

to my estimations. My calculated ground state transition including a lateral confinement (width 15 nm) is approximately 40 meV higher in energy. The calculations for QDs of Ref. [78] include the strain relaxation within the dots that have lateral extensions of 40 nm to 90 nm. They end up with ground-state transition energies of 760 meV to 650 meV for dot heights of 6 nm to 12 nm. In contrast to my calculated values, those energies are lower, which is probably due to the strain relaxation within the dots.

Table 3.2: Calculated transition energies for InAs/InP QWs of different well width at T=0 K.

width (Å)	e1-hh1 (meV)	e1-lh1 (meV)
6	1256	1361
12	1067	1234
18	936	1115
21	884	1065
24	842	1020
27	805	982
30	775	950
40	699	866
45	671	836
50	649	810

Opposite to the effect of lateral confinement, the exciton binding energy slightly lowers the transition energy. Different values are given for the exciton binding energy of InAs nanostructures in InP. They range from assumed 5 meV for thin QWs and for QDs [108], over <10 meV expected for thin QWs [160], calculated 10-20 meV in QDs [116], up to calculated >20 meV for QDs with a height below 6 nm [78]. Calculation of the exciton binding energy in an InAs quantum well (as described in [11]) based on the in-plane effective masses from Tab. 3.1, and the relative dielectric constant of 15.15 for InAs yields values below 6 meV. Except for the result of [78] all other cited binding energies are <20 meV which will be assumed also in my structures. Hence, in the relevant thickness range of 20 to 30 Å the excitonic binding contribution is less than the the energy change due to a thickness fluctuation of 1 ML and is considered of minor importance. *The net correction to the transition energies calculated for a QW due to lateral confinement in QWr and QD, and due to exciton binding energy is estimated to be approximately +35 meV.*

The temperature dependence of the transition energies is mainly determined by the decrease of the band gap E_g with increasing temperature T, which is often described by the empirical Varshni formula [185]:

$$E_g(T) = E_g(T=0) - \frac{\alpha T^2}{T+\beta} \tag{3.1}$$

with the Varshni parameters α and β. The Varshni parameters $\alpha = 0.276$ meV/K and $\beta = 93$ K for InAs [188] correspond to a bandgap reduction of 0.27(63) meV for a temperature increase from 0 K to 10(300) K. Interband transitions in nanostructures not only depend on the bandgap but also on the effective masses which enter into the confinement energy. Consequently, the bandgap dependence of the effective masses (see Ref. [188]) has an additional contribution to the temperature dependence of the interband transition energy. Thus, the interband transition energies derived from low temperature measurements at $T \leq 10$ K can be directly compared to calculated transition energies (due to the negligible band gap shift), whereas room temperature measurements include a red-shift of a couple of 10 meV.

3.2.1 Origin of polarization

The in-plane polarization of light propagating along the [001] direction (as investigated in my PL and transmission experiments) is generally considered to arise from a transitions between a mixture of lh and hh valence states, and electrons in the cb [22, 37]. The hh-lh admixture can be caused by anisotropic confinement due to shape anisotropy [37]. Ref. [22] derives theoretically that the hh-like mixed valence states result in a polarization along the QWr whereas the lh-like mixed valence states result in the opposite polarization direction. Calculations of Ref. [166] show a polarization anisotropy for InAs QDs on GaAs in the [$\bar{1}$10] and [110] directions but not in the [100] and [010]. My InAs nanostructures grown on C surfaces appear to be elongated into the [100], which would suggest a polarization into that direction. A low height-width ratio of QWrs as well as compressive strain, however, have both been shown to result in a reduction of the degree polarization [187]. The polarization measured in my QD samples, thus is likely to be the consequence of a (small) shape anisotropy. A recent publication [31] on micro-PL of InAs/InP QDs similar to mine shows the polarized emission of single QDs with a degree of polarization of 10-18%, which is similar to my results. This publication explains the polarization also with shape anisotropy but without hh-lh admixture , which contradicts Ref. [37] that explicitely excludes optical anisotropy in a single-band model of the valence band. The calculations

of optical transitions for 6-12 nm-high QDs [78] include the polarization-dependent absorption of the different states of a 6 nm-high QD elongated in the [$\bar{1}$10] direction. As a result, the ground-state absorption shows only negligible polarization anisotropy.

In addition to transmission along the [001] direction, polarization-dependent measurements of transmission along the <110> directions, yield information on the lh or hh character of the transition [37]. The hh-e transition only shows an in-plane polarization, termed TE mode, whereas the lh-e transition shows a 4 times larger absorption for the polarization in the [001] direction, termed TM mode, than for the TE mode. This type of experiment, however, is out of the scope of this thesis.

3.3 Photoluminescence

With photoluminescence non-equilibrium electron-hole pairs are generated by illuminating the sample with photons that have an energy above the energy of the transition to be measured. The carriers relax within their respective bands to the lowest available energy state, and recombine finally. The spectrum of the photons created by radiative recombination of these electron-hole pairs is measured. Prior to the recombination, the electron-hole pairs diffuse within the sample, and may get localized in potential minima such as the InAs nanostructures. In the present experiments the luminescence is excited by lasers with photon energies above the band gap of the InP matrix. Hence, electron-hole pairs are mainly created in the InP matrix which is the thickest layer that has the major contribution to the absorption of the excitation light.

Figure 3.3, left, shows a typical PL spectrum of a single layer of InAs QWr (AFM image in Fig. 2.15d). Even though most of the excitation light creates carriers in the InP matrix, neither a peak at the band-gap energy of InP nor at the wetting-layer transition energy is visible. This observation suggests an efficient capture of the carriers by the InAs nanostructures, due to their high density [150, 2, 151]. A peak due to the InAs quantum wires is visible at 857 meV. The second peak at 1.20 eV may be attributed to a 2 ML InAs wetting layer. Detailed investigations [136], however, yield that this peak is not due to the wetting layer but due to the transition of electrons from the cb of InP into the vb of the $In_{0.52}Al_{0.48}As$ buffer layer as described in [44].

In the right pane of Fig. 3.3 the room temperature PL spectra of different samples are given to show the wavelength range that can be covered by emission from InAs nanostructures embedded in InP. These wavelengths include

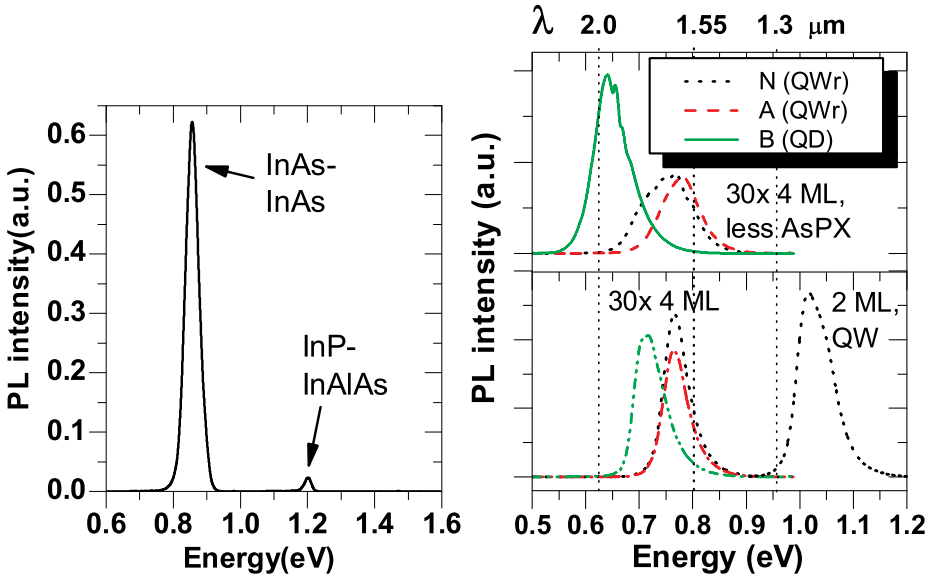

Figure 3.3: **left:** Typical PL spectrum of a sample containing InAs QWrs grown by depositing 4 ML of InAs using nominally oriented substrate and an $In_{0.52}Al_{0.48}As$ layer on InP measured at 4 K. Peaks due to radiative recombination within the InAs and between InP and $In_{0.52}Al_{0.48}As$ are marked with arrows. No peaks due to a recombination within the InP or InAs wetting layer are visible. **right:** Room temperature PL spectra of different InAs nanostructures demonstrating the wavelength range that can be covered. Vertical dotted lines indicate the reference wavelengths 2.0 μm, 1.55 μm, and 1.3 μm. The legend indicates the substrate types and in parentheses the nanostructures that form on them. The bottom part shows the spectra of a 30 layer superlattice of InAs nanostructures capped with InP at the default growth conditions. The top part shows the spectra of an identically grown sample but with a capping of the nanostructures at lower temperature after a rapid cooldown. The labels "4 ML" and "2 ML" denote the thickness of deposited InAs; the 2 ML sample is an InAs quantum well.

the telecommunication wavelengths of 1.3 and 1.55 μm, and extend at least up to 2 μm. In the bottom part, a QW sample with 2 ML of deposited InAs (AFM image in Fig. 2.15a), and three samples (AFM images Fig. 2.21b-d) with 4 ML of InAs deposited on differently oriented substrates (N,A,B) are shown. A clear red shift is visible with increased InAs thickness (from 2 to 4 ML) which qualitatively agrees with the expected dependence of transition energy with quantum well thickness (see Fig. 3.10, right). Among the 4 ML samples, the B-type substrate results in a PL peak at lower energy than the

N, and A-type substrates. This behavior agrees with the observation from AFM and TEM, that the quantum dots formed on the B substrate are higher than the quantum wires forming on N, and A-type substrates at the same amount of grown InAs. All PL peaks of the 4 ML sample consist of a single Gaussian-like band with FWHM around 50 meV. This width suggests a very uniform height of the nanostructures because fluctuations by 1 ML would result in different peaks separated by approximately 40 meV.

The three samples shown in the top part of Fig. 3.3, right, are similar to the 4 ML samples of the bottom part but a different capping procedure for the InAs was used in order to reduce the As-P exchange (as discussed in section 2.5.6) at the grown InAs nanostructures. This capping results in taller nanostructures than the "normal capping" of structures shown in the bottom part. The PL peak of the N substrate sample is significantly broader (FWHM=115 meV) than the corresponding peak of normally capped sample. This larger width is attributed to multiple peaks due to wires of different height as described in [2] for InAs/InP QWrs. The QD related peak is significantly red-shifted in comparison to the normally capped sample which shows that the dot height in the normally capped QD sample is much lower. The comparison of the PL of the samples with normal capping and low temperature capping demonstrates that the normal capping results in a drastic reduction of the dot height, and in a homogenization of the wire height.

No contribution from either excited states of the lateral confinement nor from the e1-lh1 transition to the PL spectra are visible. The excited state of the lateral confinement would yield an additional peak at about 100 meV higher in energy, whereas the e1-lh1 transition is calculated to be approximately 180 meV above the e1-hh1 transition. The measured peaks, however, are too narrow to include these additional peaks. Consequently, the measured PL is considered to stem exclusively from the e1-hh1 ground-state transition.

PL spectra at a temperature of 10 K have been measured to allow an estimation of the nanostructure height using the calculated e1-hh1 transition energies for 0 K in Fig. 3.2. The PL spectra at 10 K, at room temperature, and the temperature dependence of PL peak position are given in Fig. 3.4 for the 15 period superlattices of quantum wires, and quantum dots grown on A and B surfaces by depositing 4 ML of InAs under the default growth conditions. The red-shift with increasing temperature is mainly due to the decrease of band gap energies (Eq. 3.1). At 10 K the peak positions of the QWr and QD samples are 866 and 814 meV, roughly 50 meV above the room temperature value. (A comparison the InAs bandgap shift of 63 meV suggests some additional 10 meV due to the change of effective

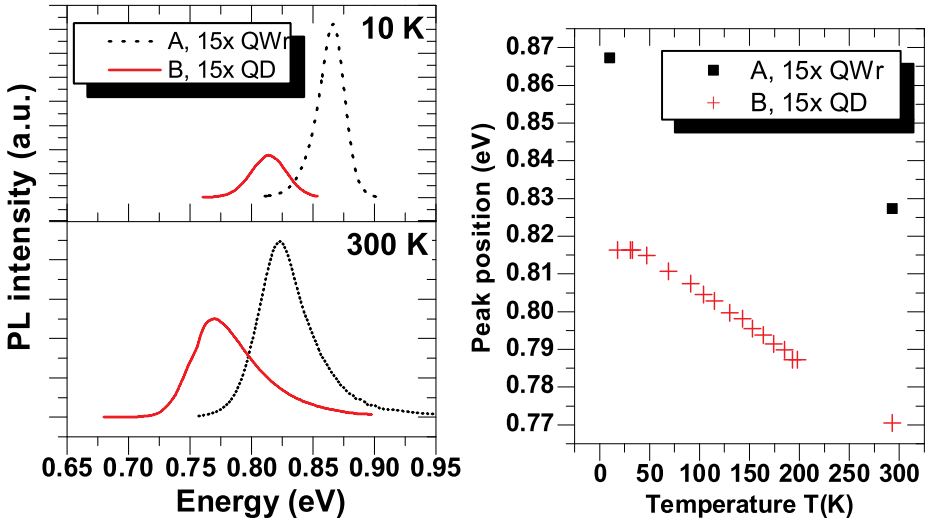

Figure 3.4: **left:** PL spectra of 15 period superlattices of quantum wire and quantum dot samples grown on A, and B surfaces, respectively, taken at 10 K and at 300 K. The 300 K spectra are shifted to lower energies with respect to the 10 K spectra. **right:** Temperature dependence of the PL peak position demonstrating the red-shift with increasing temperature.

masses.) Subtracting the estimated contribution due to lateral confinement and exciton binding energy, the transitions due to vertical confinement are at 831 meV and 779 meV. These values correspond to nanostructure heights (see Tab. 3.10) of 25 Å and 30 Å for the QWrs and QDs, respectively. These heights are in very good agreement with the InAs nanostructure thickness in these samples as determined by TEM (see Fig. 3.5d,e), which is considered a validation of the calculated transition energies. The peak position at 10 K of the high QDs (capped at low temperature) is estimated to 692 meV, based on the room temperature value of 642 meV and the shift determined with the 15 period samples. Within my estimations (considering no strain relaxation), subtracting the estimated contribution due to lateral confinement and exciton binding energy, the transitions due to vertical confinement is at 657 meV, corresponding to a dot height of 48 Å, which agrees well with the height (50 Å) of comparable surface QDs measured with AFM (see Tab. 2.1, Fig. 2.21d in chapter 2). These results demonstrate, that the QDs capped at low temperature are significantly higher (48 Å) than those capped at growth temperature (30 Å). According to Ref. [78] (which includes strain relaxation) this corresponds to a dot height obtained at low capping temperature is 85 Å, which is significantly taller than what I determined with AFM. This significant difference to the height with my model shows that strain relaxation has

a great impact on the transition energy of high QDs.

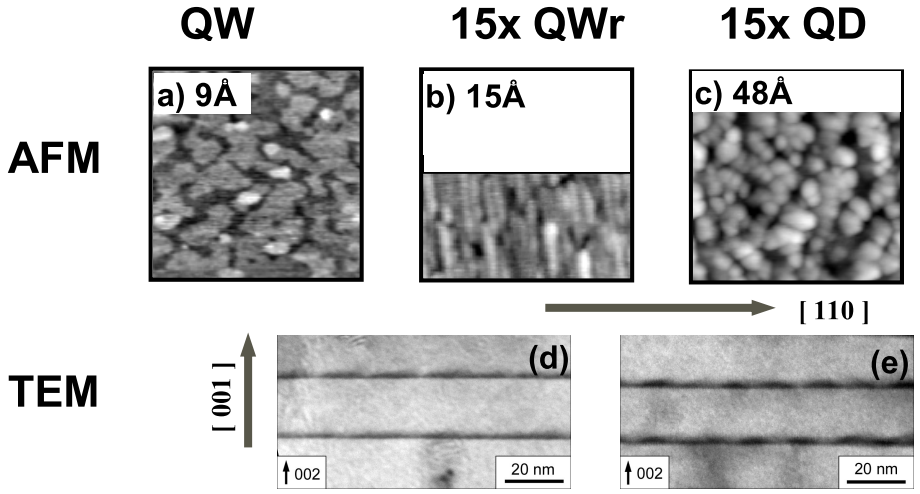

Figure 3.5: Structures of the 3 ML QW sample (a) used in polarized PL measurements, and the 15 layer superlattices of QWrs (b,d) and QDs (c,e). AFM images show an area of 500 nm ×500 nm.

3.3.1 Polarization dependence

The anisotropic nanostructure shape intuitively suggests a polarization of the luminescence whose physical origin was discussed in section 3.2.1. Experimentally, a polarization anisotropy in the photoluminescence has been shown for InAs/InP QWrs and QDs by different groups [62, 150, 119].

At first, the dependence of PL intensity on the polarization of the excitation light has been tested. No such dependence was found in agreement with published results [119], since the main absorption of the excitation light occurs in the InP buffer, which has no preferential direction.

The degree of polarization for the luminescence light of my InAs nanostructures was measured in collaboration with R. Pomraenke [136]. An elaborate setup as shown in Fig. 3.6 was used in order to rule out polarization artefacts due to polarization-selective optical components such as the spectrometer grating. The concept is to rotate the polarization of the luminescence light using a half-wave plate ($\lambda/2$-plate) and pass this light through a linear polarizer (polarization filter) set at a fixed polarization direction. Thus, behind the polarizer the luminescence light has a fixed polarization direction, and any polarization sensitivity of the following optical components does not affect the measurement. A variation of the half-wave-plate rotation allows to select the luminescence light's polarization direction that

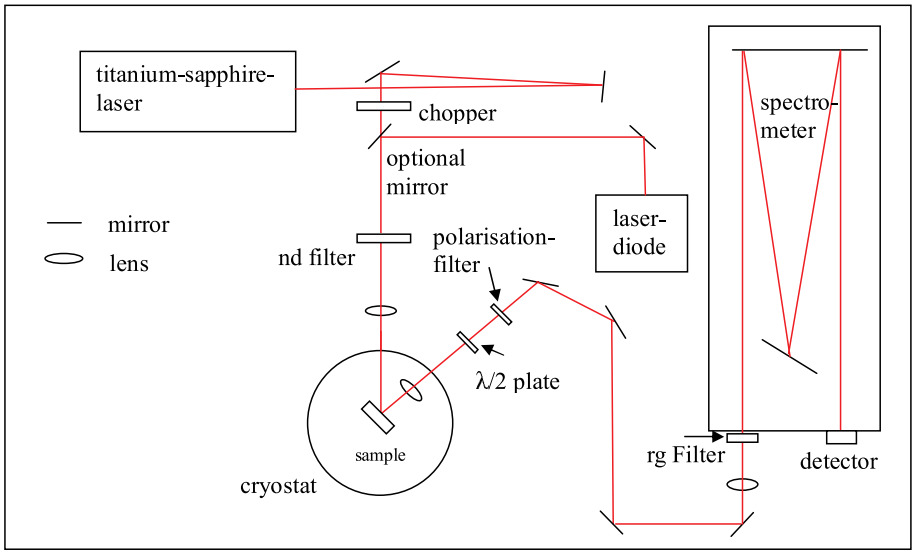

Figure 3.6: Experimental setup to measure polarization dependent PL [136].

is transmitted by the polarizer. (Rotating the half-wave plate by 45° changes the measured polarization direction by 90°.) The measured luminescence intensity at the peak position is recorded for a series of rotation angles of the half-wave plate.

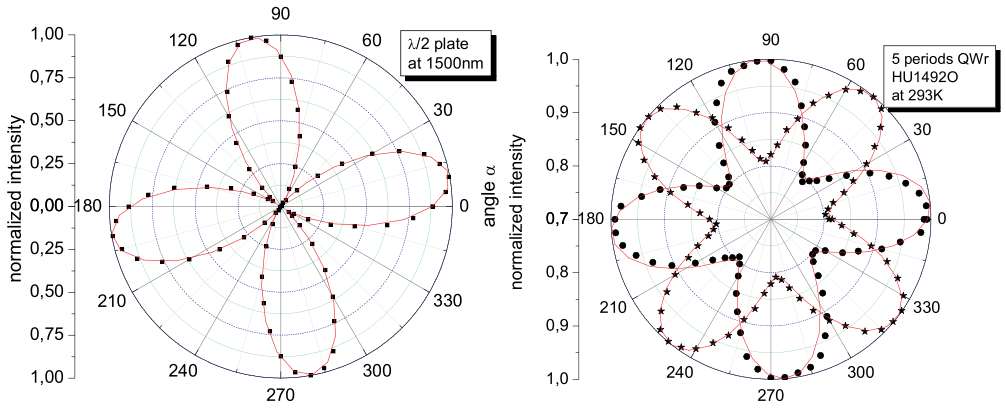

Figure 3.7: Normalized PL intensity at a fixed wavelength for different rotation angles of the half-wave plate [136]. **left:** Setup test using a polarizer between sample and half-wave plate. **right:** QWr sample at room temperature with two orthogonal sample orientations to check for polarization artefacts due to optical components between sample and half-wave plate.

The effect of the half-wave plate has been tested by placing a second polarizer between sample and half-wave plate. Figure 3.7, left,demonstrates

the efficiency of the half-wave plate. Rotating the half-wave plate by 45° changes the intensity from maximum to minimum as the polarization is rotated by 90°. The intensity ratio between maximum and minimum is 30, which is sufficient for the measurements. The right pane of Fig. 3.7 shows the PL-intensity dependence on polarization direction for two perpendicular orientations of the sample. The intensity for a polarization orthogonal to the wire direction is approximately 80% of that parallel to the wires for both orientations of the sample. This test demonstrates the reliability of the setup for polarization dependence.

Polarized PL spectra taken for polarization along the [$\bar{1}$10] and the [110] directions, and the direction dependent PL intensity for a QW sample, a QWr sample, and a QD sample are shown in Fig. 3.8. The corresponding structural information of the samples are summarized in Fig. 3.5. The QW sample consists of one QW with 3 ML deposited InAs grown at low temperature; the other samples are the 15 period superlattice QWr and QD samples already discussed in terms of temperature dependent PL.

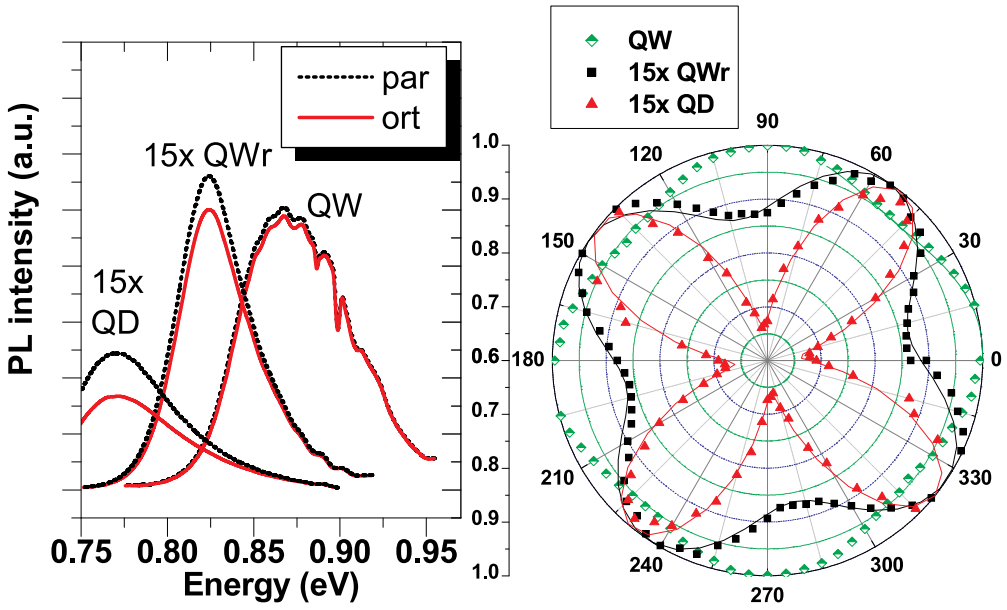

Figure 3.8: Polarization dependent PL of a QW, QWr and QD sample measured at room temperature. **left:** PL spectra taken at room temperature for linear polarization along [$\bar{1}$10] "par" and [110] "ort". (Dips in the QW spectrum due to parasitic absorption.) **right:** Dependence of PL intensity at the peak spectrum's position on polarisation direction. The direction of maximum intensity is [$\bar{1}$10] in all samples. Different angular positions of the maxima in the graph due to sample orientation in the experimental setup.

The lowest polarization degree is obtained for the QW sample as expected. The QWr, and QD show larger polarization. The QD sample, however, shows a significantly larger polarization than the QWr sample. This relation holds true for all samples measured. The degree of linear polarization P is defined as

$$P = \frac{I_{max} - I_{min}}{I_{max} + I_{min}} \tag{3.2}$$

with maximum and minimum PL intensity I_{max} and I_{min} in the mutually perpendicular polarization directions determined to be [$\bar{1}$10] and [110]. Table 3.3 summarizes P determined at room temperature and at 10 K for different samples.

Table 3.3: Degree of linear polarization P in % at 10K and room temperature. The last four columns contain P for the nanostructures denoted in the heading along with the substrate type in parentheses. The first column describes the samples in terms of deposited InAs thickness and number of periods (for superlattices). The sample in the last line is grown to form a QW on all substrates.

Sample	temperature (K)	QWr (N)	QWr (A)	QD (B)	QD (C)
4 ML single layer	293	4±1	8±1	17±1	-
4 ML single layer	10	-	12±1	-	-
4 ML 5 periods	293	9±1	11±1	19±1	14±1
4 ML 5 periods	10	13±1	15±1	-	-
4 ML 15 periods	293	6±1	6±1	21±1	19±1
4 ML 15 periods	10	9±1	13±1	20±1	19±1
3 ML, QW single layer	293	2±1	3±1	3±1	1±1

The polarization direction with higher intensity is [$\bar{1}$10] for all samples. This observation also holds true for the QDs elongated into the [100] (grown on C surfaces). With decreasing temperature, the degree of polarization increases for QWrs but not for QDs. The fact that P is larger for the QDs than for the QWrs is counterintuitive as the QWrs are much more elongated than the almost symmetric QDs. Furthermore, P in my QWr samples seems lower than the values published by other groups. For QWrs a PG of 30%/37% at 18 K/4.2 K is shown in Refs. [62]/[119] for PL peaks that correspond to the PL peak of 15x QWr sample with only $P = 6\%$ at T=10 K. The polarization degree of QWrs and QDs grown on N,A, and B substrates (similar to my

samples 15x QWr/QD) are given as 40% (QWr) and 16% (QD) at 10 K in [150]. The published result on P for the QD sample is compatible with my results, whereas a marked difference exists for the results on QWr samples. One reason for the lower degree of linear polarization in my investigated QWr samples may be their flat shape that makes them structurally similar to a QW.

It should be noted, though, that the electron and hole transport in the QWr samples as discussed in chapter 6. This contrast to the low degree of polarization in my QWrs suggests different mechanisms for transport anisotropy and polarization anisotropy.

3.4 Polarized Transmission

Theoretical calculation of the strength of interband transitions and associated polarization Refs. [22, 116, 78] generally yield absorption coefficients and no luminescence intensities. Therefore, the measurement of absorption is a more direct method than PL to investigate interband transitions. Published experimental data on polarization resolved interband absorption measurements of InAs/InP nanostructures is very rare: Ref. [2] contains a polarized absorption spectrum on InAs QWrs whose degree of polarization appears not convincing, whereas Ref. [36] presents a detailed study of the absorption of InAs QDs but without polarization dependence.

In this section, polarization dependent interband absorption of InAs QWs, QWrs and QDs is investigated and compared. The absorption is measured by transmission measurements. This type of measurement is performed by taking the continuous spectrum of an incandescent light source that passes through the sample, and a reference spectrum without sample. The ratio of the two spectra is the sample transmission spectrum. For photon energies lower than a transition the sample is transparent (transmission 100%) whereas photons of larger energy are absorbed in the sample by exciting the transition. The intensity of transmitted light I_t is the difference between the incoming light intensity I_0, and the reflected and absorbed intensity I_r and I_a:

$$I_t = I_0 - I_r - I_a \tag{3.3}$$

$$I_a = (I_0 - I_r)(1 - \exp(-\alpha d)) \tag{3.4}$$

with spectral absorption coefficient α and thickness of the absorbing layer d. The reflection contribution stems mainly from the reflection at the interfaces between sample and air. Reflections at the heterointerfaces are negligible [112] due to the small refraction index difference between InAs and InP.

The absorption coefficient of InAs and InP above their band gap energy is $\alpha \approx 10^4$ cm^{-1} [100]. Consequently, an InAs thickness of 10(100) nm is required to absorb 1(10)% of the incident light. On the other hand, a substrate of 500 μm thickness absorbs basically all light. The thickness of the InAs layers, in contrast, is approximately 2 nm which is too thin to obtain significant absorption.

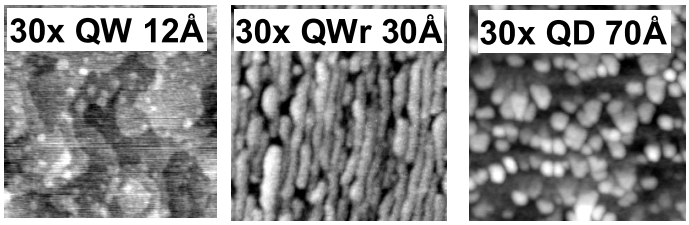

Figure 3.9: AFM images showing 500 nm ×500 nm of the nanostructures in the 30 period superlattice samples used in the transmission measurements. The nanostructure type and height scale are given in the image insets.

In order to increase the total absorption, samples with 30 periods of identical InAs layers separated by 20 nm-thick InP spacers were grown. Sample 30x QWr and 30x QD grown on A-type and B-type substrates, respectively. The 30x QW sample was grown as reference sample that contains flat InAs QWs of same nominal thickness. Figure 3.9 shows AFM images of the corresponding uncapped nanostructures.

The polarization dependent transmission of these samples was measured at room temperature in a Bruker EQUINOX 55 fourier transform infrared spectrometer (FTIR). The sample spectra and reference spectra were taken with a polarizer in front of the sample for both polarization directions, parallel and orthogonal to the [$\bar{1}$10] direction. The light passes the sample in the [001] direction, normal to the sample surface. A conventional halogen lamp served as light source. Prior to the measurement, the rough substrate backside of the samples has been manually polished to reduce optical losses due to scattering. The transmission spectra of an InP substrate, and of the QW sample are shown in Fig. 3.10. In the top left pane the substrate spectrum is shown. The absorption edge at the bandgap energy of InP is the largest feature. At energies far below the InP bandgap the transmission is only 60% instead of theoretical 100%. Reasons for this are reflections at the sample-air interfaces, and optical losses due to the not ideally flat polished substrate backside and a dirt film that accumulates on the front and backside. A residual transmission of 5% exists also for photon energies above the InP bandgap, being another experimental artefact due to parasitic scattered light that bypasses the sample. Weak oscillations due to interferences (Fabry-Perot cavity

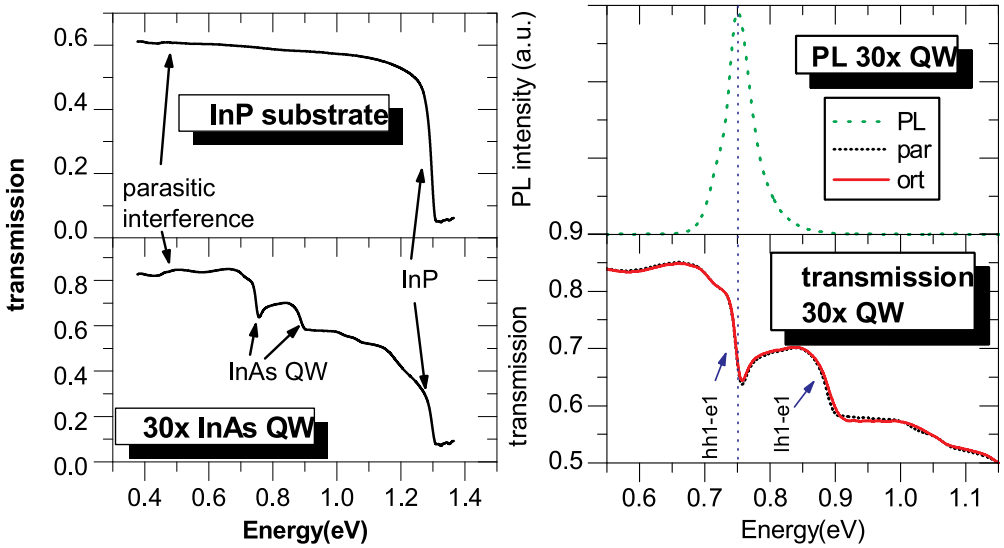

Figure 3.10: Transmission spectra taken at room temperature. Absorption features are labeled. **left:** InP substrate (top), 30x InAs QW sample (bottom). **right:** Interband transitions in 30x InAs QW sample. PL (top), transmission spectra for polarization direction parallel and orthogonal to $[\bar{1}10]$ (bottom). Transitions are labeled.

effect) are visible in the spectra but could not be completely suppressed. The oscillation period suggests that these interferences do not occur within the sample. In comparison to the substrate, the QW sample exhibits two additional absorption edges between 700 meV and 900 meV as shown in the bottom left pane. The right pane of Fig. 3.10 shows these absorption features for polarization direction parallel and orthogonal to the $[\bar{1}10]$ direction. As comparison, the room temperature PL spectrum is given in the top part. The absorption edge at lower energy coincides with the PL peak position (except for a small Stokes shift that should not be discussed here). Being the lowest energy transition it corresponds to the hh1-e1 transition (compare Fig. 3.2). In contrast to the PL spectrum, a second absorption edge shifted by +155 meV is visible. [1] Qualitative comparison to an absorption spectrum of 25 nm wide InSb quantum wells shown in [206] yields that the second edge may be either due to an excited state transition or due to the lh1-e1 transition. My calculation clearly shows that the QW is too thin to confine excited

[1]The sensitivity of transmission measurement to this higher-energy transition demonstrates the advantage as compared to PL. PL shows only the lowest energy transition. Higher energy transitions become visible in PL only if the lower ones are saturated which usually requires very high excitation intensities.

state. Consequently, this peak indicates the lh1-e1 transition even though the calculation predict larger separation of +177 meV. The difference may be due to uncertainties of the effective masses that enter the model. There is almost no difference in transmission for the different polarization directions.

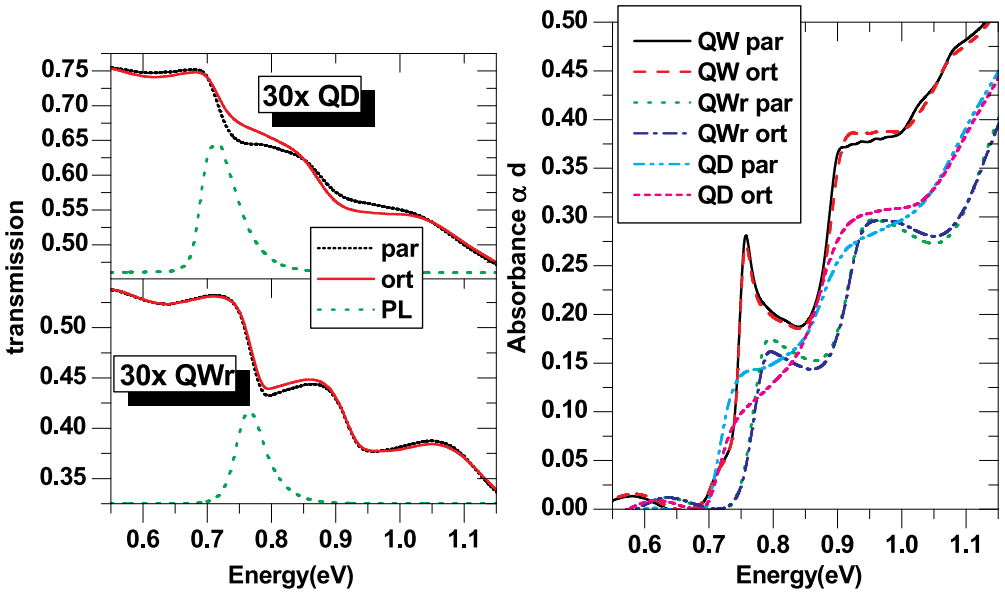

Figure 3.11: **left:** Room temperature transmission spectra of the 30x QD and a 30x QWr sample for polarization direction parallel and orthogonal [$\bar{1}$10]. The respective PL peaks are given as reference. **right:** Absorbance spectra calculated from the transmission spectra.

The transmission spectra of the QWr and QD sample are shown in Fig. 3.11, left. They exhibit the same qualitative features as the QW sample. The absorption edge at low energy corresponds to the PL peak, and the second absorption edge is shifted by 150 to 155 meV. Owing to this similarity, the transitions are assumed to be also hh1-e1 and lh1-e1. In contrast to the QW spectrum, the absorption edges are smeared out (particularly in the QD sample) and the corresponding PL peaks are wider than the peak of the QW sample. The larger peak width is due to inhomogeneous broadening since my measurements probe a large ensemble of nanostructures with fluctuating size, i.e. with different individual transition energies. The narrow PL peaks of individual InAs nanostructures (FWHM well below 1 meV) are shown in Ref. [31]. Consequently, the transmission spectrum can be understood as the superposition of a distribution of sharp transmission spectra of the individual nanostructures. The transmission spectra show a polarization sensitivity,

which is most pronounced with the QD sample. The hh1-e1 absorption feature is stronger for polarization direction parallel to $[\bar{1}10]$, whereas the lh1-e1 transition is stronger for the polarization direction orthogonal to $[\bar{1}10]$. The polarization of the hh1-e1 transition qualitatively agrees with the results from the polarized PL (see Fig. 3.8). A quantitative analysis of the transmission data can be done by extracting the absorption energy dependent coefficient. The conversion of transmission T into the absorption $\exp(-\alpha d)$ is done following the method used in [112]. This methods considers the reflections (reflection coefficient R) at the two sample-air interfaces based on the following equation.

$$T = \frac{(1-R)^2 \exp(-\alpha d)}{1 - R^2 \exp(-2\alpha d)} \tag{3.5}$$

R is experimentally determined from the transmission spectrum at energies below all transitions, at which the sample is supposed to be transparent. Then, R is used with Eq. 3.5 to calculate the absorbance $\alpha(E)d$ spectrum from the transmission spectrum $T(E)$. (This method absorbs parasitic absorptions due to dirt film on the sample into R, which results in some imprecisions in the calculated absorbance. For the shown transmission spectra this may be the case for the QWr sample, which leads to a smaller calculated absorbance. The comparison among the polarization directions, however, is not influenced by this effect.) The calculated absorbance spectra $\alpha(E)d$ are shown in Fig. 3.11, right. In order to calculate the absorption coefficient $\alpha(E)$, an effective value for the total thickness d of the absorbing material has to be assumed. The samples consist of 30 absorbing layers with approximate nominal InAs thickness of (24+/-3) Å. Assuming absorption only in the InAs nanostructures (and not in the barriers) the total thickness would be $d = (7.2 + / - 0.9) \cdot 10^{-6}$ cm. At an energy of 0.8 eV, the absorption coefficient of the QW sample is $2.8{\cdot}10^4$ cm^{-1} (only hh1-e1 transitions), which is slightly above the bulk value of $2.0{\cdot}10^4$ cm^{-1} (hh-e and lh-e transition from Ref. [100]). The absorption resonance of the hh1-e1 at 755 meV is $\alpha = 3.9{\cdot}10^4$ cm^{-1}, which is more than double the bulk value. The absorption coefficient of the QD structure is approximately $\alpha = 1.9(4.2) \cdot 10^4$ cm^{-1} for energies above the hh1-e1(lh1-e1) transition. These values are much higher than those ($\alpha = 0.44 \cdot 10^4$ cm^{-1}) obtained for InAs QDs on InP(311)B [36] with similar areal density ($5 \cdot 10^{10}$ cm^{-2}) of QDs. A possible reason is a flatter shape of my QDs that results in a higher areal coverage. The energy of 801 meV that corresponds to the technologically important wavelength of 1.55 μm is slightly above the hh1-e1 transition of my QD sample. The absorption of the QWr sample is between the values of the QD and the QW sample. (It is, however, underestimated due to the lower transmission at en-

ergies below the sample absorption edges.) The polarization dependence of all samples clearly shows a higher absorption for the [$\bar{1}$10] polarization direction at the hh1-e1 transition. This behavior reverses at the lh1-e1 transition which shows higher absorption for polarization in the [110] direction. In Ref. [22] this reversal of polarization direction from the hh-like to the lh-like hh-lh admixture has been theoretically derived. Hence, the opposite polarization of the absorption edges confirms their assignment to e-hh and e-lh transitions. The maximum degree of linear polarization P (calculated with the absorbance and Eq. 3.2) of the hh1-e1 transitions is P=+18.3/6.8/1.8% for the QD/QWr/QW sample, respectively. The lh1-e1 transition yields P=-4.3/-1.4/-1.6% (the negative sign denotes the reversed polarization direction). These P of the hh1-e1 transitions in QWs/QWrs/QDs reflect the P for the e1-hh1 transition in similar QWs/QWrs/QDs (P=+2/+10/+20%) determined by polarized PL.

The obtained degree of polarization, particularly of the QDs sample, suggest applications as polarization dependent absorber in the 1.55 μm wavelength range. Investigations of nonlinear optical properties, such a saturable absorption, with respect to the polarization may yield applications beyond those as mode-locking stabilizer, described in [81]. A rotation of polarization due to absorption saturation can be expected for my QD samples [174].

3.5 Conclusion

The emission and absorption properties of the InAs/InP nanostructures related to interband transitions have been investigated. Their relatively flat shape, allows to model the transition energies on the basis of a QW. The thickness of most of my nanostructures (<4.2 nm) does not confine excited states in the vertical direction. The minor contribution to the transition energy from lateral confinement and exciton-binding energy has been estimated.

PL experiments, that sample the hh1-e1 transition demonstrate that the wavelength range that can be covered with these structures reaches up to 2 μm, including the technologically important 1.3 and 1.55 μm, at room temperature. The larger height of the QDs grown on B-type substrates in comparison to the QWrs grown on N- and A-type substrates is shown through the PL peak energy. Quite good agreement of the calculated hh1-e1 transition energy with PL results and nanostructure thickness determined by cross-sectional TEM is obtained for thicknesses between 2 and 3 nm. The uncertainty is in the range of 1 ML=0.3 nm.

Polarization dependent PL and transmission measurements show a pref-

erential polarization in the [$\bar{1}$10] direction for all QWrs and QDs. The degree of polarization for my QWrs is around 10%. The polarization of the QDs is larger with degree of linear polarization of up to 20% strongly suggesting an anisotropic shape of the QDs.

Polarization dependent transmission measurements of QDs and QWrs show a transition at the energy of the PL peak, which agrees in polarization with the PL result. An additional transition of opposite polarization and at higher energy is found with transmission measurements. A reference sample with InAs QWs also shows both these transitions but with almost vanishing polarization. Comparison to the theoretical calculations and the polarization direction both yield that the transition at higher energy is a lh1-e1 transition.

The efficient carrier capture and radiative recombination in the nanostructures seen in PL, the nanostructures' high absorption coefficient determined by transmission spectroscopy, and their polarization makes InAs/InP nanostructures suitable candidates for optical applications such as lasers, photodetectors, and saturable absorbers.

Chapter 4

Methods for measuring anisotropic Transport

One main goal of this work is to investigate the electronic transport within the layer of the InAs nanostructures. The anisotropic morphology - in particular of the quantum wires - suggests also anisotropic transport properties, which are indeed observed in the transport measurements of this work. Irrespective of the underlying microscopic mechanisms of coupling between the nanostructures, the carrier system may be macroscopically characterized as a two dimensional system with anisotropic conductivity, i.e. different conductivities parallel and perpendicular to the quantum wires.

In this chapter methods to measure anisotropic transport properties are investigated. The fundamental method to determine the transport properties is a combination of determining the resistivity ρ by measuring a voltage drop in the sample caused by a bias current, and determining the carrier density n by virtue of the Hall effect [71]. The combination of resistivity and carrier density allows to determine the mobility μ. One way to combine both these measurements is to measure a sample in the shape of a Hall bar aligned to the direction in which transport properties should be determined.

Based on the anisotropic magneto-conductivity tensor the interpretation of Hall bar measurements along the principle axes of conductivity in anisotropic systems is clarified in section 4.1. In reality, however, these principal axes of conductivity anisotropy in a sample are not necessarily known. To solve this question, a method to determine the principal axes of conductivity using Hall-bar measurements is derived and experimentally validated in section 4.2. A widely used, experimentally easier alternative to Hall-bar measurements is the van der Pauw method. Section 4.3 gives a detailed theoretical and experimental investigation of how anisotropic transport properties can be determined with the van der Pauw measurement of a rectangularly

shaped sample. Numerical simulations based on the finite element method are developed and used for these investigations, for the calculation of electric fields in micro-Hall devices in section 4.4, and for investigations in chapter 7. The advantages and disadvantages of the van der Pauw method for anisotropic samples are explored. A versatile van der Pauw structure that reduces these disadvantages is proposed, calibrated based on simulations, and experimentally tested in section 4.3.9. The transport investigations of my InAs samples will be based on the results of this chapter.

4.1 Hall-bar measurements

4.1.1 Anisotropic magneto-conductivity tensor

A two-dimensional carrier system with anisotropic conductivity can be characterized by the carrier density n and an anisotropic drift mobility, i.e. drift mobilities μ_x, μ_y along the two principal transport directions x and y. Magneto-transport experiments such as Hall-bar or van der Pauw measurements are typically used to determine these quantities [21]. In these magneto-transport experiments a magnetic field B is applied perpendicular to the two-dimensional carrier system. An applied in-plane electric field F with the components F_x and F_y causes an in-plane current density j with components j_x and j_y according to

$$\begin{pmatrix} j_x \\ j_y \end{pmatrix} = \begin{bmatrix} \sigma_{xx} & \sigma_{xy} \\ \sigma_{yx} & \sigma_{yy} \end{bmatrix} \begin{pmatrix} F_x \\ F_y \end{pmatrix} . \tag{4.1}$$

The magneto-conductivity tensor for a carrier type with isotropic effective mass m^* can be expressed as [15]

$$\widehat{\sigma} = \begin{bmatrix} \sigma_{xx} & \sigma_{xy} \\ \sigma_{yx} & \sigma_{yy} \end{bmatrix} = \frac{-ne^2}{m^*} \begin{bmatrix} \left\langle \frac{-\tau_x}{1+\omega_c^2\tau_x\tau_y} \right\rangle & \left\langle \frac{\omega_c\tau_x\tau_y}{1+\omega_c^2\tau_x\tau_y} \right\rangle \\ \left\langle \frac{-\omega_c\tau_x\tau_y}{1+\omega_c^2\tau_x\tau_y} \right\rangle & \left\langle \frac{-\tau_y}{1+\omega_c^2\tau_x\tau_y} \right\rangle \end{bmatrix} \tag{4.2}$$

with momentum relaxation times $\tau_x(E)$ and $\tau_y(E)$ for the principal directions, and cyclotron frequency

$$\omega_c = \frac{eB}{m^*} . \tag{4.3}$$

The derivation of this tensor based on the Boltzmann transport equation is similar to [106] but considering the 2-dimensional case, and using anisotropic relaxation times. The description of anisotropic relaxation times by their

principal components is adopted from [178] in which the conductivity tensor (without magnetic field) is calculated for different anisotropic scattering potentials. My results are in principle compatible with a calculated three-dimensional conductivity tensor for many-valley semiconductors with anisotropic effective mass and anisotropic relaxation times [77].

For a general energy dependent function $g(E)$ the brackets define the following averaging procedure in two dimensions

$$\langle g(E) \rangle = \frac{\int dE E \frac{\partial f_0}{\partial E} g(E)}{\int dE E \frac{\partial f_0}{\partial E}}, \tag{4.4}$$

with Fermi function f_0, and Fermi energy E_F

$$f_0(E) = \frac{1}{1 + \exp(\frac{E - E_F}{kT})}. \tag{4.5}$$

Without magnetic field the off-diagonal components of the tensor vanish. The conductivities for the principal directions remain

$$\begin{aligned} \sigma_{xx}(B = 0) &= -en\mu_x \\ \sigma_{yy}(B = 0) &= -en\mu_y \end{aligned} \tag{4.6}$$

with drift mobilities

$$\begin{aligned} \mu_x &= \frac{e < \tau_x >}{m^*} \\ \mu_y &= \frac{e < \tau_y >}{m^*} \ . \end{aligned} \tag{4.7}$$

The ratio A of the principle conductivities

$$A = \frac{\sigma_{xx}(B = 0)}{\sigma_{yy}(B = 0)} \tag{4.8}$$

is the conductivity anisotropy. For $\tau_x = \tau_y = \tau$ the isotropic conductivity tensor is obtained.

With respect to reversal of the magnetic field, the diagonal components are symmetric and the off-diagonal components are anti-symmetric.

$$\begin{aligned} \sigma_{xx,yy}(-B) &= \sigma_{xx,yy}(+B) \\ \sigma_{xy,yx}(-B) &= -\sigma_{xy,yx}(+B) \end{aligned} \tag{4.9}$$

4.1.2 Hall-bar measurements of anisotropic transport

Magnetoresistance measurements, such as Hall-bar measurements, measure the components of the resistivity tensor

$$\widehat{\rho} = \begin{bmatrix} \rho_{xx} & \rho_{xy} \\ \rho_{yy} & \rho_{yx} \end{bmatrix} \tag{4.10}$$

of the material. For Hall-bar geometry longitudinal voltage and Hall-voltage are measured without drawing a current. For a Hall bar oriented in the x-direction there is an imposed current j_x. Measuring the Hall-voltage causes no current flow, $j_y = 0$. Taking into account these boundary conditions the longitudinal and transversal resistivities ρ_{xx} and ρ_{xy} are calculated.

$$\begin{aligned} j_y &= \sigma_{yx}E_x + \sigma_{yy}E_y = 0 \\ j_x &= \sigma_{xx}E_x + \sigma_{xy}E_y \end{aligned} \tag{4.11}$$

As longitudinal and transversal resistivities one gets

$$\begin{aligned} \rho_{xx} &= \frac{E_x}{j_x} = \frac{\sigma_{yy}}{\sigma_{xx}\sigma_{yy} - \sigma_{xy}\sigma_{yx}} \\ \rho_{xy} &= \frac{E_y}{j_x} = \frac{-\sigma_{yx}}{\sigma_{xx}\sigma_{yy} - \sigma_{xy}\sigma_{yx}} \ . \end{aligned} \tag{4.12}$$

Similarly, measuring a Hall bar oriented along y-direction yields the remaining components

$$\begin{aligned} \rho_{yy} &= \frac{E_y}{j_y} = \frac{\sigma_{xx}}{\sigma_{yy}\sigma_{xx} - \sigma_{yx}\sigma_{xy}} \\ \rho_{yx} &= \frac{E_x}{j_y} = \frac{-\sigma_{xy}}{\sigma_{yy}\sigma_{xx} - \sigma_{yx}\sigma_{xy}} \ . \end{aligned} \tag{4.13}$$

The two sets of equations above are the general relation of anisotropic resistivity tensor and anisotropic conductivity tensor. With respect to reversal of the magnetic field the diagonal components of the resistivity tensor are symmetric and the off-diagonal components are anti-symmetric.

$$\begin{aligned} \rho_{xx,yy}(B) &= \rho_{xx,yy}(-B) \\ \rho_{xy,yx}(B) &= -\rho_{xy,yx}(-B) \end{aligned} \tag{4.14}$$

The resistivities $\rho_{xx,yy}$ measured without magnetic field

$$\rho_{xx,yy}(B=0) = \frac{1}{\sigma_{xx,yy}(B=0)} \tag{4.15}$$

reflect indeed the resistivities (inverse conductivities) of the principal directions x and y.

The Hall coefficient

$$R_H = \frac{\rho_{xy}}{B} \tag{4.16}$$

is used to determine the carrier density (Hall density, n_H).

$$n_H = -\frac{1}{eR_H} = -\frac{B}{e\rho_{xy}} \tag{4.17}$$

In the approximation of low magnetic fields ($\omega_c\tau \ll 1$) putting 4.2 into 4.12 and 4.12 into 4.17 we obtain for n_H

$$n_H = n\frac{<\tau_x><\tau_y>}{<\tau_x\tau_y>} = \frac{n}{r_H} \tag{4.18}$$

with Hall scattering factor

$$r_H = \frac{<\tau_x\tau_y>}{<\tau_x><\tau_y>} \ . \tag{4.19}$$

The Hall mobility μ_H is then calculated according to

$$\mu_H = \frac{1}{e\rho_{xx}(B=0)n_H} = \frac{\sigma_{xx}(B=0)}{en_H} = \mu_x r_H \ . \tag{4.20}$$

Comparing the obtained resistivities of Hall bars oriented along the $x-$ and y-direction one finds:

1. The Hall scattering factor r_H is identical for both directions leading to the same Hall density n_H ($\rho_{xy} = -\rho_{yx}$) measured in both directions.

2. The resistivity measured without magnetic field reflects indeed the resistivity (inverse conductivity) of the principal direction parallel to respective Hall bar.

3. The ratio of the measured resistivities (and therefore Hall mobilities) is identical to the ratio of the drift mobilities.

4.1.3 Hall scattering factor for anisotropic transport

The Hall scattering factor r_H depends on the scattering mechanisms for both principal directions according to 4.19. For the isotropic case the Hall scattering factor is ≥ 1, which does not necessarily hold true for anisotropic scattering times. Also, it has been shown that transport anisotropy due to anisotropic effective mass (anisotropic Fermi surface) can result in Hall scattering factors below unity [5, 40] [1]. Generally, the energy dependence of $\tau(E)$ can be approximated using

$$\tau \propto (E - E_C)^s \tag{4.21}$$

with 2D subband edge energy E_C, and exponent s depending on the particular scattering mechanism ranging from $+3/2$ for ionized impurity scattering to $-1/2$ for acoustic deformation scattering [106, 162, 139].

In the non-degenerate case the Hall scattering factor can be analytically calculated using f_0 for Boltzmann statistics

$$f_0(E) = \exp\left(\frac{E_F - E}{kT}\right) \tag{4.22}$$

as follows. Let s (p) be the exponent of the energy dependence of τ_x (τ_y). Then r_H for anisotropic conduction of the two dimensional carrier system is

$$r_h = \frac{\Gamma(2+s+p)\Gamma(2)}{\Gamma(2+s)\Gamma(2+p)} \; . \tag{4.23}$$

The resulting values of r_H for different s, p are given in table 4.1.

Please note, that

1. in some (theoretical) anisotropic cases ($s = -1/2, p = +1/2 or + 3/2$) indeed the Hall scattering factor is below unity,

2. if the exponent for one principal direction is zero the Hall scattering factor becomes unity, and

3. the values are slightly higher than the respective values calculated in the 3-dimensional case. E.g. for the isotropic case with ionized impurity scattering ($s = p = +3/2$) r_H is 2.17 in the 2-dimensional case in contrast to 1.93 in the 3-dimensional case. Replacing all occurring 2 in equation 4.23 by 5/2 turns it into the 3-dimensional case.

[1] Allgaier [5] describes these factors in 1968 as follows: "The factor r has become a rather nebulous quantity in today's world of monstrous Fermi surfaces, and the ordinary weak-field Hall coefficient does not enjoy a very high reputation as a useful solid-state parameter.".

Table 4.1: Hall scattering factors calculated for the non-degenerate case of anisotropic scattering in a 2-dimensional carrier system. Different scattering mechanisms for the principal transport directions x, y are characterized by their exponents s, p (see Eq. 4.21).

	$p =$	-1/2	0	+1/2	+3/2
$s =$					
-1/2		1.273	1.000	0.849	0.679
0		1.000	1.000	1.000	1.000
+1/2		0.849	1.000	1.132	1.358
+3/2		0.679	1.000	1.358	2.173

4. The high value of r_H for ionized impurity scattering ($s = p = +3/2$) is a rather theoretical upper limit for very low carrier concentrations. Calculation with realistic 3-dimensional carrier concentrations [58, 135], as well as experimental determinations of r_H [14] in high purity InP bulk samples (low carrier concentration) yield a maximum of 1.45.

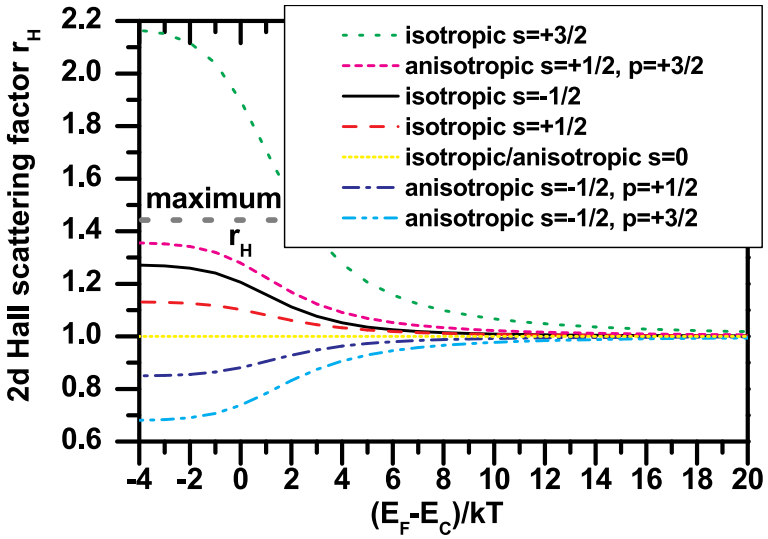

Figure 4.1: Numerically calculated Hall scattering factor using Fermi statistics. Anisotropic scattering in a two dimensional carrier system was considered with different exponents for the principal transport directions. The grey dotted horizontal line denotes the realistic maximum value as previously discussed. (The legend follows the order of the curves from top to bottom.)

In case of a degenerate electron gas (Fermi energy inside the conduction

band) r_H is closer to unity. In the extreme case zero temperatures, the averaging function of 4.4

$$\frac{\partial f_0}{\partial E} = -\frac{1}{kT} f_0(E)(1 - f_0(E)) = \delta(E - E_F) \tag{4.24}$$

becomes a delta function $\delta(E - E_F)$ leading to a Hall scattering factor of unity in the isotropic and anisotropic case. That is, measured Hall mobility and density are identical to drift mobility and carrier density.

To bridge these two extreme cases, the values of r_H were numerically calculated (Fig. 4.1) using Fermi statistics. The characteristic parameter $(E_F - E_C)/kT$ distinguishing the two extreme cases is used in the calculation. Comparing the plotted values with the tabulated ones it is justified to consider $E_F - E_C < -2kT$ as non-degenerate case. On the other hand $E_F - E_C$ should be larger than 10 kT to safely assume r_H to be unity.

4.2 Determining the principal axes of conductivity with Hall-bar measurements

In general, the direction of the principal axes x, y of conductivity are not necessarily known. This section describes a method to find the principle directions and corresponding conductivities using Hall bars.

4.2.1 Theory

Let the Hall bars be oriented along the mutually perpendicular $\widetilde{x}$ and $\widetilde{y}$ directions rotated by an angle α with respect to the principal axes. The conductivity tensor in this Hall-bar frame is consequently

$$\widetilde{\widehat{\sigma}} = \widehat{R}\widehat{\sigma}\widehat{R}^{-1} \tag{4.25}$$

with rotation matrix

$$\widehat{R}(\alpha) = \begin{bmatrix} cos\alpha & sin\alpha \\ -sin\alpha & cos\alpha \end{bmatrix} \tag{4.26}$$

Now, the experimentally obtained resistivities in the Hall-bar frame can be calculated using $\widetilde{\widehat{\sigma}}$ as conductivity tensor in 4.12 and 4.13.

$$\begin{aligned} \rho_{\widetilde{x}\widetilde{x}} &= \rho_{xx}cos^2\alpha + \rho_{yy}sin^2\alpha \\ \rho_{\widetilde{y}\widetilde{y}} &= \rho_{xx}sin^2\alpha + \rho_{yy}cos^2\alpha \\ \rho_{\widetilde{x}\widetilde{y}} &= (\rho_{yy} - \rho_{xx})sin\alpha cos\alpha + \rho_{xy} \\ \rho_{\widetilde{y}\widetilde{x}} &= (\rho_{yy} - \rho_{xx})sin\alpha cos\alpha + \rho_{yx} \end{aligned} \tag{4.27}$$

Without magnetic field, ρ_{xy} vanishes and the experimentally obtained values of $\rho_{\widetilde{xx}}$, $\rho_{\widetilde{yy}}$, and $\rho_{\widetilde{xy}}$ can be used to calculate α, ρ_{xx}, and ρ_{yy} according to

$$tan2\alpha = \frac{2\rho_{\widetilde{xy}}}{\rho_{\widetilde{yy}} - \rho_{\widetilde{xx}}} \tag{4.28}$$

$$\rho_{xx} = \frac{1}{2}\left[\rho_{\widetilde{xx}} + \rho_{\widetilde{yy}} + \frac{\rho_{\widetilde{xx}} - \rho_{\widetilde{yy}}}{cos2\alpha}\right] \tag{4.29}$$

$$\rho_{yy} = \frac{1}{2}\left[\rho_{\widetilde{xx}} + \rho_{\widetilde{yy}} - \frac{\rho_{\widetilde{xx}} - \rho_{\widetilde{yy}}}{cos2\alpha}\right] . \tag{4.30}$$

In addition, ρ_{xy} can be determined by measuring with positive and negative magnetic field. Using 4.14 and 4.27 it follows

$$\rho_{xy}(+B) = \frac{\rho_{\widetilde{xy}}(+B) - \rho_{\widetilde{xy}}(-B)}{2} . \tag{4.31}$$

A more elaborate theoretical investigation of the Hall voltage in an arbitrarily oriented Hall bar for anisotropic materials including different aspect ratios is given in [159]. It comes to the same conclusion (Eq. 4.29) about determining ρ_{xy}.

Hence, the measurement of two mutually perpendicular Hall bars is theoretically sufficient to determine the direction α of the principal axes of conductivity, the principal conductivities $1/\rho_{xx,yy}(B = 0)$, and the Hall coefficient $\rho_{xy}(B)/B$.

4.2.2 Experimental verification

The method described above, however, requires well defined Hall bars. In particular the contacts measuring the Hall voltage have to be aligned to exclude a contribution from $\rho_{\widetilde{xx}}$ to $\rho_{\widetilde{xy}}$ due to geometrical displacement of opposite Hall contacts.

The experimental test was done with mutually perpendicular Hall bars processed (detail in section 5.2) on an anisotropic sample. This sample shows a conductivity anisotropy A ranging from 2.4 (at 320 K) to 6.6 (at 10 K). For further details see section 4.3.6. One set of Hall bars was misaligned by 4° with respect to the $< 110 >$ directions while the other set of Hall bars is aligned within a precision of 0.5°. Fig. 4.2 shows a micrograph of the misaligned Hall bars and the angle of the principal axes α with respect to the $< 110 >$ directions [2] calculated with Eq. 4.28 from the transport results.

[2] The $< 110 >$ directions are equivalent to the cleaved edges of the sample pieces.

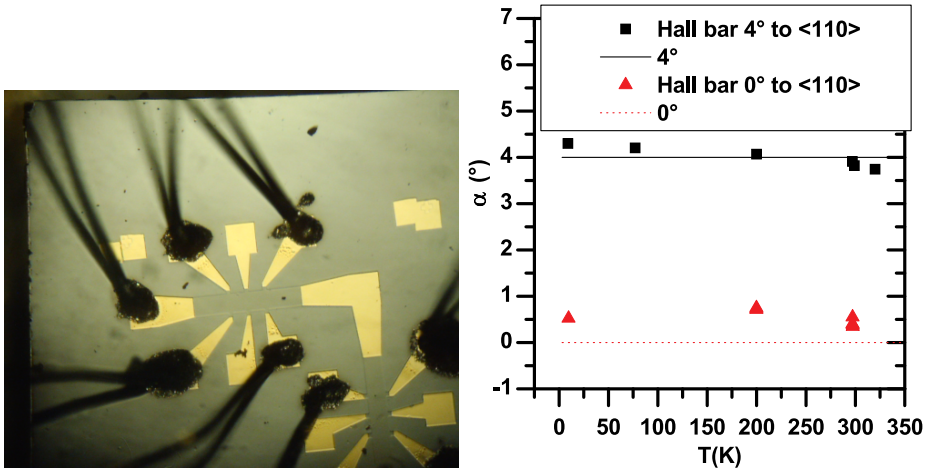

Figure 4.2: **left:** Micrograph of misaligned set of Hall bars.
right: Angle of principal axes of conductivity with respect to the Hall-bar orientation determined by transport measurements.

Comparing the angles of both sets of Hall bars the geometrically measured difference of 4° is reproduced by the transport measurements. The principal axes of conductivity are parallel to the $< 110 >$ directions in this sample for the entire range of temperatures. Finally, the precision of this method seems to be better than 1° for the anisotropies considered here.

4.3 Anisotropic transport properties revealed by van der Pauw measurements

Transport properties of isotropic semiconductors are conveniently measured with the van der Pauw (vdP) method [183] published in 1958. In contrast to Hall-bar measurements, the vdP technique requires only four sufficiently small contacts placed at the circumference of an arbitrarily shaped (but simply connected) sample. The influence of contact size on measured resistivity is taken into account by correction factors, originally calculated by van der Pauw for a circular disc [183]. Correction factors for several different geometries are summarized in [106, 21]. Transport properties of semiconductor nanostructures can be anisotropic due to anisotropic effective masses, structural corrugation in a two-dimensional electron gas (2DEG) [53], in coupled quantum-wire systems [191],[17], or in two-dimensional electrons and -holes in high Landau levels [105, 156]. The analysis of vdP measurements for anisotropic transport, however, is less than straightforward because the va-

lidity of the calculated carrier density is not obvious and the magnitude of anisotropy is overestimated. For example, transport measurements in high Landau levels of a 2DEG show an anisotropy of about 100 in vdP geometry, but only 6 in Hall-bar geometry [105]. In contrast to the vdP geometry, the four-terminal resistances of a Hall-bar geometry directly reflect the actual resistivity in the direction of the bar. The determination of anisotropic resistivity using the vdP method on a rectangular sample had been published by Wasscher [194] already in 1969 using complex algebra, however, it seems to have been lost over the years. Thus, again in 1999 a theoretical explanation of the discrepancy between anisotropy in vdP geometry and Hall-bar geometry has been given in [161]. In this publication, using simpler mathematics, the relation between anisotropies for both geometries are analytically derived, and formulas for the four-terminal resistances are given. These were also experimentally confirmed with structured lateral superlattices [47]. A general solution to the potential problem in an arbitrarily shaped two-dimensional anisotropic medium is given in [158]. With finite-element methods, the effect of a conductivity anisotropy on Hall measurements was numerically calculated for the van der Pauw method and square shaped geometry [152]. (The significant dependence of Hall voltage on anisotropy described in [152] is not, however, supported by either my numerical calculations or my experimental results.)

The aim of this section is to work out how anisotropic transport properties can be obtained from the results of van der Pauw measurements of a square shaped sample. In section 4.3.1, the conductivity tensor describing the anisotropic microscopic (magneto)transport properties of the material is defined, the van der Pauw geometry is presented, and the usual procedure of obtaining isotropic transport parameters from vdP measurements is shown. Within this framework, the four-terminal resistances for given microscopic anisotropies are *analytically* calculated for rectangular samples without magnetic field in section 4.3.2. Numerical methods (in section 4.3.3) allow the calculations to also be extended to include a magnetic field, and for given arbitrary shapes. Thus, in section 4.3.4 using finite-element methods, the four-terminal resistances as well as Hall voltages are *numerically* calculated by simulating the experiment. These numerical and analytical results allow carrier concentration and mobility in samples with anisotropic conductivity to be obtained from vdP data (section 4.3.5). This method is applied to coupled quantum-wire structures with anisotropic transport properties in section 4.3.6. The experimental results of both these measurement geometries are compared and discussed in section 4.3.7 to assess the use of van der Pauw measurements for characterizing anisotropic semiconductors.

4.3.1 Definitions

A two-dimensional anisotropic semiconductor without magnetic field is characterized by the conductivity tensor

$$\widehat{\sigma} = \begin{bmatrix} \sigma_{xx} & 0 \\ 0 & \sigma_{yy} \end{bmatrix} . \tag{4.32}$$

The ratio of the principle resistivities (Eq. 4.15)

$$A = \frac{\rho_{yy}}{\rho_{xx}} = \frac{\sigma_{xx}}{\sigma_{yy}} \tag{4.33}$$

is the conductivity anisotropy A (4.8).

The *measured* quantities are four-terminal resistances such as

$$R_{AD,BC} \equiv \frac{V_{BC}}{I_{AD}} , \tag{4.34}$$

with the voltage V_{BC}[V] measured across contacts B and C, and the current I_{AD}[A] flowing through contacts A and D. These resistances depend not only on the resistivity but also on the actual geometry (including contact placement) of the structure. Fig. 4.3, right, shows the vdP geometry used in the present study as well as several others [156, 152].

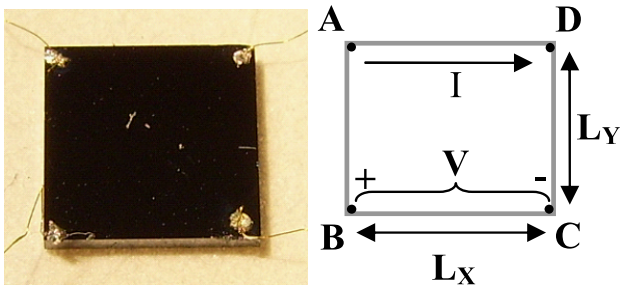

Figure 4.3: **left:** Simple square shaped vdP sample with corner contacts. **right:** Schematic of simple rectangular geometry of size $L_x \times L_y$ with contacts in the corners.

The resistances measured in both transport directions are

$$R_{xx} \equiv R_{AD,BC}, \text{ and } R_{yy} \equiv R_{AB,DC} . \tag{4.35}$$

Their ratio is the van der Pauw anisotropy

$$A_{\text{vdP}} = \frac{R_{yy}}{R_{xx}}. \tag{4.36}$$

In isotropic materials, the resistivity ρ fulfills the van der Pauw theorem [183]

$$\exp\Big(-\pi\frac{R_{xx}}{\rho}\Big)+\exp\Big(-\pi\frac{R_{yy}}{\rho}\Big)=1, \tag{4.37}$$

which is used to determine the resistivity from experimental data.

In order to determine the carrier density, a magnetic field B[T] perpendicular to the x, y-plane is applied. Ignoring the averaging of the individual tensor components over energy, the conductivity tensor in a magnetic field (Eq. 4.2) can be simplified as

$$\widehat{\sigma}=\frac{-ne}{1+\mu_x\mu_y B^2}\begin{bmatrix}\mu_x & -\mu_x\mu_y B\\ \mu_x\mu_y B & \mu_y\end{bmatrix}. \tag{4.38}$$

The four-terminal resistance $R_{AC,BD}$ measured once with and without magnetic field B result in the Hall coefficient

$$R_H=\frac{R_{AC,BD}(B)-R_{AC,BD}(B=0)}{B}. \tag{4.39}$$

By symmetry, use of the other diagonal $R_{BD,CA}$ leads to the same Hall coefficient. The carrier density relates to the Hall coefficient (see Eqs. 4.17, 4.18) by

$$N=\frac{r_H}{eR_H} \tag{4.40}$$

with the Hall scattering factor r_H (Eq. 4.19) which depends on the actual scattering processes of both principal transport directions. (In the case of the conductivity tensor defined in Eq. 4.38, this factor is unity).

4.3.2 Analytical results

In [158] it is analytically shown that in anisotropic cases the resistivity ρ obtained from the van der Pauw theorem (4.37) equals the average resistivity

$$\rho_{\text{ave}}\equiv\sqrt{\rho_{xx}\rho_{yy}}\ . \tag{4.41}$$

What is missing still, is an analytical way to calculate A from A_{vdP}. The analytical result for the 4-terminal resistance R_{xx} is a function $f(\rho_{xx},\rho_{yy},L_x,L_y)$ given in [161] but for a different geometry. This function is used to calculate

[3] R_{xx} for the geometry considered here with the result that

$$\begin{aligned} R_{xx} &= 2f(\rho_{xx}, \rho_{yy}, L_x, 2L_y) \\ &= \frac{8}{\pi}\sqrt{\rho_{xx}\rho_{yy}} \sum_{n=\mathrm{odd}^+} \left[n \sinh\left(\sqrt{\frac{\rho_{yy}}{\rho_{xx}}} \frac{L_y}{L_x} \pi n \right) \right]^{-1}. \end{aligned} \tag{4.42}$$

R_{yy} is given by exchanging all x and y in the above equation. For convenience an effective anisotropy

$$A_{\mathrm{eff}} = \frac{\rho_{yy}}{\rho_{xx}} \left(\frac{L_y}{L_x} \right)^2 = A \left(\frac{L_y}{L_x} \right)^2 \tag{4.43}$$

is introduced [4]. A_{eff} takes into account the conductivity anisotropy A and the geometrical aspect ratio of the vdP structure, and is identical to A for square geometry. It corresponds to the concept of van der Pauw [184] that an anisotropic conductor is equivalent to an isotropic conductor with average resistivity ρ_{ave}, and with dimensions along the principal directions scaled by the square root of ratio of principal resistivity to average resistivity.

Using (4.42) and (4.43), the anisotropy of the four-terminal resistance for rectangular samples is

$$A_{\mathrm{vdP}} \equiv \frac{R_{yy}}{R_{xx}} = \frac{\sum_{n=\mathrm{odd}^+} \left[n \sinh\left(\sqrt{A_{\mathrm{eff}}^{-1}} \pi n \right) \right]^{-1}}{\sum_{n=\mathrm{odd}^+} \left[n \sinh\left(\sqrt{A_{\mathrm{eff}}} \pi n \right) \right]^{-1}}. \tag{4.44}$$

The four-terminal resistances and their anisotropy in my vdP geometry are shown in Fig. 4.4 for a range of effective anisotropies. These results agree with the curve given by Wasscher [194], and will be discussed later in section 4.3.5.

4.3.3 Numerics with FEM method

Numerical methods are useful for calculation for which no analytical expressions are available. Applied to the present problem, voltages and resistances

[3] The geometry used in [161, 105, 47] is also rectangular but with the current contacts placed in the center of opposite edges. The voltage is measured in the corners. Splitting this rectangle of dimension $L_x \times L_y$ along the connection of the current contacts, we obtain two rectangles of our geometry (all contacts in the corners) with dimensions $L_x \times \frac{1}{2}L_y$, each with the same potential distribution, half the total current and therefore twice the resistance of the former structure.

[4] Please note, that Eqs. 4.42, and 4.43 are now correct - in contrast to the publication [18] in which indices were mixed up.

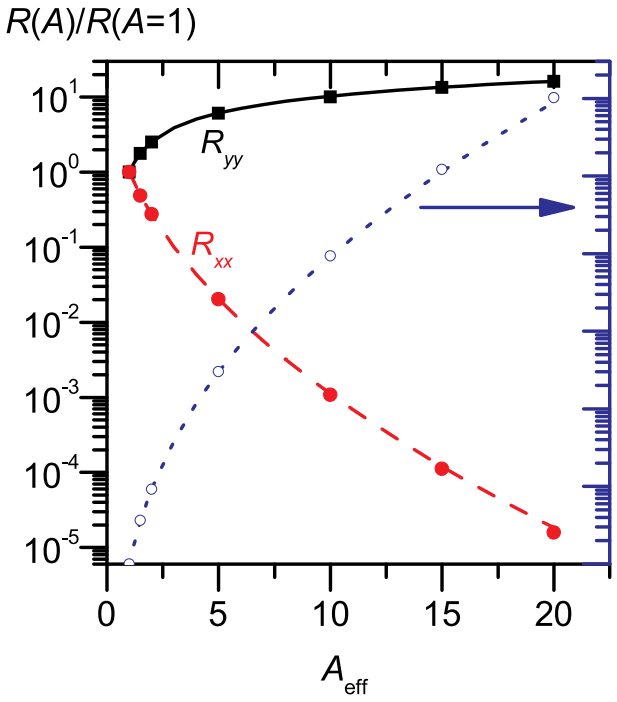

Figure 4.4: Four-terminal resistances R and their anisotropy A_{vdP} vs. effective anisotropy A_{eff}, calculated analytically (lines) and numerically (symbols).

are calculated numerically for arbitrary geometries, and arbitrary parameters (material properties, non-zero B-field, external voltages). These calculations are used to find the electric field distribution in a Greek cross Hall-plate (arbitrary geometry) [94], the measured carrier density (non-zero magnetic field) with anisotropy (section 4.3.4), the effect of contact size and placement on measured carrier density (arbitrary geometry and non-zero magnetic field, in section 4.3.8), and the relation between A and A_{vdP} for different geometries (arbitrary geometry, in this section, and section 4.3.9).

Specifically, finite-element methods are used to calculate the local electrostatic potential $\Phi(\mathbf{r})$ at the position $\mathbf{r}$ in the 2D plane of the vdP structure. The problem is solved for a square (see Fig. 4.3, right) for the magnetoconductivity tensor $\hat{\sigma}(B)$ defined in (4.38). The form of the current density

$$\mathbf{j} = \hat{\sigma}\mathbf{E} = -\hat{\sigma}\nabla\Phi(\mathbf{r}), \tag{4.45}$$

and the fact that there are no current sources/sinks inside the structure, $\nabla \cdot \mathbf{j} = 0$, results in the elliptic partial differential equation for the potential, $-\nabla \cdot \sigma\nabla\Phi = 0$, to be solved for points inside the structure. Boundary

conditions are Neumann-type, i.e. no current flow normal to the boundary, at all boundaries except for the bias contacts. The bias contacts are used as source and drain for the current, and mathematically are Dirichlet-type boundaries at *given* constant bias potentials. From the resulting potential distribution, the local current density is calculated according to (4.45). Then, integrating the normal current density over any line that divides the sample into two parts, each part containing one bias contact, the total current in the sample is obtained. The four-terminal resistances of the sample are now calculated by dividing the potential difference between the other two contacts (corners) by the current.

4.3.4 Numerical results: 4-terminal resistances and carrier density

For a square ($L_x = L_y$), R_{xx} and R_{yy}, and R_H were calculated numerically. All calculations were done for different conductivity anisotropies A assuming, $\mu_x \geq \mu_y$. For convenience of the numerics, let $Ne = 1\ \mathrm{Cm}^{-2}$, $\sqrt{\mu_x \mu_y} = 1 \frac{\mathrm{m}^2}{\mathrm{Vs}}$ therefore $\mu_x = \sqrt{A} \frac{\mathrm{m}^2}{\mathrm{Vs}}$, and $\mu_y = 1/\sqrt{A} \frac{\mathrm{m}^2}{\mathrm{Vs}}$. As bias voltage 1 V is chosen, the magnetic field was set 0.2 T. The following points should be noted: 1) The chosen bias voltage does not influence the calculated four-terminal resistances because all potentials and the current scale linearly with bias, 2) without magnetic field, the chosen scale of mobility and the carrier density do not limit the generality of my considerations as they do not influence the potential distribution, and 3) for the case with magnetic field, different scales of μB lead to the same Hall coefficient R_H. Therefore, the results also apply to more realistic numbers by scaling the mobility or carrier density appropriately. The numerical calculations were done using approximately 30000 triangles.

The results of the numerical calculation of R_H (according to Eq. 4.39) are given in table 4.2. The corresponding potential distributions for isotropic- and anisotropic ($A = 2$) case with- and without magnetic field are shown in Fig. 4.5.

I conclude that the Hall voltage as difference between the case with- and without magnetic field, is *not* sensitive to the anisotropy. For all anisotropies considered here, the vdP technique correctly determines the carrier density according to Eq. 4.40. (I find the same result for rectangularly shaped structures.) My results contradict those of [152] which (also using finite-element methods) predict considerable variations of R_H even for small anisotropies. The equivalent-potential distribution in [152] with magnetic field for the anisotropic case do not match my calculations. The reason for this disagreement remains unclear since too few details about the calculation are

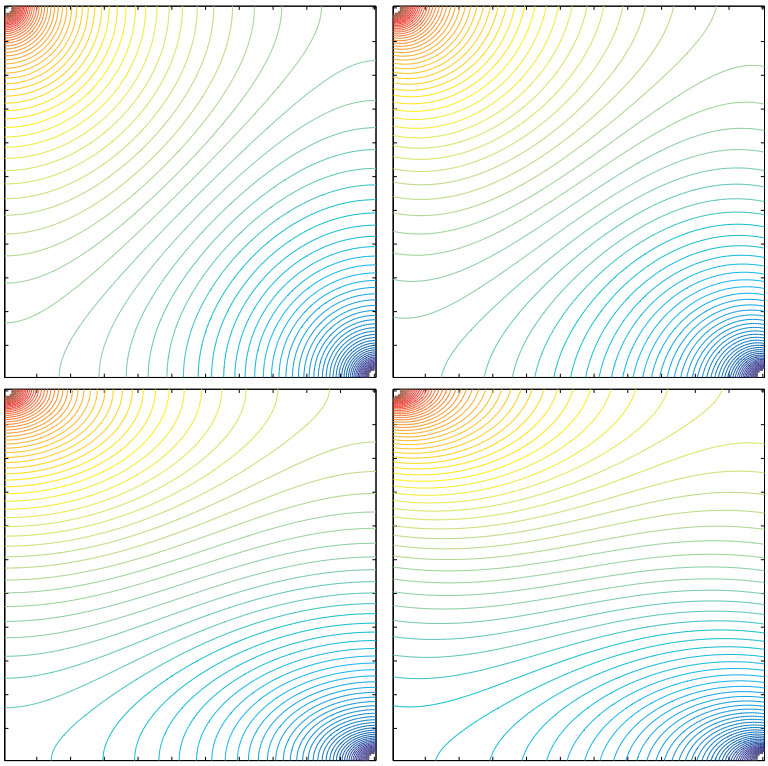

Figure 4.5: Equivalent-potential distributions in vdP geometry calculated for the same bias current and carrier density. Left column B=0, right column B=0.2 T, top row $A = 1$, bottom row $A = 2$. Bias potential is 1 V, 1 div=10 mV.

given in that paper.

4.3.5 Summary of the theoretical results

Table 4.3, and Fig. 4.4 display the analytically and numerically calculated results of the four-terminal resistances and their anisotropy. The numerical results confirm the analytical formula (4.42) for all anisotropies considered here. For extreme anisotropies ($A = 100$), however, the vdP ansiotropy is too high to be practically measured and the accuracy is probably insufficient. We can also verify both methods by putting the resulting four-terminal resistances of the isotropic case ($A = 1$) into the van der Pauw theorem (4.37) and solving it for ρ. As result a resistivity of $\rho = 1$ (that we put in as material property) is retrieved, which means that my measurement gives us the correct value. Moreover the resistivity ρ obtained from (Eq. 4.37) equals the average resistivity (Eq. 4.41) in accordance with theoretical expecta-

Table 4.2: Numerically calculated Hall coefficients for different conductivity anisotropies at a constant carrier density of $Ne = 1\ \mathrm{Cm}^{-2}$.

A	$R_{AC,BD}(B=0)/\Omega$	$R_{AC,BD}(B=0.2\ \mathrm{T})/\Omega$	$R_H/\frac{\mathrm{m}^2}{\mathrm{C}}$
1	1E-5	0.199	0.994
2	0.498	0.697	0.995
10	2.267	2.466	0.994
20	3.569	3.768	0.996
100	9.054	9.250	0.983

Table 4.3: Four-terminal resistances and their anisotropy A_{vdP} on a square without magnetic field for different conductivity anisotropies A calculated numerically (Num.) and analytically (Analyt.).

A	ρ_{xx} /Ω	ρ_{yy} /Ω	R_{xx} Num.	/Ω Analyt.	R_{yy} Num.	/Ω Analyt.	A_{vdP} Num.	$=\frac{R_{yy}}{R_{xx}}$ Analyt.
1	1	1	0.220	0.221	0.220	0.221	1.00	**1.00**
1.5	0.817	1.22	0.108	0.109	0.393	0.395	3.64	**3.63**
2	0.707	1.41	0.0604	0.0599	0.552	0.561	9.13	**9.37**
5	0.447	2.24	0.00447	0.00453	1.349	1.356	302	**299**
10	0.316	3.16	2.37E-4	2.47E-4	2.21	2.28	9334	**9236**
15	0.258	3.87	2.45E-5	2.65E-5	2.97	2.99	1.21E5	**1.13E5**
20	0.224	4.47	3.50E-6	4.03E-6	3.57	3.59	1.02E6	**8.91E5**
100	0.1	10	1.7E-14	1.2E-13	9.05	9.12	5.3E14	**7.9E13**

tions. The numerical calculations showed that, interestingly, the anisotropy of the two-terminal resistances ($R_{AD,AD}$ and $R_{AB,AB}$, i.e. bias voltage divided by total current) strongly underestimates the conductivity anisotropy (1.22, 2.37, and 5.00 for A =2, 10, and 100).

The important calculated results are how the conductivity anisotropy is determined from the vdP resistance anisotropy (4.44), and that the carrier density is correctly measured with the vdP technique.
We determine the principal resistivities from measured four-terminal vdP resistances R_{xx}, R_{yy} as follows:

1. The effective anisotropy A_{eff} is obtained from the the anisotropy of measured four-terminal resistances A_{vdP} with the help of (4.44).

2. With known aspect ratio, the conductivity anisotropy A is calculated

according to (4.43).

3. Using the van der Pauw theorem (4.37), the average resistivity $\rho_{\mathrm{ave}} = \rho$ is obtained from the measured four-terminal resistances.

4. The principal resistivities are now calculated from A and ρ_{ave} using (4.33) and (4.41),

$$\rho_{xx} = \rho_{\mathrm{ave}}\sqrt{A}^{-1} \text{ and } \rho_{yy} = \rho_{\mathrm{ave}}\sqrt{A}. \tag{4.46}$$

Numerically it is shown that the Hall coefficient R_H, experimentally obtained as usual (4.39), *does not* depend on the anisotropy. Therefore, it is used to determine the carrier density the same way as for isotropic materials.

4.3.6 Experimental verification

To test the theoretical results for different anisotropies, samples containing modulation-doped, self-organized, coupled InAs quantum wires in InP were grown by gas-source molecular beam epitaxy. These samples show a temperature-dependent conductivity anisotropy with higher conductivity parallel to the quantum wires. Hall bars (50 μm channel width) for both principal transport directions and square-shaped vdP structures (200 μm edge length) with edges along the principal transport directions, and with contacts in the corners (see Fig.4.3, right) were prepared on the *same* piece of sample by electron-beam lithography and shallow mesa etching. Thus, it is ensured that both Hall-bar and vdP structure have the same microscopic transport properties, and can be readily compared.

Transport measurements were performed with these structures at the same time in a temperature range of 10 K to 320 K thus varying the conductivity anisotropy. A constant DC bias current of 1 μA was chosen as a trade-off between minimizing sample heating and maintaining measurement accuracy. Hall coefficients were measured in a magnetic field of 0.5 T. For the Hall-bar case, the Hall coefficient was measured in the Hall bar along the low-mobility direction. In a separate measurement (not shown here) the Hall coefficients were simultaneously measured in Hall bars along both principal directions. They agree within an uncertainty of $\pm 3\%$.

The resistivities $\rho_{xx,yy}$, and two dimensional carrier density N were calculated from the data of the vdP measurements (as described in the previous section) and the Hall-bar measurements separately. The results are given in Fig. 4.6. The anisotropies A and A_{vdP} from Hall-bar- and vdP measurement range from 2.4 to 6.6 and 12 to 794 respectively.

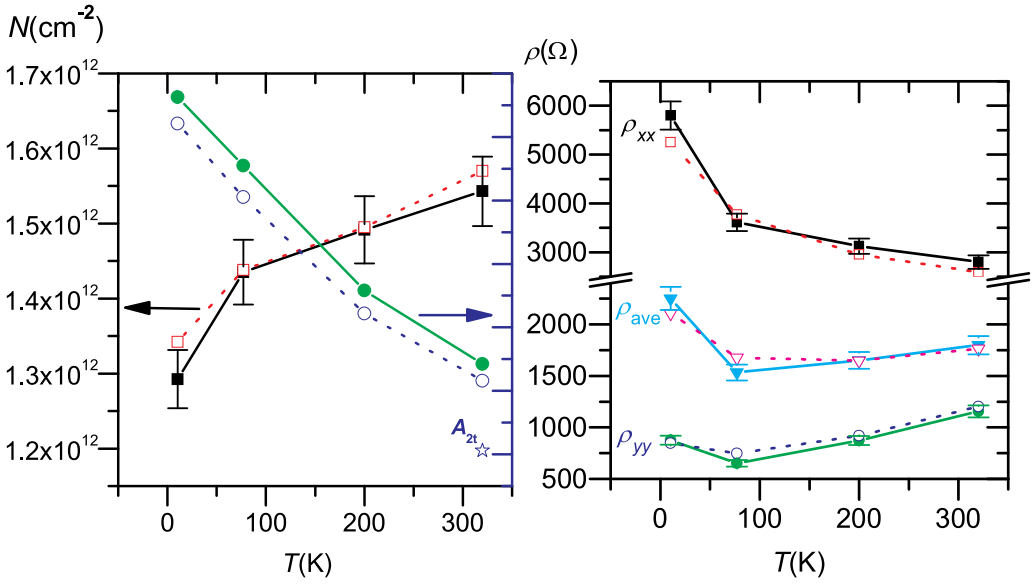

Figure 4.6: **left:** Conductivity anisotropy A and carrier density N obtained from Hall-bar measurements (solid symbols, solid lines), and van der Pauw measurements (open symbols, dotted lines) at different temperatures. The data point A_{2t} is the anisotropy of the two-terminal resistance of the vdP measurement. The error bars of N visualize a relative error of $\pm 3\%$.
right: Resistivities of both principal directions and average resistivity obtained from Hall-bar measurements (solid symbols, solid lines), and van der Pauw measurements (open symbols, dotted lines) at different temperatures. The error bars visualize a relative error of $\pm 5\%$.
The lines are to guide the eye.

4.3.7 Discussion

Despite a change of anisotropy by a factor of almost three, the measured carrier density N (Fig. 4.6, left) varies only slightly. This variation of N is considered to be independent of the anisotropy. Moreover, for the entire anisotropy range, the carrier density obtained by vdP measurement agrees very well with the Hall-bar result, confirming my analytically obtained results. Both measurement methods are equally good to determine the Hall coefficient, also in anisotropic media.

The average resistivity ρ_{ave} from the Hall-bar results agrees well with the result ρ from the vdP measurement (Fig. 4.6, right).

With the vdP method, the quantities N and ρ measured so far can be correctly obtained. This holds true even for arbitrary geometries [158]. In contrast, the anisotropy of four-terminal resistances depends also on the par-

ticular geometry, even more crucially than on the conductivity anisotropy as discussed later. In my experiment the geometry was very precisely defined using lithography. Fig. 4.6, left, shows a quite good agreement of the anisotropies but not as well as the other quantities. This also affects the calculated principal resistivities (see Fig. 4.6, right) because they are calculated with the anisotropy and the average resistivity. A possible reason for the deviation is the four-terminal resistance in the high-mobility direction (see R_{xx} in Fig. 4.4), which drops quickly with increasing anisotropies. This makes precise measurements more difficult, and is regarded as the limiting factor of accuracy in my experiment. For more complex (non-rectangular) geometries, finite element methods, as presented here, can be used to numerically calculate a relation between conductivity anisotropy and anisotropy of four-terminal resistances to substitute (4.44).

Special care has to be taken of the geometry in order to measure the conductivity anisotropy accurately. In (4.43) this is obvious with the $(L_y/L_x)^2$-factor as opposed to ρ_{xx}/ρ_{yy}. The Hall-bar geometry is more forgiving as the relevant lengthes (channel width, distance of the voltage probes) just like the conductivity anisotropy, enter linearly into the anisotropy of the four-terminal resistances. The geometry consists of the contacts, and the shape of the transport structure. The contacts have to be at the edge of the structure as a precondition for vdP measurements, the position must be well defined (e.g. in the corners of the rectangle), and the contacts should be as small as possible. The size of the contacts is an additional uncertainty to the effective contact position because it is not necessarily known which part of the contact microscopically reaches the conducting layer in the alloying process. With lithography, contacts can be made small and placed outside the vdP structure such as voltage probes of a Hall bar.

Using a *rectangular* geometry ($L_x \neq L_y$) can help to increase the measurement accuracy of the vdP anisotropy substantially by tuning the effective anisotropy A_{eff} closer to unity. For example, a conductivity anisotropy range of $1 \leq A_1 < A < A_2$ can be turned into an effective anisotropy range of $\sqrt{A_1/A_2} < A_{\text{eff}} < \sqrt{A_2/A_1}$ by using an aspect ratio of $L_x/L_y = \sqrt[4]{A_1 A_2}$.

There are also general disadvantages of the vdP method compared to the Hall-bar method. The failure of one contact renders the vdP structure unusable. Also, macroscopic defects can disturb the current pathes in the vdP structure, thus drastically changing the effective geometrical anisotropy. The vdP method cannot discriminate this effect against the conductivity anisotropy. On the other hand, Hall bars with multiple voltage probes for each transport direction can help to find out problems with macroscopic defects. Alternative contacts can be used for consistency tests, and in case

of a contact failure.

Section 4.3.9 will utilize the idea of a rectangular geometry, and present a geometry that at the same time reduce the disadvantages of the vdP method discussed so far.

4.3.8 Finite contact size - corner vs. edge

A very simple and practical van der Pauw transport sample consists of a square shaped (unprocessed) piece of the material with more or less circular contacts (e.g. small indium dots) alloyed to it as shown in Fig. 4.3, left. Experimentally, significant differences in Hall voltage were found between contact placement in the corners and in the center of the edges (corner contacts/edge contacts). This discrepancy is elucidated with the help of numerical calculations. These calculations show no significant difference in Hall voltage for very small contacts. The contact size on the transport structures, however, not only influences the measured resistivity but also the carrier density measured with the Hall effect [106]. The effect of a finite contact size on the measured Hall voltage V_H can be expressed by a geometry factor G

$$V_H = GR_H IB, \tag{4.47}$$

that is unity for the ideal case of infinitely small contacts and smaller otherwise [91]. This geometry factor depends on the actual geometry (shapes and placement) of the current injecting contacts, and the ratio of the contact size (the length of the contact boundary) to the size of the transport structure (the length of the edge of the square). Large contacts tend to short circuit the Hall voltage leading to a small G with the extreme case of $G = 0$ corresponding to the GMR effect [106]. A $G < 1$ leads to an overestimation of the carrier density n_H.

Figure 4.7 shows the contact placements considered here and the numerically calculated geometry factors. The geometry factor was calculated by the ratio of the actual (numerically calculated) Hall voltage to the ideal Hall voltage. For the same contact size corner contacts result in geometry factors substantially closer to unity than edge contacts. This is consistent with the experimental observations on doped GaAs samples with the above described geometry. On a sample with relatively large contacts measured carrier densities for edge(corner) contacts were $2.96 \cdot 10^{12}$ $(2.21 \cdot 10^{12})$ cm^{-2}. In contrast a different sample with comparably small contacts resulted in measured carrier densities of $2.75 \cdot 10^{12}$ $(2.57 \cdot 10^{12})$ cm^{-2}.

Consequently, the effect of finite size contacts on Hall voltage can be reduced by using corner contacts instead of edge contacts.

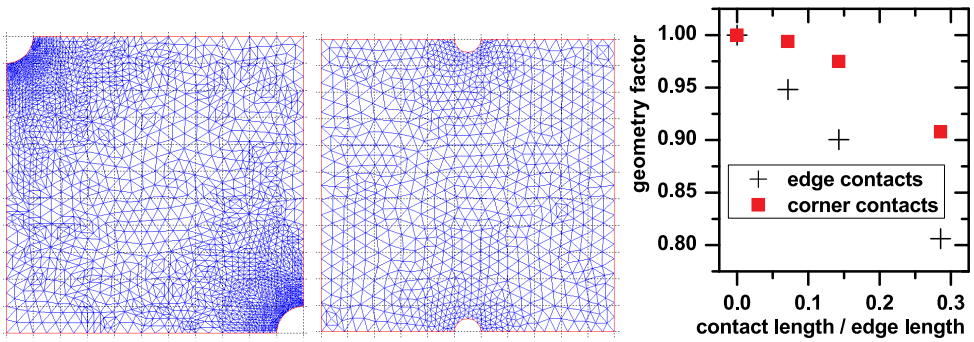

Figure 4.7: **left:** Square geometry model with current injecting contacts (rounded) in the corners. Hall voltage is measured in the other corners. Blue triangles shows the mesh used for FEM calculation.
center: Square geometry model with current injecting contacts (rounded) at the edges. Hall voltage is measured in the center of the other edges.
right: Numerically calculated geometry factors for the two presented geometries and different contact sizes.

4.3.9 A versatile van der Pauw geometry

In this section a modification of the simple square shaped geometry with contacts in the corners is proposed. This modification addresses the disadvantages of the simple structure such as limited measurable anisotropy range, fatality of failing contacts, and no possibility for consistence checking.

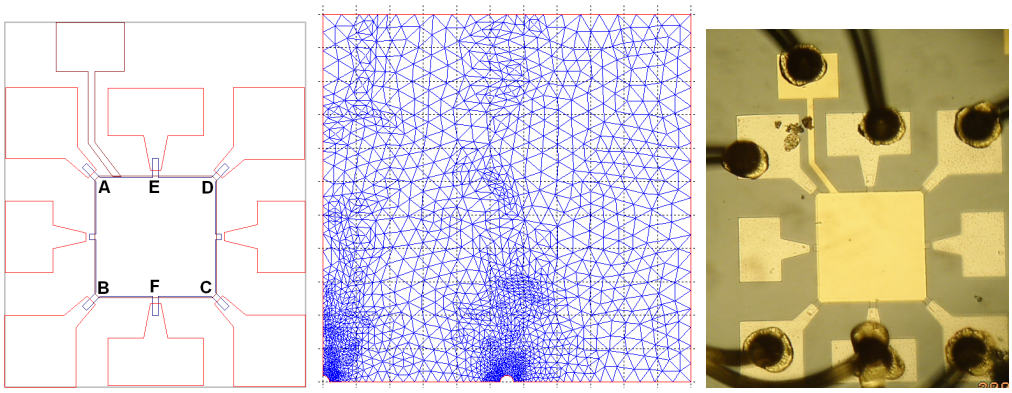

Figure 4.8: Versatile van der Pauw geometry. **left:** design, **center:** FEM model, **right:** optical micrograph.

The idea is to add further contacts to the centers of the square's edges (see Fig. 4.8). Such a structure has already been used [105, 47] but using the contacts in a different configuration. Here, I propose to measure a rectangle

instead of a square. Such a rectangle could be ABFE (shown in Fig. 4.8 left) with long edge parallel to the high conductivity direction (that is usually known). The term "semi square" will be used for this rectangle because it is not electrically isolated from the remaining part of the square.

- Thus, for highly anisotropic samples the effective anisotropy is closer to unity extending the practically measurable range of conductivity anisotropies. For samples with low anisotropy still the corner contacts can be used to measure the square.

- Additionally, for consistency checking the other semi square EFCD, and the square ABCD can be measured.

- If a corner(edge) contact fails one of the semi squares(the square) can still be measured.

For the anisotropy conversion of A_{vdP} to A, however, the model of a simple rectangle cannot be used because some of the current inevitably flows in the other rectangular part. Consequently, the 4-terminal resistance with current along the short edge $R_{BF,AE}$ has to be calculated numerically. It is advantageous that this 4-terminal resistance increases with increasing anisotropy, making the numerics precise and stabile. For the 4-terminal resistance with current along the long edge $R_{EF,AB}$ the analytical solution from [161] can be directly applied [5]. A table with the calculated 4-terminal resistances and the van der Pauw anisotropy for conductivity anisotropies ranging from 1 to 100 is given in appendix A. A graphical representation of the anisotropies is given in Fig. 4.9, left. For comparison A_{vdP} for a simple square and a rectangle (with aspect ratio of 2, same as for the semi square) is given. The factor of 2 for the anisotropy of the rectangle takes care of the fact that the entire current flows in an isolated rectangle in contrast to only half the current in a semi square. The vdP anisotropy of the semi square is smaller than that of a square (for $A > 3$) which enables one to measure larger conductivity anisotropies. With increasing conductivity anisotropy the vdP anisotropy of the semi square approaches that of a simple rectangle (which can be calculated analytically).

Similar to the experimental verification for the square vdP geometry (section 4.3.6) the calculated conversion of A_{vdP} and A was compared to the experiment. The main results given in Fig. 4.9, right, show that the conversion works well. Consistency was confirmed by comparing carrier densities,

[5] Numerical calculations for this direction were also done agreeing with the analytical results. Since this 4-terminal resistance decreases exponentially with increasing anisotropy (similar to R_{xx} in Fig. 4.4) the precision of the numerical results degrades accordingly.

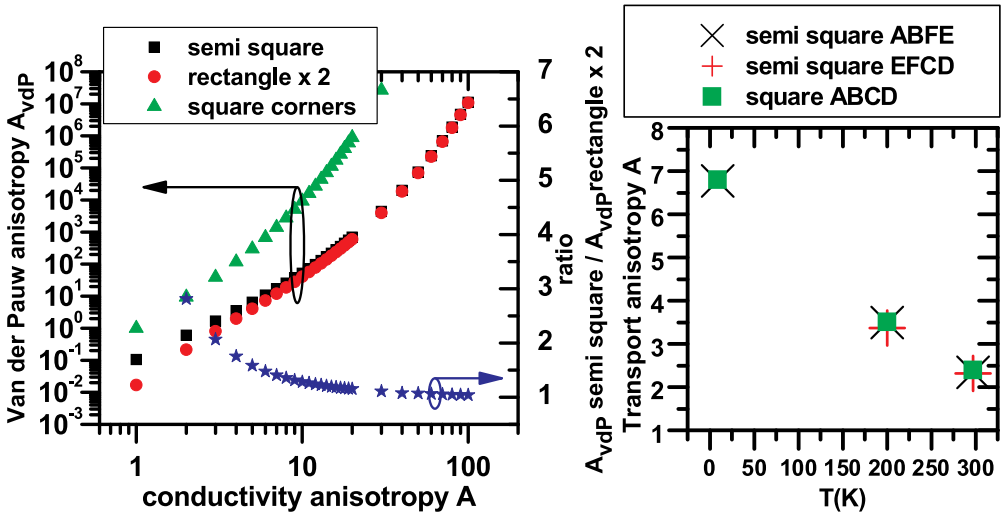

Figure 4.9: **left:** Calculated van der Pauw anisotropy over conductivity anisotropy for the presented geometry (semi square), and for similar geometries (2×vdP anisotropy of a rectangle of same size, and square) in comparison. **right:** Comparison of conductivity anisotropy at different temperatures obtained from van der Pauw measurements in semi square geometry, and square geometry using the same structure.

average resistivities, and conductivity anisotropies obtained from both semi squares, and the square. The maximum discrepancy was 1.5% for the carrier density, 1% for average resistivity, and 4% for the conductivity anisotropy.

4.4 Geometry effects on micro-Hall devices

Magnetic sensors based on the Hall effect in III-V semiconductor materials are successfully applied for studies of magnetic phenomena in physical and material sciences. Because of their high magnetic sensitivity and low noise over a wide temperature range and because their linear operation allows quantitative magnetic field imaging, miniaturized Hall devices ("micro-Hall devices") offer potential advantages over other magnetic field imaging techniques. At small sizes required for high spatial resolution measurements, Hall devices suffer from a high inhomogeneous electric field within the device active area. The high electric field spikes will result in higher background noise and lower absolute magnetic sensitivity due to the self-heating effects as well as hot electron effects degrading device performance. Performance and background noise of micro-Hall sensors with Greek-cross geometry (shown in the insets of Fig 4.10) have been studied in Refs. [92, 93].

The electric field distribution in the active device region will strongly depend on the device geometry. Any field distribution inhomogeneity like field spikes will modify the device performance. For this reason, I have investigated the role of the device geometry on the peak electric field. The distribution of the local electrostatic potential $\Phi(x, y)$ was computed in the 2D plane of a Hall element with Greek-cross geometry as described in section 4.3.3. Using the resulting potential $\Phi(x, y)$, the electric field distribution in the 2D plane of the Hall sensor was calculated using

$$E\,(x, y) = -\nabla\Phi\,(x, y)\,. \tag{4.48}$$

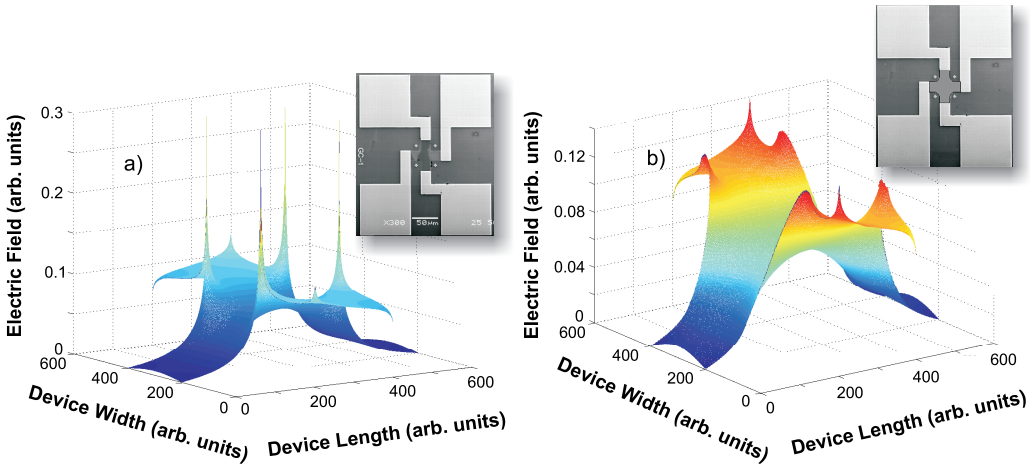

Figure 4.10: Simulated electric field distribution in the plane of micro-Hall element. **a)** With rectangular corners. **b)** With rounded corners.
The device geometry is shown in the insets. The same units are used in (a) and (b). Evident is a significant reduction of electric field spikes due to rounding of the device corners.

Figure 4.10 illustrates the computational results for two different device geometries. The Greek-cross Hall plate with sharp rectangular corners is shown in Fig. 4.10a. The computational results indicate a very high electric field inhomogeneity at all four corners of the structure. Not surprisingly, the high fields result from the sharp rectangular corners. Alternatively, a Greek-cross geometry with rounded corners (see inset on Fig. 4.10b) would be more suitable with respect to a desired homogeneous field. Figure 4.10b displays the numerical results for this modified geometry. Even though the electric field distribution also spikes at the corners, the inhomogeneity is much smaller. The value of the peak electric field E_p on the corner radius r is plotted in Fig. 4.11. The results show a significant improvement in

device performance is possible by choosing an optimum geometry. Because the numerical calculation done in arbitrary units are fully scalable, one can express r in terms of the characteristic size of the device l_c and the peak field in terms of the average field with bias voltage V, $E_{ave} = V/3l_c$ giving

$$\frac{E_p}{E_{ave}} = 1.1 \left[\frac{r}{l_c}\right]^{-0.267} , \tag{4.49}$$

which may prove useful to estimate device performance.

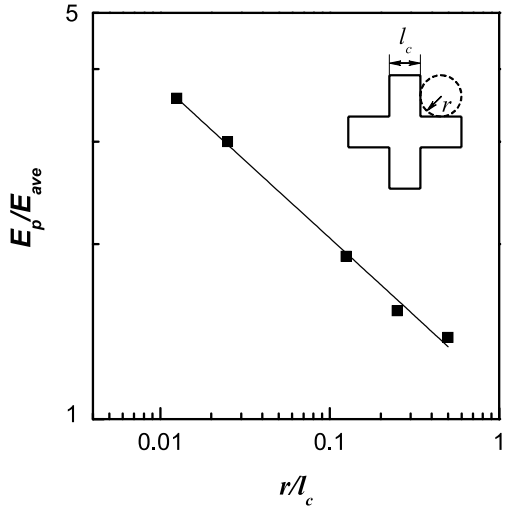

Figure 4.11: Peak electric field dependence on rounded corner radius. The solid line is a fit according to Eq. 4.49.

4.5 Conclusion

In this chapter methods to measure anisotropic transport properties were investigated.

Starting with the magneto-conductivity tensor for anisotropic 2D systems as theoretical foundation, the validity of the results of Hall-bar measurements also for anisotropic materials was shown. The Hall scattering factor for anisotropic carrier systems has been discussed, and its transition from non-degenerate to degenerate case has been calculated for different scattering mechanisms.

A method to find the principal transport directions and -properties with the help of Hall-bar measurements was then theoretically derived and experimentally proven.

I have described in detail how to accurately characterize rectangularly shaped structures with anisotropic conductivity using van der Pauw Hall measurements. An analytical correction is presented to obtain the anisotropy of the conductivity from the measured resistances. It was further shown through a numerical calculation that the Hall coefficient is, in fact, correctly obtained from the vdP data. Combining these two results, the vdP data can be used to obtain the sheet carrier concentration as well as the mobilities in the two principal directions. This anisotropic correction technique was tested on coupled quantum-wire structures with temperature-dependent anisotropy. For all investigated anisotropies, the corrected vdP results agree with those measured using Hall-bar structures.

The numerical method was further used to elucidate the effect of finite-size-contact placement on the Hall voltage, and the effect of geometry of micro-Hall devices on electric field distribution. As result, on square shaped samples corner contacts should be preferred over edge contacts in order to measure correct carrier densities, which agrees with experimental observations. A geometry with rounded corners results lower peak electric field within micro-Hall devices which can improve the device performance.

Finally, a versatile structure for vdP Hall measurements is proposed to extend the measurable anisotropy range of the square shaped structure with corner contacts, and to reduce the disadvantages compared to Hall-bar structures. A combination of numerical simulations and analytical calculations was used to obtain the anisotropy of the conductivity from the measured resistances in this structure. This geometry makes the corrected vdP technique over a wide range of anisotropies an accurate and convenient alternative to the Hall-bar geometry.

The methods developed in this chapter will be used in chapter 6 to analyze the transport in the InAs nanostructures.

Chapter 5

Processing of transport structures

Measurements of the lateral transport in the samples requires a defined lateral geometry for conducting layer as well as ohmic contacts to the conducting layer. In some cases additional gate electrodes are used. In this work, two different methods to create the transport samples were chosen. Simple transport structures were prepared by cleaving rectangular pieces of the as-grown sample to define the geometry, and using small pieces of In as contact. More sophisticated structures were processed with electron beam lithography, and an evaporated stack of metals as ohmic contact. On some of these structures also a top insulator-metal gate stack was evaporated. While the former method is much less elaborate, the latter one allows a significantly higher geometrical precision, smaller sizes, and the preparation of top gates. The preparation of both types of transport structures will be described in the two following sections.

5.1 Unprocessed

The processing steps for the creating of simple transport structures are given below.

1. Square shaped pieces of typically 5×5 mm were manually cleaved for van der Pauw samples while, rectangular pieces of typically 2×7 mm were cleaved for Hall bars. Since InP breaks easily along the $< 110 >$ directions the cleaved edges of the sample pieces are oriented exactly parallel to these directions.

2. Ohmic n-type (p-type) contacts were prepared by manually placing small (typically 0.3 mm) pieces of InSn (InZn) alloy on the clean as-grown surface of the cleaved pieces. The alloys contain 2 wt.% of

Sn(Zn). For a good mechanical contact the alloy pieces were gently squeezed to the surface.

3. To obtain an ohmic contact, the samples were subsequently annealed at approximately 375°C for 3 minutes in a forming gas ambient (90% N_2/10% H_2, to prevent oxidation). This thermal process allows the alloy to diffuse into the semiconductor. The Sn (Zn) component provide a heavy n-doping (p-doping) at the location of the contact. The effect of this heavy local doping is the creation of a local Schottky contact with a very thin depletion layer, that easily allows tunneling.

4. Finally, 30 μm diameter Au wires were soldered to the contacts with In solder.

A micrograph of a complete van der Pauw sample is shown in Fig. 4.3, left, of section 4.3.1. The geometrical precision in terms of sample dimensions and contact position is estimated to 0.5 mm.

5.2 Processed

The experimental determination of the principal axes of conductivity as suggested in section 4.2 requires a precise lateral geometry and contact placement that can be achieved only by processing. Also the processing of top gate electrodes requires more sophisticated techniques. Lithographical techniques provide the precision to process transport structures of small sizes (sub mm) and arbitrary shape at a high geometrical precision. Electron beam lithography was used in this work to define the transport geometry. It is a very flexible tool as it allows to directly write masks that have previously been designed with a CAD software.

The overall process consists of the following principal steps as shown in Fig. 5.1.

1. Processing the mesa to define the lateral geometry of the conducting layer (Fig. 5.1 a-d, dashed line marks the conducting layer).

   - An etch mask is created by spin coating the sample with negative resist (Fig. 5.1 a). The mask is then defined by e-beam lithography, which exposes the resist at the locations that will form the mesa. Subsequent developing of the resist removes the non-exposed parts of the resist leaving the resist mask (Fig. 5.1 b).

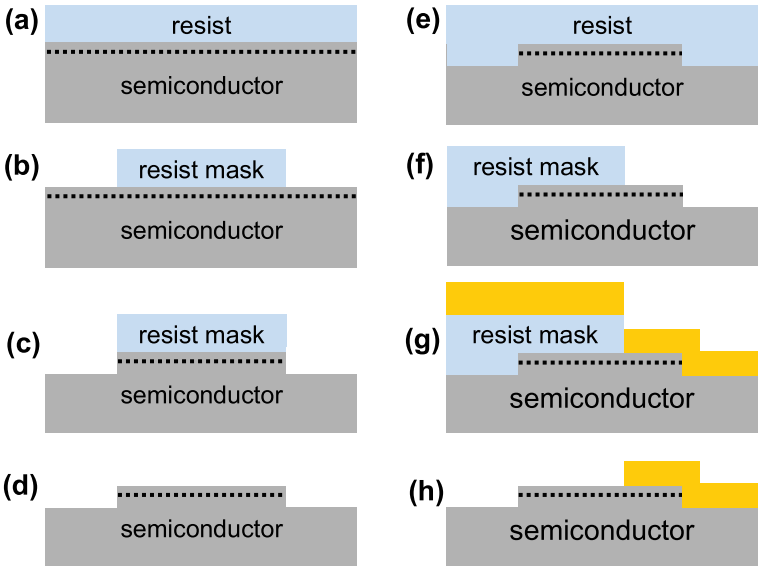

Figure 5.1: Processing of a mesa structure with contacts - cross sectional view of the sample. The dashed line marks the conducting layer. See text for further description.

- The mesa etching process removes the conducting layer from the unmasked parts of the sample (Fig. 5.1 c). Finally, the resist mask is removed (Fig. 5.1 d).

2. Processing of first metallization - the ohmic contacts to the mesa (Fig. 5.1 e-h).

   - The metallization mask is created by spin coating the mesa-sample with positive resist (Fig. 5.1 e). The mask is then defined by e-beam lithography, which exposes the resist at the locations that should be metal coated. Subsequent developing of the resist removes the exposed parts of the resist leaving the resist mask (Fig. 5.1 f).
   - The metallization stack (discussed later) is evaporated on the sample (Fig. 5.1 g). The subsequent lift-off process removes the mask including the metal deposited on top of it (Fig. 5.1 h).
   - A thermal anneal in forming gas ambient alloys the deposited metal into the sample to establish the ohmic contact.

3. Processing of second metallization - the top gate electrode. This process comprises basically the same steps as the previous one. In contrast

to the previous process, though, the gate stack (discussed later) is different, and the final thermal anneal is left out.

Detailed process protocols are given in appendix B [1]. The mask creation process was taken over from [46].

5.2.1 Electron beam lithography

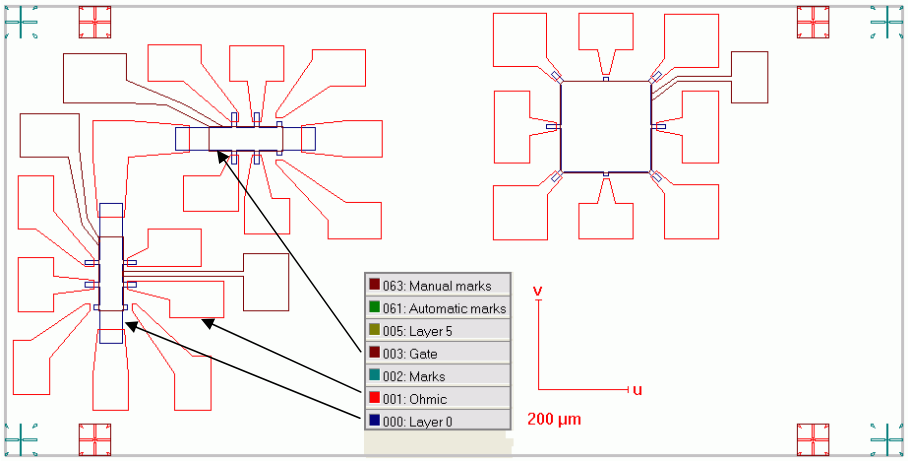

Figure 5.2: Design of the L-shaped double Hall bar and van der Pauw device. Mesa (Layer 0), ohmic contact, and gate contact are shown. The "+" are marks to align subsequent layers (ohmic to mesa, gate to ohmic).

A JEOL JSM-6360 scanning electron microscope (SEM) was used together with a RAITH Elphy Plus advanced SEM nanolithography system. L-shaped perpendicularly oriented gated double Hall bar structures and square shaped gated van der Pauw structures were designed. Figure 5.2 shows all layers (mesa, ohmic contacts, gate contact) of the L-shape double Hall bars and the van der Pauw structure.

5.2.2 Ohmic contacts n- and p-type

The ohmic contact to the n-type samples was prepared by evaporating a 260 nm-thick stack of Ni/Ge/Au. During the subsequent annealing (375°C/1 min) the Ge acts as n-dopant [80].

[1] The etching, and the deposition of metal stacks were performed externally in HHI (S. Dressler) and PDI (E. Wiebicke).

As ohmic contacts to the p-type samples, an AuBe alloy containing 1 wt.% Be was thermally evaporated to form a 160 nm-thick layer. During the subsequent annealing process (at 330°C/2 min) Be acts as acceptor to heavily p-dope the contact area [175].

The contact resistance was optimized by trying different annealing temperatures, and extracting the contact resistance from TLM measurements.

5.2.3 Gate electrode to InP surface

Deposition of a Ti gate-electrode directly on the InP surface, to form a MES structure, only yielded a Schottky contact with high leakage currents which may be explained by the comparably low Schottky barriers on InP [195]. As an alternative a MIS structure was deposited using 100 nm-thick SiN_x as insulator similar to [110]. Generally, the disadvantage of MIS structures is a high density of traps due to imperfections in the insulator-semiconductor interface.

5.2.4 Wiring the samples

Samples were mounted on chip carriers. The contact pads were subsequently connected to the chip carrier by ball bonding. This method worked only with a few samples - probably due to the low thickness of the ohmic contact pads -, which made it necessary to manually glue Au wires to the contact pads using Ag-epoxy. The micrograph of a complete, wire bonded, gated vdP structure is shown in the right panel of Fig. 4.8 in section 4.3.9.

Chapter 6

Transport in coupled InAs nanostructures

In this chapter, the in-plane transport properties of large ensembles of InAs nanostructures are investigated and discussed. Similar studies have been done in other material systems such as GaAs/AlGaAs quantum wires [122, 120, 154, 51] or InAs/GaAs quantum dots [85, 191]). In the InP based material system in-plane transport has been measured in $In_{0.53}Ga_{0.47}As$ quantum wells with optional insertions of an InAs quantum well [189, 202].

6.1 From nanostructure to transport

Electrons and holes are confined to InAs nanostructures embedded in an InP matrix due to the type-I InAs/InP heterointerface (see Fig. 6.1 d). In quantum wells, the carriers are confined only in the vertical direction (growth direction, [001]) but can move freely within the InAs QW layer ([$\bar{1}$10] and [110] directions). In contrast, the quantum-wire-like or quantum-dot-like shape of the nanostructures (see AFM and TEM images in chapter 2, and Fig. 6.1 a,b) provides an additional lateral confinement. This lateral confinement results in the localization of carriers in the quantum dots and quantum wires, which, for example, results in polarization of the nanostructure's emission (see chapter 3).

Owing to their close spacing, the self-assembled InAs nanostructures are separated only by narrow InP insertions on the order of 3 nm (see TEM images Fig. 6.1 a,b), which act as barriers. Figure 6.1 c shows a schematic lateral band diagram of two adjacent nanostructures separated by this barrier. In contrast to the free carrier transport within a QW, the transport is supposed to be impeded by the barriers Φ_B.

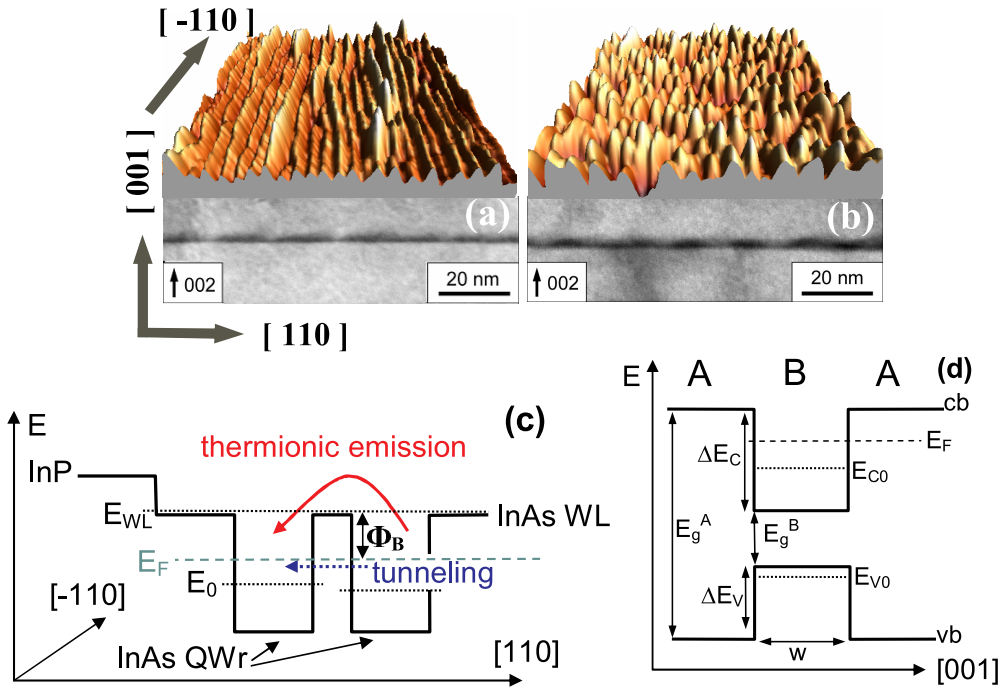

Figure 6.1: Cross sectional TEM of covered InAs nanostructures, and AFM of corresponding InAs non-covered nanostructures. AFM image scale 500 nm x 500 nm. **(a)** Quantum wires, **(b)** Quantum dots.
Band diagram models. **(c)** Lateral confinement. Model of coupling between adjacent quantum wires for lateral transport. WL denotes the InAs 2D wetting layer, E_F is the Fermi-level, and Φ_B is the energy barrier for electrons between adjacent nanostructures. **(d)** Vertical confinement. Band structure of a quantum well of material A (e.g. InAs) in a matrix of material B (e.g. InP) with a type-I interface. Dotted lines represent the ground-state subbands at energies E_{C0} and E_{V0}. E_g^A and E_g^B are the band gaps of material A and B, w the well width, cb, cv denote conduction band and valence band edges.

Current flow within the layer of InAs nanostructures is, however, observed in my transport measurements, which demonstrates that the nanostructures are coupled, i.e. carriers can transfer from one nanostructure to the next. The coupling for current flow along the quantum wires is termed "longitudinal coupling" whereas the coupling of one wire to its neighbor during current flow orthogonal to the quantum wires is called "lateral coupling". As schematically illustrated in Fig. 6.1 c, the coupling is enabled either by tunneling or by thermic excitation of the carriers into extended states above the barrier (thermionic emission).

Measurements in my layers with quantum wires reveal a strong transport anisotropy with higher conductivity parallel to the QWrs than orthogonal to the QWrs, which intuitively agrees with the QWr's elongated shape. Since the investigated layers behave like 2-dimensional (2D) carrier systems with a anisotropic conductivity, they are analyzed within the framework of anisotropic 2D systems. In this framework, a high conductivity corresponds to strong nanostructure-nanostructure coupling. Hence, a strong lateral coupling in the "coupled nanostructure" model corresponds to a low transport anisotropy in the "anisotropic 2D" model, whereas a weak lateral coupling, emphasizing the quasi 1-dimensional (1D) nature of the quantum wires, corresponds to a high transport anisotropy. In terms of effective dimensionality, isotropic transport can be considered 2D, whereas strongly anisotropic transport is quasi 1D.

Several authors have shown various origins for the anisotropy of in-plane transport. In purely 2D carrier systems, the transport anisotropy can be due to an anisotropic effective mass [35, 153], anisotropic scattering mechanisms such as interface roughness scattering [101, 85], which both result in moderate anisotropies (<4), or due to potential barriers on a length scale much larger than the electron wavelength, such as dislocations [170] or aperiodic steps [120], which may cause extremely large anisotropies such as 1000. Lateral potential modulations on length scales comparable to the carrier wavelength that localize the carrier wavefunction in one lateral direction result in quantum wires, localization in two lateral directions results in quantum dots. If the carriers can transfer between quantum wires/dots, the carrier system can be considered as coupled 1D/0D. A periodic arrangement of coupled quantum wires or quantum dots leads to the superposition of the nanostructures' energy levels to form a miniband. In one realization, in-plane superlattices (or lateral superlattices) due to periodically inserted barriers into a 2D system have been prepared, which creates electronically a system of coupled quantum wires showing anisotropic in-plane conductivity [118]. The in-plane arrangement of structural and electronic quantum dots or quantum wires is another way to form coupled quantum dots/wires. This type of coupled quantum dots or wires has been realized using periodic multiatomic steps [75, 51, 154], or strain-driven self-assembly [17, 165, 82, 89, 90]. Lateral transport through ensembles of self-assembled quantum dots has been interpreted in terms of lateral minibands [165], and resonant tunneling [82], but has not been investigated for transport anisotropy. The transport in coupled quantum wires has been explicitly shown by selecting individual wires to provide the transport using side-gates [51].

6.2 Abstract on transport investigations

The temperature dependent anisotropic in-plane transport of electrons and holes in ensembles of coupled InAs/InP nanostructures is shown in section 6.6. The results are discussed mainly in the framework of anisotropic 2D systems. Diffusive carrier transport via extended states (such as lateral minibands) and hopping transport via localized states is found in different samples. The occurrence of hopping transport only in p-type samples demonstrates the stronger localization of holes to the nanostructures than that of electrons. In the case of diffusive transport, the scattering mechanisms at low temperatures are identified as remote impurity scattering in the direction parallel, and interface roughness scattering orthogonal to the quantum wires.

In the framework of coupled nanostructures, that covers diffusive and hopping transport, the transport anisotropy is demonstrated to result from *directionally anisotropic tunnel coupling* between adjacent nanostructures rather than from the nanostructure shape anisotropy (section 6.7). The tunneling from one nanostructure to the next limits the electrical transport in ensembles both of high quality quantum wires and of closely-spaced quantum dots. Transport anisotropies in excess of 30 for electrons, and 100 for holes are measured. In extreme cases, the coupling anisotropy results in diffusive transport through extended states in one direction, and hopping transport via localized states in the other direction within the same sample. Using an empirical model to fit the directional dependence of the resistivities, the coupling strength between adjacent nanostructures in the [-110] and [110] directions is determined.

The effect of a changed Fermi level on the transport is investigated in n-type InAs QWr at low temperature in section 6.8. The resulting carrier-density dependence of mobilities corroborates the results on scattering mechanisms from the temperature dependence. The change of coupling barrier due to the change of Fermi level is found to be negligible, supporting the assumption of coupling by tunneling. The change of Fermi level using a top gate electrode demonstrates the gate-control of the transport anisotropy which is the basis for a novel electronic switching device proposed in chapter 7.

Results of Shubniko-de-Haas oscillations and quantum Hall effect in InAs QWrs are briefly shown in section 6.9.

In section 6.10 the investigation of the weak localization contribution to the transport in InAs QWs, QWrs, and QDs demonstrates that the weak-localization correction shows a directional anisotropy equal to the anisotropy of the total conductivity, which is typical for anisotropic 2D systems. This result suggests that the coupling between the quantum wires plays a more important role than the quasi-one-dimensional nature of the electron transport

in describing the quantum mechanical contributions due to weak localization. The large dephasing length extracted from the data demonstrates that the wire-wire coupling is elastic.

The investigated structures comprise modulation-doped quantum wells, wires, dots and dashes with the emphasis on wires. Transport measurements of single or only few nanostructures, however, are out of the scope of this work.

6.3 Modulation-doping, band diagram, and dimensionality

Modulation doping

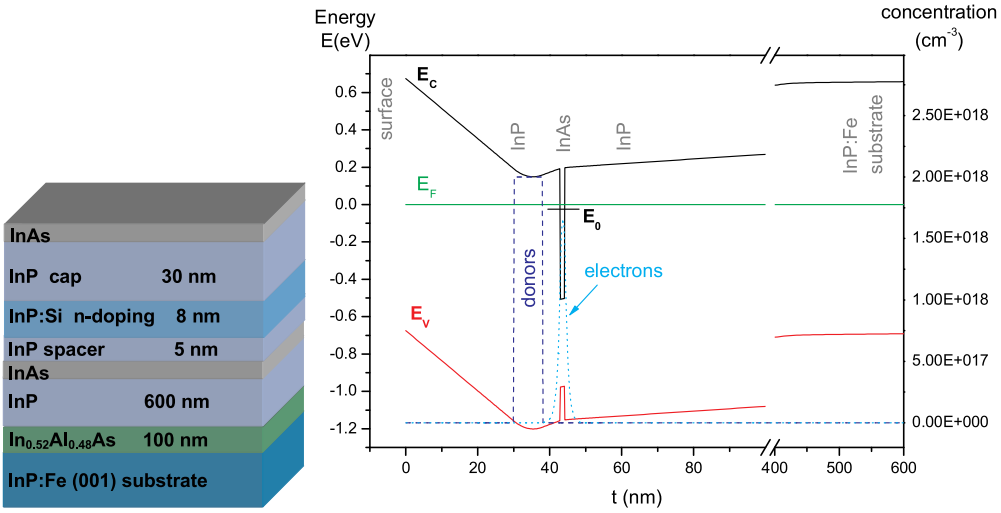

Figure 6.2: **left:** Principle layer structure of modulation-doped InAs/InP samples.
right: Band diagram from sample surface to substrate of modulation-doped InAs QW in InP. Conduction band energy E_C, valence band E_V, Fermi energy E_F, and energy of first electron subband E_0 in the QW are shown.

The layer structure of the modulation-doped samples is given in Fig. 6.2, left panel.

Modulation-doping is technique that dopes the barrier of the quantum well [42, 167, 180]. Due to the band profile the free carriers from the dopants are trapped in the quantum well where they form a 2D carrier system that is spatially separated from the ionized dopants. Thus, in contrast to the

direct doping of the quantum well, ionized impurity scattering is eliminated which results in increased mobilities. To further increase the mobility, an undoped spacer is inserted between the doped part of the barrier and the quantum well, which increases the spatial separation of 2D carrier system ionized dopants [43]. Field effect transistors (FETs) based on this concept with and without spacer have been built [115, 41]. In my work the specifics of transport due to coupled nanostructures are investigated. Therefore, modulation doping is used in order to reduce the influence of ionized impurity scattering that would obscure these specifics at low temperatures. A qualitative band profile from sample surface to substrate was calculated using a self-consistent Schrödinger-Poisson solver [163, 173]. The result, shown in Fig. 6.2, right, show the spatial separation of donors and electron gas, and the electron subband in the InAs QW.

Band diagram of coupled nanostructures

InP as barrier material provides strong confinement to both electrons and holes due to the high conduction band offset and valence band offset. With electron and hole transport, two different types of carriers will probe the same morphological structures. The main differences are the higher effective mass and higher effective barrier for holes which both lead to a stronger localization of the holes to the nanostructures. This stronger localization of holes compared to that of electrons can be understood, for example, in terms of the decreasing effective Bohr radius or decreasing tunneling probability with increasing effective mass. Comparison to InAs nanostructures in an $In_{0.53}Ga_{0.47}As$ matrix with significantly lower effective barrier will be done.

The barrier height Φ_B for coupling is the energy difference from Fermi energy E_F to the next higher electronic state that extends across the entire layer E_{ext}

$$\Phi_B \;=\; E_{ext} - E_F \;. \tag{6.1}$$

As illustrated in Fig. 6.1 c, this higher extended state E_{ext} can be the subband of a 2D InAs wetting layer (WL) or the conduction band of the surrounding matrix material (InP). In order to estimate the effective barriers (Φ_B) for lateral transport, the subband energies for electrons and holes ($E_{C0,V0}$) with respect to the conduction band edge and valence band edge of the InAs are calculated using the band parameters from table 6.1. These calculated energies will be called the confinement energies. Since the height of my nanostructures is the smallest dimension, it has the major impact on the confinement energy. The influence of the lateral confinement (height to width

Table 6.1: Band parameters of the used materials (InAs, $In_{0.53}Ga_{0.47}As$, InP) at T=0 K according to Refs. [141, 188]. Given are band gap (E_g), conduction band offsets and valence band offsets (ΔE_C, ΔE_V), effective electron mass (m_e^*) and heavy-hole, light-hole mass (m_{hh}^*, m_{lh}^*). The parameters of InAs take the strain distribution in the different types of nanostructures into account [141]. The effective masses are averaged over the nanostructure volume and over the directions that contribute to confinement. The effective hole mass given for strained InAs is taken from the highest valence subband. It is a a mixture of heavy and light holes but primarily heavy hole. The effective hole masses of the barriers (InP, $In_{0.53}Ga_{0.47}As$) are given for the direction of the confinement [001].

materials well / barrier	E_G (eV)	ΔE_C (eV)	ΔE_V (eV)	m_e^* (m_e)	m_{hh}^*/m_{lh}^* (m_e)
Bulk					
InP / InP	1.424	0	0	0.080	$m^*_{[001]}$: 0.53/0.12
$In_{0.53}Ga_{0.47}As$ / InP	0.818	0.261	0.345	0.043	$m^*_{[001]}$: 0.38/0.052
Quantum wells					
InAs / InP	0.471	0.514	0.439	0.029	0.137/-
InAs / $In_{0.53}Ga_{0.47}As$	0.471	0.253	0.094	0.029	0.137/-
Quantum dots and wires					
InAs / InP	0.586	0.465	0.373	0.032	0.064/-
InAs / $In_{0.53}Ga_{0.47}As$	0.586	0.204	0.028	0.032	0.064/-

ratio of approximately 0.1) is omitted. The nanostructures are approximated with a quantum well (well width w = nanostructure height) with finite barriers. The confinement energies $E_{C0,V0}$ of InAs quantum wells with InP or $In_{0.53}Ga_{0.47}As$ barriers are calculated in the envelope function approximation and effective mass approximation using the program *efsqw* of Ref. [72]. The case of a 24 Å-thick quantum well is investigated in depth as this is the typical thickness of my InAs quantum wires on InP. In addition to the confinement energies, the position of the Fermi energy, which at $T = 0$ K is the energy of the highest occupied state, has to be estimated. This estimation is done by calculating the energy difference between the subband edge and the Fermi energy ($E_F - E_{C0}$) resulting from the filling of the 2D subband with the carriers supplied by the modulation doping according to Eq. 6.5. The effective barrier is then calculated using Eqs. 6.1, 6.5 as $\Phi_B = E_{ext} - E_{C0} + (E_F - E_{C0})$ with E_{ext} being either ΔE_C (extended states in InP) or E_{C0}^{WL} (extended states in WL). The results are given in table 6.2 and discussed in the context of

Fig. 6.1c,d as follows:

Table 6.2: Estimated confinement energies (distance from subband $E_{C0,V0}$ to band edge in quantum well) for different well widths w, subband filling ($E_F - E_{C0,V0}$) and resulting effective barrier heights (Φ_B) for electrons and holes in InAs quantum well with InP and $In_{0.53}Ga_{0.47}As$ barriers. The effective barrier is calculated for the cases of no InAs WL (extended states in InP) and for a 6 Å InAs WL. The numbers in italics denote the estimated confinement energies (including excited states) due to lateral confinement.

w (Å)	InAs/InP: e energy (meV)	InAs/InP: hh energy (meV)	InAs/InGaAs: e energy (meV)
band offset →	$\Delta E_C = 514$	$\Delta E_V = 439$	$\Delta E_C = 253$
well width ↓	E_{C0} ↓	E_{V0} ↓	E_{C0} ↓
3	502	390	-
6	471	310	247
12	390	200	-
24	**260**	**105**	**187**
48	138	46, 206	-
150	*31, 128, 297, 511*	*8, 34, 78, 141, ...*	-
band filling concentration	$n = 6 \cdot 10^{11}$ cm^{-2}	p=$1.5 \cdot 10^{12}$ cm^{-2}	n=$6 \cdot 10^{11}$ cm^{-2}
$E_F - E_{C0,V0}$	48	26	48
Φ_B ($w = 24$ Å)			
$E_C^{InP} - E_F$	**206**	**308**	**18**
$E_{C0}^{WL} - E_F$	**163**	**179**	**12**

- For electrons there exists only one subband for thickness below 50 Å, for holes a second subband exists for well width larger than 26 Å.
- The calculated ground state energy of the lateral confinement using $w = 150$ Å(30/8 meV for electrons/holes) is smaller than the change of confinement energy due to a thickness fluctuation of 1 ML (3 Å) and can thus be left out for a rough estimate.
- The position of the Fermi energy due to band filling is estimated using the 2D density of states (see Eq. 6.5) based on the effective masses used in this calculation, and on average carrier densities measured in the samples. Shifting of Fermi level as proposed due to a change of carrier density, which will be a change by less than $1 \cdot 10^{12}$ cm^{-2}, will

result in change of less than 80 meV. The actual value is likely to be even lower due to band non-parabolicities.

- The typical measured electron carrier density of $n = 6 \cdot 10^{11}$ cm^{-2} would fill each quantum dot (areal density of $n = 6 \cdot 10^{10}$ cm^{-2}, see section 2.5.5) with 10 electrons, i.e. the 5 lowest energy levels are each filled with spin up and spin down electrons. The highest energy level is surely higher than E_F calculated for the band filling of a 2D carrier system, leading to a lower Φ_B for QDs than for QWs and QWrs.

- The effective barrier $\Phi_B < 18$ meV for electrons in InAs/$In_{0.53}Ga_{0.47}As$ nanostructures is very low.

- In contrast, an InP matrix yields $\Phi_B > 163$ meV for electrons.

- Thermionic emission may be considered to influence the coupling of InAs/$In_{0.53}Ga_{0.47}As$ nanostructures but certainly not the InAs/InP nanostructures. Tunneling is expected to govern the coupling in this case.

- A controlled change of Fermi level will change the effective barrier for electrons, probably, by less than 25%.

- The effective barrier is higher for holes than for electrons.

Dimensionality of the nanostructures

As described in chapter 1 effective confinement effects are expected if the level spacing due to the confinement is larger than the (thermal) broadening of 25 meV at room temperature, and 0.8 meV at 10 K. In the case of my QDs, the level spacing due to lateral confinement is larger than 97/26 meV for electrons/holes (see Tab. 6.2), which makes them electronically quantum dots.

The length of the quantum wires is typically $l = 200$ nm or longer with corresponding areal densities of $2.5 \cdot 10^{10}$ cm^{-2} or lower. At this length of $l = 200$ nm, the longitudinal confinement energy of electrons in the n-th level is: $E_n \propto n^2/m^* l^2 = n^2 \cdot 0.315\ meV$ for electrons (approximation of infinitely high barriers). The quantum wires with lengths of 200 nm show a level spacing smaller than the thermal broadening even at 10 K for low states n.

The filling with carriers ($6 \cdot 10^{11}$ cm^{-2}), however, fills each wire with approximately 24 electrons corresponding to $n = 12$ (spin degeneracy of 2) as the highest occupied state. This n corresponds to a confinement energy of 45 meV (approximately the same as in the 2D case) with a level spacing

of 7.5 meV. Thus, the effective barrier Φ_B is similar to that of the 2D case. Electronically, though, the 200 nm-long quantum wires are quantum-wire-like at room temperature, but quantum-dot like at 10 K. On the other hand, the 600 nm-long quantum wires show a level spacing of 0.83 meV (comparable to the thermal energy at 10 K), and are thus electronically quantum wires.

For the transport in large ensembles of nanostructures, the dimensionality elaborated above will play no role. The transport properties are rather determined by the coupling between the nanostructures.

6.4 Characteristic 2D transport quantities

A short overview of the physical quantities and formulae for the description of 2-dimensional transport is given here.

Transport through extended states can be *ballistic* or *diffusive*. In the ballistic regime the mean free path of the carriers is larger than the sample dimension and the current is only limited by scattering at the sample boundaries. In the samples investigated in this work, the mean free path is smaller than the sample dimension which results in a diffusive transport.

In the diffusive regime, the scalar resistivity ρ of a 2D system is the resistance of a square of arbitrary size (scaling shows that all squares have the same resistance). It is also called sheet-resistance $R_\square$. In the presence of one carrier type, it depends on the electronic charge $e = 1.602 \cdot 10^{-19}\ As$, the drift mobility $\mu(cm^2/Vs)$, and the 2D-carrier density $n(cm^{-2})$ according to

$$R_\square = \rho = \frac{1}{(en\mu)} \ . \tag{6.2}$$

Experimentally, ρ and n are measured, and used to calculate μ. The mobility of electron or hole depends on the momentum relaxation time (elastic scattering time) $\tau(s)$ and the transport effective mass m^* according to

$$\mu = \frac{e\tau}{m^*} \tag{6.3}$$

with scattering mechanism determining τ. Experimentally, the mobility is determined from measured ρ and n according to Eq. 6.2. The carriers that contribute to transport have energies around the Fermi energy E_F and move at the Fermi velocity v_F, which results in the mean free path l_e (average distance between two subsequent momentum re-setting scattering events)

$$l_e = v_F \cdot \tau. \tag{6.4}$$

Please note, that the Fermi velocity is not the drift velocity. The Fermi velocity is the velocity of the carrier during its random diffusive motion,

whereas the drift velocity is the resulting average velocity in the direction of the electric field.

In the effective mass approximation, the distance of Fermi energy to the subband edge $E_F - E_{C0}$ (see Fig. 6.1d) depends on the 2D carrier concentration n and the 2D density of states per subband ρ^{2D} according to

$$\begin{aligned} \rho^{2D} &= \frac{m^*}{\pi\hbar^2} \\ E_F - E_{C0} &= \frac{n}{\rho^{2D}} = n\frac{\pi\hbar^2}{m^*} \ . \end{aligned} \tag{6.5}$$

Electrons in InAs quantum wells on InP have an effective mass of $m^* = 0.03m_e$ [141] which leads to $\rho^{2D} = 1.25 \cdot 10^{10}$ cm^{-2}/meV. The density of states for holes in InAs quantum wells with m^*=0.137(0.064) [141] amounts to $5.8(2.7) \cdot 10^{10}$ cm^{-2}/meV. Band non-parabolicities, however, result in effectively higher effective masses and DOS for carrier energies above the subband edge (non-zero carrier densities). Therefore, the calculated DOS has to be regarded as lower limit to the effective DOS.

The carriers at the Fermi energy have a de-Broglie wavelength (Fermi wavelength) λ_F in the plane of the 2D carrier system, which may also be expressed as Fermi wavevector $k_F = 2\pi/\lambda_F$. Consequently, the quantities v_F, λ_F, k_F depend on the 2D-carrier density and effective mass according to

$$\begin{aligned} v_F &= \frac{\hbar}{m^*}\sqrt{2\pi n} \\ \lambda_F &= \sqrt{\frac{2\pi}{n}} \\ k_F &= \sqrt{2\pi n} \ . \end{aligned} \tag{6.6}$$

The Fermi wavelength for a typical carrier concentration of $1 \cdot 10^{12}$ cm^{-2} is 25 nm. The quantities ρ and n are determined experimentally. These allow the other quantities to be calculated - partially only if the effective mass is known. Some quantities, however, do not require the effective mass to be put into the calculation. These are μ, l_e, λ_F, k_F.

For mean free paths much smaller than the Fermi wavelength,

$$k_F l_e < 1/2\pi \text{ (Ioffe-Regel criterion)}, \tag{6.7}$$

the carrier wavefunction is no longer extended. Instead, the carriers are localized and transport takes place in the regime of *hopping conduction* [9]. Hopping conduction through localized states results in conductivities below the predicted minimum metallic conductivity in two dimensions $\sigma < \sigma_m =$

$0.1e^2/\hbar$, which corresponds to a resistivity ρ in excess of 40 kΩ [9]. Usually, hopping transport is thermally activated which results in an decreasing resistivity with increasing temperature. The three mechanisms of hopping transport are summarized following Ref. [162].

1. Hops can connect localized states via extended states (energetically these are above the "mobility edge") by exciting the carrier with the help of phonons above the barrier Φ_B (compare Fig. 6.1), which results in resistivities
$$\rho \propto \exp\left[\frac{\Phi_B}{kT}\right] . \tag{6.8}$$

2. For *nearest-neighbor hopping* between adjacent localized states with distance R, localization length of the wavefunction a^*, average energetical separation ΔE, and attempt frequency (=phonon frequency) ν_{ph} the resisivity is calculated according to
$$\rho = \frac{1}{2e^2R^2\nu_{ph}\rho^{2D}(E_F)} \exp\left[2\frac{R}{a^*} - \frac{\Delta E}{kT}\right] , \tag{6.9}$$
which depends strongly on the wavefunction overlap R/a^* and has an activation-type temperature dependence.

3. At low temperatures, however, hops between states of same energy becomes favorable even if they are not adjacent to each other. This *variable-range hopping* shows a temperature dependence of
$$\rho \propto \exp\left[\left(\frac{T_0}{T}\right)^{1/3}\right] . \tag{6.10}$$

6.4.1 Scattering mechanisms

In the diffusive transport regime, the temperature dependent mobility is usually approximated according to
$$\mu \propto T^r , \tag{6.11}$$
with exponent r depending on the scattering mechanism. The total mobility μ_{tot} in case of multiple independent scattering mechanisms with associated mobilites μ_i is calculated according to Mathiessen's rule
$$\frac{1}{\mu_{\text{tot}}} = \sum_i \frac{1}{\mu_i} . \tag{6.12}$$
In Fig. 6.3 the qualitative temperature dependence of the different scattering mechanisms that are relevant for my samples, and their combination is shown.

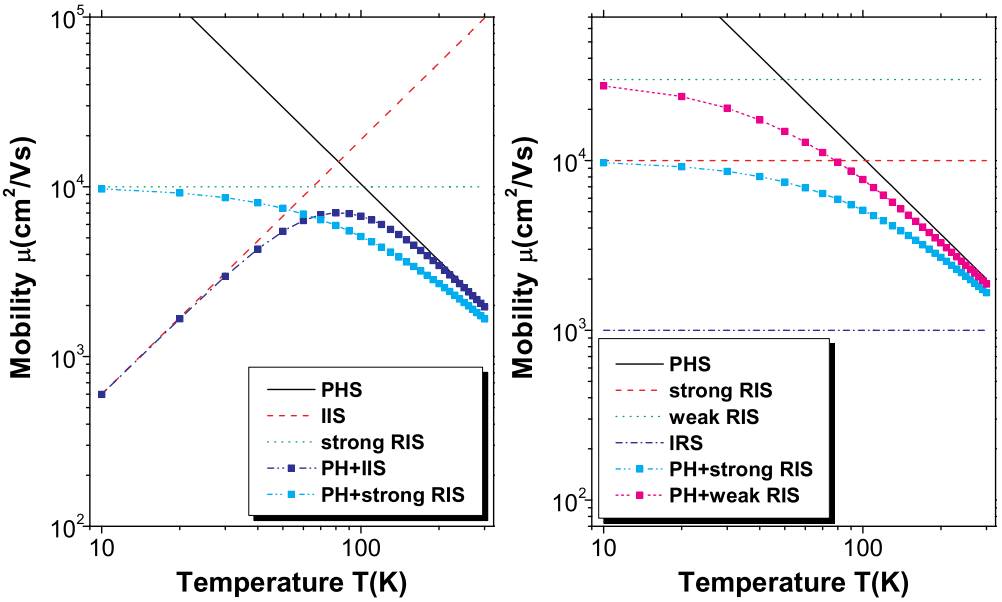

Figure 6.3: Schematic of temperature dependent mobilities due to phonon scattering (PHS), ionized-impurity scattering (IIS), remote-impurity scattering (RIS with $r = 0$), interface roughness scattering (IRS with $r = 0$), and their combinations calculated with Eq. 6.12. **left:** phonon scattering, ionized impurity scattering, remote impurity scattering, and their combinations. **right:** Phonon scattering, remote impurity scatterings with different strengths, and their combinations, strong interface roughness scattering.

- At high temperatures the strongest scattering is caused by phonons (phonon scattering, PHS) in most cases. The temperature dependence is typically characterized by $r = -3/2$ [106] as the number of phonons reduces at decreasing temperature.

- If the carrier wavefunction has a significant overlap with ionized impurities (e.g. donors or acceptors in doped InP) they are subjected to ionized impurity scattering (IIS), which can be described as Rutherford scattering and is most effective at low temperatures ($r = +3/2$, [106]).

- In modulation-doped samples, the ionized impurities are spatially separated from the carriers and the carriers are only subjected to a weakly varying potential caused by the remote impurities leading to remote impurity scattering (RIS) [8, 60].

- Roughness of the InAs can be regarded as fluctuations in the width of an InAs quantum well which in turn cause lateral fluctuations of the

confinement energy. These fluctuations represent a scattering potential that acts on the carriers (interface roughness scattering, IRS). The scattering strength mainly depends on the well width and the lateral size of the fluctuations [148, 9, 60, 178].

Remote impurity scattering and interface roughness scattering usually have a weak temperature dependence, which is approximated with $r = 0$ here. Experimental results show that the exponent r can deviate from the theoretical values. In high mobility samples, for example, r can be in excess of -3/2 for phonon scattering. For ionized impurity scattering, r can also be different from -3/2 theoretically [135] and experimentally. The qualitative behavior (sign of r) of the temperature dependent mobility, however, agrees with experiments.

6.5 Experimental details of transport measurements

This section gives details of the experiments as well as substantial challenges that had to be tackled.

6.5.1 The temperature-dependent magneto-transport experiments

Most of the temperature dependent transport measurements were performed in a closed-cycle Helium refrigerator cryostat that allows a temperature range of 320 K to approximately 10 K. A conventional electromagnet provided magnetic field up to 0.7 T. DC technique with current reversal (to eliminate thermovoltages) was used for the measurements with typical bias currents of 1 to 100 μA. Two van der Pauw samples or one L-shaped double Hall bar could be measured in one run.

Transport measurements at lower temperature and higher magnetic fields were performed in an Oxford liquid He^4 cryostate with variable temperature insert (VTI) and a superconducting solenoid for fields up to 12 T. Reducing the pressure in the VTI filled with liquid He^4 allows a base temperature of approximately 1.4 K. Measuring and regulating the He^4 pressure allows the temperature to be tuned very sensitively in the range from 4.2 K down to the base temperature. DC measurement technique with currents from 1 to 10 μA and current reversal was used.

Further transport measurements were performed in an Oxford He cryostate

with He^3 insert allowing a base temperature of 0.3 K [1]. The superconducting solenoid of this cryostate can generate magnetic fields up to 16 T. AC lock-in technique at a 13 Hz current of 100 nA was employed to minimize the sample heating and have a high signal to noise ratio.

Some samples contain traps that can be phenomenologically modeled as a potential well with a barrier at the well edges (capture barrier) that is smaller than the well depth. This type of trap lead to a decrease of carrier density with decreasing temperature since the thermal energy to retrieve the carriers from the trap decreases. With illumination these carriers can be retrieved from the trap but the thermal energy drives them back across the capture barrier into the traps. If the thermal energy is much lower than the barrier height, however, this barrier prevents the carriers from being re-trapped. This leads to a persistent photo conductivity (ppc) which is used to increase the carrier density in trap-containing samples (see Ref. [52] for alternative mechanisms of ppc). Thus, by stepwise illumination with short pulses a dependence of transport properties on carrier density can be measured. (In the present work, a blue LED was used as illumination source, that had a measurable effect on the sample carrier density at LED currents as low as 10 nA demonstrating the high efficiency of this type of LED compared to red or green LEDs).

Another way to control the carrier density is the use of a top gate electrode. In contrast to the ppc effect, this method takes a lot of effort as it requires extensive processing of the sample. The advantage, though, is a reversible control of carrier density over a larger range and the independence of trap states. Depending on the potential difference between gate and electron gas the carrier density is increased or decreased. This effect is used in field effect transistors (FETs). The leakage current through the gate was monitored in all experiments to prevent a breakthrough that destroys the gate insulation. It was kept below 1 nA.

Owing to their experimental simplicity, temperature dependent van der Pauw measurements on rectangularly shaped, unprocessed samples were the main method to obtain the sample's transport characteristics. The results were analyzed as described in section 4.3.5. The aspect ratio of the almost rectangular samples was measured and enters the calculations as a constant factor to the principle resistivities. *Hence, the uncertainty of the aspect ratio does not influence the qualitative temperature characteristics of the principle resistivities.* The uncertainty of aspect ratio (of less than 10%) constitutes mainly an uncertainty to the magnitude of transport anisotropy which is be-

[1] These measurements were performed at Paul-Drude Institut, Berlin together with K.J. Friedland.

low 20%. For samples with transport anisotropies in excess of 10 rectangular van der Pauw samples with aspect ratio of 2-3 or Hall bars were prepared and measured. The comparison of data obtained by Hall-bar and Van der Pauw measurements of the same sample show the validity of the Van der Pauw results.

6.5.2 Parasitic conductivities

Unintentional carrier systems in the samples form layers with a conductivity in parallel to the intentionally doped layers that should be measured. This parasitic parallel conductivity contributes to the overall results of the transport measurements. Thus, the results of transport measurements with parallel conductivity show only a distorted characteristics of the intentionally doped layer. Consequently, parasitic parallel conductivity should be eliminated if possible.

As an example, a conductive (doped) substrate would provide such a parallel conductivity. For this reason, Fe-doped, semi-insulating InP substrates are chosen for samples in which lateral transport should be investigated. The growth of InP on these semi-insulating InP(001):Fe, however, involves the formation of an unintentional, parasitic, highly-conductive layer at the substrate-epilayer interface. The conductivity found in GSMBE, and MOVPE grown samples is caused by a Si contamination on the substrate surface [142, 86]. InP substrates of different vendors were comparatively checked for this n-type charge accumulation layer occuring with MBE growth with the result that this layer (Si or S contamination) varies (from clean interface to layer present) from vendor to vendor and also among different lots [48]. Non-intentionally doped samples with InP buffer on the substrate, grown in the present work, show carrier densities around 10^{12} cm^{-2} at room temperature with mobilities around 2000 cm^2/Vs. Those mobilities have also been measured in doped InP at room temperature, indicating carriers in an InP layer. Capacitance voltage (c-v) measurements to determine the location of the carriers are shown in Fig. 6.4. There is a clear peak for the carrier concentration in each sample. The peak position correlates well with the sample thickness indicating the localization of the carriers at the substrate-epilayer interface. A remedy to this problem is suggested in [129] by growing a low-temperature $In_{0.52}Al_{0.48}As$ layer directly on the substrate prior to the designed epilayer. This method is used for the growth of high electron mobility transistors (HEMTs) on InP subtrates [29]. In the present work the same method is used, and the dependence of parasitic carrier concentration at room temperature on the thickness of this $In_{0.52}Al_{0.48}As$ layer has been obtained from Hall measurements for a series of samples. The results, sum-

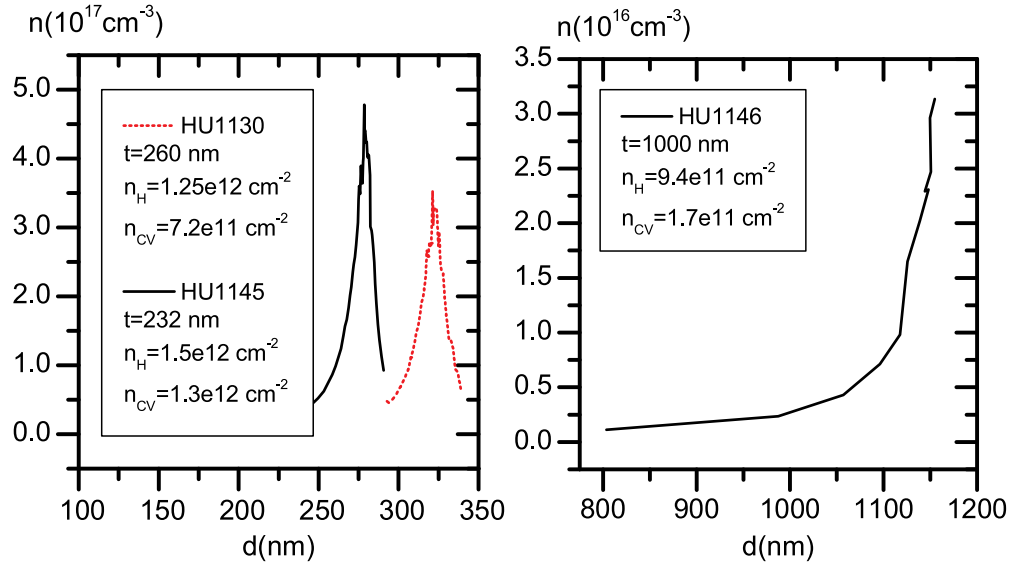

Figure 6.4: Carrier density profiles determined by c-v measurements for non-intentionally doped samples of different thickness. The total sample thickness (t), Hall sheet carrier concentration (n_H), integrated concentration by c-v (n_{CV}) is given in the figures.

marized in Fig. 6.5, allow the following conclusions.

- Without $In_{0.52}Al_{0.48}As$ interlayer (thickness of 0) carrier concentration from $3 \cdot 10^{11}$ to $2 \cdot 10^{12}$ cm^{-2} were found.
- Increasing the thickness reduces the carrier density, and at a thickness of 100 nm the density is well below 10^{-10} cm^{-2}.
- Already a thin InP layer (30 or 50 nm) between substrate and $In_{0.52}Al_{0.48}As$ restores the parasitic conductivity, which also proves that the parasitic carriers are indeed located at the substrate interface.
- Growing $In_{0.53}Ga_{0.47}As$ instead of $In_{0.52}Al_{0.48}As$ directly on the substrate also results in parasitic conductivity, with a higher mobility, which agrees with generally higher mobilities in $In_{0.53}Ga_{0.47}As$ than in InP.
- Different surface preparations before growth, such as etching or no etching etc. did not remove the parasitic layer.

Besides the substrate-epilayer interface, also InAs surface-layers (grown for AFM measurements) are a candidate for parallel conductivity. On clean,

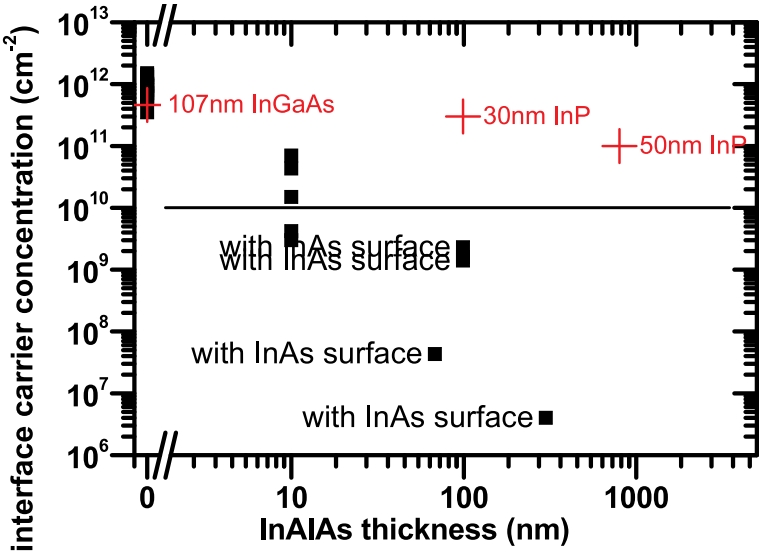

Figure 6.5: Parasitic sheet carrier density at interface between InP substrate and epilayer for different thickness of InAlAs grown directly on the substrate. Cases with a layer inserted between substrate and InAlAs are marked with red crosses and labeled with the layer thickness and material. Samples with an additional InAs surface layer are labeled "with InAs surface".

reconstructed InAs(001) surfaces carrier densities of up to $1 \cdot 10^{12}$ cm^{-2} have been measured with high-resolution electron-energy-loss spectroscopy [121], and have been attributed to intrinsic donor-like surface states. Angle-resolved photoelectron spectroscopy [123] on clean InAs(001) and InAs(111) surfaces also showed a charge accumulation layer. In contrast to these results, no conducting surface layer was found in my samples (see Fig. 6.5, labeled samples) with approx. 4 ML of InAs on the surface.

The transport samples discussed in the following sections contain a 100 nm $In_{0.52}Al_{0.48}As$ layer on the substrate, most of them have also an InAs layer for AFM on the top. As empirical result of the Hall measurements from this section, parasitic conduction at the substrate interface is effectively suppressed by growing a 100 nm thick $In_{0.52}Al_{0.48}As$ layer directly on the substrate, and the thin InAs layer on the sample surface does not contribute to conductivity. Consequently, these parallel conductivities are ruled out in the transport samples discussed in the following sections.

6.5.3 Freeze-in in InAs/InP samples

The transport behavior discussed in the subsequent sections will be based on the electron and hole mobility μ, which makes it a key parameter. Experimentally, the mobility is measured by a combination of resistivity measurement, and measurement of the carrier density using Hall measurements. The calculation of electron mobility

$$\mu = \frac{1}{en\rho} \tag{6.13}$$

depends vitally on the measured carrier density n and resistivity ρ. While the results of resistivity measurements are correct (if the experiment is properly done) the results of Hall measurement yielding the Hall carrier density n_H are somewhat obscured by the Hall scattering factor r_H (see section 4.1.3, $n = n_H \cdot r_H$), and possible effects of parallel conductivity. In contrast to the physical expectation of a decreasing carrier density with decreasing temperature (freeze-out) my measurements show a significant increase in Hall carrier density ("freeze-in") with many samples. To my knowledge, nothing has been published about the effect with this extent, which poses the question if the freeze-in be real or an artefact. This important question will be answered in the present section.

Figure 6.6 shows the temperature dependence of the measured Hall carrier density n_H for three representative n-doped samples, a modulation-doped InAs QW in an $In_{0.53}Ga_{0.47}As$ matrix (HU1521N), a n-doped 8 nm-thick InP layer (HU1543N), and a modulation-doped InAs QW in an InP matrix (HU1463N). In agreement with physical expectations, the InAs/$In_{0.53}Ga_{0.47}As$ heterostructure (HU1521N) shows freeze-out. In contrast, the doped 8 nm InP (HU1543N) and the modulation-doped InAs QW/InP (HU1463N) show an increase of Hall concentration from $2.5 \cdot 10^{11}$ cm^{-2} to $6.30 \cdot 10^{11}$ cm^{-2} and from $1.2 \cdot 10^{11}$ cm^{-2} to $4.30 \cdot 10^{11}$ cm^{-2} (lowest concentration measured to highest concentration measured). This increase has dramatic consequences for the calculated mobilities, as these concentration variations by a factor of up to 3.6 influence the calculated mobilities by the same factor. In terms of absolute change the maximum increase is $3.8 \cdot 10^{11}$ cm^{-2}. InAs/InP samples with higher carrier concentrations ($1.5 \cdot 10^{12}$ to $2 \cdot 10^{12}$ cm^{-2}) also show a freeze-in but with a maximum absolute change of $2.5 \cdot 10^{11}$ cm^{-2}. All samples mentioned here, are degenerate electron gases with the Fermi level above the conduction (sub)band. Consequently, at low temperature (e.g. the bottom temperature of the cryostat used for the shown measurements of approximately 10 K) the Hall scattering factor should be close to unity, i.e. Fermi level in conduction band, which makes these Hall concentrations most

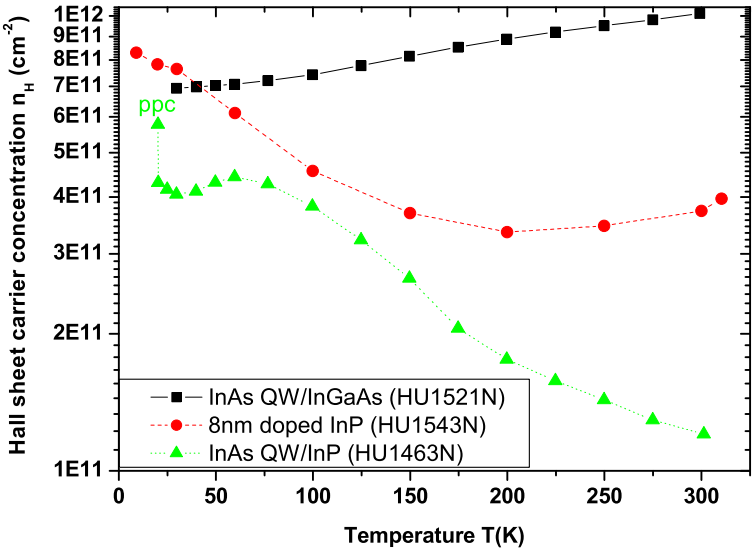

Figure 6.6: Temperature dependence of electron sheet concentration n_H measured with the Hall effect in three representative samples. For comparison, the nominal 2-dimensional doping concentrations are $5 \cdot 10^{11}$, $8 \cdot 10^{11}$, and $5 \cdot 10^{11}$ cm^{-2} for HU1521, HU1543, and HU1463 respectively.

trustworthy. The transport is quite isotropic (anisotropy of 1.2, 1.0, and 1.3 in HU1521N, HU1543N, and HU1463N). Refering to Fig. 4.1 of section 4.1.3 these facts yield a Hall scattering factor between unity (not anisotropic) and 1.45 (realistic upper limit for ionized impurity scattering). Consequently, the maximum change of Hall concentration explainable by Hall scattering factor is a relative change by a factor of 1.45. Hence, the increase in Hall carrier density by factors of up to 3.6 cannot be explained by the Hall scattering factor.

To gain more insight, the behavior of mobility with temperature is investigated (see section 6.4.1 for a brief review of the mobility's temperature dependence). Two hypotheses are compared:

1. The freeze-in be real which makes makes the measured Hall mobility μ_H the real mobility.

2. The carrier concentration is constant instead of freezing-in. (In this case, the observed freeze-in might be explained by misleading Hall concentration due to parallel conductivity.)

Temperature dependent mobilities are calculated from the measured resistivity with both hypotheses yielding the Hall mobility μ_H based on hypothesis 1

vs. a pseudo-mobility μ_{pseudo} based on hypothesis 2. The carrier density used to calculate the pseudo mobility is set the Hall carrier density measured at the lowest temperature. To compare both hypotheses, double logarithmic plots of Hall mobility and pseudo mobility for both samples showing freeze-in are given in Figure 6.7. From high to low temperatures, an initial increase

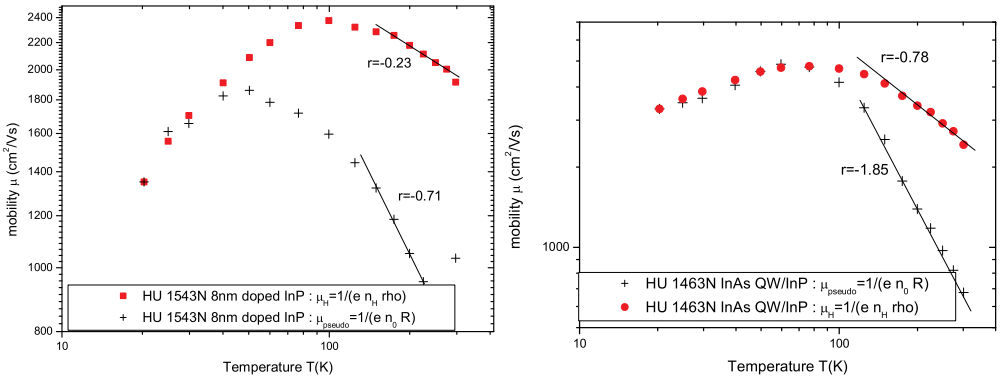

Figure 6.7: Temperature dependence of Hall mobility and pseudo mobility of doped InP sample HU1543N, and modulation-doped InAs QW sample HU1463N. The exponent r characterizes the temperature dependence of the mobility μ at high temperatures according to: $\mu \propto T^r$.

in mobility is expected for both samples, which is due to the reduction of dominant phonon scattering. In both plots the exponents r of the this temperature dependence $\mu \propto T^r$ are obtained from linear fits. The magnitude of this exponent r is larger if other scattering mechanisms (ionized impurity, remote impurity, interface roughness, alloy scattering) are less pronounced. (Reference data for n-doped InP with different doping levels such as those given in Ref. [100] show the described dependence.) The n-doped InP sample HU1543N shows an initial decrease in pseudomobility, which cannot be physically explained, whereas the Hall mobility increases as physically expected. Hence, the initial freeze-out observable in the Hall carrier density (Fig. 6.6) is real. A comparison of HU1543N with a 3-d doping concentration of $1 \cdot 10^{18}$ cm^{-3} to data of Ref. [192] on bulk doped n-InP with comparable 3-d carrier concentration of n=$7 \cdot 10^{17}$ cm^{-3} is done. In my sample, r obtained from Hall mobility ($r = -0.23$) agrees well with $r = -0.19$ extracted from the published date, whereas the pseudo mobility of my sample yields $r = -0.71$ that seems rather unrealistic.[2] Similar, the exponents r of the InAs QW are $r = -0.78$ in case of Hall mobility and $r = -1.85$ in case of pseudo

[2]Assuming a freeze-out instead of constant carrier density would lead to even larger values of r.

mobility. For comparison, the exponent r was also determined in modulation doped InAs QWs in InP (samples HU1578N, HU1604N), that show negligible freeze-in. Since the difference between Hall mobility and pseudo mobility is negligible in these reference samples, the obtained value of r can be taken as real. Additionally, these reference samples (HU1578N, HU1604N) have a higher maximum mobility than HU1463N which means that scattering other than phonon scattering is less dominant than in HU1463N. The exponents of the reference samples are $r = -0.98, -0.94$ (see Fig. 6.8). The smaller exponent of $r = -0.78$ from the Hall mobility of HU1463N is therefore consistent with the exponent from HU1578, HU1604N, whereas the value of -1.85 from the pseudomobility is unrealistic in comparison to the reference samples.

In conclusion, comparison to reference samples yields that the Hall mobility shows a plausible behavior. In contrast, the pseudo mobility, behaves unrealistically which invalidates the hypothesis of no freeze-in. Consequently, the freeze-in observed in InAs/InP samples is real, and the mobility calculated from Hall carrier density is considered the real mobility.

A survey of all samples used in this work suggests the physical origin of the freeze-in to be a reduced carrier depletion at lower temperatures. The depletion layer thickness is controlled by surface and interface properties and is strong if the carrier system is close to the surface or interface which is the case in my samples with the carrier system only 30 nm below the surface. In one sample, for example, the as grown sample showed slight freeze-in whereas the lithography-processed sample showed a slight freeze-out. This behavior is consisting with the fact that processing inherently modifies the sample surface but not the buried layers. Freeze-in has been also observed in low doped bulk GaAs samples and attributed to the same mechanism [88].

6.6 Temperature dependent transport

Temperature dependent transport measurements are the main tool to clarify the nature of lateral coupling between the nanostructures, and to determine the main scattering mechanisms.

6.6.1 n-type InAs quantum wells in InP, and doped InP

To verify the effect of nanostructures on transport, reference samples were grown. The temperature dependent mobility of these samples is given in Figure 6.8 and discussed as follows.

- Non-intentionally doped samples, discussed in section 6.5.2 are basically isolating (i.e. their conductivity is orders of magnitude lower

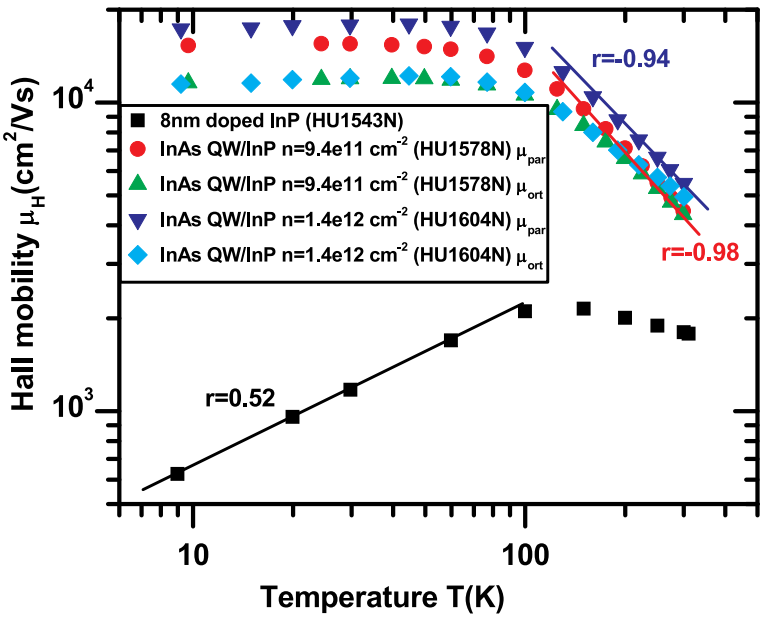

Figure 6.8: Temperature dependence of Hall mobility of 8 nm doped InP (HU1543N) and modulation-doped InAs QWs in InP (HU1578N, HU1604N). For the QW mobilities along the $[\bar{1}10]$ and [110] direction are denoted by μ_{par} and μ_{ort}. The exponent r characterizes the temperature dependence of the mobility μ according to: $\mu \propto T^r$.

than the conductivity of intentionally doped samples) which allows to exclude parasitic parallel conductivity effects.

- As next step, a typical transport sample was grown but without buried InAs layer, which results in a capped, n-doped, 8 nm-thick InP layer (HU1543N). This sample shows a typical mobility characteristics for highly doped InP in good agreement with published data [192] as discussed in section 6.5.3. From high to low temperatures (310 K to 9 K) the mobility increases slightly ($r \approx -0.2$) due to phonon scattering but decreases at lower temperatures with ($r \approx 0.5$) due to ionized impurity scattering of the electrons at the ionized donors (Si atoms on group III sites). This behavior is qualitatively reproduced in Fig. 6.3, left. At 9 K the mean free path $l_e = 9$ nm, which agrees quite well with the average distance of 10 nm between the donors. The mobility of this sample grown on nominal N substrates, and the same structure grown on vicinal A, B, and C substrates (HU1543O, HU1543P, and HU1543Q) are completely isotropic (see Fig. 6.9). This confirms that the transport anisotropy observed in other samples is not due to the

doping layer.

- The insertion of a nominally flat (2D) InAs layer underneath the doped InP separated by an undoped InP spacer layer results in a modulation-doped InAs QW. The spatial separation of donors (in the InP) and electron gas (in the InAs) leads to a reduction of ionized impurity scattering to the weaker remote impurity scattering. As a result, the slope r of increasing mobility at high temperatures is high (about 0.9 to 1.0), and no reduction of mobility occurs at low temperatures (compare to Fig. 6.3, left). Depending on sample and transport direction, the mobility saturates with decreasing temperatures in the range of 10000 to 20000 cm^2/Vs. The mobility limiting scattering is remote impurity scattering and interface roughness scattering. The slight transport anisotropy (see Fig. 6.9) suggests a slightly anisotropic interface roughness which, however, does not lead to qualitatively different mobility characteristics for both transport directions. The tendency of vicinal substrates (particularly B surfaces) to form rougher layers leads to a higher anisotropy of HU1604P than HU1604N. Anisotropic interface roughness scattering is theoretically treated in [177, 178].

6.6.2 n-type InAs quantum wires in InP

Three quantum-wire transport samples were grown with the same nominal InAs layer morphology and thickness. The nominal parameters of the modulation doping, i.e. remote donor concentration and spacer thickness, were varied as shown in Table 6.3. These parameters result in different strengths of remote impurity scattering ranging from the strongest scattering for sample HU1547 (higher ionized donor concentration) to the weakest scattering in sample HU1662 (larger distance from electron gas to ionized donors).

The transport anisotropy for different temperatures is given in Fig. 6.10. In contrast to the QW samples, a marked transport anisotropy is present in the QWr samples, which is intuitively expected from their elongated shape. The high-mobility direction is parallel to the QWrs (along $[\bar{1}10]$). The increasing transport anisotropy with decreasing temperature suggests a thermally activated coupling between the nanostructures (thermionic emission). A similar conclusion was drawn in [122] for a corrugated AlGaAs/GaAs heterointerface, and an lateral potential modulation of few meV for electrons was determined.

A detailed analysis of the temperature dependent mobilities of the principal transport directions is performed to test this assumption. The mobilities

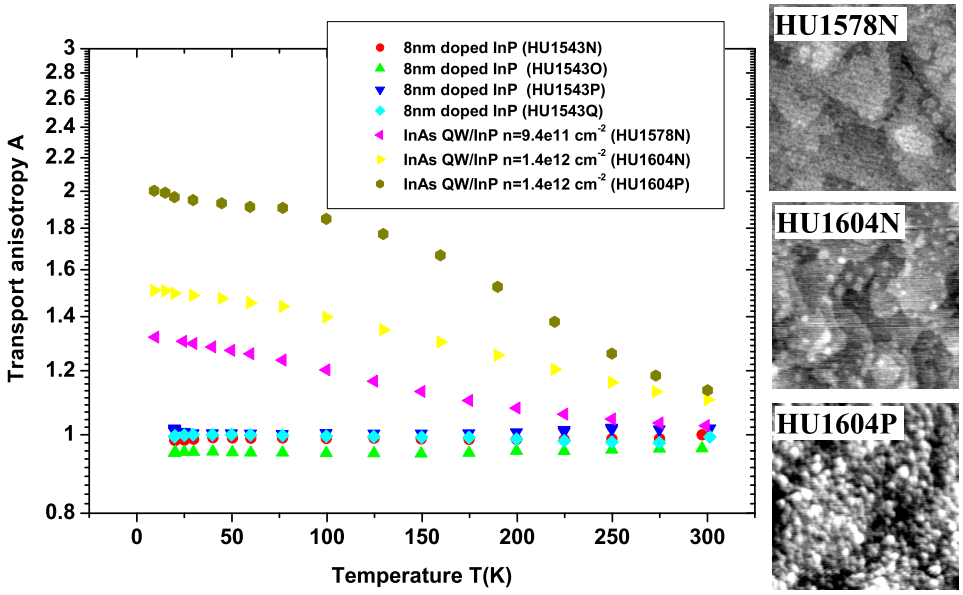

Figure 6.9: **Left:** Temperature dependence of transport anisotropy of 8nm doped InP (HU1543N,O,P,Q) and modulation-doped InAs QWs in InP (HU1578N, HU1604N,P) grown on nominal substrates (N), and vicinal substrates (O,P,Q). **Right:** Morphology of quantum well layers. AFM images, size 1000 nm × 1000 nm, black/white scale 1.2 nm, $[\bar{1}10]$ is vertical direction.

for different temperatures of modulation-doped quantum wire samples are given in Fig. 6.11. As reference, comparable quantum well samples, which differ only in the morphology of the InAs layer, are added. The following observations are made.

1. The mobility orthogonal to the quantum wires (orthogonal mobility) shows the same qualitative behavior for all three QWr samples. At room temperature, the orthogonal mobility is approximately a third the mobility parallel to the quantum wires (parallel mobility) corresponding to a transport anisotropy of 3 (see Fig. 6.10).

2. With decreasing temperature, the orthogonal mobility decreases to only approximately 2/3 its room temperature value at 20 K. This almost temperature-independent characteristics would correspond to an exponent of $r = 0.1$. It does not depend on the varying parameters of modulation doping either. These observations demonstrate that the transport perpendicular to the quantum wires is neither limited by phonon scattering nor by remote impurity scattering. At 10 K the orthogonal mobility is roughly 1000 cm^2/Vs with mean free paths of

Table 6.3: Modulation doping parameters and measured carrier density n at T=10 K of n-type QWr, QD, and QW samples. The parameters are: donor concentration N_d of the 8 nm InP:Si layer, and thickness d of the InP spacer between InAs and doped InP (compare Fig. 6.2 left). Deviations from the standard parameters are marked with bold numbers. Carrier densities in parenthesis were measured after illumination (persistent photoconductivity, ppc).

sample	N_d (cm^-3)	d (nm)	substrate: nanostructure	n (10^{11} cm^{-2})
HU1578N	$1.0 \cdot 10^{18}$	5	N:QW	9.4
HU1604N	$1.0 \cdot 10^{18}$	5	N:QW	14
HU1468O	$1.0 \cdot 10^{18}$	5	A:QWr	9.4
HU1547N	$\mathbf{1.7 \cdot 10^{18}}$	5	N:QWr	15
HU1662N	$1.0 \cdot 10^{18}$	**10**	N:QWr	3.8(6.3)
HU1468P	$1.0 \cdot 10^{18}$	5	P:QD	6.2
HU1547P	$\mathbf{1.7 \cdot 10^{18}}$	5	B:QD	20
HU1662P	$1.0 \cdot 10^{18}$	**10**	B:QD	3.1(4.9)

l_e = 12 to 21 nm.

3. The parallel mobility shows the same qualitative behavior for all three QWr samples and coincides with the behavior of the QW samples. From high to low temperatures it increases drastically, and saturates at about 50 K. The further cooling down leads to a slight degradation of the mobility in some samples. The quantitative details change with the variation of modulation-doping parameters, which shows that the mobility-limiting mechanism is remote impurity scattering.

4. The mobility of HU1468O, grown with the same modulation-doping parameters as the QW references, is in quantitative agreement with the QW references. The mobility increases to a maximum of 3.4 times the room temperature value.

5. A thicker spacer layer (HU1662), that increases the spatial separation of ionized donors and electron gas, results in a higher maximum mobility (5.4× the room temperature value), and an exponent of $r = -1.1$ at high temperatures. The mobility degradation below 50 K is due to a reduction of the carrier density by trapping. Retrieving these carriers at 8 K by a short illumination, significantly increases the mobility to a value of approximately 35000 cm^2/Vs, which results in a maximum

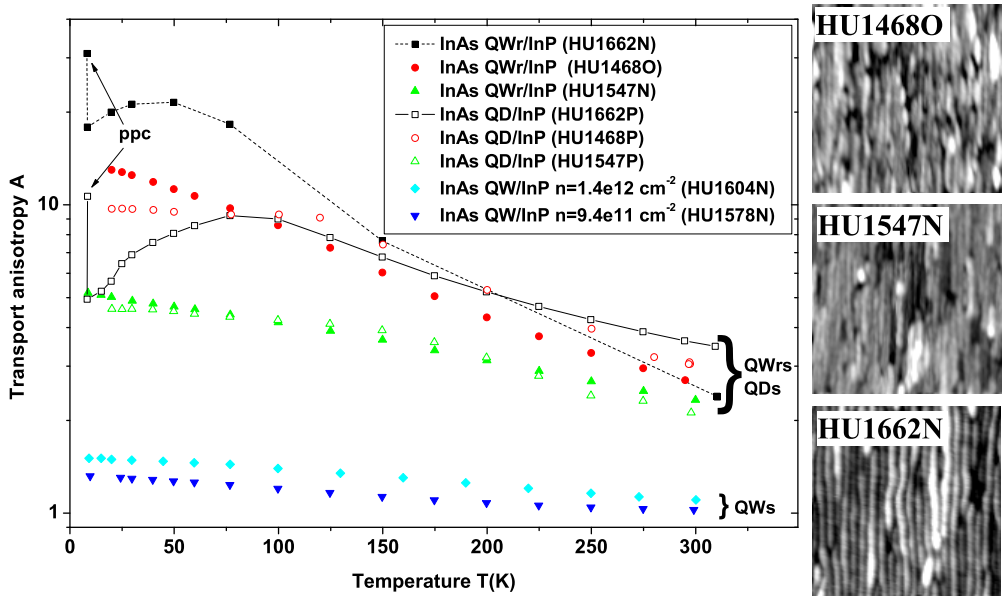

Figure 6.10: **Left:** Temperature dependence of transport anisotropy in n-type modulation-doped InAs/InP quantum wires (solid symbols), quantum dots (open symbols) and quantum wells (solid symbols at bottom). The label "ppc" denotes datapoints measured after illumination to increase the carrier density. Also note the decreasing anisotropy at these curves due to carrier trapping which reduces the carrier density. **Right:** Morphology of quantum wire layers. AFM images, size 500 nm × 500 nm, black/white scale 1.4, 1.0, 2.0 nm (from top to bottom), $[\bar{1}10]$ is vertical direction.

anisotropy of 31. Interpolation to the mobility at 50 K suggests no mobility degradation at decreasing temperature if the carrier density would remain constant (without trapping).

6. A higher donor concentration (HU1547) results in a significantly lower maximum mobility of only 1.6× the room temperature value. The stronger degradation of mobility below 50 K suggests a situation at the transition from phonon and remote impurity scattering to phonon and ionized impurity scattering (compare Fig. 6.3, left).

7. At the lowest temperature (9 to 20 K) the mean free path of the QW samples in the parallel direction is 210 and 270 nm. In comparison, l_e = 240 nm in the QWr sample with the same modulation-doping parameters (HU1468O), which agrees well with that of the QW samples. Modification of these parameters results in a lower l_e of 102 nm (HU1547N, higher donor concentration), or higher l_e of 210/450 nm

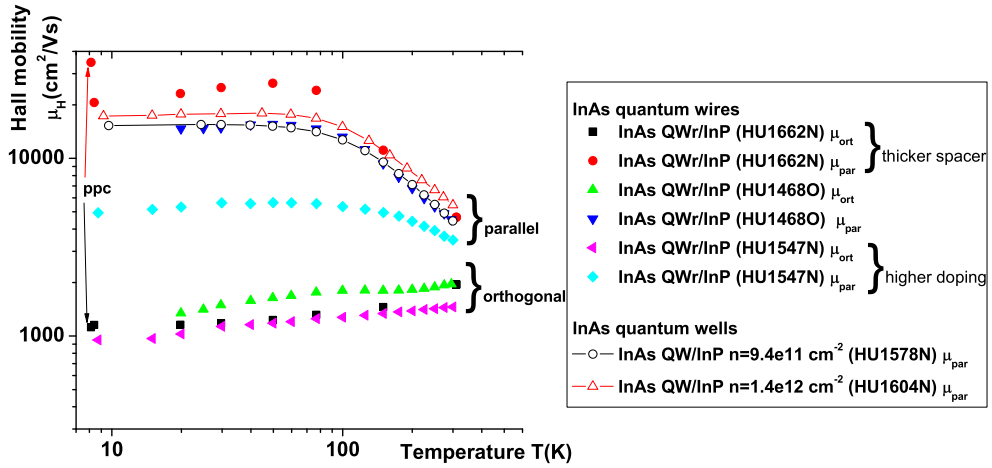

Figure 6.11: Temperature dependence of Hall mobility in the [$\bar{1}$10]-direction (parallel) and [110]-direction (orthogonal) of quantum wire samples (solid symbols). Mobility of quantum wells (open symbols and lines) is given as reference.

(HU1662N thicker spacer, before/after illumination).

These observations allow the following conclusions.

1. The transport in my structures is in the diffusive regime as the mean free path is much lower than the sample dimension (no ballistic transport) and $k_F l_e > 1/(2\pi)$ with $k_F \simeq 0.25$/nm (no hopping transport according to Ioffe-Regel criterion Eq. 6.7).

2. The increasing transport anisotropy with decreasing temperature is an effect of the reduction of phonon-scattering in the high mobility direction. This behavior is opposite to the observation in GaAs/AlGaAs heterojunctions on periodic multiatomic step arrays of Ref. [120], in which the change of anisotropy is mainly due to decreasing mobility in the low mobility direction. In those heterojunctions, an activation energy of 5 meV for transport across the steps has been observed. In contrast, Arrhenius plots of the orthogonal mobility of my samples yield a barrier height of less than 0.6 meV, which is much lower than the results for the corrugated AlGaAs/GaAs heterointerface from Refs. [122, 120].

3. In the parallel direction, comparison of the mean free path to QW samples and the dependence on the modulation-doping parameters yields that the mobility limiting mechanism is remote impurity scattering. The mean free path of 450 nm in the sample with weakest remote impurity scattering is close to the average wire length of $\approx$ 600 nm in

this sample. Hence, the transport within the wires is quasi ballistic. In the context of coupled quantum wires, this corresponds to a very efficient longitudinal wire-wire coupling. Further optimization of the modulation-doping parameters and the comparison to quantum well samples of same nominal thickness would be required to test if there is a mobility limit due to longitudinal coupling. This comparison may also help to test the predicted higher mobility in wires compared to quantum wells due to reduced backscattering [146].

4. In the orthogonal direction, the mean free path is less or equal the average lateral wire-wire spacing, which is much smaller than the mean free path in QW samples. The transport is limited due to the strong lateral wire-wire scattering, which corresponds to a weak lateral coupling in the context of coupled quantum wires. The coupling, however, is not thermally activated because the empirically determined barrier of less than 0.6 meV is too small to explain the low mobility at room temperature ($kT = 25$ meV), and is much less than the estimated barrier $\Phi_B \simeq 200$ meV.

5. In the context of anisotropic two-dimensional systems, the scattering mechanisms for the parallel mobility (phonon scattering, remote impurity scattering) are isotropic and, hence, also effective for the orthogonal mobility. Therefore, using Eq. 6.12 the mobility contribution that acts exclusively in the orthogonal direction (μ_{lat}) can be extracted as

$$\frac{1}{\mu_{lat}} = \frac{1}{\mu_{ort}} - \frac{1}{\mu_{par}} \ . \tag{6.14}$$

Figure 6.12 shows the extracted μ_{lat} in comparison to the total mobility μ_{ort} in the orthogonal direction. The similarity to the calculated temperature dependence of interface roughness scattering in Ref. [148] having lateral fluctuation size (70 to 100 Å) similar to mine (see section 6.8) allows me to tentatively assume interface roughness scattering to be dominating the orthogonal mobility.

6.6.3 n-type InAs quantum dots in InP

Similar to the QWr samples, the QD samples, also show pronounced transport anisotropies up to 10 (see Fig. 6.10) with the same high-mobility direction. (In layers containing self-assembled InAs QDs grown on GaAs lower transport anisotropies between 1 and 2 have been observed [89, 90]. These anisotropies have been attributed to the formation of dot-chains forming

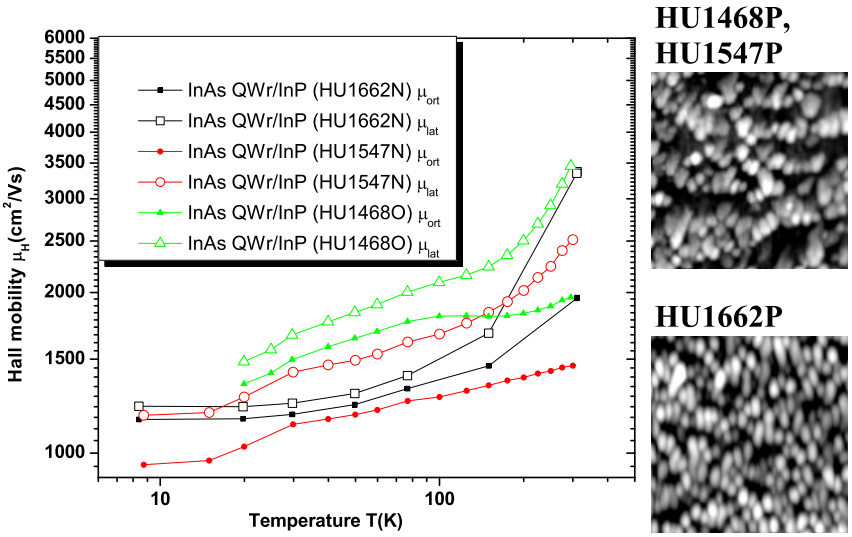

Figure 6.12: **Left:** Temperature dependence of Hall mobility contribution that acts exclusively in the [110]-direction (orthogonal) of quantum wire samples (large open symbols). The total orthogonal mobility is given for comparison (small solid symbols). **Right:** Morphology of quantum dot layers. AFM images, size 500 nm × 500 nm, black/white scale 5 nm, [$\bar{1}$10] is vertical direction.

along steps, and in terms of dislocations.) The temperature dependence of mobility as shown in Fig. 6.13 has striking similarities to that of the quantum wire samples. The absolute mobilities, however, are lower (around 3000 cm^2/Vs parallel, 300 cm^2/Vs orthogonal) than in the QWr samples. Also the mobility in the high mobility direction ("parallel") decreases more pronounced with decreasing temperature after its maximum. Comparison to samples with same modulation doping parameters but a quantum wire morphology (same sample number) demonstrates that the quantum dot morphology limits the parallel mobility. The mobilities are still large enough to be described by diffusive transport. Hence, interface roughness scattering is assumed the mobility-limiting scattering for both transport directions in the QD samples. Thermal activation seems to play no role for the same reasons as in the QWr samples.

Given the random spatial distribution of almost isotropic appearing QDs the transport anisotropy cannot be explained with the apparent InAs morphology. The high mobility direction is the same as for the quantum wires, suggesting the same underlying physics. In terms of coupled nanostructures, a stronger coupling in the parallel direction than in the orthogonal direction should be responsible for the anisotropic transport as will be discussed in sec-

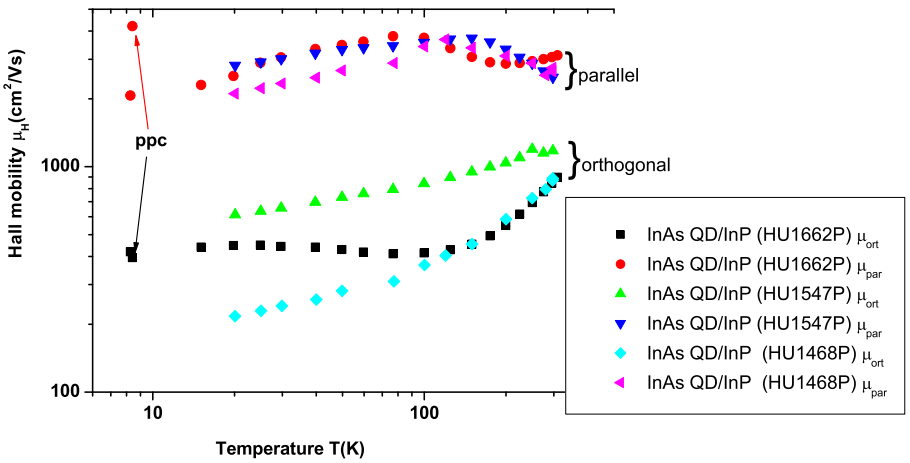

Figure 6.13: Temperature dependence of Hall mobility in the [$\bar{1}$10]-direction (parallel) and [110]-direction (orthogonal) of quantum dot samples.

tion 6.7. Plan view TEM images (out of the scope of this work) could give more detailed information of the shape of the covered dots, which contribute to transport.

6.6.4 n-type InAs nanostructures in $In_{0.53}Ga_{0.47}As$

A variation of the electronic properties by keeping the same basic structural properties was done by growing modulation-doped quantum wires in an $In_{0.53}Ga_{0.47}As$ matrix. These wires are structurally similar to the wires in an InP matrix. Electronically, however, the carrier confinement is reduced due to the smaller conduction band offset of 0.25 eV compared to 0.5 eV in InP. In addition, the smaller effective mass in $In_{0.53}Ga_{0.47}As$ results in a weaker localization of the carriers in the InAs, and in higher total mobilities. The estimation of effective barrier $\Phi_B \simeq 15$ meV between adjacent InAs nanostructures suggests much stronger coupling than in an InP matrix. The temperature dependent principal mobilities and corresponding transport anisotropy of InAs QW and QWr in $In_{0.53}Ga_{0.47}As$ are shown in Fig. 6.14. The characteristics of the InAs QW in $In_{0.53}Ga_{0.47}As$ is qualitatively similar to InAs QW in InP. There is also a small transport anisotropy which may be attributed to anisotropic interface roughness scattering. The mobilities, however are higher than in the InAs/InP structures. In contrast to InAs/InP, the mobilities parallel and orthogonal to InAs QWrs in $In_{0.53}Ga_{0.47}As$ show qualitatively the same behavior and the transport anisotropy is only in the range of 2. It is concluded that ΔE_C of InAs to $In_{0.53}Ga_{0.47}As$ does not provide sufficient confinement of the electrons to the InAs wires.

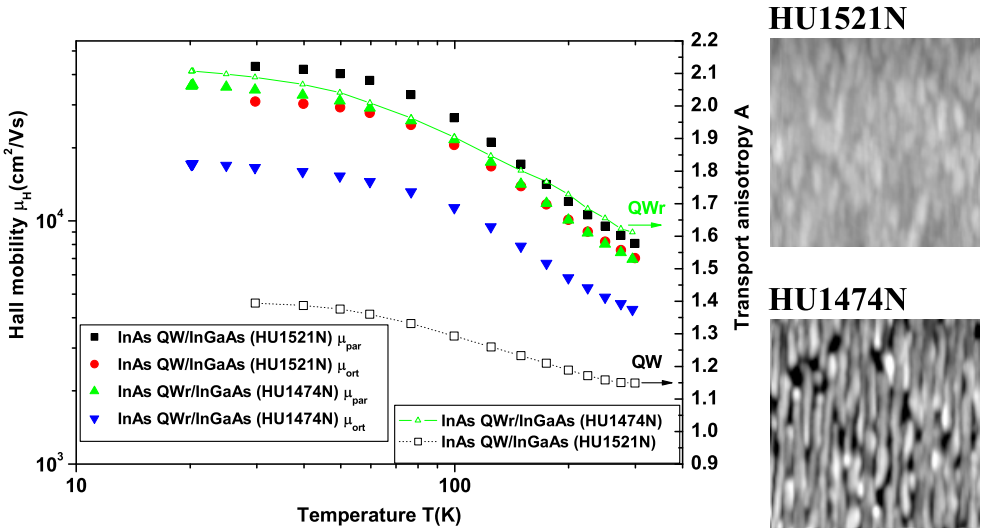

Figure 6.14: **Left:** Temperature dependence of Hall mobility and transport anisotropy in n-type modulation-doped InAs/$In_{0.53}Ga_{0.47}As$ quantum well and quantum wires. **Right:** Morphology of InAs/InGaAs quantum well and quantum dot layers. AFM images, size 500 nm × 500 nm, black/white scale 2.5 nm, $[\bar{1}10]$ is vertical direction.

6.6.5 p-type InAs nanostructures in InP

The transport of holes in coupled InAs/InP nanostructures, on the other hand, allows to enter the opposite regime of a very strong confinement. Even though the band discontinuity for holes is lower than the for electrons, the net confinement for holes is larger than for electrons (see table 6.2) due to their significantly higher effective mass (by a maximum factor of 5). In particular, the higher effective mass leads to a generally stronger localization of the holes in comparison to electrons as the tunneling probability and the wavefunction size (e.g. Bohr radius) decrease with increasing effective mass. Since the mobility is inversely proportional to the effective mass (see Eq. 6.3) lower mobilities than in n-doped samples are expected in the p-doped samples (if same scattering times are assumed).

P-type modulation-doped InAs/InP nanostructures were grown and investigated. The nominal doping was in the range of 1 to $2 \cdot 10^{12}$ cm^{-2}. Hall measurements yielded consistent carrier density results for the QW sample (HU1661N, p_H varying between 1.25 and $1.38 \cdot 10^{12}$ cm^{-2}). The other samples, however, did not allow to measure the carrier density in the entire temperature range. Assuming the same qualitative behavior as the QW sample, i.e. mainly constant carrier density, a pseudo-mobility was calculated based

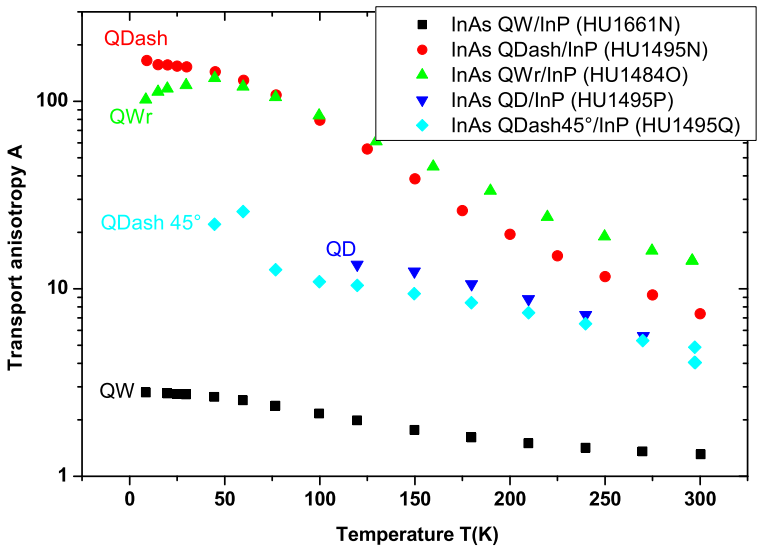

Figure 6.15: Temperature dependence of transport anisotropy in p-doped InAs nanostructures in InP.

on the measured carrier density at 275 K. The temperature dependent principle mobilities are given in Fig. 6.16 with corresponding transport anisotropies in Fig. 6.15. These are discussed as follows.

- Qualitatively, the mobilities show the same characteristics as the electron mobilities. An analysis of the quantitative details yields the following results.

- The p-type quantum well sample HU1661N was grown to have the same structure as the n-type QW sample HU1604N. It shows transport anisotropies (attributed to anisotropic interface roughness scattering) from 1.3 to 2.8 (300 K to 9 K) which is larger than 1.1 to 1.5 in the n-type QW sample. This larger transport anisotropy indicates stronger confinement of holes to potential fluctuations caused by interface roughness.

- Along this trend, the transport anisotropy of the QWr samples is significantly larger for holes than for electrons. At low temperatures, values in excess of 100 are obtained. At room temperature, already transport anisotropies of 7, and 14 are present in the QWr and QDash containing samples.

- The maximum parallel mobility of HU1661N (QW) and HU1495N (QDash) in the range of 2000 to 4000 cm^2/Vs is in the range of 1/5

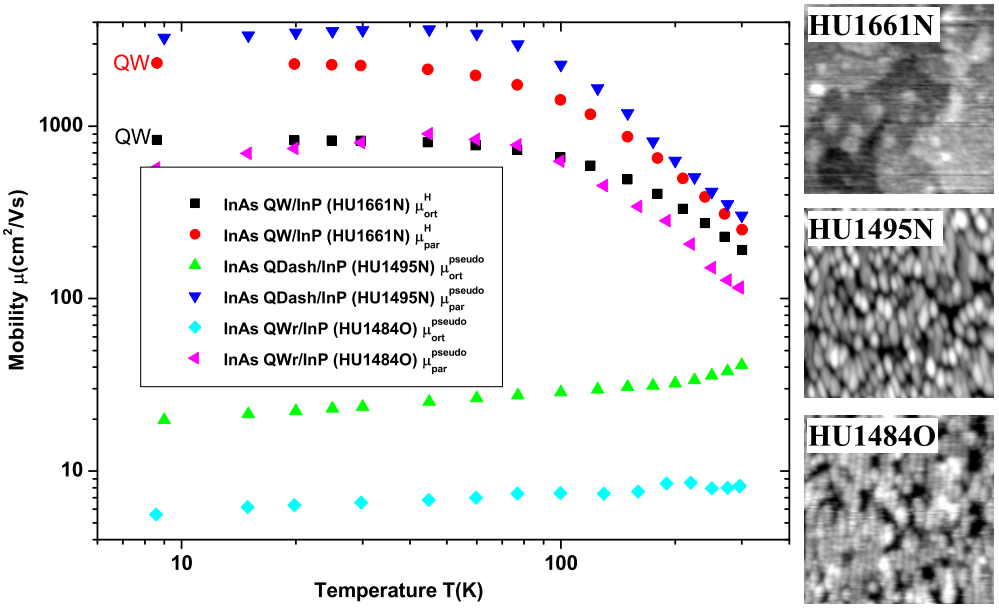

Figure 6.16: **Left:** Temperature dependence of mobility in the [$\bar{1}$10]-direction (parallel) and [110]-direction (orthogonal) of p-type InAs quantum well, -dash, and -wire samples. **Right:** Morphology of p-type InAs/InP quantum well, -dash, and -wire layers. AFM images, size 500 nm × 500 nm, black/white scale 1.2, 5.0, 2.5 nm (from top to bottom), [$\bar{1}$10] is vertical direction.

the maximum mobility of comparable n-doped samples and can thus be explained by the higher effective mass but comparable scattering times τ. The relative mobility increase with decreasing temperature is higher (by up to 12 times) than that for electrons. The calculated mean free paths at T=9 K in the parallel direction of $l_e = 45; 70; 3.2$ nm for HU1661N (QW), HU1495N (QDash), and HU1484O (QWr), respectively, are consistent with diffusive transport.

- On the other hand, the calculated mean free paths of the orthogonal direction of $l_e = 16; 0.4; 0.08$ nm for the same samples suggests diffusive transport only in the QW sample. According to Eq. 6.7, the hole wavefunctions of the other samples are localized and transport along the orthogonal direction is in the hopping regime. This assumption is consistent with the resistivities of $\rho_{ort} \approx 80$ kΩ in HU1495N and in particular $\rho_{ort} \approx 1$ MΩ in HU1484O, which both are above the maximum metallic resistivity of 40 kΩ. Furthermore, the hopping can explain that the Hall measurements yield strongly fluctuating results

because the orthogonal transport can be regarded as a percolation with percolation paths that cannot shift easily due to the magnetic field. More details on the ortogonal hopping conductivity are discussed in section 6.6.6.

- In the context of coupled nanostructures, the longitudinal coupling is very high, an effect in particular visible with the structurally short quantum dashes of HU1495N. Laterally, however, the QWr can be considered quasi decoupled.

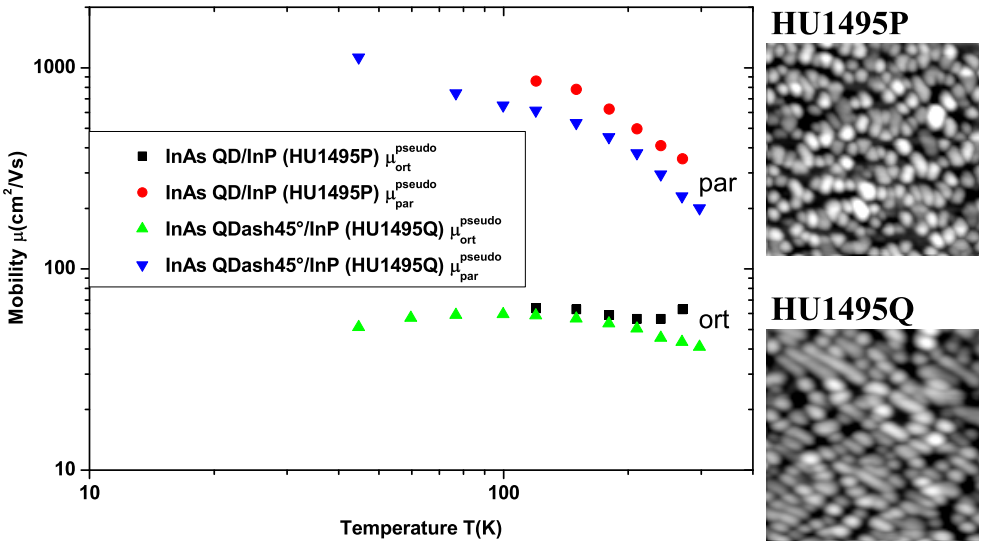

Figure 6.17: **Left:** Temperature dependence of Hall mobility in the [$\bar{1}$10]-direction (parallel) and [110]-direction (orthogonal) of p-type InAs quantum dash, and -dot samples. **Right:** Morphology of p-type InAs/InP quantum dash, and -dot layers. AFM images, size 500 nm × 500 nm, black/white scale 10.0, 5.0 nm (from top to bottom), [$\bar{1}$10] is vertical direction.

The p-type quantum dots show also similar behavior to the n-type quantum dots. The parallel mobility, however, is lower (at low temperatures typically 900 cm^2/Vs). Similarly to the n-type samples the parallel direction has a higher mobility, but with lower anisotropy than the QWr samples.

6.6.6 Lateral hopping conductivity

In the hopping regime, the mobility has no physical meaning. Instead, the conductivity or resistivity should be discussed. Nevertheless, the pseudo-mobility is discussed to have a direct comparison to other samples and to the

parallel transport direction. Due to the assumed constant carrier density, the mobility is proportional to the conductivity which makes the discussion of mobility equivalent to the discussion of conductivity. The temperature dependence of the orthogonal hole mobility shows the same qualitative behavior as the corresponding electron mobility. From 300 K to 9 K, it decreases only to a value between 1/2 and 2/3 its 300 K-value. The hole mobility, however, is approximately one to two orders of magnitude lower than the electron mobility which is beyond the effect of the effective mass in Eq. 6.3. At 10 K the orthogonal mobility ranges from 5 to 20 cm^2/Vs. Arrhenius plots of the orthogonal conductivity in Fig. 6.18 show an activation energy ΔE (see Eq. 6.8) below 0.5 meV, as well as best fits of the variable-range-hopping model (see Eq. 6.10) to my data. The non-agreement of these fits to the data is considered to show that neither of the processes (thermally activated hopping or variable range hopping) can explains the conductivity satisfyingly. Due to the high barrier, hopping via activation into extended states (with $\Phi_B \geq 180$ meV, see Tab. 6.2) is unlikely, either. The small relative change in conductivity with temperature is in marked contrast to published works describing hopping conductivities that change by orders of magnitude [200, 52, 165]. Consequently, nearest neighbor hopping (Eq. 6.9) is considered the dominant hopping path. One reason for the small temperature dependence may be the formation of bands for the the parallel transport. Adjacent bands should have an energy overlap (due to their band width) resulting in a disappearing ΔE. The conductivity only depends on the lateral overlap R/a^* of adjacent bands.

6.6.7 Principle directions of transport

Electron transport

The principle conductivity axes of the quantum wire samples HU1547N were determined with a processed sample. Fig. 4.2 in section 4.2.2 shows the results. Within a precision of 1° the principal axes are aligned to the <110> crystallographic directions, i.e. to the direction of the quantum wires, with the high-mobility direction [$\bar{1}$10]. The processed quantum dot sample HU1547P showed leakage problems (either due to too shallow mesa etch or through buffer layer) at elevated temperatures. Consistent results could, however, be obtained with negligible leakage at T=20 K and below. At these temperatures, alpha was below 0.4° with the high-mobility direction [$\bar{1}$10]. Thus, the principal axes of conductivity are aligned to the <110> directions for the n-type QWr samples, and for QD samples grown on B-substrate.

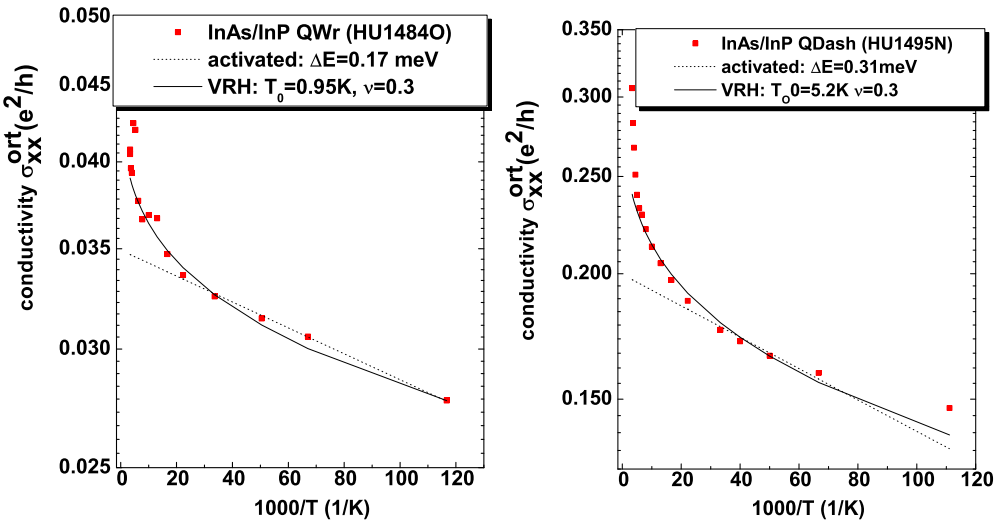

Figure 6.18: Arrhenius plots of orthogonal hopping conductivity of p-doped QDash and QWr samples. Activated vs. variable range hopping transport.

Hole transport

The angle α between principal axes of conductivity and <110> directions was determined as a function of temperature for p-type modulation-doped InAs nanostructures in InP. The angle α of quantum dashes (sample HU1495N, on N surface substrate), dots (HU1495P, on B surface substrate), and dashes oriented 45° towards <110> (HU1495Q, on C surface substrate) is shown in Fig. 6.19. Similar to the n-type samples, the principle axes for the nanostructures on N, and B substrate are aligned (within 1°) to the <110> directions in the entire temperature range. In constrast, the 45° quantum dashes show a principle axis rotated by (13+/-2)° to the <110> direction. The angle of alpha between 0° and 45° demonstrates that the transport is not only influenced by the direction of the nanostructures (45°, see AFM image Fig. 6.17).

6.6.8 Conclusions from temperature dependent mobility

- In the samples containing InAs quantum wires and quantum dots, a high transport anisotropy is observed. The principal axes of transport are aligned with the <110> directions, the high-mobility direction being [$\bar{1}$10]. The transport anisotropy is attributed to transport in coupled nanostructures and not in the wetting layer.

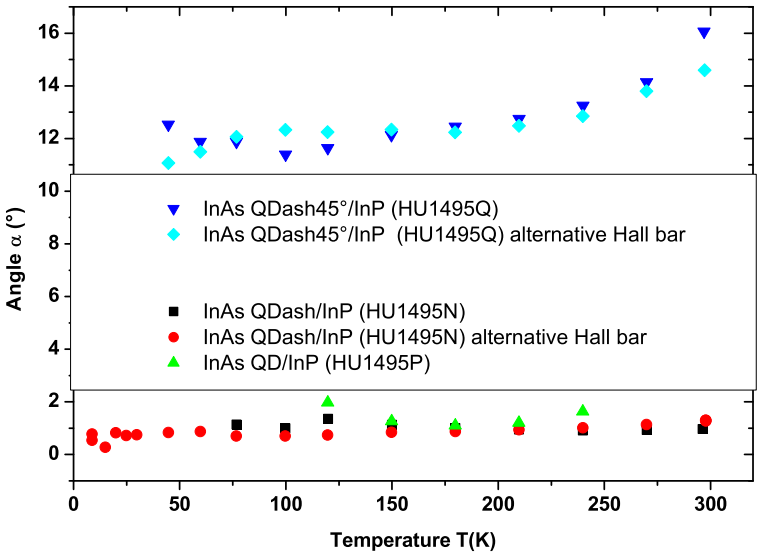

Figure 6.19: Angle of principal directions of conductivity with respect to the parallel wire direction in p-type InAs nanostructures.

- The lateral coupling between the nanostructures is due to tunneling and not thermally activated.

- A comparison of the mobilities in the parallel direction of quantum wires to that of quantum wells shows that the transport of electrons and holes in parallel direction is almost not impeded during longitudinal wire-wire coupling. The elastic scattering lengths indicate quasi ballistic transport inside the quantum wires. The high parallel mobilities in the quantum wire samples suggest strong longitudinal wire-wire coupling.

- The transport orthogonal to the n-type quantum wires shows a low mobility which is compatible with interface-roughness scattering. In the coupled nanostructure picture this low orthogonal mobility corresponds to a weak lateral coupling. The transport in the orthogonal direction of p-type samples is in the hopping regime which indicates laterally almost decoupled p-type quantum wires.

- Thus transport regimes from quasi ballistic inside n-type QWr, over diffusive, to hopping in p-type samples are observed in InAs/InP quantum wires. In p-type samples the transport in the parallel direction is diffusive whereas the transport in the orthogonal direction is of hopping type.

- In terms of effective dimensionalities, the transport is 2D in InAs/InGaAs nanostructures due to almost vanishing lateral confinement, inbetween 1D and 2D in n-type InAs/InP, quasi 1D in p-type InAs QWr/QDash/InP.

6.7 Anisotropic tunneling-mediated coupling

The high transport anisotropy ($A > 10$) with almost isotropic structures (QD, QDash, length/width≤ 2) cannot be only explained by the larger number of tunneling barriers for transport in the orthogonal direction compared to the parallel direction. It rather suggests an additional difference between longitudinal and lateral coupling strengths. An empirical model of coupled nanostructures as shown in Fig. 6.20 is utilized to quantify the longitudinal and lateral coupling strengths.

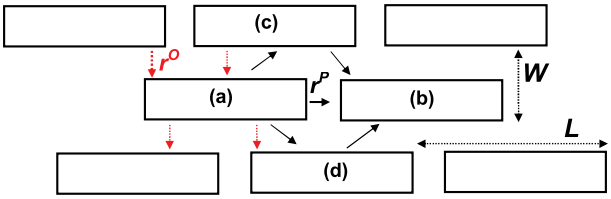

Figure 6.20: Empirical model of transport in coupled nanostructures based on nearest neighbor coupling. Nanostructures of average length L and width W are considered. (The length and width in this model include the spacing between the nanostructures, which is small compared to the nanostructure dimensions.) The barriers between adjacent wires in the parallel (orthogonal) direction are modeled by longitudinal (lateral) coupling resistivities (in Ωmm) $r^P(r^O)$. Red, dotted arrows denote the coupling in case of orthogonal transport. Black, solid arrows denote the coupling in case of parallel transport. The diagonal black arrows represent the orthogonal coupling that also contributes to parallel transport by connecting the two wires (a) and (b) through percolation via their neighboring wires (c) and (d).

Coupling of nanostructures with isotropic resistivity is assumed to lead to the measured transport anisotropy. Within this model, the principal resistivities (resistance of a square with arbitrary edge length S) in the parallel (orthogonal) direction $\rho^{par}(\rho^{ort})$ consists of a chain of S/L (S/W) wires in the parallel (orthogonal) direction , and S/W (S/L) of these chains in parallel:

$$\rho^{par} = \frac{W}{L}R^P + \rho^0,\ \rho^{ort} = \frac{L}{W}R^O + \rho^0 \tag{6.15}$$

with nanostructure length(width) $L(W)$, effective resistance for longitudinal(lateral) coupling $R^P(R^O)$ between adjacent nanostructures, and resistivity for transport within the nanostructure ρ^0. Thus, the coupling contribution to the principal resistivities is separated from the residual resistivity ρ^0 which is the resistivity of a comparable quantum well, that takes care of the parasitic scattering mechanisms such as remote impurity scattering. Within the model given in Fig. 6.20, the effective coupling resistances are

$$\begin{aligned} R^O &= \frac{r^O}{L} \\ R^P &= \left[\frac{W}{r^P} + G^{perc}_{avg}\right]^{-1} \end{aligned} \tag{6.16}$$

since the coupling resistance decreases with boundary length, and R^P is the effective coupling due to direct wire-wire coupling process ((a)→(b), first term) which is acting in parallel to the percolation through the adjacent wires ((a)→(c)→(b), (a)→(d)→(b), second term, given as conductance G^{perc}, i.e. inverse of the resistance).

The second (percolation) term G^{perc} in Eq. 6.16 is calculated as follows: Let the common boundary length of wire (a) and (c) be L_{ac}, then that of (c) and (b) is $L - L_{ac}$. The associated coupling resistance to couple from wire (a) into (c) is r^O/L_{ac}, and that to from couple from (c) into (b) is $r^O/(L - L_{ac})$. The total coupling resistance for the percolation path (a)→(c)→(b) is the sum of these two. The same considerations are done for (a)→(d)→(b) with the common boundary of (a) and (d), L_{ad}. Since both percolation paths, (a)→(c)→(b) and (a)→(d)→(b) act in parallel, their reciprocal total coupling resistances (the total coupling conductance) add. Hence, the total coupling conductance due to both percolation paths G^{perc} is:

$$G^{perc}(L_{ac}, L_{ad}) = \left[\frac{r^O}{L_{ac}} + \frac{r^O}{L - L_{ac}}\right]^{-1} + \left[\frac{r^O}{L_{ad}} + \frac{r^O}{L - L_{ad}}\right]^{-1} . \tag{6.17}$$

The average G^{perc} is now calculated by averaging $G^{perc}(L_{ac}, L_{ad})$ over the evenly distributed values L_{ac} and L_{ad} ranging from 0 to L and obtain:

$$G^{perc}_{avg} = \frac{\int_0^L \int_0^L G^{perc}(L_{ac}, L_{ad}) dL_{ac} dL_{ad}}{\int_0^L dL_{ac} \int_0^L dL_{ad}} = \frac{L}{3r^O} , \tag{6.18}$$

which can be readily put into Eq. 6.16.

The measured principal resistivities are used to estimate the coupling resistances. From Eq. 6.15 follows

$$\begin{aligned} \rho^{ort} \geq \frac{L}{W} R^O &\geq \rho^{ort} - \rho^{par} \\ \frac{W}{L} R^P &= \rho^{par} - \rho^0 \end{aligned} \tag{6.19}$$

which together with Eq. 6.16 is used to estimate the coupling resistivites from the measured principal resistivities as shown in Tab. 6.4. The upper limit and lower limit of the orthogonal coupling resistivity is estimated according to

$$\begin{aligned} r^O &\geq r^O_{min} = W(\rho^{ort} - \rho^{par}) \\ r^O &\leq r^O_{max} = W\rho^{ort} \ . \end{aligned} \tag{6.20}$$

The parallel coupling resistivity is calculated according to

$$r^P = W\Big[\frac{W/L}{\rho^{par} - \rho^0} - \frac{L}{3r^O}\Big]^{-1} \ . \tag{6.21}$$

The upper limit of r^P is obtained for ρ^0 set zero resulting in the estimations for the n-type QD sample (HU1468P), and the p-type samples. The value of $\rho^0 = 0.38\,\mathrm{k}\Omega$ for the n-type QWr sample HU1468O is calculated by using the mobility of the comparable QW sample (HU1604N) and the carrier density of HU1468O. No such reference data exists for HU1662N.

Table 6.4: Calculation of coupling resistivities r^P, r^O for n- and p-doped nanostructures. The transport resistivities $\rho^{par,ort}$ are taken at the lowest measured temperature, the length and width (L, W) of the nanostructures are deduced from AFM images of non-covered nanostructures.

Sample	ρ^{par} (k$\Omega/\square$)	ρ^{ort} (k$\Omega/\square$)	L (nm)	W (nm)	r^P (Ωmm)	r^O_{min}/r^O_{max} (Ωmm)
n-type						
QWr, HU1468O	0.45	5.27	200	20	0.031	0.092/0.100
QWr, HU1662N	0.37	11.4	600	20	-	0.22/0.23
QD, HU1468P	3.20	34.2	30	30	$<$0.15	1.30/1.45
QD, HU1662P	3.20	34.2	60	30	$<$0.22	0.93/1.02
p-type						
QDash, HU1495N	1.06	176	60	24	$<$0.065	4.20/4.22
QWr, HU1484O	9.00	930	200	20	$<$2.67	18.4/18.6

The calculated values in Tab. 6.4 yield a larger lateral coupling resistivity than longitudinal resistivity for all samples. This result is most pronounced with the shorter nanostructures than with the longer ones, and with the hole transport than electron transport. Possible reasons for the larger lateral coupling resistivity may be a thicker barrier than in the longitudinal direction, or the effect of anisotropic in-plane strain. The higher coupling resistivities

for holes are attributed to the stronger localization of holes compared to electrons. The higher coupling resistivities for n-type QDs compared to n-type QWrs is attributed to a larger separation between QDs than between QWrs equivalent to thicker tunneling barriers.

6.8 Controlled transport anisotropy and interface roughness scattering

In addition to the temperature dependency of mobility, further information on the transport can be obtained by a variation of the Fermi energy. With the Fermi energy, the effective coupling barrier (Φ_B, see Fig. 6.1) can be modified which, in the context of coupled nanostructures, allows to investigate the longitudinal and lateral coupling as a function of effective barrier height. Furthermore, the Fermi wavelength (Eq. 6.6) can be tuned to find Bragg reflections of the electrons at the the lateral periodicity of the quantum wires (lateral superlattice). Finally, in the context of anisotropic 2D systems additional information on the scattering mechanisms are gained due to their characteristic carrier-density dependence. A change of Fermi energy is equivalent to a change of the carrier density. Typically, the carrier density can be changed by no more than $1 \cdot 10^{12}$ cm^{-2}.

- This change of carrier density results in a maximum obtainable variation of Fermi energy of less than 80 meV (see section 6.3). Taking into account band non-parabolicities the actual value will be even lower. Comparison to the effective barrier of $\Phi_B \approx 200$ meV yields that it will not be possible to occupy extended states in the wetting layer or InP nor to thermally activate carriers into these states. Hence, the carrier will still remain localized in the quantum wires.

- Bragg reflections of the electrons in a lateral superlattice formed by the quantum wires would result in a conductivity minimum if the lateral periodicity a (roughly 20 nm) coincides with half the Fermi wavelength, $a \simeq \lambda_F/2$ [12]. According to Eq. 6.6 this coincidence is expected at a carrier density of $3.9 \cdot 10^{11}$ cm^{-2}.

- The mobility dependence on carrier density in case of remote impurity scattering is approximated by $\mu \propto n^{\gamma}$. Numerical calculations [8, 60] obtain exponents γ in the range of 1 to 1.7 depending on the thickness of the undoped spacer that separates the electron gas from the remote donors. The positive exponent is a result of the better screening of the remote impurity potential with higher n.

The relevant facts about interface roughness scattering are summarized following Ref. [148]. The roughness of the interface is typically described by a Gaussian fluctuation of the interface $< \Delta(r)\Delta(r') >= \Delta^2 \exp\left[-\frac{|r-r'|}{\Lambda^2}\right]$ with the lateral size Λ of the Gaussian fluctuation and roughness Δ. The $<>$ brackets denote an ensemble average. The mobility dependence on carrier density for interface roughness scattering is governed by the product $k_F\Lambda$. It has a minimum for $\lambda_F = 4\Lambda$ at which the electrons are most effectively scattered, and monotonically increasing mobility to both sides of the minimum. With increasing Fermi wavelength the mobility increases as the electron cannot resolve the roughness to a lower degree.

The top interface of the InAs has the major contribution to the roughness since the bottom interface to the underlying InP layer is comparably smooth. Consequently, Λ can be determined in my quantum wires from AFM images of the surface morphology. The analysis shown

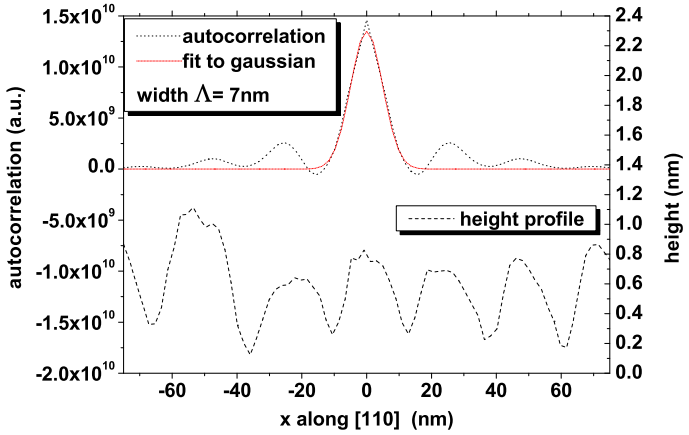

Figure 6.21: Surface profile of InAs quantum wires in InP along the perpendicular direction. Autocorrelation function and gaussian fit.

in figure 6.21 yields a lateral size of fluctuation of $\Lambda = 7$ nm, which means that the scattering is most effective at a Fermi wavelength of $\lambda_F = 28$ nm or a carrier concentration of $8 \cdot 10^{11}$ cm^{-2}. In contrast for the parallel direction $\Lambda^{par} = 34$ nm, and the strongest scattering would occur at $3.5 \cdot 10^{10}$ cm^{-2}. Due to the carrier concentrations between $3 \cdot 10^{11}$ and $2 \cdot 10^{12}$ cm^{-2} in my samples, strong interface roughness scattering is theoretically expected for the ortogonal direction but not for the parallel direction.

- The transport anisotropy A calculated in Ref. [178] for a roughness

anisotropy $\Lambda^{par}/\Lambda^{ort} = 2$ is in the range of 2 to 3 for my Λ and λ_F, which is much lower than my experimentally obtained A for quantum dots with shape anisotropy between 1 and 2. In addition, the significantly larger shape anisotropy of my quantum wires is out of the range treated in Ref. [178]. Both these facts show that the theory of anisotropic interface roughness scattering presented in Ref. [178] does not describe the mobility anisotropy of my structures.

In two n-type modulation-doped QWr samples, viz. HU1547N and HU1662N (see Tab. 6.3), the carrier density is varied at a constant temperature of 9 K. In HU1547N, a gate electrode on top of a square shaped Van der Pauw structure with additional center contacts was used to control the carrier density. Measurements using the additional center contacts verified the consistence of the measured data and extend the measurable range of transport anisotropies as described in detail in section 4.3.9. In HU1662N the ppc effect was used to stepwise increase the electron concentration by taking advantage of existing traps. Measurements of this sample were done with unprocessed Hall bars and with an unprocessed rectangular Van der Pauw sample with corner contacts.

The dependence of the principal mobilities on the carrier concentration, and the resulting transport anisotropies are shown in Fig. 6.22 for HU1662N. The carrier concentration could be increased from $n = 3.8 \cdot 10^{11}$ to $n = 6.3 \cdot 10^{11}$ cm^{-2} which corresponds to Fermi wavelengths from 40.5 to 31.5 nm. In this range the parallel mobility increases from 21000 to

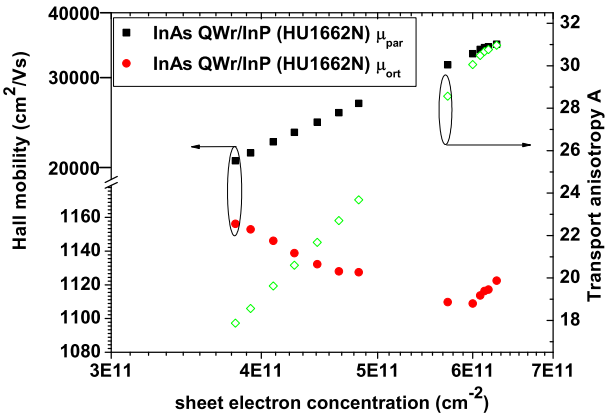

Figure 6.22: Transport in n-type InAs/InP QWr sample HU1662N at T=9 K. Principal mobilities and transport anisotropy vs. carrier concentration.

35000 cm^2/Vs with an exponent $\gamma = 1.0$. This behavior indicates remote impurity scattering. The experimentally obtained exponent is, however,

somewhat lower than the numerically calculated values. In contrast, the orthogonal mobility is almost constant over the entire range of n. Even though strong Bragg reflection of the electrons at the lateral periodicity of the quantum wires is expected at $n = 3.9 \cdot 10^{11}$ cm^{-2}, no increasing mobility is observed as the carrier density increases (which drives the Fermi wavelength away from the Bragg condition). These data give no evidence for a lateral superlattice. Also in terms of effective coupling barrier an increasing mobility would be expected with increasing carrier concentration. Rather, the mobility is slightly decreasing from 1160 to 1110 cm^2/Vs up to a carrier concentration of $n = 6.0 \cdot 10^{11}$ and slightly increases beyond. This behavior strongly indicates interface roughness scattering. The carrier concentration at minimum mobility corresponds to a Fermi wavelength of 32 nm suggesting a gaussian roughness lateral size of 8 nm. The transport anisotropy increases in the entire range of carrier density, mainly due to the increase of parallel mobility.

The regime of higher carrier concentrations is probed with HU1547N that differs from the preceding sample in the paramaters of modulation doping but is supposed to have the same InAs morphology. The effect of gate voltage on carrier concentration, the dependence of the principal mobilities on the carrier concentration, and the resulting transport anisotropies are shown in Fig. 6.23 for HU1547N. The left panel demonstrates the gate-control of

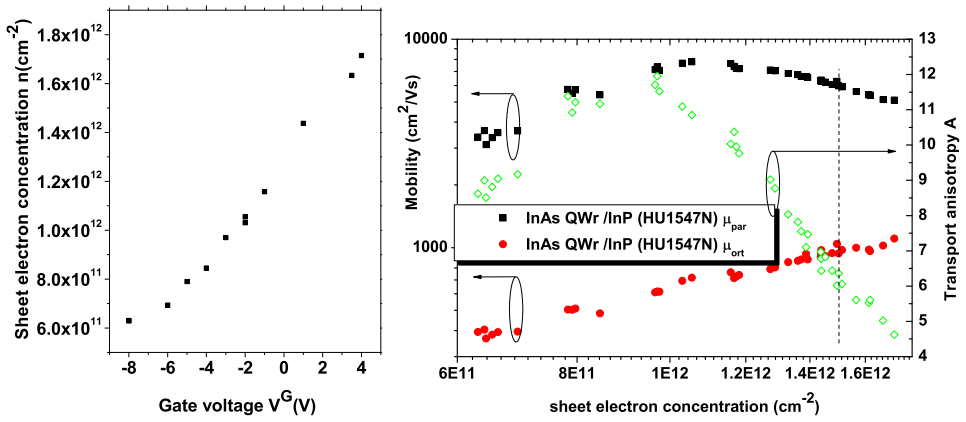

Figure 6.23: Transport in n-type InAs/InP QWr sample HU1547N at T=9 K. **left:** Dependence of sheet electron concentration on gate voltage. **right:** Principal mobilities and transport anisotropy vs. carrier concentration. The vertical broken line denotes the transport without applied gate voltage.

the carrier density in the range of 0.6 to $1.7 \cdot 10^{12}$ cm^{-2} using gate voltages from -8 to +4 V with respect to the semiconductor. These high voltage

are attributed to the high thickness of the insulator between gate and semiconductor. With increasing carrier density, λ_F decreases from 32 to 19 nm and the orthogonal mobilities increases monotonically. In terms of interface roughness scattering this behavior is consistent with the results from the previous sample. The parallel mobility is increasing up to a carrier density of $1.1 \cdot 10^{12}$ cm^{-2} and decreases beyond. The increasing mobility can be explained with remote impurity scattering. The decrease at higher carrier densities remains unexplained, so far. The drastic change of transport anisotropy at carrier concentrations above $1 \cdot 10^{12}$ cm^{-2} is a joint effect of the decreasing parallel mobility and the increasing orthogonal mobility. This behavior is beneficial to the device application proposed in chapter 7.

In conclusion, the mobility dependence on carrier concentration supports the assumption of interface roughness scattering for the orthogonal transport in agreement with theoretical considerations involving the lateral size of the roughness as obtained from AFM images. The mobility dependence of the parallel direction confirms the assumption of remote impurity scattering as mobility-limiting mechanism. The lateral coupling is not enhanced due to the effective decrease of Φ_B with higher n. Electron Bragg reflection at the lateral superlattice formed by the wires were not detected. More detailed investigations in the direction of effects due to lateral superlattices and resonant tunneling may require smaller, processed transport structures that those used in my investigations.

6.9 Shubnikov-de-Haas oscillations and Quantum Hall regime

This section gives a brief overview of the results from the magneto transport measurements at low temperatures and high magnetic fields. A complete discussion of the results and the underlying theories is, however, out of the scope of this work.

The quantization of the electron gas into Landau levels (LLs, with spacing of $\hbar\omega_c$) offers additional possibilities to characterize the transport properties. Shubnikov-de-Haas (SdH) oscillations of the longitudinal resistivity ρ_{xx} allow to measure the 2D carrier concentration from the oscillation period in inverse magnetic field, and to determine the transport effective mass from the oscillation amplitudes at different temperatures [96, 9]. The advantage in comparison to Hall measurement is that the resulting carrier density is not obscured by a Hall scattering factor, finite contact size effects, or parallel conductivity. Plateaus in transversal resistivity ρ_{xy} due to the quantum Hall

effect (QHE, [182]) occur at the same magnetic fields as the oscillation minima (with ideally vanishing resistivity). At these magnetic fields, the Fermi energy is located between adjacent LLs. Following the extensive review of [12], the occupied LLs (i.e. with energy below E_F) are localized within the sample while they form extended states only along the sample boundaries (edge channels). Thus, each Landau level contributes with the fundamental 1D-resistivity $\frac{h}{e^2}$ to the transverse resistivity. Consequently, the plateaus of transverse resistivity are located at resistivities of

$$\rho_{xy} = \frac{h}{e^2}\frac{1}{\nu} = 25.818 \text{ k}\Omega/\nu \ , \tag{6.22}$$

with the filling factor ν that indicates the number of occupied Landau levels. In absence of spin splitting (applies all data shown here for InAs/InP nanostructures) these levels have a spin degeneracy of two. The spatial extent of wavefunction of the Landau level with index n (n=1, 2, ...) is the cyclotron radius r_l which decreases with increasing magnetic field as

$$\begin{aligned} r_l(B,n) &= l_m(B)\sqrt{2n-1} \\ l_m(B) &= \sqrt{\frac{\hbar}{eB}} \ , \end{aligned} \tag{6.23}$$

with magnetic length l_m (≈ 25 nm at 1 T). Similarly to the Fermi wavelength for interface roughness scattering, this wavefunction extent can be regarded as a probe the characteristic length of the potential variations due to InAs nanostructures for the electrons.

Figure 6.24, left, shows the SdH oscillations of the longitudinal resistivity, and QHE plateaus in the transversal resistivity of an InAs QW sample at different temperatures.

At the lower temperature of 0.3 K, the thermal broadening of the LL is small enough, to yield a pronounced QHE plateau and vanishing ρ_{xx} at 10 T. The filling factor $\nu = 4$ ($\rho_{xy} = 6.45$ kΩ) which corresponds to occupied spin degenerate LLs with $n = 1, 2$. The quantum wire sample (shown in 6.24, right), on the other hand, shows no pronounced QHE plateaus, probably due to the strong remote impurity scattering that does not allow the formation of pronounced LLs. SdH oscillations of ρ_{xx}, however, are already present and show the same qualitative behavior in both transport directions. Analysis of the oscillation amplitude's temperature dependence of both samples yield an effective mass $m^* \geq 0.15\ m_e$. This value is much larger than the theoretically calculated value of $\approx 0.03\ m_e$ for InAs nanostructures on InP [141]. The significantly larger effective mass obtained from my data is tentatively attributed to band nonparabolicities leading to a different curvature of the

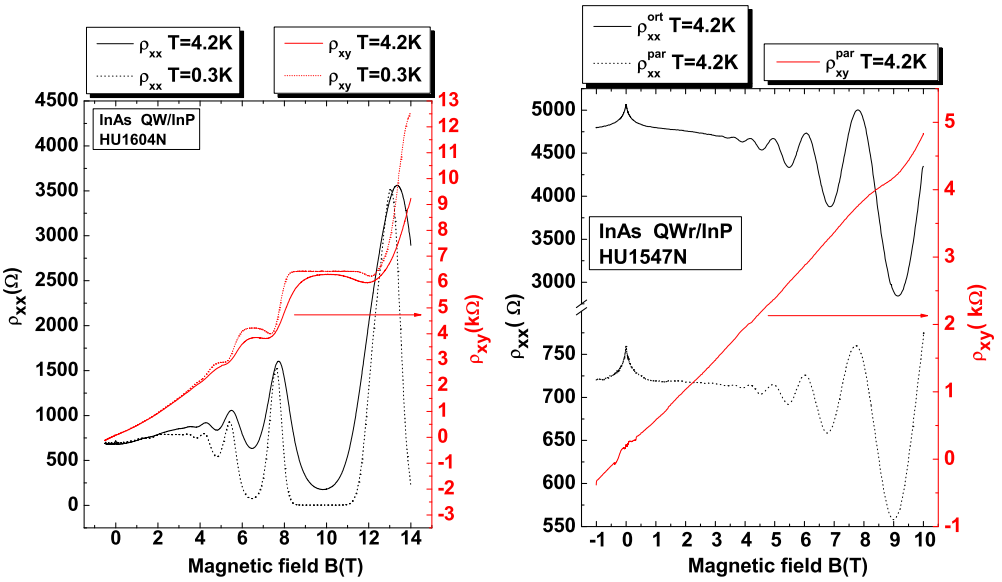

Figure 6.24: Shubnikov-de-Haas oscillation and quantum Hall plateaus of an InAs QW and a QWr sample.

conduction subband at the Fermi energy than at the band minimum. Investigations at higher magnetic fields, outside the scope of this work, may check the consistency of the data.

The SdH and QHE in another InAs QWr sample (HU1662N, with weak remote impurity scattering and high anisotropy) measured at two different carrier concentrations (adjusted using persistent photoconductivity) is given in Fig. 6.25.

At the lower carrier density (left panel), a clear transition from diffusive transport to transport in the QHE-regime is visible. At $B \approx 6.5$ T a QHE plateau with filling factor $\nu = 2$ forms, and the SdH oscillation minimum is close to zero in comparison to the zero field resistivity. At zero magnetic field, diffusive transport with longitudinal resistivities of $\rho_{xx}^{ort} = 26$ kΩ and $\rho_{xx}^{par} = 2.8$ kΩ is observed. The transport in the QHE regime, in contrast, yields resistivities of 710 and 560 Ω. The filling factor of 2 corresponds to the spin degenerate ground state LL ($n = 1$) which has a cyclotron radius of $r_l = l_m = 10$ nm. That this value is smaller than the lateral period of the potential due to the InAs QWrs (of 20 nm) is considered to allow the pronounced formation of LLs. This assumption is supported by the argument that in disordered conductors strong potential variations (the InAs nanostructures are strong potential fluctuations and lead to the disorder in my samples) should appear on a spatial scale that is large compared to l_m

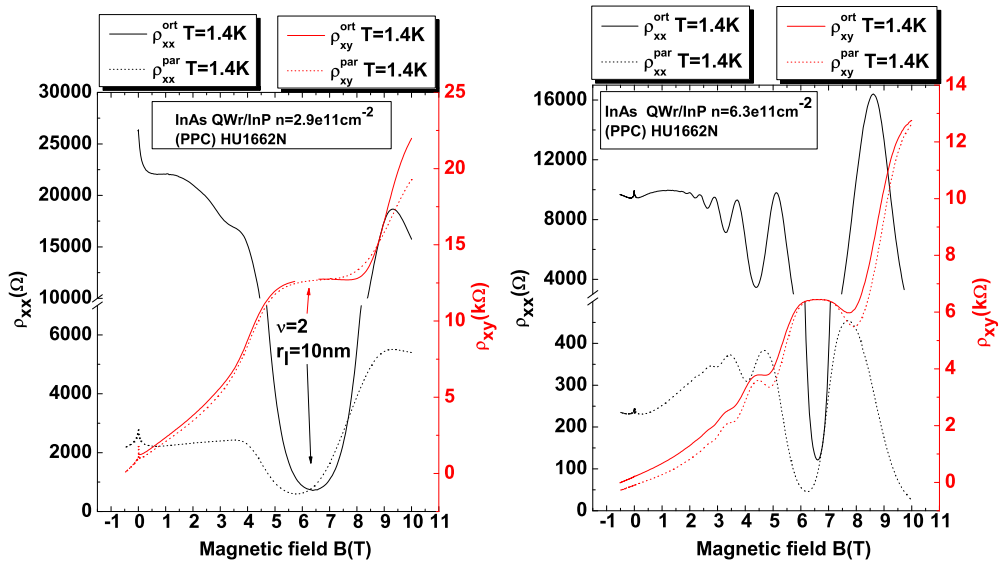

Figure 6.25: Shubnikov-de-Haas oscillation and quantum Hall plateaus of a QWr sample at two different carrier densities.

[12]. At a higher carrier density (right panel), the SdH oscillation period is higher, and the QHE plateau at $B \approx 6.5$ T has a filling factor of $\nu = 4$, both indicating the higher carrier density.

The peak of the longitudinal resistivity at $B = 0$ is a macroscopic consequence of quantum mechanical self-interference of the electron. Section 6.10 will discuss this effect in depth.

6.10 Weak localization in coupled nanostructures

In this section, the magnetotransport properties of quantum wells, and laterally-coupled self-organized InAs quantum wires and dots are investigated with respect to the contributions to conductivity resulting from weak localization. The influence of the type of nanostructure on the weak localization will be compared with focus on the quantum wires.

I demonstrate that the weak-localization correction shows a directional anisotropy equal to the anisotropy of the total conductivity. This result suggests that even for a conductivity anisotropy ratio as high as 38, the coupling between the quantum wires plays a more important role than the quasi-one-dimensional nature of the electron transport in describing the quantum mechanical contributions due to weak localization.

6.10.1 Theory of localization

According to the scaling theory of localization [98], at zero temperature in 2D disordered systems the conductivity can be divided into a classical- and a length-dependent term, σ_0 and $\delta\sigma(L)$, with L describing the system's characteristic size and l_e being the elastic scattering length. The total conductivity is given by

$$\sigma_{2D}(L) = \sigma_0 + \delta\sigma \tag{6.24}$$

$$\delta\sigma = -\frac{2e^2}{\pi h}\ln\left(\frac{L}{l_e}\right) . \tag{6.25}$$

Therefore the conductivity decreases with increasing system size. At finite temperature, inelastic scattering processes cause the electron to lose its phase while traveling a distance of l_Φ (dephasing length). This length is of crucial importance in devices using quantum interference. If the dephasing length l_Φ is smaller than L, then $l_\Phi(T)$ replaces L in Eq.6.25. The logarithmic term $\delta\sigma$ is a correction to the classical conductivity σ_0 resulting from the quantum mechanical effect of localization.

Weak localization is a purely quantum mechanical interference phenomenon in disordered conductors. At low temperature T, the dephasing length l_Φ becomes large, allowing the coherent self-interference of an electron. Diffusing along a closed path, the electron interferes constructively with its time-reversed path resulting in a higher-than-classical probability of backscattering. This interference is enabled by the non-phase-randomizing nature of the elastic scattering that causes the diffusion. The enhanced backscattering results in a decrease of conductivity whose contribution is of order of the elementary conductivity e^2/h. Applying a magnetic field perpendicular to the plane of motion destroys the constructive interference as it introduces an Aharonov-Bohm phase shift between both time-reversed amplitudes. This is a concurrent process which causes dephasing on the scale of the magnetic length l_m as opposed to l_Φ. Therefore, the quantum correction $\delta\sigma$ is also dependent on the magnetic field B. In addition to weak localization, electron-electron interaction gives rise to other quantum corrections. These corrections are also magnetic field dependent, but less so than the weak localization.

The scaling theory of localization can be further generalized to show that in 2D systems with anisotropic σ, the correction $\delta\sigma$ due to localization or electron-electron scattering is also anisotropic with the same anisotropy as σ [196]. This effect was demonstrated experimentally in the (110)-oriented Si metal-oxide-semiconductor (MOS) system, in which the 2DEG at the silicon-oxide interface shows a directional anisotropy of about 2 [20].

My data show that although the semi-classical transport appears quasi-one-dimensional, the weak localization is well described as an anisotropic 2D system. Without lateral coupling, the lateral confinement would be defined by the wire width, which is much smaller than the dephasing length l_Φ. Therefore, the success of the 2D description signifies that in this system the lateral coupling determines the fundamental behavior of the weak localization.

6.10.2 Analysis and discussion of experimental data

In the transport measurements, samples containing one modulation-doped InAs layer embedded in InP were investigated. Table 6.5 summarizes their transport properties at T=1.4 K along with their morphology.

Table 6.5: Transport properties at T=1.4 K of the analyzed samples. Hall sheet electron concentration (n_H), transport anisotropy (A), Hall mobility parallel (μ_{par}) and orthogonal (μ_{ort}) to the [$\bar{1}$10]-direction. Values in parentheses are measured after illumination (PPC). Values marked with * are subject to high uncertainty from the Hall measurement in these samples.

Sample	Morphology	A	n_H (10^{12} cm^{-2})	μpar (cm^2/Vs)	μ_{ort} (cm^2/Vs)
HU1604N	QW	1.5	1.6	7350	-
HU1547N	QWr	6.7	1.35	6340	947
HU1547P	QD	8.1	1.3	3102	383
HU1468O	QWr	11.2	0.76	6325	565
HU1662N	QWr	13.8(37.9)	0.2(0.6)*	4718(38700)*	342(1022)*
HU1662P	QD	2.6(13.2)	0.2(0.6)*	616(3670)*	237(278)*

In their magneto-transport characteristics, shown in Figs. 6.24 and 6.25, the resistivity ρ_{xx} exhibits a characteristic peak at $B = 0$. Figure 6.26 shows these peaks of the QWr sample HU1662N in detail for both transport directions. In the left part, the peak measured at three different temperatures is shown. The right part displays the weak localization peak of the same sample at a higher carrier concentration (after illumination). Additionally, the magneto-resistance in a magnetic field oriented *parallel* to the InAs layer at higher carrier concentration, is shown in Fig. 6.26, right. The corresponding change of conductivity is calculated according to

$$\Delta\sigma(B) = \sigma(B) - \sigma(0) = \rho_{xx}(B)^{-1} - \rho_{xx}(0)^{-1} \ . \tag{6.26}$$

Because for small B, the classical conductivity σ_0 is independent of B (as shown in experiments at T=77 K), the peak in ρ_{xx} is solely a measure of the magnetic field dependence of the quantum correction $\delta\sigma$. Also, the smaller peak height at higher temperatures (see Fig. 6.26, left) indicates a suppression of the quantum correction due to increased inelastic scattering.

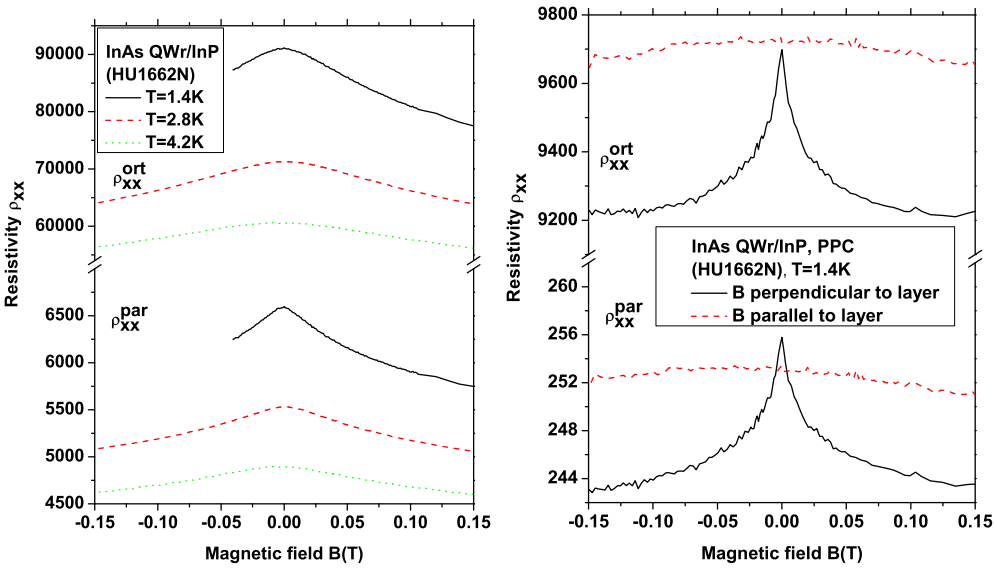

Figure 6.26: **left:** Magnetoresistance peak of an InAs QWr sample for transport parallel (ρ_{xx}^{par}) and orthogonal (ρ_{xx}^{ort}) to the wire direction measured at three different temperatures. **right:** Magnetoresistance peak of the same sample at T=1.4 K after illumination. Additionally, dotted lines show the magnetoresistance with magnetic field B parallel to the InAs layer.

The measurement with B parallel to the InAs layer allows to distinguish between electron-electron interaction and weak localization as cause of the magneto-resistance peak. Electron-electron interaction yields a peak that consists of a large contribution from spin-splitting, not depending on magnetic field direction, and a contribution due to the perpendicular magnetic field, which is often considerably smaller than the weak localization peak [12]. Consequently, it is the spin-splitting contribution to electron-electron interaction that is likely to distort the weak-localization peak. Comparison of the magneto-resistance peaks in perpendicular and parallel B (Fig. 6.26, right) yields, that the spin-splitting contribution from electron-electron interaction (measured in parallel magnetic field) is negligible for the measured perpendicular magneto-resistance peak. Thus, the magneto-resistance peaks measured in my samples are mainly related to weak localization.

Using Eqs. 6.24 and 6.26, the experimental quantity $\Delta\sigma$ measures the dependence of the quantum correction to the conductivity on magnetic field. Furthermore, the directional anisotropy of $\Delta\sigma(B)$, defined as $\Delta\sigma^{\mathrm{par}}(B)/\Delta\sigma^{\mathrm{ort}}(B)$, is a measure of the anisotropy of the quantum correction to the conductivity $\delta\sigma(B)$. A comparison of $\Delta\sigma(B)$ for both principal transport directions by plotting them on a log scale (Fig. 6.27, left) shows that its directional anisotropy (the vertical distance of the curves of both directions) remains fairly constant for the entire range of B. The anisotropy in $\Delta\sigma(B)$ is shown for several values of B and compared with the anisotropy of the total conductivity σ in Table 6.6. It is theoretically expected that in a 2D system with directional anisotropy these values will be identical; the similarity in the experimental values is regarded as another confirmation of this theoretical prediction at (to my knowledge) the highest anisotropy to date.

Table 6.6: Anisotropy $\Delta\sigma^{\mathrm{par}}(B)/\Delta\sigma^{\mathrm{ort}}(B)$ in magnetic field B for a QWr sample (compare to Fig. 6.27, left) and a QD sample.

$B(mT)$	QWr HU1662N (ppc, A=37.9)	QD HU1662P (ppc, A=13.2)
10	33.7	12.8
30	34.1	13.0
100	35.6	13.1

According to the theory of 2D weak localization, the suppression of the conductivity caused by a magnetic field is given by [12]

$$\begin{aligned}\Delta\sigma_{2D}^{\mathrm{ort,par}}(B) &= \alpha^{\mathrm{ort,par}}\frac{e^2}{\pi h}\left[\Psi\left(\frac{1}{2}+\frac{\tau_B}{2\tau_\Phi}\right)-\right.\\ &\left.\Psi\left(\frac{1}{2}+\frac{\tau_B}{2\overline{\tau}}\right)+\ln\left(\frac{\tau_\Phi}{\overline{\tau}}\right)\right]. \qquad (6.27)\end{aligned}$$

In contrast to the isotropic case ($\alpha^{\mathrm{ort,par}}=1$) the following modifications are done to include the anisotropy [98].

$$\alpha^{\mathrm{ort,par}}=\frac{\sigma^{\mathrm{ort,par}}(B=0)}{\sqrt{\sigma^{\mathrm{ort}(B=0)}\sigma^{\mathrm{par}}{}_{(B=0)}}} \qquad (6.28)$$

The coefficient $\alpha^{\mathrm{ort,par}}$ scales $\Delta\sigma$ due to anisotropy, and $\overline{\tau}=\sqrt{\tau^{\mathrm{ort}}\tau^{\mathrm{par}}}$ is the average elastic scattering time. The other quantities used are the

magnetic relaxation time τ_B and the diffusion constant D

$$\tau_B = \frac{l_m^2}{2D}, \quad D = \tfrac{1}{2} v_F^2 \overline{\tau} \tag{6.29}$$

with magnetic length l_m (Eq. 6.23, equals cyclotron radius of 0-th Landau level) and Fermi velocity v_F.

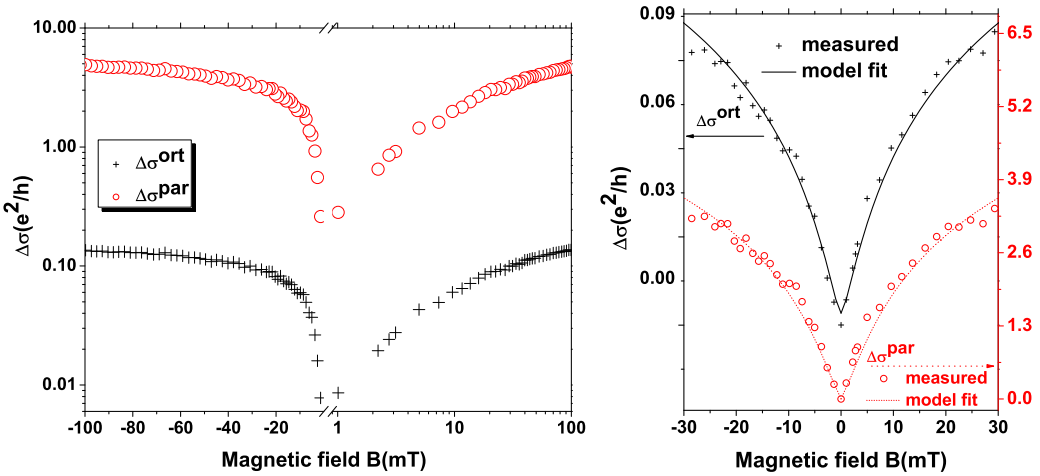

Figure 6.27: Change of conductivity in magnetic field $\Delta\sigma(B)$ of QWr sample HU1662N for both transport directions after illumination at T=1.4 K. Black crosses=orthogonal, red circled=parallel to QWr. **left:** Logarithmic scale for positive B. **right:** Lines show the model of anisotropic 2D weak localization.

The experimental data are fit to the model of weak localization for low magnetic fields ($B < 30$ mT). The dephasing time τ_ϕ was used as a fitting parameter; all other quantities (τ, α, v_F) were determined from classical transport measurements (of ρ and n) at T=10 K, at which the correction term is negligible due to inelastic scattering. This procedure allows a determination of the dephasing time τ_Φ and the dephasing length $l_\Phi = \sqrt{D\tau_\Phi}$. Figure 6.27, right, shows that the model of anisotropic 2D weak localization describes the low field magnetoconductance of the sample well. That the τ_Φ from both transport direction of all samples agree within less than 15% confirms the validity of the model for my data.

A closer inspection of the formulas yield that the fundamental input for the fit are the measured classical resistivity ρ along with its change in magnetic field, the carrier concentration n, and the effective mass m^* of electrons at the Fermi energy. These values enter the calculation through v_F and τ (Eqs. 6.6,6.3). While the resistivity is quite reliably measured, there is some uncertainty with the carrier density n, and m^* is not precisely known. The

theoretically calculated value of $m^* \approx 0.03\ m_e$ is used for the effective mass. The real value may, however, be larger as suggested from the SdH data. Therefore, m^* and n are considered parameters put into the calculation. To what extent these parameters influence the results from the fit (dephasing time and length) is investigated. All involved characteristic times $(\tau, \tau_B, \tau_\Phi)$ scale linearly with the parameter m^*. As a consequence, the ratio τ_Φ/τ, and the dephasing length l_Φ do not depend on m^*. The impact of the carrier density n put into the calculation as parameter was tested by varying its value. As result, a variation, e.g. by factor of 2, has almost no influence on the resulting τ_Φ for my data. This makes the τ_Φ determined for sample HU1662N,P before and after illumination reliable, even though the actual carrier density is not precisely known. Since D is independent of the parameter n the dephasing length l_Φ is quite independent of n as well. Thus, τ_Φ as obtained from the fit can be compared among different samples, and within one sample at different carrier densitities, as long as they have the same effective mass, and the same effective mass (which can differ from the actual effective mass) is put into the calculation. Moreover, the dephasing length l_Φ is completely independent of the exact value of the parameter m^* and only weakly depending on the parameter n put into the model.

The dephasing times and respective dephasing lengths are plotted as a function of temperature in Fig. 6.28. The consequences of the shown data are discussed as follows.

- Typically, τ_Φ is two orders of magnitude larger than τ which is a necessary condition for weak localization, since multiple elastic-scattering events are required for return trajectories.

- With increasing temperature, the dephasing times decrease due to temperature-dependent inelastic scattering following roughly a $\tau_\Phi \propto T^r$ law with $r \simeq -0.8$. This value suggests electron-electron scattering with $r = -1$ to be the dominant inelastic scattering process [20].

- The dephasing times are similar for all analyzed nanostructures and do not correlate to their morphology. A change of carrier concentration in HU1662N,P significantly changes the mobility and elastic scattering times but shows only a negligible influence on the inelastic scattering time (compare full and open triangles and stars in Fig. 6.28, left).

- Hence, the inelastic scattering is considered merely temperature induced, and independent of the nanostructure type.

- The dephasing lengths l_Φ (distance between subsequent inelastic scattering events) as shown in Fig. 6.28, right, are significantly larger than

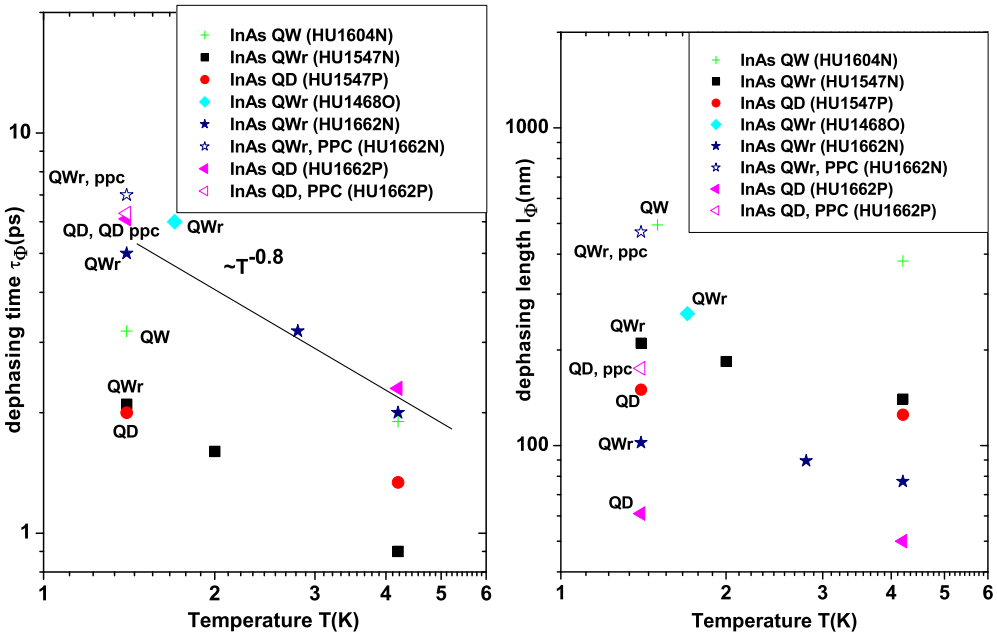

Figure 6.28: Dephasing time τ_Φ (left) and corresponding dephasing length l_Φ (right) as a function of temperature for different nanostructures. The dephasing time and length was extracted from the analysis of the weak localization peaks.

the wire-wire distance, and not at all related to the morphology (also compare l_Φ in HU1662N,P for different carrier concentrations). Hence, the nanostructure-nanostructure coupling is not inelastic, which is compatible with interface roughness scattering being elastic [203, 186, 27].

In conclusion, the anisotropy of quantum corrections to conductivity for InAs quantum wells, and coupled self-organized InAs quantum wires and dots embedded in InP are investigated. Despite high anisotropies in coupled nanostructures which suggests a low degree of lateral coupling between the nanostructures, the weak localization is successfully modeled by regarding the system as a 2DEG with anisotropic conductivities. The anisotropy of weak localization (along with other quantum corrections) has the same value as the anisotropy of the total conductivity for values as large as 38; this result confirms the theory of Ref. [196] for high anisotropy in 2 dimensions. The independence of dephasing time on the actual morphology and coupling strength (carrier density) indicates that the nanostructure-nanostructure scattering is elastic.

6.11 Conclusion

The in-plane transport of electrons and holes in large ensembles of InAs nanostructures, comprising quantum wires, quantum dashes, quantum dots, and quantum wells as reference, was investigated.

The transport of quantum wire-, quantum dash- and quantum dot containing samples is highly anisotropic with the principal axes of conductivity aligned to the <110> directions. The direction of higher mobility is $[\bar{1}10]$, which is parallel to the direction of the quantum wires. In extreme cases, the anisotropies exceed 30 for electrons, and 100 for holes.

The experimentally inexpensive anisotropic Van der Pauw method developed in section 4.3 was successfully used for the determination of the anisotropic transport properties.

The transport characteristics are interpreted in the framework of a 2D carrier system with different scattering mechanisms in both principal directions, and in the framework of longitudinally and laterally coupled nanostructures. The temperature dependence and carrier-density dependence of mobility was analyzed with the following results:

In the anisotropic 2D framework, the dominating scattering mechanisms at low temperature are remote-impurity scattering in the parallel direction for quantum wires, and interface-roughness scattering in both directions for quantum dots, and in the orthogonal direction for quantum wires, -dashes. In p-type samples, though, the hole transport in the orthogonal direction cannot be described by scattering but is described as hopping between laterally localized states.

Although the transport in the n-type samples is well described in the described framework of anisotropic 2D carrier systems, the coupled nanostructure picture is supported by the structural properties in conjunction with band offsets, and the localization in the p-type nanostructures.

In the coupled nanostructure framework, the transport anisotropy is demonstrated to result from *directionally anisotropic tunnel coupling* between adjacent nanostructures rather than from the nanostructure shape anisotropy. This coupling controlled transport anisotropy is in marked contrast to the shape-dependent polarization anisotropy of optical emission. The strong longitudinally coupling has no significant impeding effect on transport, whereas the weak lateral coupling substantially impedes transport, which in extreme cases results in hopping transport for holes between laterally localized states. An empirical model describing the transport in coupled nanostructures was developed to determine the direction dependent coupling strengths from the experimental data.

The weak-localization contribution to conductivity is successfully mod-

eled by regarding the system as a 2DEG with anisotropic conductivities. The anisotropy of weak localization has the same value as the anisotropy of the total conductivity for values as large as 38; confirming the theory of Ref. [196] for high anisotropy in 2 dimensions. The independence of dephasing time, extracted from the weak localization data, on the actual morphology and coupling strength (carrier density) indicates a a strong coupling and elastic nanostructure-nanostructure scattering.

The successful gate-control of transport anisotropy in n-type coupled quantum wires provides the basis for a novel electronic switching device proposed in chapter 7.

Chapter 7

Electronic switching device based on gate-controlled conductivity anisotropy

A novel 5-terminal electronic switching device based on gate-controlled transport anisotropy is proposed in this chapter. By means of the gate voltage, two output voltages can be contrariwise adjusted to values between the two input voltages yielding a possible logic application as an exchange gate. The modulation-doped, self-organized InAs quantum wires embedded in InP investigated in chapter 6 are shown to be a candidate for implementation of this device.

The possibility to change the transport anisotropy for both n- and p-type structures by applying a gate voltage, as demonstrated in section 6.8 and in Refs. [143, 120, 122, 118, 75], serves as the basis for the device proposed here. Similar to a gated, square-shaped van der Pauw structure used in the previous

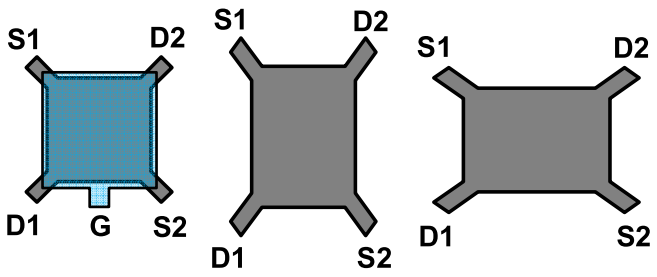

Figure 7.1: **Left:** Schematics of x device. The gate electrode G controls the effective anisotropy A_{eff}. **Center:** Equivalent geometry of x device with $A_{\mathrm{eff}} > 1$ and isotropic conductivity. **Right:** Equivalent geometry with $A_{\mathrm{eff}} < 1$ and isotropic conductivity.

chapter, the proposed device consists of 5 terminals: two source contacts (S1 and S2), two drain contacts (D1 and D2), and a gate electrode (G). A possible geometrical realization, given in the left panel of Fig. 7.1, is a square-shaped active reagion with contacts in the corners. The contact arrangement resembles the letter "x". The diagonally opposite corner contacts, S1 and S2, act as input electrodes (source), the other two corner contacts, D1 and D2, act as output electrodes (drain) [1]. The "x device" is run in voltage mode, i.e. the output voltages ($V_{\mathrm{D1}}, V_{\mathrm{D2}}$) at (D1, D2) are functions of input voltages ($V_{\mathrm{S1}}, V_{\mathrm{S2}}$) at (S1, S2) and of the gate bias Φ^{G} at contact G. The x device has a switching functionality by virtue of the gate controlled transport anisotropy $A = \sigma_{xx}/\sigma_{yy}$ with conductivities σ_{xx},σ_{yy} along the principal axes x, y of conductivity. This functionality is illustrated in Fig. 7.1. The edges of the device are aligned to the principal axes of conductivity (horizontal x axis, vertical y axis). Tuning A to a value greater than unity ($A > 1$), the x device behaves like an isotropic conductor with the geometry shown in the central panel. This correspondence is based on the concept of van der Pauw [184] that an anisotropic conductor is equivalent to an isotropic conductor with average resistivity (geometrical average of principal resistivities of the anisotropic conductor) and dimensions along the principal directions scaled by the square root of ratio of principal resistivity to average resistivity. Since D1 is spatially closer to S2 than to S1, the resistance between D1 and S2 is lower than that between D1 and S1. Consequently, the voltage of D1 will be closer to the voltage of S2 than of S1. Vice versa, D2 is closer to S1 than to S2, and the voltage of D2 is closer to the voltage of S1 than of S2. This situation can be inverted by tuning A to a value below unity ($A < 1$), as shown in the right panel. This condition results in D1 being switched from S1 to S2 while at the same time D2 is switched from S2 to S1. A possible logic application is an "e**x**changer". Depending on the gate bias, the logic levels of (D1, D2) equal the input (S1, S2) or the exchanged input (S2, S1) (see Table. 7.1). This exchanger could potentially be used as a single-device logic gate for exchanging bit values and in demultiplexing of analogue signals.

Table 7.1: Logic functionality of x device. The logic levels at S1, S2 are "high" or "low".

	D1	D2
$A < 1$	S1	S2
$A > 1$	S2	S1

[1] This is the configuration used in the van der Pauw structure for the Hall measurement.

The proposed application requires a transport anisotropy that can be varied from values less than unity to values greater than unity, a condition not usually met in anisotropic carrier systems. For any given transport anisotropy A, however, the device can be geometrically scaled (stretching of the square shaped device in Fig. 7.1 in x or y direction) to behave like a square shaped device with effective transport anisotropy A_{eff} of unity. The transport anisotropy can then be mapped into the effective anisotropy according to (same as Eq. 4.43 in section 4.3.2)

$$A_{\text{eff}} = \frac{\sigma_{xx}}{\sigma_{yy}}\left(\frac{L_y}{L_x}\right)^2 = A\left(\frac{L_y}{L_x}\right)^2 \tag{7.1}$$

with the lengths of the stretched edges of the square L_x, L_y in x, y directions. Thus, any gate-controllable range of A is suitable for the application proposed here.

7.1 Characteristics with low source voltage

The characteristic of an "x device" with uniform anisotropy and carrier density across the device, the case of negligible source voltages compared to the gate voltage, is analyzed in the following discussion. The trivial operation of exchanging two identical logic levels is clearly given with the x device: If the same voltage is applied to both S1 and S2 then D1 and D2 will also be at the same voltage ($V_{\text{D1}} = V_{\text{D2}} = V_{\text{S1}} = V_{\text{S2}}$), irrespective of the gate voltage. Different voltages at S1 and S2 are therefore the non-trivial case. In this case, however, the voltages of D1 and D2 cannot be completely switched between the voltages of S1 and S2 but are always between V_{S1}, and V_{S2}. Numerical calculations using the finite element method, as described in section 4.3.3 and Ref. [18], were used to obtain the drain voltages. The potential at S1 is defined as 0 V, and a non-zero voltage is applied to S2. In this situation the voltages of D1, and D2 scale linearly with V_{S2}, and reduced drain voltages $V_{\text{D1,D2}}/V_{\text{S2}}$ describe the characteristics of the x device. These reduced drain voltages are plotted as a functions of effective anisotropy in Fig. 7.2. Exchanging the voltages of S1 and S2 results in exchanged characteristics of D1 and D2. The characteristics of D1 and D2 cross at an effective anisotropy of unity, as intuitively expected. For the application as logic exchanger, all drain voltages above an upper voltage (denoted by the higher-lying blue dotted line) are defined as "logic high"; voltages below a lower voltage are defined as "logic low". The logic swing becomes larger with an increased gate-control of the anisotropy. An example of a relatively large logic swing is denoted by the green dashed lines. More specifically, the logic swing ΔV increases with

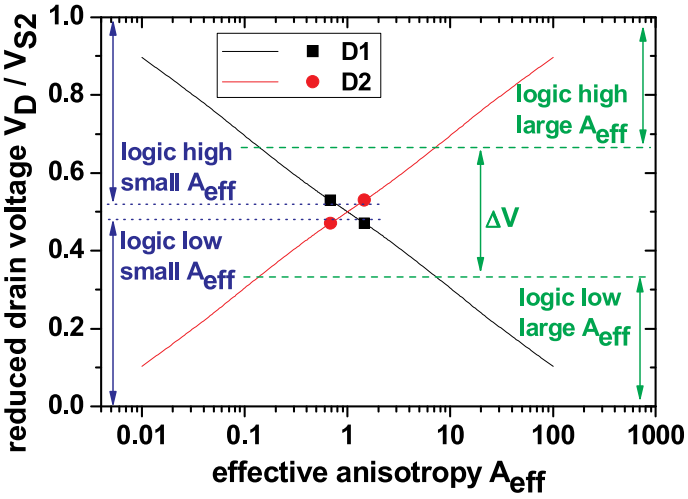

Figure 7.2: X device with uniform anisotropy and carrier density across the device. Simulated reduced drain voltage dependence on effective anisotropy. A non-zero voltage is applied to S2 while S1 is at the reference potential of zero volts. Exchanging the voltages of S1, S2 results in exchanged curves of D1, D2 (not shown here). The datapoints indicate the measured anisotropy range in the self-organized InAs quantum wires.

the ratio $\alpha = A_2/A_1$ of maximum transport anisotropy A_2 to minimum transport anisotropy $A_1 > 1$. Based on geometrical scaling (Eq. 7.1) the range of effective anisotropies A_{eff} that can be realized symmetrically around unity is $\sqrt{1/\alpha} < A_{\text{eff}} < \sqrt{\alpha}$, using an aspect ratio of $L_x/L_y = \sqrt[4]{A_1 A_2}$.

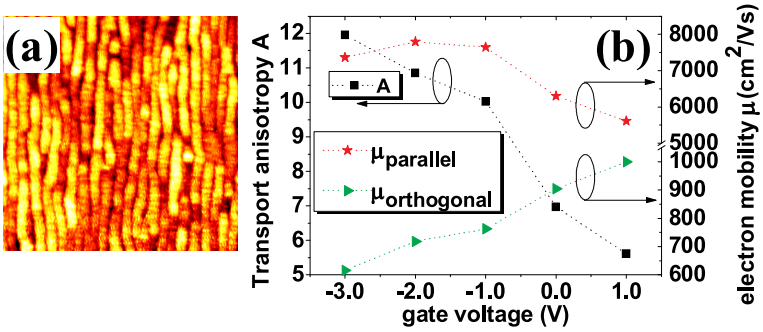

Figure 7.3: a) AFM image showing a 500 nm x 500 nm area covered with self-organized InAs quantum wires. b) Experimental results on gate-controlled electron mobilities parallel and orthogonal to self-organized InAs quantum wires embedded in InP and corresponding transport anisotropy at 10 K.

In one realization of the device, self-organized laterally coupled InAs

quantum wires can be used. (See Fig. 7.3a.) At low temperatures, the transport anisotropy could be increased from $A_1 = 5.6$ to $A_2 = 12.0$ by changing the electron concentration with a top gate (see Fig. 7.3b, and section 6.8). Thus, with an appropriate choice of geometry these nanostructures are suitable for a realization of the x device. The following considerations are quantitatively exemplified with the transport properties shown in Fig. 7.3 but are qualitatively not limited to them. Using an aspect ratio of $L_x/L_y = 2.86$ the corresponding effective anisotropy ranges from 0.68 to 1.46. This allows the drain voltages to switch between 0.467 V_{S2} and 0.533 V_{S2} (applied source voltage V_{S2} at S2; $V_{S1} = 0$) with a maximum logic swing of $\Delta V = 0.066\ V_{S2}$. A realistic logic application would, therefore, require well-defined voltages at the source contacts, and discriminators at the drain contacts to restore the output logic voltage levels. The necessary conditions for the exchanger to work are crossing characteristics of D1 and D2 within the available range of effective anisotropies, and that their slopes have opposite signs.

7.2 Characteristics with high source voltage

The analysis described above is applicable for the case of a uniform carrier concentration and a uniform anisotropy across the device; these conditions typify the situation for low lateral electric fields. Practical applications with high switching speeds and parasitic capacitances, however, are likely to require higher currents, and consequently higher source voltages. In addition, the logic swing for a given swing in anisotropy is also proportional to the source voltage. For source voltages in the range of the applied gate voltage the local gate-channel voltage varies considerably across the device and has to be included in the simulations. Thus, a more realistic analysis must take the local variation of the gate-channel voltage into account as is done for field effect transistors in saturation. The local gate-channel voltage

$$V^G(\mathbf{r}) = \Phi^G - \Phi(\mathbf{r}) \tag{7.2}$$

is the difference between applied gate potential Φ^G, and local potential $\Phi(\mathbf{r})$ at position $\mathbf{r}$ in the conducting channel. The variation of V^G is negligible for variations of $\Phi(\mathbf{r}) << \Phi^G$ justifying the assumption of uniform carrier concentration and transport anisotropy across the device. Simulations were carried out using a linear approximation of V^G dependent carrier concentration n, and principal mobilities $\mu^x > \mu^y$:

$$\begin{aligned} n &= n_1(1 - c_n V^G(\mathbf{r})) \\ \mu^x &= \mu_1^x(1 + c_x V^G(\mathbf{r})), \quad \mu^y = \mu_1^y(1 - c_y V^G(\mathbf{r})) \end{aligned} \tag{7.3}$$

with index 1 for zero gate voltage Φ_1^G, and index 2 for gate voltage Φ_2^G that results in the maximum anisotropy A_2. The coefficients c are calculated as follows

$$c_n = \frac{n_1 - n_2}{n_1 \Phi_2^G}, \quad c_x = \frac{\mu_2^x - \mu_1^x}{\mu_1^x \Phi_2^G}, \quad c_y = \frac{\mu_1^y - \mu_2^y}{\mu_1^y \Phi_2^G} \ . \tag{7.4}$$

In this approximation, the principal conductivities used for the simulation are

$$\begin{aligned} \sigma_{xx}(\mathbf{r}) &= e n_1 \mu_1^x \left[1 + V^G(\mathbf{r})(c_x - c_n) - c_x c_n (V^G(\mathbf{r}))^2\right] \\ \sigma_{yy}(\mathbf{r}) &= e n_1 \mu_1^y \left[1 - V^G(\mathbf{r})(c_y + c_n) + c_y c_n (V^G(\mathbf{r}))^2\right] \ . \end{aligned} \tag{7.5}$$

The off-diagonal elements of the conductivity tensor are zero because no magnetic field is applied, and the device is aligned at the principle axes of conductivity. Within the linear gate-voltage-dependent range the transport characteristics measured in section 6.8 for the coupled quantum wires are $n_1 = 1.57 \cdot 10^{12}$ cm^{-2}, $n_2 = 0.97 \cdot 10^{12}$ cm^{-2}, $\mu_1^x = 5611\,\mathrm{cm}^2/\mathrm{Vs}$, $\mu_2^x = 7365\,\mathrm{cm}^2/\mathrm{Vs}$, $\mu_1^y = 1000\,\mathrm{cm}^2/\mathrm{Vs}$, $\mu_2^y = 616$ cm^2/Vs. Using Eq. 7.4 and assuming a gate voltage range of 0 V to -1 V [2], these transport characteristics result in the coefficients $c_n = -0.38, c_x = -0.31, c_y = -0.38$. These characteristics are used in Eq. 7.5 for the simulation of an x device with aspect ratio of 2.78. In this simulation, the same polarity (negative) of applied source voltage at S2, and gate bias at G was chosen. Using the same polarity keeps the transport characteristics for an applied gate potential $\Phi^G = \Phi_2^G$ in the linear gate-dependent range (local gate-channel potential $V^G \geq \Phi_2^G$). Furthermore, the local gate-channel voltage can become positive ($V^G \leq -V_{\mathrm{S2}}$) for an applied gate potential of 0 V. Therefore, the simulation is applicable to the real device only for the positive gate voltage range with linear gate dependence of transport properties. S1 is kept at 0 V.

The simulated gate-voltage dependence of the drain voltages is plotted in Fig. 7.4 with the following results:

- For a source voltage of 10% of the maximum gate voltage, the characteristic is close to that with uniform carrier density and anisotropy across the device.

- With increasing source voltage, however, the crossing voltage increases, the logic swing of voltage at D1 and D2 for maximum gate bias decreases, and the characteristic becomes more and more asymmetric.

[2] The actual gate voltage in the experiment range was +1 to -3 V. This fact, however, does not invalidate the following discussion which is based on the ratio of applied source voltage at S2 and gate potential. In reality, optimizing the gate dielectrics (thinner, higher dielectric constant) can reduce the gate voltage range required to achieve the same effect.

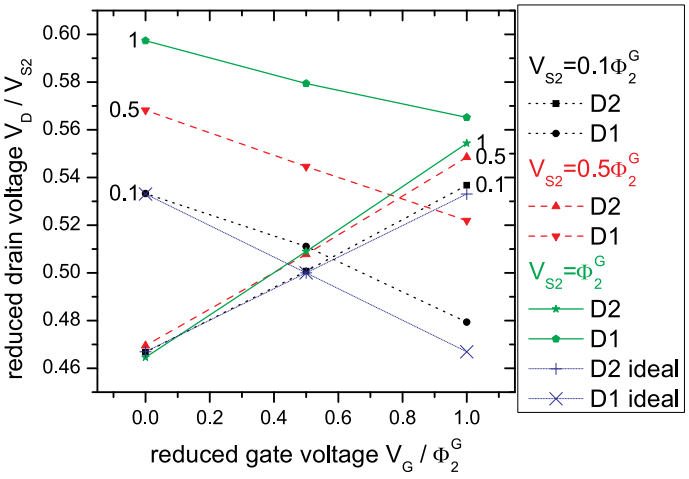

Figure 7.4: X device at different high source voltages. Simulated reduced drain voltage dependence on gate voltage for source voltage of 10%, 50%, and 100% of maximum gate voltage. The characteristics for negligible source voltage ("ideal") is given as reference. The simulation is based on the measured transport characteristics of my InAs quantum wires. Labels at the curves denote the respective source voltage.

- As soon as the source voltage equals the maximum gate voltage ($V_{S2} = \Phi_2^G$), the voltages of D1 and D2 do not cross any more, and the functionality is lost.

7.3 Geometry tuning for high source voltage

Changing the aspect ratio of the x device can restore its functionality for high source voltage. This is exemplified for the case of source voltage equal to the maximum gate voltage Φ_2^G. Simulations for different aspect ratios were done and the results are given in Fig. 7.5 allowing for the following conclusions.

- Apparently, a change of aspect ratio can shift the drain voltage characteristics up and down but leaves the slopes unchanged.

- As seen in the previous section, with optimum aspect ratio (2.78) for the low voltage situation the x device does not work in the present case.

- Reducing the aspect ratio, therefore, improves the situation with an optimum aspect ratio of 2.25. (Vice versa, at this value the device does not work any more in the low-voltage case.) At the optimum aspect ratio, the drain voltages at (D1, D2) are $(0.561\ V_{S2}, 0.497\ V_{S2})$

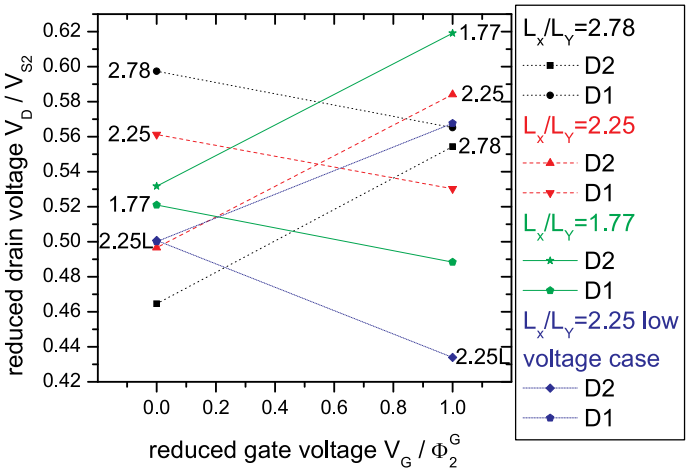

Figure 7.5: X device at high source voltage equal to maximum gate voltage. Simulated reduced drain voltage dependence on aspect ratio. The characteristics for negligible source voltage ("low voltage case") is given as reference. The simulation is based on the measured transport characteristics of my InAs quantum wires. Labels at the curves denote the respective aspect ratio.

at zero gate bias, and $(0.530\ V_{S2}, 0.584\ V_{S2})$ at maximum gate bias. In contrast to the low voltage case this is worse because ΔV decreases from $0.066\ V_{S2}$ to only $0.561\ V_{S2} - 0.530\ V_{S2} = 0.031\ V_{S2}$.

- Decreasing the aspect ratio further, e.g. to 1.77, also leads to a loss of functionality because the voltages do not cross any more.

7.4 Device optimization - coefficient wishlist

Even though this magnitude of ΔV based on my coupled quantum wires clearly does not meet the specification of today's VLSI logics applications, other logic implementations with lower required ΔV than that for VLSI circuits are conceivable. On the other hand, as yet unexplored, anisotropic systems could be developed with the large ratio α of maximum anisotropy to minimum anisotropy necessary to result in a logic swing ΔV compatible with today's VLSI circuit applications. How the properties of an anisotropic system influence the device performance is discussed as follows: The logic swing ΔV improves with increasing α. For a given α, the optimum results are obtained for source voltages much lower than the gate voltage. If source voltages V_{S2} are in the range of the maximum gate voltage Φ_2^G the device functionality can be maintained by adjusting the geometrical aspect ratio.

Nevertheless, the performance is always worse than in the low-voltage case.

An additional analysis of the case $V_{S2} = \Phi_2^G$ was done varying the coefficients c defined in Eq. 7.4 but maintaining the same range of transport anisotropies. The dependencies shown in Fig. 7.6 were investigated numerically for a constant given ratio of anisotropies $\alpha = 2.29$, with a source voltage equal to the maximum gate potential, and the optimum aspect ratio for this case of 2.25. Unless otherwise stated, $c_n = -0.38$. Please note that for fixed α the coefficients c_x, c_y are interdependent. Different scenarios for the

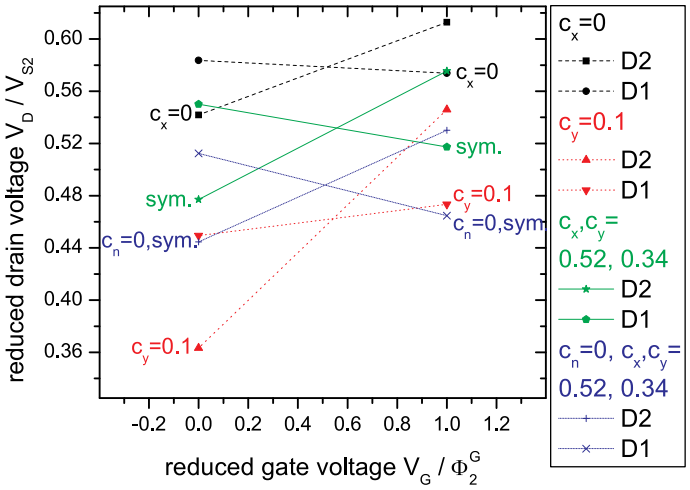

Figure 7.6: X device at high source voltage equal to maximum gate voltage. Simulated reduced drain voltage dependence on different parameters (coefficients c) describing the gate-voltage dependence of the transport characteristics. The transport anisotropy range is based on the measured transport characteristics of my InAs quantum wires. Labels at the curves indicate the respective parameters, "sym" denotes a symmetric distribution of the gate-controlled anisotropy change on the gate-controlled change of both principal mobilities.

gate-dependent principal mobilities, which all result in the same gate dependent change of anisotropy α, are represented by the characteristics "$c_x = 0$", "$c_y = -0.1$", and "$c_x = -0.52$". These are briefly discussed on the basis of Fig. 7.6.

- In the case of $c_x = 0$, the mobility μ_x remains constant, and the resulting ΔV reaches only a modest 0.0098 V_{S2}.
- The opposite case of $c_y = -0.1$ with an almost constant μ_y leads to a complete loss of functionality because the D1 and D2 characteristics are inclined into the same direction.

- In the optimum case of $c_x = 0.52$ the anisotropy change α is symmetrically distributed among μ_x and μ_y, with a resulting ΔV of 0.033 V_{S2}.
- A reduced dependence of the carrier density on the gate voltage but maintaining the dependence of mobility on gate voltage can still improve the situation. In the limit of no change of carrier concentration with gate voltage ($c_n = 0$) a maximum ΔV of 0.048 V_{S2} is obtained for $c_x = -0.52$, which is still smaller than the value ΔV of 0.066 V_{S2} for the low voltage situation.

As result, the performance can be optimized by having the change of anisotropy distributed symmetrically among μ_x and μ_y, and minimizing the change of carrier concentration necessary for the anisotropy change.

7.5 Conclusion

In summary, an electronic 5-terminal switching device based on gate-controlled transport anisotropy is proposed and investigated. By means of a gate voltage the two output voltages can be contrariwise adjusted to values between the two input voltages yielding a possible logic application as an exchange gate. The device performance was simulated as a function of range of gate-adjustable transport anisotropy. A realization based on laterally-coupled self-organized InAs quantum wires with gate-controlled transport anisotropies from 5.6 to 12 was experimentally investigated. The data show that this quantum wire system is suitable for a realization of this device. An extended analysis that includes high source voltages (in the range of the gate voltage), necessary for fast switching times, elucidate the limits and opportunities for optimization of this device.

Chapter 8

Summary

The growth and anisotropic transport properties of self-assembled InAs nanostructures, ranging from quantum wells, over quantum wires, to quantum dots were investigated.

Self-assembled InAs nanostructures were grown by gas-source molecular beam epitaxy on InP(001) substrates with focus on the influence of misorientation on the nanostructure shape. Surface steps on misoriented substrate were found to play a decisive role in the self-organized formation, shape, and alignment of InAs nanostructures. Most prominent is the formation of quantum dots on substrates misoriented toward $[\bar{1}10]$ and [100] under a wide range of growth conditions. On nominally oriented substrates, on the other hand, the growth conditions determine the resulting morphology: quantum wells, quantum wires, or quantum dots. The decisive phases of the nanostructure formation were identified and investigated by variation of the respective growth conditions. Quantum well, quantum wire, and quantum dot single layer and multi-layer samples were grown for the investigation of their optical and transport properties.

The emission and absorption properties related to interband transitions of the InAs/InP nanostructures were investigated with polarization-dependent photoluminescence and transmission spectroscopy. It was demonstrated that the hh1-e1 transition of my nanostructures covers a large wavelength range up to 2 μm, and including the technologically important 1.3 and 1.55 μm, at room temperature. Polarization dependent PL and transmission measurements show a preferential polarization in the $[\bar{1}10]$ direction for all QWrs and QDs. The degree of polarization for my QWrs and QDs is around 10% and 20%, respectively, suggesting an anisotropic QD shape. Polarization dependent transmission shows an additional transition that was identified as the lh1-e1 transition, and has the opposite polarization direction to the hh1-e1 transition. The shown optical properties suggest a high potential

of InAs/InP nanostructures for optical applications ranging from lasers and photodetectors to nonlinear optical applications.

Experimental methods to determine the anisotropic transport properties were explored. The application of conventional Hall-bar measurements for determining the transport properties *and principle directions* of anisotropic two dimensional carrier systems was theoretically and experimentally shown. An experimentally more convenient method to determine transport properties of isotropic carrier systems is the van der Pauw method. I investigated in detail how to extend this method to accurately characterize rectangularly shaped structures with anisotropic conductivity. An analytical correction is presented to obtain the anisotropy of the conductivity from the resistances measured with the van der Pauw method. In addition, numerical calculations were developed to show that the Hall coefficient used to determine the carrier density is correctly obtained from Van der Pauw measurements. This anisotropic correction technique was successfully tested on coupled quantum-wire structures with temperature-dependent anisotropy, and was routinely used for the characterization of the anisotropic transport in my samples. A versatile structure for Van der Pauw method to extend the measurable anisotropy range of the square shaped structure with corner contacts, and to reduce the disadvantages compared to Hall-bar structures was proposed, simulated, and experimentally demonstrated. The developed numerical method was further used to elucidate the effect of finite-size-contact placement on the Hall voltage, and the effect of geometry of micro-Hall devices on electric field distribution.

The in-plane transport of electrons and holes in large ensembles of InAs nanostructures, comprising quantum wires, quantum dashes, quantum dots, and quantum wells as reference, was investigated. The transport of quantum wire-, quantum dash- and quantum dot containing samples is highly anisotropic with the principal axes of conductivity aligned to the <110> directions. The direction of higher mobility is $[\bar{1}10]$, which is parallel to the direction of the quantum wires. In extreme cases, the anisotropies exceed 30 for electrons, and 100 for holes. The data is discussed in terms of anisotropic 2D carrier systems, and in terms of a coupled 1D or 0D system. The temperature dependence and carrier-density dependence of mobility was analyzed with the following results:
In the anisotropic 2D framework, the dominating scattering mechanisms at low temperature are remote-impurity scattering in the parallel direction for quantum wires, and interface-roughness scattering in both directions for quantum dots, and in the orthogonal direction for quantum wires, -dashes. In p-type samples, though, the hole transport in the orthogonal direction cannot be described by scattering but is described as hopping between lat-

erally localized states. In the coupled nanostructure framework, the transport anisotropy is demonstrated to result from *directionally anisotropic tunnel coupling* between adjacent nanostructures rather than from the nanostructure shape anisotropy. An empirical model describing the transport in coupled nanostructures was developed to determine the direction dependent coupling strengths from the experimental data.

The weak-localization contribution to conductivity in quantum wire and quantum dot samples is successfully modeled by regarding the system as a 2DEG with anisotropic conductivities. The anisotropy of weak localization has the same value as the anisotropy of the total conductivity for values as large as 38; confirming the theory for high anisotropy in 2 dimensions. The independence of dephasing time, extracted from the weak localization data, on the actual morphology and coupling strength (carrier density) indicates a a strong coupling and elastic nanostructure-nanostructure scattering.

As potential application of the coupled quantum wires, an electronic 5-terminal switching device based on gate-controlled transport anisotropy is proposed and investigated. By means of a gate voltage the two output voltages can be contrariwise adjusted to values between the two input voltages yielding a possible logic application as an exchange gate. The device performance was simulated as a function of range of gate-adjustable transport anisotropy. A realization based on laterally-coupled self-organized InAs quantum wires with gate-controlled transport anisotropies from 5.6 to 12 was experimentally investigated. The data show that this quantum wire system is suitable for a realization of this device.

Bibliography

[1] A. Ponchet and A. Le Corre and H. L'Haridon and B. Lambert, and S. Salaün. Relationship between self-organization and size of InAs islands on InP(001) grown by gas-source molecular beam epitaxy. *Appl. Phys. Lett.*, 67(13):1850–1852, September 1995.

[2] B. Alén, J. Martínez-Pastor, A. García-Cristobal, L. González, and J. M. García. Optical transitions and excitonic recombination in InAs/InP self-assembled quantum wires. *Appl. Phys. Lett.*, 78(25): 4025–4027, June 2001.

[3] B. Alén, J. Martínez-Pastor, L. González, J. M. García, S. I. Molina, A. Ponce, and R. García. Size-filtering effects by stacking InAs/InP (001) self-assembled quantum wires into multilayers. *Phys. Rev. B*, 65: 241301R(1–4), May 2002.

[4] C. Nì. Allen, P. J. Poole, P. Marshall, J. Fraser, S. Raymond, and S. Fafard. InAs self-assembled quantum-dot lasers grown on (100) InP. *Appl. Phys. Lett.*, 80:3629–3631, 2002.

[5] R. S. Allgaier. New Method for Computing the Weak-Field Hall Coefficient. *Phys. Rev.*, 165:775–768, 1968.

[6] S. Anantathanasarn, R. Nötzel, P. J. van Veldhoven, T. J. Eijkemans, and J. H. Wolter. Wavelength-tunable (1.55-mu m region) InAs quantum dots in InGaAsP/InP (100) grown by metal-organic vapor-phase epitaxy. *J. Appl. Phys.*, 98:013503(1–7), July 2005.

[7] S. Anantathanasarn, R. Nötzel, P. J. van Veldhoven, F. W. M. van Otten, Y. Barbarin, G. Servanton, T. de Vries, E. Smalbrugge, E. J. Geluk, T. J. Eijkemans, E. A. J. M. Bente, Y. S. Oei, M. K. Smit, and J. H. Wolter. Lasing of wavelength-tunable (1.55um region) InAs/InGaAsP/InP(100) quantum dots grown by metal organic vapor-phase epitaxy. *Appl. Phys. Lett.*, 89:073115(1–3), 2006.

[8] T. Ando. Self-consistent results for a GaAs/AlxGa1-xAs heterojunction. II. Low temperature mobility. *J. Phys. Soc. Jpn.*, 51:3900–3907, 1982.

[9] T. Ando, A. B. Fowler, and F. Stern. Electronic properties of two-dimensional systems. *Rev. Mod. Phys.*, 54:437–672, 1982.

[10] Y. Arakawa and H. Sakaki. Multidimensional quantum well laser and temperature dependence of its threshold current. *Appl. Phys. Lett.*, 40: 939–941, 1982.

[11] G. Bastard, E. E. Mendez, L. L. Chang, and L. Esaki. Exciton binding energy in quantum wells. *Phys. Rev. B*, 26:1974–1979, 1982.

[12] C. W. J. Beenakker and H. van Houten. *Solid State Physics, Volume 44*. Academic Press, New York, 1991.

[13] J. M. Benoit, L. Le Gratiet, G. Beaudoin, A. Michon, G. Saint-Girons, R. Kuszelewicz, and I. Sagnesa. Nanoepitaxy of InAs/InP quantum dots by metalorganic vapor phase epitaxy for 1.55 μm emitters. *Appl. Phys. Lett.*, 88:041113(1–3), January 2006.

[14] R. Benzaquen, M. Benzaquen, S. Charbonneau, P. J. Poole, T. Sudersena Rao, C. Lacelle, A. P. Roth, and R. Leonelli. Evidence from electrical transport and photoluminescence spectroscopy of a band of localized deep donors in high-purity n-type InP grown by chemical-beam epitaxy. *Phys. Rev. B*, 50:16964–16972, 1994.

[15] O. Bierwagen. Wachstum und Transportuntersuchungen an selbstorganisierten Quantendrähten im InAs/InP Materialsystem. Master's thesis, Humboldt-Universität zu Berlin, September 2001.

[16] O. Bierwagen and W. T. Masselink. Self-organized growth of InAs quantum wires and dots on InP(001): The role of vicinal substrates. *Appl. Phys. Lett.*, 86:113110(1–3), March 2005.

[17] O. Bierwagen, C. Walther, W. T. Masselink, and K.-J. Friedland. Weak localization in laterally coupled quantum wires. *Phys. Rev. B*, 67: 195331–195335, 2003.

[18] O. Bierwagen, R. Pomraenke, S. Eilers, and W. T. Masselink. Mobility and carrier density in materials with anisotropic conductivity revealed by van der Pauw measurements. *Phys. Rev. B*, 70:165307–1 – 165307–6, 2004.

[19] D. Bimberg, M. Grundmann, and N. N. Ledentsov. *Quantum Dot Heterostructures*. Wiley, 1999.

[20] D. J. Bishop, R. C. Dynes, B. J. Lin, and D. C. Tsui. Anisotropy in weakly localized electronic transport: A parameter-free test of the scaling theory of localization. *Phys. Rev. B*, 30:3539–3541, 1984.

[21] P. Blood and J. W. Orton. *Techniques of Physics: 14, THE ELECTRICAL CHARACTERIZATION OF SEMICONDUCTORS: MAJORITY CARRIERS AND ELECTRON STATES*. Academic Press, 1992.

[22] U. Bockelmann and G. Bastard. Interband absorption in quantum wires. I. Zero-magnetic field case. *Phys. Rev. B*, 45:1688–1699, 1992.

[23] M. Borgstrom, L. Samuelson, W. Seifert, A. Mikkelsen, L. Ouattara, and E. Lundgren. Spontaneous InAs quantum dot nucleation at strained InP/GaInAs interfaces. *Appl. Phys. Lett.*, 83(23):4830–4832, December 2003.

[24] J. Brault, M. Gendry, G. Grenet, G. Hollinger, Y. Desières, and T. Benyattou. Role of buffer surface morphology and alloying effects on the properties of InAs nanostructures grown on InP(001). *Appl. Phys. Lett.*, 73(20):2932–2934, November 1998.

[25] J. Brault, M. Gendry, G. Grenet, G. Hollinger, J. Olivares, B. Salem, T. Benyattou, and G. Bremond. Surface effects on shape, self-organization and photoluminescence of InAs islands grown on InAlAs/InP(001). *J. Appl. Phys.*, 92(1):506–510, July 2002.

[26] W. Braun. *Applied RHEED*. Springer, 1999.

[27] Ethan H. Cannon, Feodor V. Kusmartsev, Kirill N. Alekseev, and David K. Campbell. "". *Phys. Rev. Lett.*, 85:1302–1305, 2000.

[28] N. Carlsson, T. Junno, L. Montelius, M.-E. Pistol, L. Samuelson, and W. Seifert. Growth of self-assembled InAs and InAs(x)P(1-x) dots on InP by metalorganic vapour phase epitaxy. *J. Cryst. Growth*, 191: 347–356, 1998.

[29] N. Cavassilas, F. Aniel, P. Boucaud, R. Adde, H. Maher, J. Deécobert, and A. Scavennec. Electroluminescence of composite channel InAlAs/InGaAs/InP/InAlAs high electron mobility transistor. *J. Appl. Phys.*, 87:2548–2552, 2000.

[30] C. Çelebi, J. M. Ulloa, P. M. Koenraad A. Simon, A. Letoublon, and N. Bertru. Capping of InAs quantum dots grown on (311)B InP studied by crosssectional scanning tunneling microscopy. *Appl. Phys. Lett.*, 89: 023119(1–3), 2006.

[31] N. Chauvin, B. Salem, G. Bremond, G. Guillot, C. Bru-Chevallier, and M. Gendry. Size and shape effects on excitons and biexcitons in single InAs/InP quantum dots. *J. Appl. Phys.*, 100:071702(1–5), 2006.

[32] Y. Chen and J. Washburn. Structural Transition in Large-Lattice-Mismatch Heteroepitaxy. *Phys. Rev. Lett.*, 77:4046–4049, 1996.

[33] D. Chithrani, R. L. Williams, J. Lefebvre, P. J. Poole, and G. C. Aers. Optical spectroscopy of single, site-selected, InAs/InP self-assembled quantum dots. *Appl. Phys. Lett.*, 84:978–980, February 2004.

[34] T. H. Chiu, W. T. Tsang, J. E. Cunningham, and Jr. A. Robertson. Gallium- and arsenic-induced oscillations of intensity of reflection high-energy electron diffraction in the growth of (001)GaAs by chemical beam epitaxy. *J. Appl. Phys.*, 62:2303–2307, 1987.

[35] D. Colman, R. T. Bate, and J. P. Mize. Mobility anisotropy and piezoresistance in Silicon p-type inversion layers. *J. Appl. Phys.*, 39: 1923–1931, 1968.

[36] C. Cornet, C. Labbé, H. Folliot, N. Bertru, O. Dehaese, J. Even, A. Le Corre, C. Paranthoen, C. Platz, and S. Loualiche. Quantitative investigations of optical absorption in InAs/InP(311) quantum dots emitting at 1.55um wavelength. *Appl. Phys. Lett.*, 85:5685–5687, 2004.

[37] S. Cortez, O. Krebs, P. Voisin, and J. M. Gérard. Polarization of the interband optical dipole in InAs/GaAs self-organized quantum dots. *Phys. Rev. B*, 63:233306(1–4), 2001.

[38] M. A. Cotta, C. A. C. Mendonça, E. A. Meneses, , and M. M. G. de Carvalho. On the onset of InAs islanding on InP: influence of surface steps. *Surface Science*, 388:84–91, 1997.

[39] Dan Dalacu, Simon Frédérick, Alexei Bogdanov, Philip J. Poole, Geof C. Aers, Robin L. Williams, Murray W. McCutcheon, and Jeff F. Young. Fabrication and optical characterization of hexagonal photonic crystal microcavities in InP-based membranes containing InAs/InP quantum dots. *J. Appl. Phys.*, 98:023101(1–5), July 2005.

[40] J. E. Dijkstra and W. Th. Wenckebach. Effects of strain and alloying on the Hall scattering factor for holes in Si and Si(1-x)Gex. *J. Appl. Phys.*, 85:1587–1590, 1999.

[41] J. V. DiLorenzo, R. Dingle, M. Feuer, A. C. Gossard, R. Hendel, J. C. M. Hwang, A. Kastalsky, V. G. Keramidas, R. A. Kiehl, and P. O'Connor. Material and device considerations for selectively doped heterojunction transistors. *IEEE IEDM*, 25:578–581, 1982.

[42] R. Dingle, H. L. Störmer, A. C. Gossard, and W. Wiegmann. Electron mobilities in modulation-doped semiconductor heterojunction superlattices. *Appl. Phys. Lett.*, 33:665–667, 1978.

[43] T. J. Drummond, H. Morkoç, and A. Y. Cho. Dependence of electron mobility on spatial separation of electrons and donors in AlxGa1-xAs/GaAs heterostructures. *J. Appl. Phys.*, 52:1380–1386, 1981.

[44] V. Duez, O. Vanbésien, D. Lippens, D. Vignaud, X. Wallart, and F. Mollot. Type II and mixed type I-II radiative recombinations in AlInAs-InP heterostructures. *J. Appl. Phys.*, 85:2202–2206, 1999.

[45] E. Dupuy, P. Regreny, Y. Robach, M. Gendry, N. Chauvin, E. Tranvouez, G. Bremond, C. Bru-Chevallier, and G. Patricarche. Low density of self-assembled InAs quantum dots grown by solid-source molecular beam epitaxy on InP(001). *Appl. Phys. Lett.*, 89:123112(1–3), 2006.

[46] S. Eilers. Herstellung und Charakterisierung von Submikro-Hall-Bauelementen. Master's thesis, Humboldt-Universität zu Berlin, October 2004.

[47] A. Endo and Y. Iye. Measurement of Anisotropic Transport Using Unidirectional Lateral Superlattice with Square Geometry. *J. Phys. Soc. Jpn.*, 71:2067, 2002.

[48] J. M. Fastenau, D. Lubyshev, Y. Wu, C. Doss, and W. K. Liu. Comparative studies of the epireadiness of 4 in. InP substrates for molecular-beam epitaxy growth. *J. Vac. Sci. Technol. B*, 23:1262–1266, 2005.

[49] C. T. Foxon, B. A. Joyce, and M. T. Norris. Composition effects in the growth of Ga(In)As(y)P(1-y) alloys by MBE. *J. Cryst. Growth*, 49: 132–140, 1980.

[50] S. Fréchengues, N. Bertru, V. Drouot, B. Lambert, S. Robinet, S. Loualiche, D. Lacombe, and A. Ponchet. Wavelength tuning of

InAs quantum dots grown on (311)B InP. *Appl. Phys. Lett.*, 74(22): 3356–3358, May 1999.

[51] K.-J. Friedland, H.-P. Schönherr, R. Nötzel, and K. H. Ploog. Selective Control of Electrons in Quantum Wires Formed by Highly Uniform Multiatomic Step Arrays on GaAs(331) Substrates. *Phys. Rev. Lett.*, 83:156–159, 1999.

[52] K.-J. Friedland, M. Hoerike, R. Hey, I. Shlimak, and L. Resnick. Giant persistent photoconductivity induced crossover from strong to weak localization in Si-delta-doped GaAs compensated with Be acceptors. *Physica A*, 302:375–381, 2001.

[53] K.-J. Friedland, R. Hey, O. Bierwagen, H. Kostial, Y. Hirayama, and K. H. Ploog. Conductance anisotropy of high-mobility, modulation-doped GaAs single quantum wells. *Physica E*, 13:642 – 645, 2002.

[54] David Fuster, María Ujué González, Luisa González, Yolanda González, Teresa Ben, Arturo Ponce, and Sergio I. Molina. Stacking of InAs/InP(001) quantum wires studied by in situ stress measurements: Role of inhomogeneous stress fields. *Appl. Phys. Lett.*, 84(23): 4723–4725, June 2004.

[55] David Fuster, María Ujué González, Luisa González, Yolanda González, Teresa Ben, Arturo Ponce, Sergio I. Molina, and Juan Martínez-Pastor. Size control of InAs/InP(001) quantum wires by tailoring P/As exchange. *Appl. Phys. Lett.*, 85(8):1424–1426, August 2004.

[56] J. M. Gaines, P. M. Petroff, H. Kroemer, R. J. Simes, R. S. Geels, and J. H. English. Molecular-beam epitaxy growth of tilted GaAs/AlAs superlattices by depostion of fractional monolayers on vicinal (001) substrates. *J. Vac. Sci. Technol. B*, 6:1378–1381, 1988.

[57] J. M. García, L. González, M. U. González, J .P. Silveira, Y. González, and F. Briones. InAs/InP(001) quantum wire formation due to anisotropic stress relaxation: in situ stress measurements. *J. Cryst. Growth*, 227–228:975–979, 2001.

[58] B. Gelmont and M. S. Shur. Hall factor for ionized impurity scattering. *J. Appl. Phys.*, 78:2846–2847, 1995.

[59] M. Gendry, C. Monat, J. Brault, P. Regreny, G. Hollinger, B. Salem, G. Guillot, T. Benyattou, C. Bru-chevallier, G. Bremond, and

O. Marty. From large to low height dispersion for self-organized InAs quantum sticks emitting at 1.55 μm on InP (001). *J. Appl. Phys.*, 95 (9):4761–4763, May 2004.

[60] A. Gold. Scattering time and single-particle relaxation time in a disordered two-dimensional electron gas. *Phys. Rev. B*, 38:10798–10810, 1988.

[61] Q. Gong, R. Nötzel, P. J. van Veldhoven, T. J. Eijkemans, and J. H. Wolter. Wavelength tuning of InAs quantum dots grown on InP(100) by chemical-beam epitaxy. *Appl. Phys. Lett.*, 84:275–277, 2004.

[62] L. González, J. M. García, R. García, F. Briones, J. Martínez-Pastor, and C. Ballesteros. Influence of buffer-layer surface morphology on the self-organized growth of InAs on InP(001) nanostructures. *Appl. Phys. Lett.*, 76(9):1104–1106, February 2000.

[63] M. U. González, L. González, J. M. García, Y. González, J. P. Silveira, and F. Briones. Stress evolution aspects during InAs/InP (001) quantum wires self-assembling. *Microel. J.*, 35:13–17, 2004.

[64] F. Grosse and M. F. Gyure. Island and Step Morphology in InAs(001) Homoepitaxy. *phys. stat. sol.*, 234:338–345, 2002.

[65] F. Grosse and M. F. Gyure. Ab initio based modeling of III-V semiconductor surfaces: Thermodynamic equilibrium and growth kinetics on atomic scales. *Phys. Rev. B*, 66:075320(1–13), 2002.

[66] F. Grosse, W. Barvosa-Carter, J. Zink, M. Wheeler, and M. F. Gyure. Arsenic Flux Dependence of Island Nucleation on InAs(001). *Phys. Rev. Lett.*, 89:116102(1–4), 2002.

[67] H. R. Gutiérrez, M. A. Cotta, and M. M. G. de Carvalho. Faceting evolution during self-assembling of InAs/InP quantum wires. *Appl. Phys. Lett.*, 79(23):3854–3856, December 2001.

[68] H. R. Gutiérrez, M. A. Cotta, J. R. R. Bortoleto, and M. M. G. de Carvalho. Role of group V exchange on the shape and size of InAs/InP self-assembled nanostructures. *J. Appl. Phys.*, 92(12):7523–7526, December 2002.

[69] H. R. Gutiérrez, R. Magalhães-Paniago, J. R. R. Bortoleto, and M. A. Cotta. Stability of self-assembled InAs/InP nanostructures: kinetic and thermodynamic analysis. *MRS Fall Meeting, Boston, USA*, 2003.

[70] H. R. Gutiérrez, R. Magalhães-Paniago, J. R. R. Bortoleto, and M. A. Cotta. Three-dimensional mapping of the strain anisotropy in self-assembled quantum-wires by grazing incidence x-ray diffraction. *Appl. Phys. Lett.*, 85(16):3581–3583, October 2004.

[71] E. H. Hall. On a New Action of the Magnet on Electric Currents. *American Journal of Mathematics*, 2:287–292, 1879.

[72] Paul Harrison. *Quantum wells, wires and dots : theoretical and computational physics.* Wiley, 1999.

[73] F. Hatami, L. Schrottke, and W. T. Masselink. Radiative recombination from InP quantum dots on (100)GaP. *Appl. Phys. Lett.*, 78: 2163–2165, 2001.

[74] Fariba Hatami. *Indium Phosphide Quantum Dots in GaP and in* $In_{0.48}Ga_{0.52}P$. PhD thesis, Humboldt-Universität zu Berlin, 2002.

[75] J. J. Heremans, M. B. Santos, K. Hirakawa, and M. Shayegan. Mobility anisotropy of two-dimensional hole systems in (311)A GaAs/AlxGa1-xAs heterojunctions. *J. Appl. Phys.*, 76:1980–1982, 1994.

[76] M. A. Herman and H. Sitter. *Molecular Beam Epitaxy.* Springer, 1996.

[77] Conyers Herring and Erich Vogt. Transport and Deformation-Potential Theory for Many-Valley Semiconductors with Anisotropic Scattering. *Phys. Rev.*, 101:944–961, 1956.

[78] M. Holm, M.-E. Pistol, and Craig Pryor. Calculations of the electronic structure of strained InAs quantum dots in InP. *J. Appl. Phys.*, 92(2): 932–936, July 2002.

[79] H. Q. Hou, C. W. Tu, and S. N. G. Chu. Gas-source molecular beam epitaxy growth of highly strained device quality InAsP/InP multiple quantum well structures. *Appl. Phys. Lett.*, pages 2954–2956, 1991.

[80] Wen Chang Huang, Tan Fu Lei, and Chung Len Lee. AuGePt ohmic contact to n-type InP. *J. Appl. Phys.*, 79:9200–9205, 1996.

[81] Jun Inoue, Toshiro Isu, Kouichi Akahane, and Masahiro Tsuchiya. Saturable absorption of highly stacked InAs quantum dot layer in 1.5um band. *Appl. Phys. Lett.*, 89:151117(1–3), 2006.

[82] S. K. Jung, S. W. Hwang, B. H. Choi, S. I. Kim, J. H. Park, Y. Kim, E. K. Kim, and S.-K. Min. Direct electronic transport through an ensemble of InAs self-assembled quantum dots. *Appl. Phys. Lett.*, 74: 714–716, 1999.

[83] B. Junno, S. Jeppesen, M. S. Miller, and L. Samuelson. A comparison of RHEED reconstruction phases on (100) InAs, GaAs and InP. *J. Cryst. Growth*, 164:66–70, 1996.

[84] P. R. C. Kent, Gus L. W. Hart, and Alex Zunger. Biaxial strain-modified valence and conduction band offsets of zinc-blende GaN, GaP, GaAs, InN, InP, and InAs, and optical bowing of strained epitaxial InGaN alloys. *Appl. Phys. Lett.*, 81:4377–4379, 2002.

[85] Gil-Ho Kim, D. A. Ritchie, C.-T. Liang, G. D. Lian, J. Yuan, M. Pepper, and L. M. Brown. Transport properties of two-dimensional electron gases containing linear ordering InAs self-assembled quantum dots. *Appl. Phys. Lett.*, 78:3896–3898, 2001.

[86] A. Knauer, E. Richter, and M. Weyers. Effect of storage time of epi-ready InP:Fe substrates on the quality of metalorganic vapour phase epitaxial grown InP. *J. Cryst. Growth*, 146:549–553, 1995.

[87] N. Kobayashi and Y. Kobayashi. In situ control of heterointerface quality in MOVPE by surface photo-absorption. *J. Cryst. Growth*, 124:525–530, 1992.

[88] H. Kostial. . *private communication*, 2006.

[89] V. A. Kul'bachinskii, R. A. Lunin, V. G. Kytin, A. V. Golikov, A. V. Demin, V. A. Rogozin, B. N. Zvonkov, S. M. Nekorkin, and D. O. Filatov. Electrical transport and persistent photoconductivity in quantum dot layers in InAs/GaAs structures. *J. Exp. Theo. Phys. (JETP)*, 93: 815–823, 2001.

[90] V. A. Kul'bachinskii, R. A. Lunin, V. A. Rogozin, V. G. Mokerov, K. Kindo, and A. de Visser. Lateral electronic transport in short-period InAs/GaAs superlattices at the threshold of quantum dot formation. *Semiconductors*, 37:70–76, 2003.

[91] Vas. P. Kunets. *Micro-Hall Devices Based on High-Electron-Velocity Semiconductors*. PhD thesis, Humboldt-Universität zu Berlin, 2004.

[92] Vas. P. Kunets, W. Hoerstel, H. Kostial, H. Kissel, U. Müller, G.G. Tarasov, Yu. I. Mazur, Z. Ya. Zhuchenko, and W.T. Masselink. High electric field performance of $Al_{0.3}Ga_{0.7}As/GaAs$ and $Al_{0.3}Ga_{0.7}As/GaAs/In_{0.3}Ga_{0.7}As$ quantum well micro-Hall devices. *Sens. Actuators A*, 101:62–68, 2002.

[93] Vas. P. Kunets, U. Müller, J. Dobbert, R. Pomraenke, G. G. Tarasov, H. Kostial, H. Kissel, Yu. I. Mazur, and W. T. Masselink. Generation-recombination noise in doped-channel $Al_{0.3}Ga_{0.7}As/GaAs/In_{0.2}Ga_{0.8}As$ quantum well micro-Hall devices. *J. Appl. Phys.*, 94:7590–7593, 2003.

[94] Vas. P. Kunets, Yu. I. Mazur, G. J. Salamo, O. Bierwagen, and W. T. Masselink. Doped-channel micro-Hall devices: Size and geometry effects. *J. Appl. Phys.*, 98:094503–1–094503–5, 2005.

[95] V. P. LaBella, Z. Ding, D. W. Bullock, C. Emery, and P. M. Thibado. Reflection high-energy electron diffraction and scanning tunneling microscopy study of InP(001) surface reconstructions. *J. Vac. Sci. Technol. A*, 18:1492–1496, 2000.

[96] L. Landau. . *Z. Physik*, 64:629, 1930.

[97] L. Landin, H. Pettersson, M. Kleverman, M. Borgström, X. Zhang, W. Seifert, and L. Samuelson. Interband transitions in InAs quantum dots in InP studied by photoconductivity and photoluminescence techniques. *J. Appl. Phys.*, 95(12):8007–8010, June 2004.

[98] P. A. Lee and T. V. Ramakrishnan. Disordered electronic systems. *Rev. Mod. Phys.*, 57:287–337, 1985.

[99] A. Létoublon, V. Favre-Nicolin, H. Renevier, M.G. Proietti, C. Monat, M. Gendry, O. Marty, and C. Priester. Strain, Size, and Composition of InAs Quantum Sticks Embedded in InP Determined via Grazing Incidence X-Ray Anomalous Diffraction. *Phys. Rev. Lett.*, 92(18): 186101–186104, May 2004.

[100] M. Levinshtein, S. Rumyantsev, and M. Shur. *Handbook Series on Semiconductor Parameters*. World Scientific, 1996.

[101] A. Y. Lew, S. L. Zuo, E. T. Yu, and R. H. Miles. Correlation between atomic-scale structure and mobility anisotropy in InAs/Ga1-xInxSb superlattices. *Phys. Rev. B*, 57:6534–6539, 1998.

[102] C. H. Li, L. Li, D. C. Law, S. B. Visbeck, and R. F. Hicks. Arsenic adsorption and exchange with phosphorus on indium phosphide (001). *Phys. Rev. B*, 65:205322(1–7), May 2002.

[103] H. Li, J. Wu, Z. G. Wang, and T. Daniels-Race. High-density InAs nanowires realized *in situ* on (100) InP. *Appl. Phys. Lett.*, 75(8):1173–1175, August 1999.

[104] H. Li, T. Daniels-Race, and M.-A. Hasan. Effects of the matrix on self-organization of InAs quantum nanostructures grown on InP substrates. *Appl. Phys. Lett.*, 80(8):1367–1369, February 2002.

[105] M. P. Lilly, K. B. Cooper, J. P. Eisenstein, L. N. Pfeiffer, and K. W. West. Evidence for an Anisotropic State of Two-Dimensional Electrons in High Landau Levels. *Phys. Rev. Lett.*, 82:394, 1999.

[106] David C. Look. *ELECTRICAL CHARACTERIZATION OF GaAs MATERIALS AND DEVICES*. WILEY, 1989.

[107] E. Finkmanand S. Maimon, V. Immer, G. Bahir, S. E. Schacham, F. Fossard, F. H. Julien, J. Brault, and M. Gendry. Polarized front-illumination response in intraband quantum dot infrared photodetectors at 77 K. *Phys. Rev. B*, 63:045323(1–7), 2001.

[108] L. Malikova, F. H. Pollak, R. A. Masut, P. Desjardins, and Lev G. Mourokh. Temperature dependent contactless electroreflectance study of intersubband transitions in a self-assembled InAs/InP (001) quantum dot structure. *J. Appl. Phys.*, 94(8):4995–4998, October 2003.

[109] H. Marchand, P. Desjardins, S. Guillon, J.-E. Paultre, Z. Bougrioua, R. Y.-F. Yip, and R. A. Masut. Metalorganic vapor phase epitaxy of coherent self-assembled InAs nanometer-sized islands in InP(001). *Appl. Phys. Lett.*, 71(4):527–529, July 1997.

[110] I. Mártil, A. del Prado, E. San Andrés, and G. González Díaz. Rapid thermally annealed plasma deposited SiNx:H thin films: Application to metal-insulator-semiconductor structures with Si, In0.53Ga0.47As, and InP. *J. Appl. Phys.*, 94:2642–2653, 2003.

[111] J.-Y. Marzin, J.-M. Gérard, A. Izraël, D. Barrier, and G. Bastard. Photoluminescence of Single InAs Quantum Dots Obtained by Self-Organized Growth on GaAs. *Phys. Rev. Lett.*, 73:716–719, 1994.

[112] W. T. Masselink, P. J. Pearah, J. Klem, C. K. Peng, H. Morkoç, G. D. Sanders, and Yia-Chung Chang. Absorption coefficient and exciton oscillator strengths in AlGaAs-GaAs superlattices. *Phys. Rev. B*, 32: 8027–8034, 1985.

[113] J. W. Matthews and A. E. Blakeslee. Defects in epitaxial multilayers, I. misfit dislocations. *J. Cryst. Growth*, 27:118–125, 1974.

[114] A. Mazuelas, L. González, J. M. García, Y. González, T. Schuelli, C. Priester, and H. T. Metzger. Strain determination in MBE-grown InAs quantum wires on InP. *Phys. Rev. B*, 73:045312(1–6), January 2006.

[115] T. Mimura, S. Hiyamizu, T. Fujii, and K. Nanbu. A new field-effect transistor with selectively doped GaAs/n-AlxGa1-xAs heterojunctions. *Jpn. J. Appl. Phys.*, 18:L225–L227, 1980.

[116] P. Miska, J. Even, C. Platz, B. Salem, T. Benyattou, C. Bru-Chevalier, G. Guillot, G. Bremond, Kh. Moumanis, F. H. Julien, O. Marty, C. Monat, and M. Gendry. Experimental and theoretical investigation of carrier confinement in InAs quantum dashes grown on InP(001). *J. Appl. Phys.*, 95(3):1074–1080, February 2004.

[117] J. M. Moison, M. Bensoussan, and F. Houzay. Epitaxial regrowth of an InAs surface on InP: An example of artificial surfaces. *Phys. Rev. B*, 34:2018–2021, 1986.

[118] J. Motohisa, M. Tanaka, and H. Sakaki. Anisotropic transport and nonparabolic miniband in a novel in-plane superlattice consisting of grid-inserted selectively-doped heterojunctions. *Appl. Phys. Lett.*, 55: 1214–1216, 1989.

[119] X. Mu, I. B. Zotova, Y. J. Ding, H. Yang, and G. J. Salamo. Observation of an anomalously large blueshift of the photoluminescence peak and evidence of band-gap renormalization in InP/InAs/InP quantum wires. *Appl. Phys. Lett.*, 79(8):1091–1093, August 2003.

[120] Y. Nakamura, S. Koshiba, and H. Sakaki. Large conductance anisotropy in a novel two-dimensional electron system grown on vicinal (111)B GaAs with multiatomic steps. *Appl. Phys. Lett.*, 69:4093–4095, 1996.

[121] M. Noguchi, K Hirakawa, and T. Ikoma. Intrinsic Electron Accumulation Layers on Reconstructed Clean InAs(100) Surfaces. *Phys. Rev. Lett.*, 66:2243–2246, 1991.

[122] R. Nötzel, D. Eissler, M. Hohenstein, and K. H. Ploog. Periodic mesoscopic step arrays by step bunching on high-index GaAs surfaces. *J. Appl. Phys.*, 74:431–435, 1993.

[123] L. Ö. Olsson, C. B. M. Andersson, M. C. Håkansson, J. Kanski, L. Ilver, and U. O. Karlsson. Charge Accumulation at InAs Surfaces. *Phys. Rev. Lett.*, 76:3626–3629, 1996.

[124] W. Ostwald. Über die vermeintliche Isometric des roten und gelbem Quacksilberoxyds und dieOberflächenspannung fester Körper. *Zeit. Phys. Chem.*, 34:495–503, 1900.

[125] J. H. G. Owen, W. Barvosa-Carter, and J. J. Zinck. Growth oscillation decay rates for control of III-V molecular beam epitaxy near stoichiometry. *Appl. Phys. Lett.*, 76:3070–3072, 2000.

[126] K. B. Ozanyan, P. J. Parbrook, M. Hopkinson, and C. R. Whitehouse. Static and growing InP and InAs surfaces: reflection-anisotropy spectroscopy under the conditions of solid-source MBE. *Thin Solid Films*, 364:6–11, 2000.

[127] T. Ozeki, B. X. Yang, and H. Hasegawa. A new method of flux calibration for gas source molecular beam epitaxy of InP and its application to migration enhanced epitaxy. *J. Cryst. Growth*, 150:602–606, 1995.

[128] P. Paki, R. Leonelli, L. Isnard, and R. A. Masut. Optical properties of submonolayer InAs/InP quantum dots on vicinal surfaces. *J. Appl. Phys.*, 86(12):6789–6792, December 1999.

[129] N. Pan, J. Carter, J. Elliott, H. Hendriks, S. Brierley, and K. C. Hsieh. Low temperature InAlAs buffer layers using trimethylarsenic and arsine by metalorganic chemical vapor deposition. *Appl. Phys. Lett.*, 63:3029–3031, 1993.

[130] M. B. Panish and H. Temkin. *Gas Source Molecular Beam Epitaxy: Growth and Properties of Phosphorus Containing III-V Heterostructures*. Springer Verlag, Berlin, 1993.

[131] C. Paranthoen, N. Bertru, O. Dehaese, A. Le Corre, S. Loualiche, B. Lambert, and G. Patriarche. Height dispersion control of InAs/InP

quantum dots emitting at 1.55 μm. *Appl. Phys. Lett.*, 78(12):1751–1753, March 2001.

[132] R. People and J. C. Bean. Calculation of critical layer thickness versus lattice mismatch for Ge(x)Si(1-x)/Si strained-layer heterostructures. *Appl. Phys. Lett.*, 47:322–324, 1985.

[133] H. Pettersson, R. J. Warburton, J. P. Kotthaus, N. Carlsson, W. Seifert, M.-E. Pistol, and L. Samuelson. Electronic structure of self-assembled InAs quantum dots in InP: An anisotropic quantum-dot system. *Phys. Rev. B*, 60(6):R11289–R11292, October 1999.

[134] H. Pettersson, L. Bååth, N. Carlsson, W. Seifert, and L. Samuelson. Optically induced charge storage and current generation in InAs quantum dots. *Phys. Rev. B*, 65:073304(1–4), January 2002.

[135] N. A. Poklonski, S. A. Vyrko, V. I. Yatskevich, and A. A. Kocherzhenko. A semiclassical approach to Coulomb scattering of conduction electrons on ionized impurities in nondegenerate semiconductors. *J. Appl. Phys.*, 93:9749–9752, 2003.

[136] R. Pomraenke. Charakterisierung von epitaktische gewachsenen selbstorganisierten InAs Quantendrähten auf InP. Master's thesis, Humboldt-Universität zu Berlin, March 2004.

[137] P. J. Poole, J. McCaffrey, R. L. Williams, J. Lefebvre, and D. Chithrani. Chemical beam epitaxy growth of self-assembled InAs/InP quantum dots. *J. Vac. Sci. Technol. B*, 19(4):1467–1470, July/August 2001.

[138] P. J. Poole, R. L. Williams, J. Lefebvre, and S. Moisa. Using As/P exchange processes to modify InAs/InP quantum dots. *J. Cryst. Growth*, 257:89–96, 2003.

[139] R. S. Popović. *HALL EFFECT DEVICES*. Adam Hilger, 1989.

[140] J. A. Prieto, G. Armalles, C. Priester, J. M. García, L. González, and R. García. Strain-induced optical anisotropy in self-organized quantum structures at the E1 transition. *Appl. Phys. Lett.*, 76(16):2197–2199, April 2000.

[141] C. E. Pryor and M.-E. Pistol. Band-edge diagrams for strained III-V semiconductor quantum wells wires and dots. *Phys. Rev. B*, 72: 205311(1–11), 2005.

[142] K. Rakennus, K. Tappura, T. Hakkarainen, H. Asonen, R. Laiho, S. J. Rolfe, and J. J. Dubowski. Interface effects on electrical properties of high purity InP grown by gas-source molecular beam epitaxy. *J. Cryst. Growth*, 110:910–914, 1991.

[143] A. Richter, M. Koch, T. Matsuyama, Ch. Heyn, and U. Merk. Transport properties of modulation-doped InAs-inserted-channel In(0.75)Al(0.25)As/In(0.75)Ga(0.25)As structures grown on GaAs substrates. *Appl. Phys. Lett.*, 77:3227–3229, 2000.

[144] A. Rudra, R. Houdré, J. F. Carlin, and M. Ilegems. Dynamics of island formation in the growth of InAs/InP quantum wells. *J. Cryst. Growth*, 136:278–281, 1994.

[145] H. Saito, K. Nishi, and S. Sugou. Ground-state lasing at room temperature in long-wavelength InAs quantum-dot lasers on InP(311)B substrates. *Appl. Phys. Lett.*, 78(3):267–269, January 2001.

[146] H. Sakaki. Scattering suppression and high-mobility effect of size-quantized electrons in ultrafine semiconductor wire structures. *Jpn. J. Appl. Phys.*, 19:L735–L738, 1980.

[147] H. Sakaki. Quantum wire superlattices and coupled quantum box arrays: A novel method to suppress optical phonon scattering in semiconductors. *Jpn. J. Appl. Phys.*, 28:L314–316, 1989.

[148] H. Sakaki, T. Noda, K. Hirakawa, M. Tanaka, and T. Matsusue. Interface roughness scattering in GaAs/AlGaAs quantum wells. *Appl. Phys. Lett.*, 51:1934–1936, 1987.

[149] Y. Sakuma, M. Takeguchi, K. Takemoto, S. Hirose, T. Usuki, and N. Yokoyama. Role of thin InP cap layer and anion exchange reaction on structural and optical properties of InAs quantum dots on InP (001). *J. Vac. Sci. Technol. B*, 23(4):1741–1746, July 2005.

[150] B. Salem, J. Olivares, G. Guillot, G. Bremond, J. Brault, C. Monat, M. Gendry, G. Hollinger, F. Hassen, and H. Maaref. Optical properties of self-assembled InAs quantum islands grown on InP(001) vicinal substrates. *Appl. Phys. Lett.*, 79(26):4435–4437, December 2001.

[151] B. Salem, T. Benyattou, G. Guillot, C. Bru-Chevallier, G. Bremond, C. Monat, G. Hollinger, and M. Gendry. Strong carrier confinement and evidence for excited states in self-assembled InAs quantum islands grown on InP(001). *Phys. Rev. B*, 66:193305(1–4), November 2002.

[152] Y. Sato and S. Sato. Simulation of the van der Pauw Measurement for Electically Anisotropic Semiconductors using the Finite-Element Method. *Jpn. J. Appl. Phys.*, 40:4256, 2001.

[153] S. Schmult, C. Gerl, U. Wurstbauer, C. Mitzkus, and W. Wegscheider. Carbon-doped high-mobility two-dimensional hole gases on (110) faced GaAs. *Appl. Phys. Lett.*, 86:202105(1–3), 2005.

[154] Hans-Peter Schönherr, Jörg Fricke, Zhichuan Niu, Klaus-Jürgen Friedland, Richard Nötzel, and Klaus H. Ploog. Uniform multiatomic step arrays formed by atomic hydrogen assisted molecular beam epitaxy on GaAs (331) substrates. *Appl. Phys. Lett.*, 72:566–568, 1998.

[155] R. Schwertberger, D. Gold, J. P. Reithmaier, and A. Forchel. Long-wavelength InP-based quantum-dash laser. *IEEE Photon. Technol. Lett.*, 14:735–737, 2002.

[156] M. Shayegan, H. C. Manoharan, S. J. Papadakis, and E. P. De Poortere. Anisotropic transport of two-dimensional holes in high Landau levels. *Physica E*, 6:40, 2000.

[157] V. A. Shchukin, D. Bimberg, V. G. Malyshkin, and N. N. Ledentsov. Vertical correlation and anticorrelation in multisheet arrays of two-dimensional islands. *Phys. Rev. B*, 57:12262–12274, 1998.

[158] H. Shibata and R. Terakado. A potential problem for point contacts on a two-dimensional anisotropic medium with an arbitrary resistivity tensor. *J. Appl. Phys.*, 66:4603, 1989.

[159] Hisashi Shibata and Jun ichi Oide. Analysis of the Hall effect device using an anisotropic material. *J. Appl. Phys.*, 88:4813–4817, 2000.

[160] N. Shtinkov, P. Desjardins, and R. A. Masut. Electronic states of ultra-thin InAs/InP (001) quantum wells: A tight-binding study of the effects of band offset, strain, and intermixing. *Phys. Rev. B*, 66:195303(1–8), November 2002.

[161] S. H. Simon. Comment on "Evidence for an Anisotropic State of Two-Dimensional Electrons in High Landau Levels". *Phys. Rev. Lett.*, 83: 4223, 1999.

[162] Jasprit Singh. *PHYSICS OF SEMICONDUCTORS AND THEIR HETEROSTRUCTURES.* McGraw-Hill, 1993.

[163] G. L. Snider, I.-H. Tan, and E. L. Hu. Electron states in mesa-etched one-dimensional quantum well wires. *J. Appl. Phys.*, 68:2849, 1990.

[164] A. Somers, W. Kaiser, J. P. Reithmaier, and A. Forchel. InP-based quantum dash lasers for broadband optical amplification and gas sensing applications. *Proc. IPRM 2005*, 2005.

[165] H. Z. Song, K. Akahane, S. Lan, H. Z. Xu, Y. Okada, and M. Kawabe. In-plane photocurrent of self-assembled InxGa1-xAs/GaAs(311)B quantum dot arrays. *Phys. Rev. B*, 64:085303(1–7), 2001.

[166] O. Stier, M. Grundmann, and D. Bimberg. Electronic and optical properties of strained quantum dots modeled by 8-band kp theory. *Phys. Rev. B*, 59:5688–5701, 1999.

[167] H. L. Störmer, R. Dingle, A. C. Gossard, W. Wiemann, and M. D. Sturge. Two-dimensional electron gas at a semiconductor-semiconductor interface. *Solid State Commun.*, 29:705–709, 1979.

[168] I. N. Stranski and L. Krastanov. "". *Sitzungsberichte d. Akad. d. Wissenschaften in Wien, Abt. IIb, Band 146*, page 797, 1937.

[169] F. Suárez, D. Fuster, L. González, Y. González, J. M. García, and M. L. Dotor. Self-assembled InAs quantum wire lasers on (001)InP at 1.6um. *Appl. Phys. Lett.*, 89:091123(1–3), 2006.

[170] Q. Sun, C. Lacelle, D. Morris, M. Buchanan, P. Marshall, P. Chow-Chong, and A. P. Roth. Effects of substrate misorientation on anisotropic electron transport in InGaAs/GaAs heterostructures. *Appl. Phys. Lett.*, 59:1359–1361, 1991.

[171] Z. Sun, S. F. Yoo, J. Wu, and Z. Wang. Origin of the vertical-anticorrelation arrays of InAs/InAlAs nanowires with a fixed layer-ordering orientation. *J. Appl. Phys.*, 91(9):6021–6026, May 2002.

[172] A. Tabata, T. Benyattou, G. Guillot, M. Gendry, G. Hollinger, and P. Viktorovitch. Optical properties of InAs/InP surface layers formed during the arsenic stabilization process. *J. Vac. Sci. Technol. B*, 12: 2299–2304, 1994.

[173] I.-H. Tan, G. L. Snider, and E. L. Hu. A self-consistent solution of Schrödinger-Poisson equations using a nonuniform mesh. *J. Appl. Phys.*, 68:4071, 1990.

[174] G. G. Tarasov. . *private communication*, 2005.

[175] H. Temkin, R. J. McCoy, V. G. Keramidas, and W. A. Bonner. Ohmic contacts to p-type InP using Be-Au metallization. *Appl. Phys. Lett.*, 36:444–446, 1979.

[176] J. Tersoff and R. M. Tromp. Shape Transition in Growth of Strained Islands: Spontaneous Formation of Quantum Wires. *Phys. Rev. Lett.*, 70:2782–2785, 1993.

[177] Y. Tokura, T. Saku, S. Tarucha, and Y. Horikoshi. Anisotropic roughness scattering at a heterostructure interface. *Phys. Rev. B*, 46:15558–15561, 1992.

[178] Yasuhiro Tokura. Two-dimensional electron transport with anisotropic scattering potentials. *Phys. Rev. B*, 58:7151–7161, 1998.

[179] E. Tournié and K. H. Ploog. Virtual-surfactant epitaxy of strained InAs/In0.48Al0.52As quantum wells. *Appl. Phys. Lett.*, 62:858–860, 1993.

[180] D. C. Tsui and R. A. Logan. Observation of two-dimensional electrons in LPE-grown GaAs-AlxGa1-xAs heterojunctions. *Appl. Phys. Lett.*, 35:99–101, 1979.

[181] A. A. Ukhanov, R. H. Wang, T. J. Rotter, A. Stintz, L. F. Lester, P. G. Eliseev, and K. J. Malloy. Orientation dependence of the optical properties in InAs quantum-dash lasers on InP. *Appl. Phys. Lett.*, 81: 981–983, 2002.

[182] K. v. Klitzing, G. Dorda, and M. Pepper. New Method for High-Accuracy Determination of the Fine-Structure Constant Based on Quantized Hall Resistance. *Phys. Rev. Lett.*, 45:494–497, 1980.

[183] L. T. van der Pauw. A method of measuring specific resistivity and Hall effect of discs of arbitrary shape. *Philips Res. Rep.*, 13:1–9, 1958.

[184] L. T. van der Pauw. Determination of resistivity tensor and Hall tensor of anisotropic conductors. *Philips Res. Rep.*, 16:187–195, 1969.

[185] Y. P. Varshni. Temperature depoendence of the energy gap in semiconductors. *Physica*, 34:149–154, 1967.

[186] I. Vurgaftman and J. R. Meyer. . *Phys. Rev. B*, 60:14294–14301, 1999.

[187] I. Vurgaftman and J. Singh. Polarization dependence of the absorption coefficient for an array of strained quantum wires. *J. Appl. Phys.*, 77: 4931–4934, 1995.

[188] I. Vurgaftman, J. R. Meyer, and L. R. Ram-Mohan. Band parameters for III-V compound semiconductors and their alloys. *J. Appl. Phys.*, 89:5815–5875, 2001.

[189] X. Wallart, B. Pinsard, and F. Mollot. High-mobility InGaAs/InAlAs pseudomorphic heterostructures on InP(001). *J. Appl. Phys.*, 97: 053706(1–6), 2005.

[190] Xavier Wallart. A combined RHEED and photoemission comparison of the GaP and InP(001) (2 ×4) surface reconstructions. *Surface Science*, 506:203–212, 2002.

[191] C. Walther, J. Bollmann, H. Kissel, H. Kirmse, W. Neumann, and W. T. Masselinka). Characterization of electron trap states due to InAs quantum dots in GaAs. *Appl. Phys. Lett.*, 76:2916–2918, 2000.

[192] W. Walukiewicz, J. Lagowski, L. Jastrzebski, P. Rava, M. Lichtensteiger, C. H. Gatos, and H. C. Gatos. Electon mobility and free-carrier absorption in InP; determination of the compensation ratio. *J. Appl. Phys.*, 51:2659–2668, 1980.

[193] Z. M. Wang, K. Holmes, Yu. I. Mazur, , and G. J. Salamo. Fabrication of (In,Ga)As quantum-dot chains on GaAs(100). *Appl. Phys. Lett.*, 84: 1931–1933, 2004.

[194] J. D. Wasscher. A method for determining the anisotropy of the resistivity. *Philips Res. Rep., Suppl.*, 8:15–19, 1969.

[195] H. H. Wieder. Problems and prospects of compound semiconductor field-effect transistors. *J. Vac. Sci. Technol.*, 17:1009–1018, 1980.

[196] P. Wölfle and R. H. Bhatt. Electron localization in anisotropic systems. *Phys. Rev. B*, 30:3542–3544, 1984.

[197] H. Yang, V. P. LaBella, D. W. Bullock, and P. M. Thibado. Role of As4 in Ga diffusion on the GaAs(001)-(2 x 4) surface: A molecular beam epitaxy-scanning tunneling microscopy study. *J. Vac. Sci. Technol. B*, 17:1778–1780, 1999.

[198] H. Yang, P. Ballet, and G. J. Salamo. Formation of quantum wires and dots on InP(001) by As/P exchange. *J. Appl. Phys.*, 89(12):7871–7874, June 2001.

[199] H. Yang, X. Mu, I. B. Zotova, Y. J. Ding, and G. J. Salamo. Self-assembled InAs quantum wires on InP(001). *J. Appl. Phys.*, 91(6): 3925–3927, March 2002.

[200] Qiu yi Ye, B. I. Shklovskii, A. Zrenner, F. Koch, and K. Ploog. Hopping transport in delta-doping layers in GaAs. *Phys. Rev. B*, 41:8477–8484, 1990.

[201] S. Yoon, Y. Moon, T.-W. Lee, E. Yoon, and Y. D. Kim. Effects of As/P exchange reaction on the formation of InAs/InP quantum dots. *Appl. Phys. Lett.*, 74(14):2029–2031, April 1999.

[202] J. K. Zahurak, A. A. Iliadis, S. A. Rishton, and W. T. Masselink. Transistor performance and electron transport properties of high performance InAs quantum-well FET's. *IEEE Electron. Device Lett.*, 15: 489–492, 1994.

[203] N. A. Zakhleniuk, C. R. Bennett, N. C. Constantinou, B. K. Ridley, and M. Babiker. Theory of optical-phonon limited hot-electron transport in quantum wires. *Phys. Rev. B*, 24:17838–17849, 1996.

[204] S. B. Zhang and A. Zunger. Method of linear combination of structural motifs for surface and step energy calculations: Application to GaAs(001). *Phys. Rev. B*, 53:1343–1356, 1996.

[205] W. Zhang, H. Lim, M. Taguchi, S. Tsao, B. Movaghar, and M. Razeghi. High-detectivity InAs quantum-dot infrared photodetectors grown on InP by metal-organic chemical-vapor deposition. *Appl. Phys. Lett.*, 86: 191103(1–3), May 2005.

[206] X. H. Zhang, R. E. Doezema, N. Goel, S. J. Chung, and M. B. Santos. Photoluminescence study of InSb/Al(x)In(1-x)Sb quantum wells. *Appl. Phys. Lett.*, 89:021907(1–3), 2006.

[207] Z. H. Zhang, G. W. Pickrell, K. L. Chang, H. C. Lin, K. C. Hsieh, and K. Y. Cheng. Surface morphology control of InAs nanostructures grown on InGaAs/InP. *Appl. Phys. Lett.*, 82(25):4555–4557, June 2003.

[208] M. Zinnke-Allmang, L. C. Feldman, and M. H. Grabaw. Clustering on surfaces. *Surf. Sci. Rep.*, 16:377–463, 1929.

Appendix A

Semi square vdP anisotropies

Table A.1: Four terminal resistances and their anisotropy A_{vdP} on a semi-square with long edge in the x-direction (high conductivity direction). Resistances calculated for an average resistivity $\rho_{\mathrm{avg}} = 1\ \Omega$.

A	R_{yy} Ω	R_{xx} Ω	A_{vdP} $= R_{yy}/R_{xx}$	A	R_{yy} Ω	R_{xx} Ω	A_{vdP} $= R_{yy}/R_{xx}$
1.00	5.925E-2	5.611E-1	1.056E-1	16.00	1.330E0	4.755E-3	2.798E2
2.00	1.685E-1	2.805E-1	6.007E-1	17.00	1.391E0	3.919E-3	3.549E2
3.00	2.802E-1	1.686E-1	1.662E0	18.00	1.450E0	3.248E-3	4.465E2
4.00	3.873E-1	1.103E-1	3.511E0	19.00	1.507E0	2.706E-3	5.568E2
5.00	4.887E-1	7.604E-2	6.427E0	20.00	1.565E0	2.265E-3	6.910E2
6.00	5.842E-1	5.435E-2	1.075E1	30.00	2.063E0	4.671E-4	4.415E3
7.00	6.747E-1	3.992E-2	1.690E1	40.00	2.461E0	1.234E-4	1.994E4
8.00	7.605E-1	2.996E-2	2.539E1	50.00	2.849E0	3.821E-5	7.457E4
9.00	8.423E-1	2.288E-2	3.682E1	60.00	3.182E0	1.324E-5	2.404E5
10.00	9.202E-1	1.773E-2	5.190E1	70.00	3.486E0	4.993E-6	6.983E5
11.00	9.959E-1	1.391E-2	7.158E1	80.00	3.773E0	2.015E-6	1.873E6
12.00	1.067E0	1.104E-2	9.665E1	90.00	4.040E0	8.593E-7	4.702E6
13.00	1.137E0	8.837E-3	1.287E2	100.00	4.296E0	3.838E-7	1.120E7
14.00	1.203E0	7.136E-3	1.686E2				
15.00	1.267E0	5.806E-3	2.182E2				

Appendix B

Processing protocols for transport samples

B.1 Mesa etch mask

1. Cleaned sample on spinner, spin at 6000rpm, 60 s while blowing with dry N_2. This provides a dry surface to ensure a good adhesion of the resist.

2. (From here on yellow light necessary to prevent the premature exposure.) Put a drop of negative resist (Allresist, AR7500.08) on sample. (For very small samples - soak off most of the drop with clean tissue paper.) Spin at 6000 rpm/40 s to obtain an 80 nm coverage.

3. Pre-bake resist on hotplate, 85°C/120s.

4. Expose resist with e-beam lithography at an area dose of 115 μC/cm^{-2}.

5. Postbake resist on hotplate 110°C/120s.

6. Develop in fresh (not older than two days) developer (Allresist, AR-300-47), 21°C/50s, by gently stirring developer with the sample that is kept by tweezers.

7. Stop developing in two subsequent baths of DI water, 30 s.

8. (No more yellow light necessary.) Blow dry with dry N_2. (Direct N_2 stream towards the tweezers to avoid contamination from the tweezers.)

9. Check mask in microscope.

B.2 Mesa etching

1. Reactive ion etching (to avoid under-etching) of 65 nm InP to create a 65 nm high mesa [1].

2. Remove mask in remover (Allresist, AR300-70) 70°C/20 min. (Alternatively, aceton can be used.)

3. Rinse with DI water.

4. Blow dry with N_2.

B.3 Metallization mask - double layer

This type of mask was used for the ohmic contacts and for the gate contacts. The resist should be at least twice as thick as the metallization in order to enable the lift-off process. Additionally, a double layer is employed to provides an undercut. This undercut prevents the metal deposition from covering the side-walls of the resist.

1. Cleaned sample on spinner, spin at 6000rpm, 60 s while blowing with dry N_2.

2. Put a drop of positive resist (Allresist, AR-P610.06) on sample. Spin at 2000 rpm/40 s to obtain a 400 nm coverage.

3. Pre-bake resist in convection oven hotplate, 190°C/60 min.

4. Put a drop of positive resist (Allresist, AR-P679.02) on sample. Spin at 2000 rpm/40 s to obtain a 120 nm coverage.

5. Pre-bake resist in convection oven hotplate, 190°C/60 min.

6. Expose resist with e-beam lithography at an area dose of 100 $\mu C/cm^{-2}$.

7. Develop in fresh (not older than two days) developer (Allresist, AR-600-50), 21°C/120s, by gently stirring developer with the sample that is kept by tweezers.

8. Stop developing in stopper (Allresist, AR600-60) 21°C/30 s.

9. Rinse in two subsequent baths of DI water.

[1] Etching done by S. Dreßler in Heinrich-Hertz-Institut, Berlin.

10. Blow dry with dry N_2.

11. Check mask in microscope.

(Caution! Alkaline solutions corrode this resist.)

B.4 N-type ohmic contacts

Contacts were evaporated using an e-beam evaporator EBEV UV600 in UHV ($6 \cdot 10^{-8}$ mbar) [2].

1. HF dip HF(5%):H_2O 1:25, 10 s, to remove oxide layer.

2. Rinse in DI water.

3. Blow dry with N_2.

4. Ar sputter, 20 s/100 V, to clean the surface.

5. Ti getter.

6. Evaporate Ge, 10 nm.

7. Evaporate Ni, 10 nm.

8. Evaporate Ge, 30 nm.

9. Evaporate Ni, 10 nm.

10. Evaporate Au, 200 nm.

11. Lift-off. Sample in hot remover and ultrasonic-bath. If ripples visible, remover successfully crept under the resist. Use tweezers to gently pull metallization off the resist, or use syringe to spray developer onto sample surface to facilitate lift-off.

12. Rinse with DI water.

13. Blow dry with N_2.

14. Annealing at 375°C/60 s in forming gas (90% N_2, 10% H_2) to form an ohmic contact.

[2] N-type metallization done by S. Dreßler in Heinrich-Hertz-Institut, Berlin.

B.5 P-type ohmic contacts

Contact were evaporated using thermal evaporation of an AuBe alloy. [3].

1. Plasma oxidation (of possible resist remnants on the contact areas) at 40 W/60 s. This did not decrease the resist thickness significantly.
2. HF dip HF(40%):H_2O 1:500, 15 s, to remove oxide layer.
3. Rinse in DI water.
4. Blow dry with N_2.
5. Thermally evaporate Au:Be (1 wt.% of Be) to form a 160 nm thick metallization layer.
6. Lift-off in acetone and ultrasonic-bath.
7. Clean in ethanol.
8. Blow dry with N_2.
9. Annealing at 330°C/120 s in forming gas (90% N_2, 10% H_2) to form an ohmic contact.

B.6 Gate stack

The gate stack consists of 100 nm SiN_x as insulator and a Ti/Pt/Au metal gate electrode to form a MIS structure with the semiconductor [4].

1. HF dip HF(5%):H_2O 2:25, 15 s, to remove oxide layer.
2. Rinse in DI water.
3. Blow dry with N_2.
4. PECVD of 100 nm SiN_x.
5. E-beam evaporator: Ar sputter, 100V/60s.
6. Ti 20 nm.
7. Pt 30 nm.

[3] P-type metallization done by E. Wiebicke in Paul-Drude-Institut, Berlin.
[4] The gate deposition was done by S. Dreßler in Heinrich-Hertz-Institut, Berlin.

8. Au 140 nm.
9. Lift-off (Caution! Use of ultrasonic tends to removes the gate stack also from the semiconductor surface.).
10. Rinse in DI water.
11. Blow dry with N_2.

Acknowledgements

I am grateful to the members and former members of our group who supported my work in many ways:
Prof. Dr. William Ted Masselink gave me the opportunity to research, work, and teach in his group. I appreciate the stimulating discussions with him spiced with his enthusing optimism, and his open mind to new ideas.
Dr. Carsten Walther, who was the first of our group to grow InAs on InP, is acknowledged for providing preliminary samples.
Dr. Mykhaylo Semtsiv has introduced me to GSMBE, and is deeply acknowledged for our co-operation in all MBE-lab related issues.
Dipl. Phys. Robert Pomraenke, Karin Braune, and Dr. Anne Gerlitzke (Institut für Kristallzüchtung) are thanked for performing parts of the AFM measurements.
Dipl. Phys. Robert Pomraenke is further acknowledged for the polarized PL measurements and some of the transport characterization.
I am grateful to Dipl. Phys. Stefan Eilers who did parts of the e-beam lithography, and to Martin Wienold for introducing me to ebl.
I like to thank Dr. Uwe Müller for introducing me to transmission measurements.
I am particularly grateful to Dr. Fariba Hatami for proof-reading this thesis. In addition, she, and Thi Lien Tran often cheered me up.
I like to thank Dipl. Phys. Sebastian Dressler for uncomplicated help with processing at the Heinrich-Hertz Institut.
Dr. Holm Kirmse (AG Kristallografie) is acknowledged for TEM imaging.

The members of Paul-Drude Institut are acknowledged for their support: Dr. Helmar Kostial patiently answered lots of questions regarding transport, associated processing and measurements, and helped with the processing. Dr. K.-J. Friedland provided me the opportunity to do magneto-transport measurements at 0.3 K, and helped with stimulating discussion and critical questions. Claudia Herrmann provided me access to the AFM. Edith Wiebicke, is thanked for her processing support.

Dr. Yuriy Mazur and Dr. Vasyl Kunets of University of Arkansas are acknowledged for their interest in my work, for motivation and fruitful discussions during their time in our group.

Last but not least Prof. G. J. Salamo and Prof. R. Fornari are deeply appreciated for refereeing this thesis.

Selbständigkeitserklärung

Hiermit erkläre ich, die vorliegende Dissertation selbständig und nur unter Verwendung der angegebenen Hilfen und Hilfsmittel angefertigt zu haben.

Berlin, 13.02.2007 Oliver Bierwagen